The thermal and rheological state of the Northern Argentinian foreland basins

Kumulative Dissertation
zur Erlangung des akademischen Grades

„doctor rerum naturalium"
(Dr. rer. nat.)

im Fachbereich Geowissenschaften

von
Christian Meeßen
M. Sc. Geowissenschaften

Eingereicht an der
Mathematisch-Naturwissenschaftlichen Fakultät
Institut für Geowissenschaften
der Universität Potsdam

und

Sektion 4.5 Sedimentbeckenanalyse
Deutsches GeoForschungsZentrum Potsdam

Datum der Disputation:
07. Oktober 2019

Abstract

The foreland of the Andes in South America is characterised by distinct along strike changes in surface deformational styles. These styles are classified into two end-members, the thin-skinned and the thick-skinned style. The superficial expression of thin-skinned deformation is a succession of narrowly spaced hills and valleys, that form laterally continuous ranges on the foreland facing side of the orogen. Each of the hills is defined by a reverse fault that roots in a basal décollement surface within the sedimentary cover, and acted as thrusting ramp to stack the sedimentary pile. Thick-skinned deformation is morphologically characterised by spatially disparate, basement-cored mountain ranges. These mountain ranges are uplifted along reactivated high-angle crustal-scale discontinuities, such as suture zones between different tectonic terranes.

Amongst proposed causes for the observed variation are variations in the dip angle of the Nazca plate, variation in sediment thickness, lithospheric thickening, volcanism or compositional differences. The proposed mechanisms are predominantly based on geological observations or numerical thermomechanical modelling, but there has been no attempt to understand the mechanisms from a point of data-integrative 3D modelling. The aim of this dissertation is therefore to understand how lithospheric structure controls the deformational behaviour. The integration of independent data into a consistent model of the lithosphere allows to obtain additional evidence that helps to understand the causes for the different deformational styles. Northern Argentina encompasses the transition from the thin-skinned fold-and-thrust belt in Bolivia, to the thick-skinned Sierras Pampeanas province, which makes this area a well suited location for such a study. The general workflow followed in this study first involves data-constrained structural- and density-modelling in order to obtain a model of the study area. This model was then used to predict the steady-state thermal field, which was then used to assess the present-day rheological state in northern Argentina.

The structural configuration of the lithosphere in northern Argentina was determined by means of data-integrative, 3D density modelling verified by Bouguer gravity (Meeßen et al., 2018). The model delineates the first-order density contrasts in the lithosphere in the uppermost $200\,\mathrm{km}$, and discriminates bodies for the sediments, the crystalline crust, the lithospheric mantle and the subducting Nazca plate. To obtain the intra-crustal density structure, an automated inversion approach was developed and applied to a starting structural model that assumed a homogeneously dense crust. The resulting final structural model indicates that the crustal structure can be represented by an upper crust with a density of $2800\,\mathrm{kg\,m^{-3}}$, and a lower crust of $3100\,\mathrm{kg\,m^{-3}}$. The Transbrazilian Lineament, which separates the Pampia terrane from the Río de la Plata craton, is expressed as a zone of low average crustal densities.

In an excursion, we demonstrate in another study, that the gravity inversion method developed to obtain intra-crustal density structures, is also applicable to obtain density variations in the uppermost lithospheric mantle. Densities in such sub-crustal depths are difficult to constrain from seismic tomographic models due to smearing of crustal velocities. With the application to the uppermost lithospheric mantle in the north Atlantic, we demonstrate in Tan et al. (2018) that lateral density trends of at least 125 km width are robustly recovered by the inversion method, thereby providing an important tool for the delineation of subcrustal density trends.

Due to the genetic link between subduction, orogenesis and retroarc foreland basins the question rises whether the steady-state assumption is valid in such a dynamic setting. To answer this question, I analysed (i) the impact of subduction on the conductive thermal field of the overlying continental plate, (ii) the differences between the transient and steady-state thermal fields of a geodynamic coupled model. Both studies indicate that the assumption of a thermal steady-state is applicable in most parts of the study area. Within the orogenic wedge, where the assumption cannot be applied, I estimated the transient thermal field based on the results of the conducted analyses.

Accordingly, the structural model that had been obtained in the first step, could be used to obtain a 3D conductive steady-state thermal field. The rheological assessment based on this thermal field indicates that the lithosphere of the thin-skinned Subandean ranges is characterised by a relatively strong crust and a weak mantle. Contrarily, the adjacent foreland basin consists of a fully coupled, very strong lithosphere. Thus, shortening in northern Argentina can only be accommodated within the weak lithosphere of the orogen and the Subandean ranges. The analysis suggests that the décollements of the fold-and-thrust belt are the shallow continuation of shear zones that reside in the ductile sections of the orogenic crust. Furthermore, the localisation of the faults that provide strain transfer between the deeper ductile crust and the shallower décollement is strongly influenced by crustal weak zones such as foliation. In contrast to the northern foreland, the lithosphere of the thick-skinned Sierras Pampeanas is fully coupled and characterised by a strong crust and mantle. The high overall strength prevents the generation of crustal-scale faults by tectonic stresses. Even inherited crustal-scale discontinuities, such as sutures, cannot sufficiently reduce the strength of the lithosphere in order to be reactivated. Therefore, magmatism that had been identified to be a precursor of basement uplift in the Sierras Pampeanas, is the key factor that leads to the broken foreland of this province. Due to thermal weakening, and potentially lubrication of the inherited discontinuities, the lithosphere is locally weakened such that tectonic stresses can uplift the basement blocks. This hypothesis explains both the spatially disparate character of the broken foreland, as well as the observed temporal delay between volcanism and basement block uplift.

This dissertation provides for the first time a data-driven 3D model that is consistent with geophysical data and geological observations, and that is able to causally link the thermo-rheological structure of the lithosphere to the observed variation of surface deformation styles in the retroarc foreland of northern Argentina.

Zusammenfassung

Das Vorland der südamerikanischen Anden ist durch lateral variierende Deformationsre-
gimes des östlichen Vorlands geprägt. Dabei treten zwei grundlegend verschiedene Endglie-
der mit charakteristischer Architektur auf: flach abgescherte Falten- und Überschiebungsgür-
tel einerseits und Vorland-Sockelüberschiebungen („zerbrochenes Vorland") andererseits. Das
morphologische Erscheinungsbild der Falten- und Überschiebungsgürtel entspricht lateral aus-
gedehnten, dicht aneinander gereihten Abfolgen von Hügeln und Tälern. Die Hügel werden
durch eine darunter liegende Überschiebung definiert, die in einem subhorizontalen Abscher-
horizont in 10 bis 20 km Tiefe endet. Sockelüberschiebungen hingegen sind in Gebieten mit
geringer Sedimentmächtigkeit zu finden und sind durch weit auseinander liegende Erhebun-
gen charakterisiert, welche von steil einfallenden, reaktivierten krustenskaligen Verwerfungen
begrenzt werden.

Als Ursachen der beobachteten Deformationsvariationen wurden präexistente Schwäche-
zonen, Sedimentmächtigkeiten, Lithosphärenverdickung, Vulkanismus oder kompositionelle
Eigenschaften aufgeführt. Diese Vorschläge waren überwiegend konzeptuell und meist auf
Grundlage von Feldbeobachtungen oder synthetischen numerischen, thermo-mechanischen
Modelle abgeleitet. Die vorliegende Dissertation beleuchtet zum ersten mal die Ursachen der
beobachteten Deformationsstile aus der Perspektive von dreidimensionaler, Daten-integrativer
Modellierung. Durch die Integration voneinander unabhängiger Daten erlaubt diese Art der
Beschreibung des physikalischen Zustands der Lithosphäre die Erlangung zusätzliche Hin-
weise auf die zugrundeliegenden Ursachen der verschiedenen Derformationsregimes. Für eine
solche Studie bietet sich Nord-Argentinien an, da dort beide Vorland-Endglieder vorzufinden
sind. Die dafür im wesentlichen durchgeführten Arbeitsschritte beinhalten die Erstellung ei-
nes strukturellen Dichtemodells des Untersuchungsgebiets, die Berechnung des 3D stationären
thermischen Feldes, sowie die Analyse der rheologischen Eigenschaften der Lithosphäre.

Das datenbasierte strukturelle Dichtemodell (Meeßen u. a., 2018) ist mit verschiedenen geo-
logischen und geophysikalischen Beobachtungen sowie dem Bouguer-Schwerefeld konsistent.
Dieses Modell bildet die primären Dichtekontraste der oberen 200 km der Lithosphäre ab
und differenziert Körper für die Sedimente, die kristalline Kruste, den lithosphärischen Man-
tel, und die subduzierende Nazca-Platte. Um die krusteninterne Dichteverteilung zu erhalten
wurde ein automatisierter Inversionsprozess entworfen der es erlaubt eine leichtere Oberkruste
und eine schwerere Unterkruste geometrisch zu definieren. Die Modellierung zeigt, dass die
Kruste in Nord-Argentinien durch eine leichtere Oberkruste ($2800\,\mathrm{kg\,m^{-3}}$) und eine dichtere
Unterkruste ($3100\,\mathrm{kg\,m^{-3}}$) repräsentiert werden kann. Das Transbrasilianische Linement, wel-
ches das Pampia Terran im Westen vom Río de La Plata Kraton im Osten trennt, ist durch
eine im Vergleich zur Umgebung geringere durchschnittliche Krustendichte charakterisiert.

In einem Exkurs wird anschließend demonstriert, dass die hier entwickelte Inversionsme-

thodik zur Ermittlung von intrakrustalen Dichtekontrasten auch im obersten lithosphärischen Mantel angewandt werden kann. Dichten zwischen der Kruste-Mantel-Grenze und etwa 50 km Tiefe sind besonders schwer zu bestimmen, da tomographische Modelle die Geschwindigkeits- variationen von seismischen Wellen in diesen Bereichen nicht auflösen. In Tan u. a. (2018) demonstrieren wir, dass die Inversionsmethode Dichteverläufe mit einer lateralen Ausdehnung von 125 km oder weniger ermitteln kann, und somit einen wichtigen Beitrag zur Bestimmung von subkrustalen Dichteverteilungen im Mantel liefert.

Wegen der genetischen Verbindung zwischen Subduktion, Orogenese und Retroarc Vorland- becken stellt sich die Frage, ob die Annahme eines stationären thermischen Feldes für solch ein dynamisches Modelliergebiet zulässig ist. Um diese Frage zu beantworten wurde zum einen der Einfluss von Subduktion auf das konduktive thermische Feld auf die kontinentale Lithosphäre untersucht. Zum anderen wurde die Abweichung zwischen transientem und stationären ther- mischen Feld eines gekoppelten geodynamischen Modells untersucht. Beide Untersuchungen weisen darauf hin, dass die Annahme eines stationären thermischen Felds für den Großteil des Modelliergebiets zulässig ist. Im orogenen Keil, in dem diese Annahme nicht gilt, wurde das transiente thermische Feld mithilfe der erfolgten Untersuchungen abgeschätzt.

Entsprechend kann für das Arbeitsgebiet im Vorland das strukturelle Modell aus dem er- sten Schritt zur Berechnung des stationären 3D konduktiven thermischen Feldes herangezo- gen werden. Basierend auf der ermittelten Dichte- und Temperatur-Konfigurationen konnte anschließend die rheologische Konfiguration berechnet werden. Die rheologischen Analysen zeigen, dass die Lithosphäre in Falten- und Überschiebungsgürteln nur eine gerine Festig- keit besitzt und die Kruste Großteil zur integrierten Festigkeit beiträgt. Das benachbarte Vorlandbecken jedoch weist eine vollständig gekoppelte und starke Lithosphäre auf, weshalb Krustenverkürzung nur im vergleichsweise schwachen orogenen Keil aufgenommen werden kann. Daher komme ich zu der Schlussfolgerung, dass die Abscherhorizonte der Falten- und Überschiebungsgürtel die oberflächennahe Fortsetzung von Scherzonen in der duktilen Kruste unterhalb des Orogens sind. Die Lokalisation der Transferzonen zwischen der duktilen Kru- ste und dem Abscherhorizont sind dabei maßgeblich durch präexistente Schwächezonen in der Kruste beeinflusst. Im zerbrochenen Vorland der Sierras Pampeanas ist die Lithosphäre vollständig gekoppelt und durch einen Mantel hoher Festigkeit charakterisiert. Die sehr hohe integrierte lithosphärische Festigkeit des zerbrochenen Vorlands verhindert die Bildung von Störungen durch tektonische Kräfte. Selbst krustenskalige Schwächezonen können die Festig- keit nicht ausreichend reduzieren, weshalb eine thermische Schwächung benötigt wird. Daher spielt der Magmatismus, der in direkter Nachbarschaft zu den Schwächezonen in der Sier- ras Pampeanas nachgewiesen wurde, eine Schlüsselrolle in der Entstehung des zerbrochenen Vorlands. Diese Hypothese erklärt die große räumliche Distanz zwischen den Vorlandsockel- überschiebungen, sowie die beobachtete zeitliche Verzögerung zwischen Magmatismus und Hebung der Gebirgskämme.

Die vorliegende Studie kann somit aufgrund Daten-integrativer Modellierung einen kausalen Zusammenhang zwischen der Lithosphärenstruktur, den beobachteten Deformationsmechanis- men und unabhängigen geologischen Beobachtungen herstellen.

Declaration of author contributions

In this cumulative dissertation, chapters 2.1, 2.2 and 3.1 consist of published studies where C. Meeßen is either first author or co-author. Mathematical expressions, symbols and orthography in these chapters were adjusted in order to comply with the prevailing style of this document. The bibliography relevant for all chapters and the appendices are located at the end of the dissertation.

In **Chapter 2.1**, the crustal structure of the foreland in Northern Argentina is analysed by means of data integrative, three-dimensional modelling, published in *C. Meeßen, J. Sippel, M. Scheck-Wenderoth, C. Heine and M. R. Strecker (2018). 'Crustal Structure of the Andean Foreland in Northern Argentina: Results From Data-Integrative Three-Dimensional Density Modeling'. In:* Journal of Geophysical Research: Solid Earth *123.2, pp. 1875–1903.* ISSN*: 2169-9356.* DOI*: 10.1002/2017JB014296.* This study was entirely designed and conducted by C. Meeßen under the supervision of M. Scheck-Wenderoth, M. R. Strecker and J. Sippel. Based on published studies, C. Meeßen developed the code to obtain temperature and density distributions in the mantle that was used in this study. C. Meeßen furthermore designed the gravity inversion method that was used to obtain the thickness distribution of the lower crust. C. Heine provided data on the sedimentary thickness distribution on the study area and adjoining regions. All co-authors were involved in the discussion of the manuscript.

In **Chapter 2.2**, the gravity inversion method developed by C. Meeßen for Chapter 2.1, is applied to the upper mantle near Iceland. The study was published in *P. Tan, J. Sippel, A. J. Breivik, C. Meeßen and M. Scheck-Wenderoth (2018). 'Lithospheric Control on Asthenospheric Flow From the Iceland Plume: 3-D Density Modeling of the Jan Mayen-East Greenland Region, NE Atlantic'. In:* Journal of Geophysical Research: Solid Earth *123.10, pp. 9223–9248.* ISSN*: 2169-9356.* DOI*: 10.1029/2018JB015634.* The study was mainly designed by P. Tan and J. Bott. C. Meeßen aided in the discussion part, and study design, applied the inversion method with variable initial conditions on the upper mantle and conducted the robustness tests. All authors were involved in the discussion of the manuscript.

Chapter 3.1 analyses whether subduction is capable of modifying the thermal field of a retroarc foreland basin by thermal conduction. This study was submitted to the International Journal of Earth Sciences on 13. March 2019 (IJES-D-19-00077). The study was designed and conducted by C. Meeßen under the supervision of M. Scheck-Wenderoth, M. R. Strecker and J. Bott. A. Jacquey supported the effort by providing pre-release versions of the process simulator LYNX and aided C. Meeßen during the implementation of additional code. All co-authors were involved in the discussion of the manuscript.

Contents

List of Figures

List of Tables

List of symbols and abbreviations

Symbol	Property	Unit
α	Isobaric expansion coefficient	K^{-1}
$\dot{\epsilon}$	Strain rate	s^{-1}
λ	Bulk thermal conductivity	$W\,m^{-1}\,K^{-1}$
μ	Shear modulus	Pa
μ_f	Friction coefficient	–
ω	Wave frequency	Hz
ϕ_0	Porosity at time of deposition	–
Φ	Internal friction angle	°
ρ_{bulk}	Bulk rock density	$kg\,m^{-3}$
ρ_S	Solid rock density	$kg\,m^{-3}$
ρ_L	Pore fluid density	$kg\,m^{-3}$
σ_b	Byerlee's law yield strength	Pa
A_D	Dorn's law strain rate	s^{-1}
A_p	Power law pre-exponential factor	$Pa^{-n}s^{-1}$
C_p	Bulk specific heat capacity	$J\,kg^{-1}\,K^{-1}$
f_f	Byerlee's law friction coefficient	–
f_p	Pore fluid factor	–
g	Gravitational acceleration	$m\,s^{-2}$
g_z	Gravity anomaly	$mGal^{\dagger}$
g_{obs}	Observed gravity anomaly	$mGal^{\dagger}$
g_{calc}	Computed gravity anomaly	$mGal^{\dagger}$
k	Compaction coefficient	km^{-1}
K	Bulk modulus	Pa
n	Power law exponent	–
Q	Anelasticity attenuation	–
Q_D	Dorn's law activation energy	$kJ\,mol^{-1}$
Q_R	Radiogenic heat production	$W\,m^{-3}$
Q_p	Power law activation energy	$kJ\,mol^{-1}$
R	Universal gas constant	$J\,mol^{-1}\,K^{-1}$
R^2	Empirical correlation coefficient	–
T	Temperature	K or °C
T_L	Transition temperature for T-dependent λ	K
v_p	p-wave velocity	$m\,s^{-1}$
v_s	s-wave velocity	$m\,s^{-1}$
z	Depth	m

† $1\,mGal = 10^{-5}\,m\,s^{-2}$

Abbreviation	Explanation
CPB	Chaco-Paraná basin
LAB	Lithosphere-Asthenosphere boundary
Ma	Million years ago
Moho	Mohorovičić discontinuity (crust-mantle interface)
Myr	Million years
RMS	Root mean square
TBL	Transbrazilian Lineament

1. Introduction

In the following section, I provide a short introduction into the topic of my dissertation. The geological framework in Chapter 1.1 provides the fundamental information on the regional geological background. For a more complete geological introduction of the study area, please refer to Chapter 2.1.1.

1.1. Geological framework

The Andes extend for more than 7000 km along the active margin of the South American continent (Fig. 1.1a). This margin has been subject to active tectonics most of the Phanerozoic, resulting in a complex melange of terranes that were accreted and tectonically overprinted by mountain building and rifting processes (Charrier et al., 2015; Ramos et al., 1986). From west to east, the major morphotectonic provinces of the Cenozoic central Andes comprise the Principal Cordillera, the Altiplano-Puna plateau, the Eastern Cordillera and a thrust belt. The precise onset of the Andean orogeny is a matter of debate, but recent studies estimate that the Bolivian Orocline and the Eastern Cordillera formed in the Eocene around 45 Ma (Arriagada et al., 2008; Capitanio et al., 2011).

The mass of the Andean orogen which had been lifted above mean sea level exerts a vertical force on the underlying lithosphere (Flemings and Jordan, 1989). As a response to this load, the lithosphere bends and generates (in cross-section view) a dampened sinusoidal profile with its deepest point at the thrust-wedge facing side (DeCelles, 2012). This sinusoidal profile is the fundamental form of a flexural foreland basin. Retro-foreland basins are laterally subdivided into four sections (Fig. 1.1b): adjacent to the orogenic thrust wedge, the wedge-top is the sedimentary load that covers the actively migrating thrust wedge. From the tip of the thrust wedge, the foredeep marks the section of the crust that has bent below mean sea level. Wedge-top and foredeep constitute the bulk sediment accommodation space in foreland basins. On the continent-facing side, the foredeep is limited by the forebulge - the zone where the lithosphere bends upwards due to its flexural response. In the Andean foreland basin system, the forebulge is mostly buried by sediments and only partly inferred from Geoid anomalies (Chase et al., 2009; DeCelles, 2012). Adjacent to the forebulge, the backbulge depozone represents the strongly dampened tail of the profile, extending several hundreds of kilometres into the continent. The precise nomenclature for the Andean foreland basins system is that of a retroarc foreland basin, as it is situated on continent-side of the orogen which incorporates a volcanic arc.

The idealised lateral segmentation of retroarc foreland basins, as depicted in Fig. 1.1b,

is not persistent in the Andean retroarc foreland basins. Instead, along-strike the Andes a segmentation of deformational styles of the thrust wedge is observed that can be categorised into two end-members (Jordan et al., 1983; Kley, 1999). One end-member is the *thin-skinned* style (Fig. 1.1c), where a thick sedimentary cover is detached from the underlying crust by a décollement situated within the sedimentary strata of a Paleozoic basin (Kley et al., 1999). The resulting fold-and-thrust belts, e.g. the Subandean ranges in Bolivia, are characterised by laterally continuous and densely spaced thrust faults with a prevailing eastward vergence. The surface expression of thin-skinned deformation are successions of fold trains with narrow hills and valleys, each bounded by an individual thrust fault (Strecker et al., 2011).

The other end-member of foreland deformation is the *thick-skinned* style (Fig. 1.1d), resulting in a broken foreland (Jordan et al., 1983; Kley et al., 1999; Strecker et al., 2011). In map view, this style generates spatially disparate mountain ranges which are basement-rooted by steep reverse faults (DeCelles and Giles, 1996; Kley et al., 1999; Strecker et al., 2011), e.g. the Sierras Pampeanas in western Argentina. Evidence from receiver functions in the eastern Sierras Pampeanas (Perarnau et al., 2012) suggests that these reverse faults cross-cut the whole crust, offsetting the Mohorovičić discontinuity (Moho).

An intermediate style represents the broken foreland of the Santa Barbara System of north-western Argentina (Kley et al., 1999; Pfiffner, 2017). This foreland province is located between the Sierras Pampeanas and the Subandes thrust belt. The Santa Barbara System constitutes a compressionally reactivated Cretaceous extensional province where numerous normal-fault bounded basins are inverted (Mon and Salfity, 1995).

The mechanisms that are causing these different deformation styles in the central Andes have been a matter of debate since the 1980s. Jordan et al. (1983) pointed out the spatial coincidence between deformation styles and the angle of the subducting Nazca plate. Allmendinger et al. (1983) and Pearson et al. (2013) on the other hand suggested that the absence of thick sedimentary strata in the thick-skinned Sierras Pampeanas is responsible for the observed deformation styles. Other authors suggest lithospheric thickening (Kley et al., 1999) or variations in temperature and strength of the crystalline crust (Babeyko and Sobolev, 2005).

From a global perspective, Mouthereau et al. (2013) found that the thermotectonic age of the lithosphere and deformation style correlate. The authors found that lithosphere with a thermotectonic age of up to 1 Gyr at time of collision correlates with provinces of thick-skinned deformation (less than 35% shortening), and older lithosphere is dominated by thin-skinned deformation (35% to 70% shortening). Other studies utilising numerical modelling (Bauville and Schmalholz, 2015; Jammes and Huismans, 2012; Nilfouroushan et al., 2013) yield similar conclusions. They identified systems with a weak crust to be correlated with thick-skinned deformation, whereas a shallow decoupling at intermediate crustal levels, with a strong lower crust, results in thin-skinned deformation.
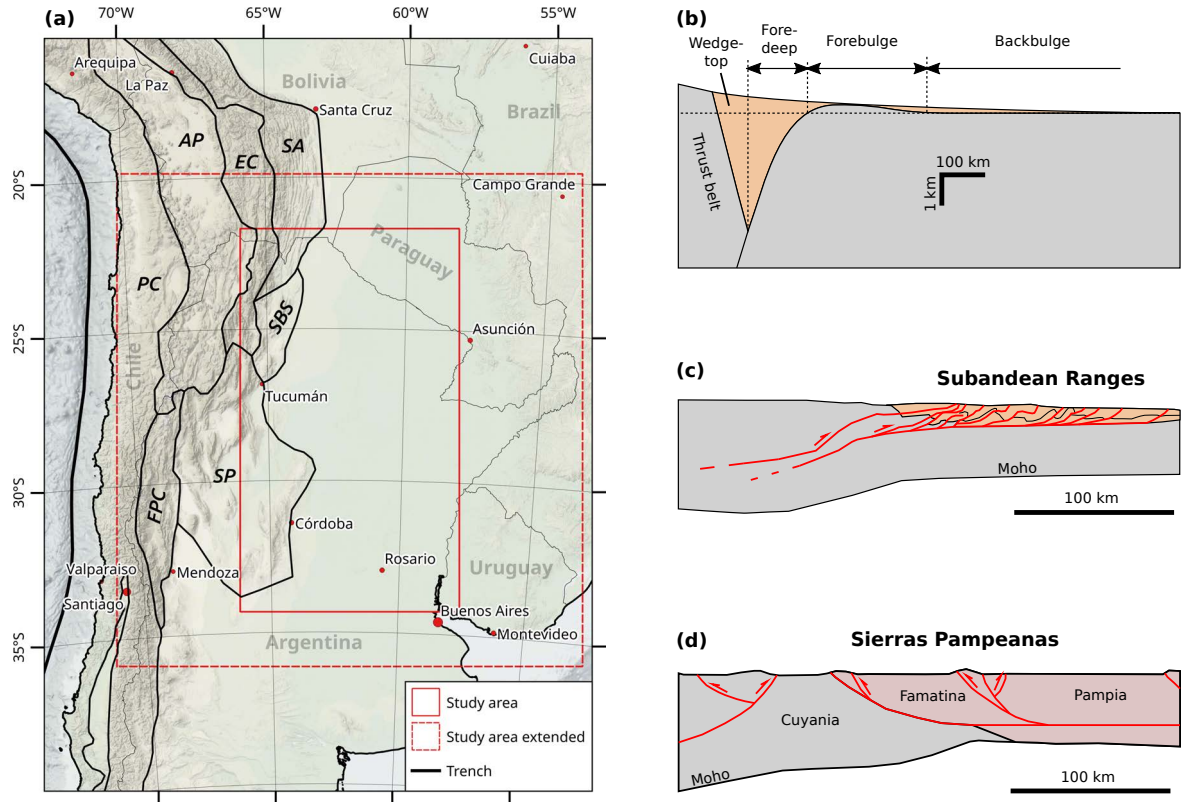
Figure 1.1.: (a) Map of the southern central Andes with the major morphotectonic provinces after Jordan et al. (1983): Altiplano-Puna plateau (AP), Eastern Cordillera (EC), Frontal- and Pre-Cordillera (FPC), Principal Cordillera (PC), Subandean thrust belt (SA), Santa-Barbara System (SBS) and the Sierras Pampeanas (SP). The study area is outlined in red. The dashed frame represents the extended study area used to compute the gravity field in Chapter 2.1; **(b)** idealised retroarc foreland segmentation after Flemings and Jordan (1989); **(c)** thin-skinned deformation style in the Subandean ranges after Kley et al. (1999) and Pfiffner (2017); **(d)** thick-skinned deformation in the western Sierras Pampeanas after Pfiffner (2017); **(b)** lateral segmentation of an ideal retroarc foreland basin, after Flemings and Jordan (1989);

1.2. Principal scientific question and workflow

The primary aim of this dissertation is to understand, how the structural configuration of the lithosphere is related to the observed deformational styles of the central Andean foreland. The study focusses on the Chaco-Paraná basin (CPB) in northern Argentina (Fig. 1.1a). This region is particularly suited for such a study as it encompasses the southern extension of the thin-skinned Subandean, the thick-skinned Sierras Pampeanas, as well as the intermediate Santa Barbara System.

The principal workflow I followed in this study contains the construction of a structural and density model of the study area, the assessment of the present-day conductive thermal field, and the evaluation of the rheological behaviour of the lithosphere. In order to successfully complete this workflow, several associated questions arose, which I also addressed during my work, and which will be outlined in the following paragraphs.

The first major challenge in the construction of the structural model that I encountered

3

was the sparse data coverage in the foreland of northern Argentina. It therefore arises the question which, and how, additional data sources could be used to constrain the structural configuration of the lithosphere in the study area. This question is tackled in Chapter 2.1 by means of data constrained 3D density modelling. In this chapter, published in Meeßen et al. (2018), I utilised tomographic models of the upper lithospheric mantle and gravity inversion to unravel the crustal density structure of the study area. To demonstrate the potential of the techniques applied in Meeßen et al. (2018), I applied them in another geological setting east of Iceland, see Chapter 2.2 (published in Tan et al., 2018).

To assess the present-day thermal field of the study area, I aimed to compute the steady-state conductive thermal field. However, the adjacent subduction zone and the orogen, which both are genetically linked to the CPB, are inherently transient in character. It is therefore not straightforward to assume a thermal steady-state in the CPB. I therefore conducted two studies to assess how subduction zone dynamics and orogenic processes may affect the thermal field of retroarc foreland basins with respect to their modelled steady-state. Therefore, in Chapter 3.1 (in review, International Journal of Earth Sciences), I first aimed to understand whether subduction itself is capable to modify the thermal field of a foreland basin by conductive thermal processes. In a second attempt to understand how elastic-plastic processes perturb the thermal field, I analysed a coupled geodynamic model representing the evolution of the Central Andes (Sobolev et al., 2006) in Chapter 3.2.

The outcomes of those two studies aided in the interpretation of the study conducted in Chapter 4. Here, I computed two end-member steady-state conductive thermal fields in the CPB. The resulting thermal fields were utilised to obtain the rheological behaviour of the lithosphere, i.e. the differential stress distribution and integrated lithospheric strength.

Finally, in Chapter 5, I summarised and reviewed the outcomes of the conducted studies and related them to other published studies on surface deformation styles.

2. The utilisation of gravity methods to obtain the density structure of the lithosphere

2.1. Crustal structure of the Andean foreland in northern Argentina: Results from data-integrative three-dimensional density modelling

2.1.1. Introduction

The foreland of the Central Andes is characterized by a change of deformation styles at about 23°S latitude (e.g., Jordan et al., 1983). North of this latitude, thin-skinned deformation dominates, where shortening is accommodated by décollements in thick Paleozoic to Tertiary sedimentary strata. In contrast, to the south, thick-skinned deformation with deep-seated reverse faults leads to spatially and temporally disparate uplift of basement-cored ranges. The mechanisms causing this change in deformation style have been a matter of discussion for more than two decades.

Early studies investigating the mechanisms causing this change pointed out the spatial coincidence of flat-slab subduction (Jordan et al., 1983) and the absence of thick sedimentary strata (Allmendinger et al., 1983) in the thick-skinned provinces of the Andean foreland. Further mechanisms proposed are lithospheric thickening (e.g., Kley et al., 1999) and variations in the temperature and strength of the crystalline crust (e.g., Babeyko and Sobolev, 2005; Mon, 1979).

Although modelling by Babeyko and Sobolev (2005) confirmed the possibility of crustal strength variations as a cause for varying foreland deformation styles, there is little evidence for this hypothesis from integrated modelling. A data-integrative approach requires a model of the lithosphere and therefore profound knowledge of its composition and internal architecture. The structure and composition of the crust in particular are crucial parameters for the temperature distribution in the lithosphere, and are therefore important factors influencing its rheological and geodynamic behaviour (e.g., Burov et al., 1998; Scheck-Wenderoth et al., 2014).

Several studies have revealed the existence of different tectonic terranes constituting the

crystalline crust beneath the Andean foreland basin; however, especially the boundary between the Río de la Plata craton and the Pampia terrane, is still a matter of debate (e.g., Chernicoff and Zappettini, 2004; Peri et al., 2015, 2013; Ramos et al., 2010). Although some wells reach basement rocks (e.g., Marengo, 2015), the intracrustal structure and composition remain poorly constrained.

Well mapped terrane boundaries also help provide an understanding of the nature of intraplate earthquakes, such as the 1811 earthquakes in New Madrid in the United States (Johnston and Schweig, 1996). With respect to the mainly east-west trending stress field in northern Argentina (e.g., Assumpção, 1992) a north-south or northeast-southwest trending boundary between the Pampia terrane and Río de la Plata craton has significantly different implications on the seismic potential of the region. Given these problems, gravity-constrained density modelling is a method well-suited for obtaining better insight into the compositional structure of the crystalline crust.

Density modelling utilizes the observed gravity field of the Earth to gain insight into its interior density structure. The deviations from the expected gravity field, the gravity anomalies, contain valuable information on the distribution of masses in the Earth's subsurface. However, direct inversion of observed gravity anomalies without additional data constraints does not yield a unique density distribution. To minimize this non-uniqueness of the density models, we integrated constraints on densities of major geological units and on the configuration of the first-order density interfaces within the lithosphere. First-order density interfaces generally exist between the atmosphere and the Earth's surface (topography), water bodies and the solid earth (bathymetry), sediments and crystalline crust (basement), and at the crust-mantle boundary (Fowler, 1990).

Previously published gravity-constrained models of the Central Andes and their foreland (Tassara, 2006; Tassara and Echaurren, 2012) have used approaches that filter the observed gravity field to obtain the geometries of these interfaces. However, although deep-seated density contrasts create long-wavelength anomalies in the observed gravity field, the argument that long-wavelength anomalies solely originate from deep-seated density contrasts is not straightforward. This is due to the fact that gravity anomalies are non-unique, and the superposition of density variations of different shapes can produce the same gravity anomaly if placed at different depths.

In light of these complexities, in this study we attempted to integrate observations that define the major density interfaces (between sediments, crystalline crust and lithospheric mantle) a priori and derive the geometry of present-day intracrustal interfaces using three-dimensional density modelling. We assessed the validity of the inferred crustal density structure by performing a detailed sensitivity analysis of the model. The results of this study enable further evaluation of the thermal field and the rheological behaviour of the lithosphere, so that primary mechanisms responsible for deformation style variations in the foreland of the Central Andes can be identified.

2.1.1.1. Geological setting
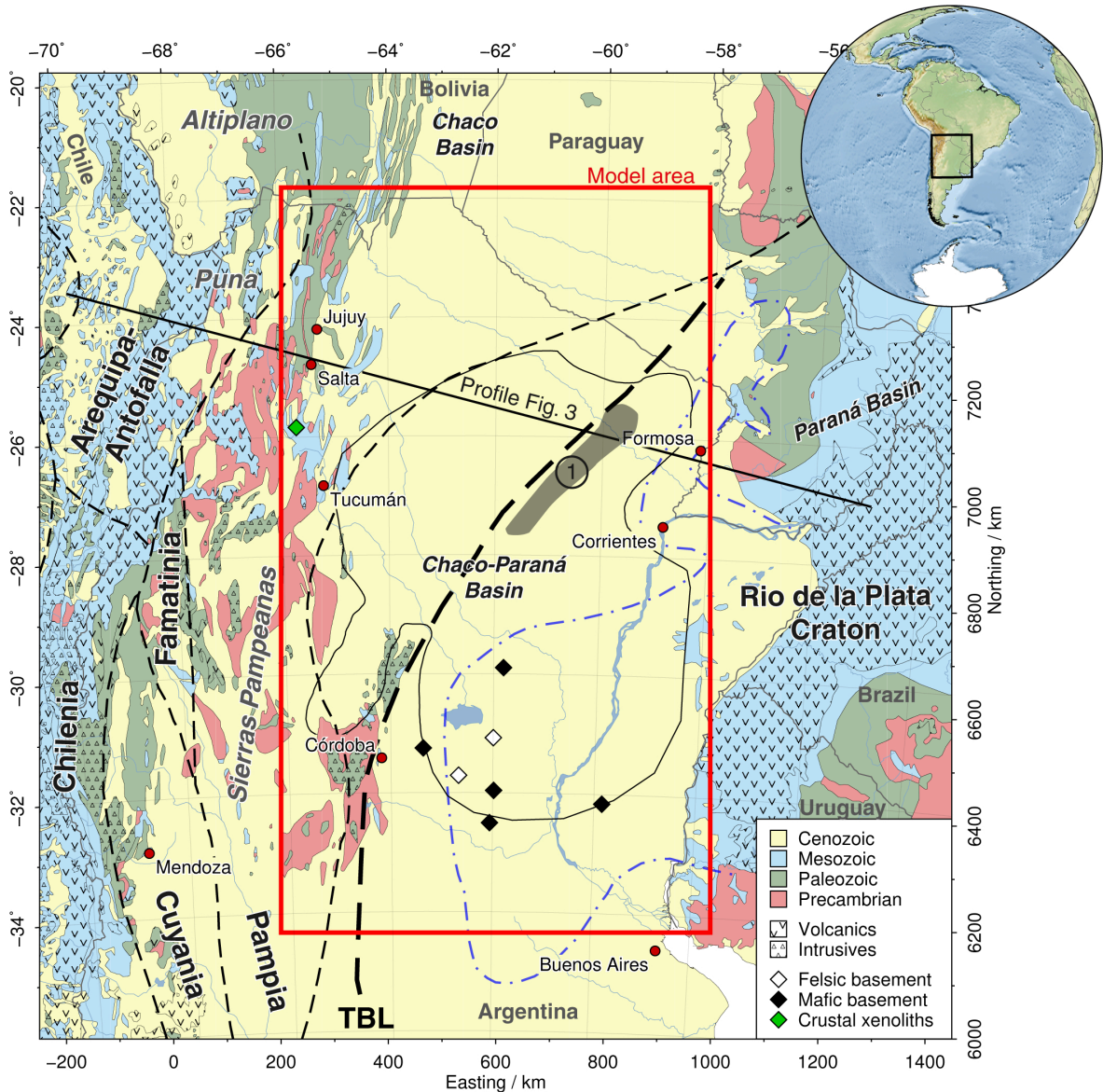
Figure 2.1.: Map overview showing a simplified geology (Schenk et al., 2000), terranes, and the modelling area. The index map at the top right shows the map extent as a black rectangle. The density model area is outlined by the red box. Bold black dashed lines separate terranes and cratons which are in bold letters (Chernicoff and Zappettini, 2004). The thick dashed line marked TBL represents the Transbrasiliano Lineament (Peri et al., 2015; Ramos et al., 2010). The Las Breñas trough is marked by (1). The blue dash-dotted line marks the western extent of the Serra Geral flood basalts (Pezzi and Mozetic, 1989). Black/white diamonds indicate basement rock types observed in boreholes (Rapela et al., 2007; Winn Jr and Steinmetz, 1998), green diamond is the sample location of lower crustal xenoliths (Lucassen et al., 1999).

The South American continent is an amalgamation of Archean to Proterozoic terranes (Fig. 2.1) that were accreted to its western margin in the Paleozoic (Almeida et al., 2000; Charrier et al., 2015; Ramos, 1988). During the formation of western Gondwana at around 620 Ma, the amalgamation of a series of terranes led to the 6000-km-long Transbrasiliano-

Kandi mega shear zone (Cordani et al., 2013). In northern Argentina and Paraguay the Transbrasiliano Lineament (Fig. 2.1), which is the southern manifestation of this shear zone, has been inferred to separate the Pampia terrane from the Río de la Plata craton (Cordani and Sato, 1999). The precise trajectory of this lineament in northern Argentina has been a matter of debate (Chernicoff and Zappettini, 2004; Ramos et al., 2010), but recently magnetotelluric studies (Peri et al., 2015, 2013) have favoured the hypothesis posited by Ramos et al. (2010).

From the Ediacaran to the early Cambrian the Puncoviscana formation, which consists of predominantly siliciclastic turbidites, deposited at the western margin of the Pampia terrane. The formation is found at present-day in northern Argentina west of -64°E within a 200 km-wide band from the Bolivian border to Tucumán. The depositional setting of this formation has been a matter of debate, but geochemical analyses indicate that it originates from arc-like volcanic rocks, which has recently led Escayola et al. (2011) to propose a deposition west of a coeval arc terrane.

The amalgamation of continents was followed by a phase of extension during the early Paleozoic, when several basins formed along the Transbrasiliano Lineament, e.g., the Las Breñas halfgraben in northern Argentina (Fig. 2.1 and Nr. 2 in Fig. 2.2b). The Las Breñas formation, that was deposited in the halfgraben consists of quartzites, siltstones, and claystones (Chebli et al., 1999), and at present day is situated at depths between 5 and 7.2 km. During the late Cambrian to the early Ordovician, thick sequences of gabbronorites and diorites were emplaced into metasedimentary sequences at the western margin of the Famatinian terrane (Otamendi et al., 2009). Back-arc extension during Ordovician to Silurian times marked the first phase of areally extensive subsidence and sediment accumulation and initiated the Chaco-Paraná (CPB, Fig. 2.1) and Paraná basins (Milani and Zalan, 1999; Padula and Mingramm, 1963; Winn Jr and Steinmetz, 1998). Both basins share a common evolution until the late Cretaceous (Milani and Zalan, 1999). The present-day expression of the Neopaleozoic to Mesozoic depocentre of the CPB (Nr. 3 in Fig. 2.2b) is a north-south elongated basin filled with up to 6 km of sediments.

At the beginning of the Silurian, during the Famatinian orogenic cycle, the northwestern Chaco plain was probably an integral part of a foreland basin (Mpodozis and Ramos, 1990; Winn Jr and Steinmetz, 1998). The present-day manifestation of this paleo-foreland basin is a southwest to northeast trending basin up to 7 km deep that is limited to the west by the Andean orogenic wedge (1a,b in Fig. 2.2b). The basin is mainly filled with quartzitic sandstones and micaceous shales (Chebli et al., 1999; Milani and Zalan, 1999). Deposits of the Gondwana I supersequence record the sedimentation history of the Paraná and Chaco-Paraná basin from the late Carboniferous to the early Triassic (Milani and Zalan, 1999). The sequence comprises glacigenic sediments, conglomerates, sandstones to shales and minor amounts of limestones and evaporites (Milani and Zalan, 1999). In the CPB, sediments equivalent to Gondwana I are dominated by siliciclastic deposits (Chebli et al., 1999; Milani and Zalan, 1999). Rifting and , ultimately, the opening of the South Atlantic during the Late Jurassic led to the formation of the conjugate margins of South America and southern Africa (e.g., Heine et al., 2013; Nürnberg and Müller, 1991). This episode was associated with the widespread

extrusion of the Serra Geral flood basalts (Fig. 2.1) in the Chaco-Paraná and Paraná basins (Winn Jr and Steinmetz, 1998). The basalts reach a thickness of up to 1.2 km in the east and gradually thin out westward (Chebli et al., 1999). Results from integrated density modelling indicate magmatic underplating in the Paraná basin, inferred to have been associated with the eruption of the flood basalts (Dragone, 2013). Such underplating is not observed in the CPB, however, and may have contributed to the different evolution of the Chaco-Paraná and Paraná basins in the Cenozoic.

The onset Andean uplift around 25 Ma (Mpodozis and Ramos, 1990) also marks the initiation of the Altiplano Plateau , 1988; (Fig. 2.1) and the present-day Chaco-Paraná foreland basin (Allmendinger et al., 1997; Isacks, 1988; Prezzi et al., 2014; Uba et al., 2006). Commencing uplift of the Puna Plateau bordering the Altiplano to the south was initiated between 20 and 15 Ma (Allmendinger et al., 1997). This early episode of the Andean orogeny was accompanied by the Laguna Pavia transgression from the late Oligocene to the early Miocene, and was followed by the Entrerriense-Paranense transgression from the middle to late Miocene (Heine et al., 2015; Marengo, 2015; Ramos and Alonso, 1995). Both transgressions deposited sandstones, clay and mudstone in the Chaco plain (Marengo, 2015). The Entrerriense-Paranense transgression reached as far inland as the region of the northwestern Sierras Pampeanas, which were uplifted after 13 Ma, marking the initiation of thick-skinned tectonics and the onset of the broken-foreland structural province (Bossi et al., 2001; Strecker et al., 1989). At the time, underthrusting of the Brazilian shield beneath the Andean orogen led to thickening of the lithosphere beneath the Altiplano plateau to 60-70 km (DeCelles and Horton, 2003). Between 12 and 6 Ma, shortening in the Altiplano ceased and shifted eastwards into the foreland (Allmendinger et al., 1997). In contrast, shortening in the Puna plateau continued until 2-1 Ma (Allmendinger et al., 1989).

As a result of the tectono-sedimentary history, most of the crystalline basement in the CPB today is covered by sediments. Accordingly, little information is available from field studies on the configuration and composition of the crystalline basement.

Geophysical observations on the intracrustal structure were obtained during the PANDA and CHARGE seismic experiments, which explored the vertical velocity structure of the Cuyania, Pampia and Famatinia terranes (Fig. 2.1) (Alvarado et al., 2007). The authors inferred a rather felsic, quartz-rich composition for the Pampia terrane and the Río de la Plata craton from low v_p and v_p/v_s ratios. The author's inferences on the composition of the Pampia terrane agree with basement outcrops of granites and migmatites in the Sierras Pampeanas (Mon, 1979; Simpson et al., 2003), but contrast with observations taken from drill cores of the southern Río de la Plata craton (diamonds in Fig. 2.1). In addition to felsic basement rocks (granite, quartzite), mafic rocks (gabbro, granodiorite) were also identified as the plutonic crystalline basement in five out of seven wells that reached basement (Rapela et al., 2007; Winn Jr and Steinmetz, 1998).

A recent study exploited local seismic events in the southeastern Sierras Pampeanas to obtain high-frequency receiver functions (Perarnau et al., 2012). The authors found that the Moho lies around 35 km beneath the city of Córdoba and deepens to about 39 km at the west-

ern end of the Sierras de Córdoba (Fig. 2.2a). They discovered two to three intracrustal interfaces, of which the deepest lies between 22 to 27 km depth, and an average v_p of 6.2 km s^{-1} for the crust.

Early tomographic studies in South America already identified an average depth of the Mohorovičić discontinuity (Moho) below the CPB of 32 km (Snoke and James, 1997). This was confirmed by Assumpção et al. (2013) and Rosa et al. (2016), who inferred Moho depths of up to 28 km below the CPB. Snoke and James (1997) identified a rather asthenospheric character for the upper mantle below the CPB with s-wave velocities of about 4.2 km s^{-1}. Assumpção et al. (2013) obtained velocities between 4.3 and 4.2 km s^{-1} in the upper mantle below the northwestern part of the CPB, and higher shear wave velocities of 4.5 to 4.6 km s^{-1} in the south of the CPB (Sec. 2.1.2.3.3). At greater depths, the velocity pattern inverts, and areas of former low velocity display high velocities. A high-velocity zone is furthermore observed above the flat slab beneath the Sierras Pampeanas, which coincides with a zone of increased seismicity and lower temperatures (Marot et al., 2014).

West of the modelled area, the Nazca plate is being subducted beneath the South American continent. The subduction angle between 15 and 27°S latitude is about 30°, and becomes subhorizontal between 27 and 32°S (Cahill and Isacks, 1992).

2.1.2. Methods and data

We followed a stepwise approach of data integration and three-dimensional modelling, incorporating forward and inversion techniques. Therefore, we first defined the geometry for the starting structural and density model.

These geometries intend to represent the major density interfaces in the lithosphere and delineate the boundaries for bodies with similar physical properties. We approximated these bodies as units of homogeneous density and tested the impact of their geometrical configuration on the gravity field. The respective densities assigned to these bodies are in agreement with available geological observations.

We used the misfit between observed and predicted gravity fields to invert for variations in the interface of a lighter upper and a heavier lower crystalline crust. Throughout the inversion, only the interface between these two units was calculated. To further assess the validity of the obtained differentiated crystalline crust, we calculated the isostatic response of the model, assuming local isostasy. Finally, we performed a sensitivity analysis in which we also assessed the impact of mantle density variations.

2.1.2.1. Setup of starting structural and density model

During structural modelling, we defined the major density interfaces within the lithosphere: the topography, the top of the crystalline basement, and the Moho. The data for these interfaces were collected from literature and gridded onto regular two-dimensional grids using the convergent interpolation by Petrel (ⓒ Schlumberger Ltd.). The structural model covers the map area of Figure 2.1 with a lateral grid resolution of 25 x 25 km, and extends in depth from
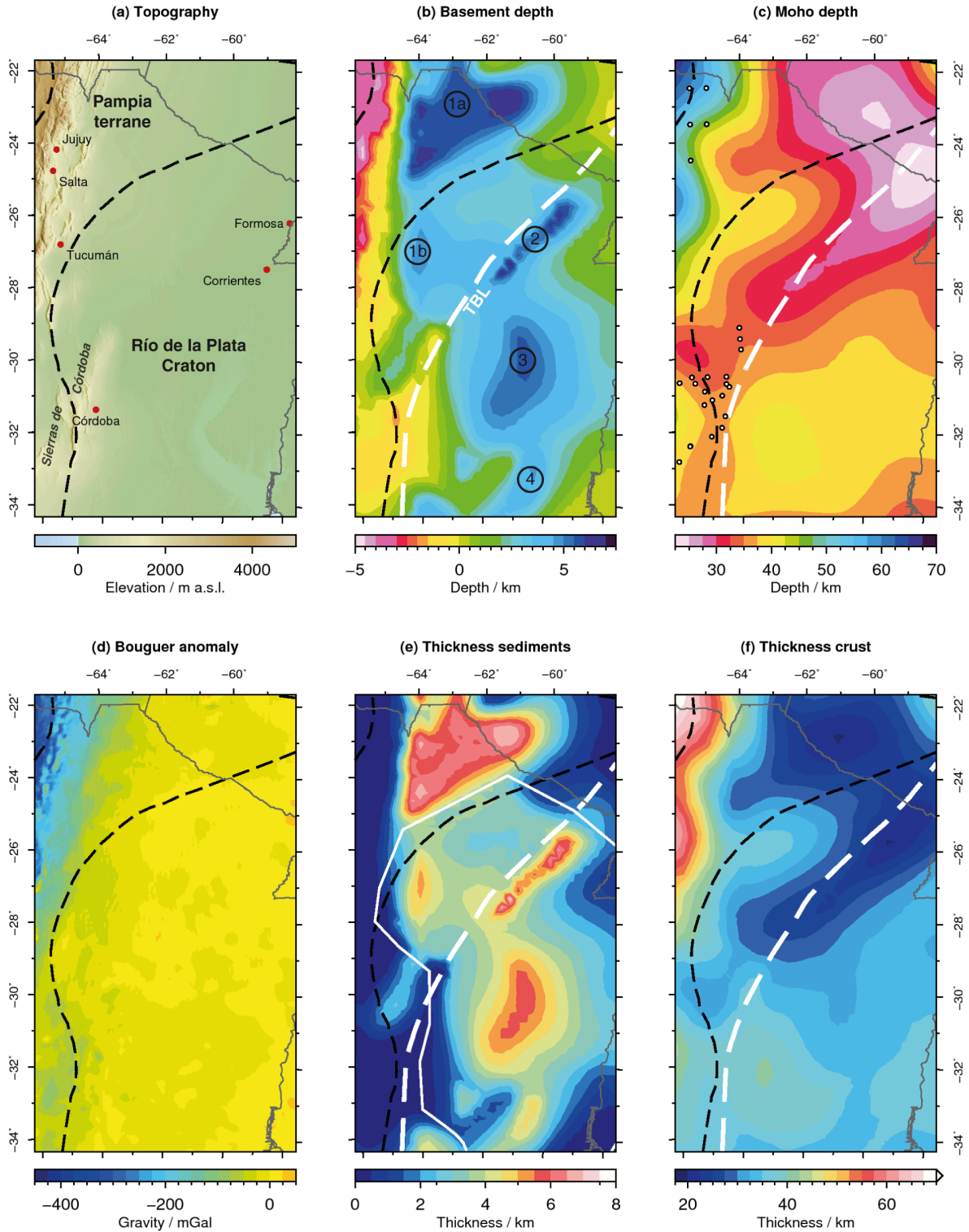
Figure 2.2.: Initial model configuration: **(a)** topography (Amante and Eakins, 2009); **(b)** basement depth derived from sediment thickness map with main features: 1a)/1b) Silurian-Devonian foreland basin, 2) Las Breñas trough, 3) Neopaleozoic to Mesozoic depocentre, 4) Rosario subbasin (Pezzi and Mozetic, 1989; Ramos, 1999); **(c)** Moho depth from Model B2 (Assumpção et al., 2013) with point constraints indicated by circles; **(d)** Free-air anomaly map (Barthelmes and Köhler, 2012; Förste et al., 2014); **(e)** sediment thickness derived from Heine (pers. comm.) and Pezzi and Mozetic (1989); the area to the SE of the white line is derived from the latter; **(f)** thickness of the crust derived from taking the difference between the top crystalline basement and the Moho depth.

the topography down to 200 km.

2.1.2.1.1. Data on structural interfaces The topography (Fig. 2.2a) was obtained from ETOPO1 (Amante and Eakins, 2009), which we used to infer the basement depth from sediment isopachs. For the CPB , we used isopach maps by Pezzi and Mozetic (1989). The remaining parts of the area were complemented by sediment thickness data from a global sediment thickness compilation of the Exxon Tectonic Map of the World (Exxon, 1985), which had been re-gridded using spherical splines in tension at a grid increment of 6 arc minutes. The compiled sediment thickness map and resulting basement depth are plotted in Figs. 2.2e and, 2.2b, respectively. To derive the depth to the top of the crystalline basement, the total sediment thickness was subtracted from the topography.

The Moho depth corresponds to model B2 of Assumpção et al. (2013), which mainly takes into account seismic point constraints (seismic reflection/refraction and receiver functions (dots in Fig. 2.2c), wave-form modelling, and Rayleigh-wave group dispersion. Note that in the largest part of the model area, point constraints are absent. Additionally, the authors fitted oceanic areas by an empirical relationship between Bouguer anomaly and crustal thickness from the given seismic point constraints. Around the seismic point constraints , the error of Moho depth is estimated around ± 4 km (Assumpção et al., 2013).

We implemented the subducting Nazca plate using digitized depth contours from Tassara (2006). The bodies of the Nazca plate were adapted from Kirchner (1997), who subdivided the plate into three bodies, of which the upper body is the oceanic crust composed of basalt, which transforms into eclogite at a depth of about 80 km(Fig. 2.3). The lithospheric mantle is represented by a rigid upper body (Olivine 1) and a plastic transition layer (Olivine 2). The individual thickness relations of these bodies (8 km oceanic crust or 8 km eclogite, 23 km olivine layer 1, 29 km olivine layer 2) were adapted from Kirchner (1997) as well. To account for the dip α of the Nazca plate, we calculated the true vertical thickness h according to $h = t \, \cos^{-1} \alpha$, where t is the thickness of the individual layer.

Although gravitational attraction decays $\propto r^{-2}$, strong density contrasts can impact the gravity field at great distance. Therefore, we extended the modelling area (red rectangle, Fig. 2.1) to include the far-field influence of the subducting Pacific Plate beneath South America. For the impact of the modelled Nazca Plate on the gravity field of the modelling area see Fig. 15 in the Supplement.

2.1.2.2. Density modelling

We differentiated bodies confined between the main density interfaces within the Earth. The stronger the contrast in density and the shallower the interface, the greater the impact of an individual body on the gravity field. At the same time, shallow density contrasts, e.g., between crystalline crust and sediments, cause gravity anomalies of shorter wavelengths than deeper density contrasts, as, for example, in the crystalline crust or the upper mantle (e.g., Fowler, 1990).
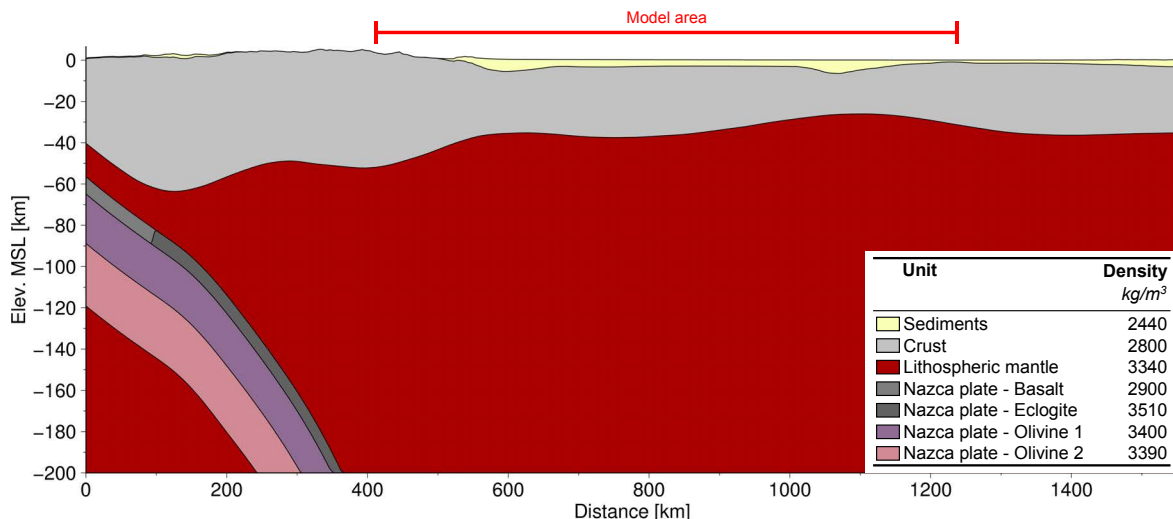
Figure 2.3.: Initial model setup (vertical exaggeration: 3x) with individual densities of the extended density model with homogeneous crust. For profile location, see Fig. 2.1.

2.1.2.2.1. Gravity observations   For density modelling, we used the global EIGEN-6C4 model (Förste et al., 2014) up to degree 2190 with mean tide, obtained from the ICGEM website (Barthelmes and Köhler, 2012). According to the functions implemented on the website, the gravity model was reduced to Bouguer anomaly using ETOPO1 (Amante and Eakins, 2009) with the same degree as the gravity model and a crustal density of $\rho_c = 2670\,\mathrm{kg\,m^{-3}}$. For elevations below mean sea level, i.e.,in the oceans, a density of $\rho_w = (2670 - 1025)\,\mathrm{kg\,m^{-3}}$was applied. The resulting Bouguer gravity field (Fig. 2.2d) was then re-gridded onto a $10\,\mathrm{x}\,10\,\mathrm{km}$ regular grid, covering the area of interest (red square, Fig. 2.1).

2.1.2.3. Density constraints

2.1.2.3.1. Sediments   For the basin fill of the CPB, we assumed a homogeneously dense body composed of siliciclastic rocks (Sec. 2.1.1.1). To determine a representative density for this body, we integrated Athy's law of compaction (Athy, 1930) over the maximum sediment thickness of $7.2\,\mathrm{km}$ (Fig. 2.2e, Appendix A.1).

Applying $\phi_0 = 0.41$ and $k = 0.31\,\mathrm{km^{-1}}$ for typical sandstone (Hantschel and Kauerauf, 2009) yields an average density of approximately $2440\,\mathrm{kg\,m^{-3}}$for the sediment body.

2.1.2.3.2. Continental crust and Nazca plate   The density of the crystalline crust was prescribed as $2800\,\mathrm{kg\,m^{-3}}$, which is consistent with estimates for the upper crust by made Kirchner (1997) and Lucassen et al. (2001) as well as estimates for metamorphic crustal rocks by Vilà et al. (2010).

We adapted the densities of the Nazca plate bodies from Kirchner (1997) as well. Accordingly, the basalt layer density was defined as $2900\,\mathrm{kg\,m^{-3}}$, and the eclogite layer density was defined as $3510\,\mathrm{kg\,m^{-3}}$. The rigid upper olivine layer 1 was assigned a density of $3400\,\mathrm{kg\,m^{-3}}$. Due to the elevated temperatures in the plastic olivine layer 2, a slightly reduced density of

Table 2.1.: Mineral assemblages used for the conversion from shear wave velocity to density in the upper lithospheric mantle between depths of 50 and 200 km. We normalized the sum of the mineral phases to 100 %.

Name	Ol %	Cpx / Di %	Opx / En %	Sp %	Gnt %	XFe	Source
Xenolith	75.4	4.6	18.7	1.3	0.0	8.6	Comin-Chiaramonti et al. (1986)
HP_Tc2	61.1	9.6	20.4	0.0	9.0	8.1	Griffin et al. (2009)
HP_Tc3	65.8	7.5	17.1	9.6	0.0	8.2	Griffin et al. (2009)
Off-cratonic	68.0	11.0	18.0	0.0	3.0	10.0	Shapiro and Ritzwoller (2004)

Ol - olivine, cpx - clinopyroxene, di - diopside, opx - 7orthopyroxene, en - enstatite, sp - spinel, gnt - garnet, XFe - iron content.

$3390 \, \mathrm{kg \, m^{-3}}$ was prescribed to this lower layer.

2.1.2.3.3. Lithospheric mantle   Seismic tomography allows obtaining information on the velocity distribution of the lithospheric mantle that can then be used to infer its density structure. The resolution of these models is limited by their data coverage and quality, and is typically in the order of a few hundred km (e.g., Feng et al., 2007; Schaeffer and Lebedev, 2013). Since our model covers an area that is several times larger than the potential resolution of those tomographic models, we can use them to assess how density variations in the upper lithospheric mantle affect the results of our study. Therefore, we inverted observed s-wave velocities from the tomographic models *aVs_2013_Tecto* (Assumpção et al., 2013), *3D2016_03Sv* (Debayle et al., 2016) and *SL2013* (Schaeffer and Lebedev, 2013) to densities following a modified version (Meeßen, 2017) of the approach taken by Goes et al. (2000). Details on the conversion are provided in appendix A.2.

We tested the effect of four different mineralogical assemblages on the density distribution in the lithospheric mantle (Table 2.1) and the gravity forward model. The *Xenolith* assemblage represents the most recent data on the mineralogy of the mantle that available in the study area. This assemblage, characterized by high olivine content, represents the average of 56 to 23 Ma old mantle xenolith assemblages from southern Paraguay (Comin-Chiaramonti et al., 1986). Detailed information on the assemblage of each sample and the normalized average are available in the Supplement. *HP_Tc2* and *HP_Tc3* are proposed mineralogies for Tectons at a depth of 100 km and 800 °C provided by Griffin et al. (2009). These were calculated from xenolith compositions using the thermodynamic database by Holland and Powell (1998). The term "Tecton" refers to a crust that has been formed or modified during the last 1 Ga (Griffin et al., 2009) and is therefore applicable to the South American craton, as it has been subjected to a series of tectonic events since the Precambrian. We chose those specific Tecton assemblages because they vary strongly in diopside, spinel, and garnet content compared to the *Xenolith* assemblage. Besides those assemblages thought to be representative of the lithospheric mantle beneath the foreland of northern Argentina, we additionally tested the *off-cratonic* assemblages by Shapiro and Ritzwoller (2004). These represent a more fertile mantle and this assemblage serves as an endmember with high iron content.

To transfer the shear wave velocity models to the modelling domain, we interpolated the original data onto a regular, three-dimensional grid (voxel) with a lateral resolution of 50 km and

a vertical resolution of 15 km, equivalent to a total of 10 layers between 50 and 200 km depth. These velocity grids were then converted to density and temperature for each mineralogical assemblage listed above.

The resulting density distributions for all mantle voxels are shown in Figure A.3. The differences in average density for the same mineralogical assemblage, but varying shear wave velocity model, fall within $\pm 1\,\mathrm{kg\,m^{-3}}$. Differences between the individual assemblages lie within $\pm 8\,\mathrm{kg\,m^{-3}}$.

For the gravity forward model, we prescribed the lithospheric mantle density to the average of the Assumpção et al. (2013) voxel with Xenolith assemblage ($3340\,\mathrm{kg\,m^{-3}}$). The full density variations from all mantle voxels and assemblages were tested during the sensitivity analysis (Section 2.1.4.1).

2.1.2.4. Gravity forward modelling

During gravity forward modelling, we calculated the gravity response of the initial structural model. Calculation of the this model was carried out using IGMAS+. This software calculates the gravity field from a triangulated, interconnected network of polyhedra along multiple vertical 2D profiles (working sections). Because IGMAS+ requires laterally continuous surfaces for the triangulation of the interfaces, triangulation errors would occur where a layer has zero thickness and the nodes of two interfaces overlap. The modelled thickness of layers was therefore defined as 1 m where the layer is not present. Equivalent to the lateral target resolution of 25 km, the forward model was subdivided into 73 working sections with a distance of 25 km running E-W. Because we modelled the Bouguer anomaly field, we only implemented the bodies for the depth range from 0 to 200 km.b.s.l. and defined the IGMAS+ specific bodies *Top* and *reference* to the average density of all implemented bodies. A table with the densities and volumes used for averaging is available in the Supplement.

In the initial forward model , we regarded the crystalline crust as a body of homogeneous density. Since global observations (e.g., Rudnick and Fountain, 1995) as well as recent seismic experiments in northern Argentina(Perarnau et al., 2012) call for a more complex density structure of the crystalline crust, we can expect that the gravity field of the initial model would deviate from the observed gravity field. This deviation, the gravity residual, indicates which areas of the model exhibit mass deficits or mass excess with regard to the actual density distribution in the lithosphere. We used the residual gravity to assess the density configuration of the crust by following an inverse modelling approach, assuming the difference between the gravity response of the model and the observed gravity was mainly produced by variations in the intracrustal structure of the initial model.

2.1.2.5. Gravity inversion

To obtain a differentiated density distribution for the crystalline crust, we assumed that it is composed of two layers with two different average densities. We defined those layers as the upper ($2800\,\mathrm{kg\,m^{-3}}$) and lower crust ($3100\,\mathrm{kg\,m^{-3}}$). To minimize the gravity residual of the for-

ward model, we inverted for the depth of the intracrustal density interface and kept all other interfaces fixed. In doing so, we applied the *harvester* module (Uieda and Barbosa, 2012), which is part of the open-source *fatiando a terra* library (Uieda et al., 2013) for Python 2.7. The *harvester* is an iterative algorithm that propagates initial density perturbations (seeds) through a prism mesh (regular mesh of rectangular prisms). After each propagation step, the harvester compares the calculated gravity field with the input gravity field and continues to propagate the densities until the difference between the input and the calculated gravity fields reaches a prescribed minimum threshold. The initial seed distribution in our inversion represented a spatially continuous layer of 500 m thickness at the base of the crystalline crust. To reduce the amount of possible solutions for the inversion, we imposed two boundary conditions on the harvester. First, we modified the harvester to grow seeds only in the upward direction instead of growing them in all directions. Without this modification, the solution would be highly non-unique, and would result in heterogeneous bodies with density distributions that could hardly be interpreted. Secondly, the harvester was restricted to grow seeds only within the volume of the crystalline crust.

The resolution of the prism mesh was set to 25 km laterally and 500 m vertically in order to fit the gravity residuals of the initial model (Fig. 2.4d, e). Due to the high vertical resolution, the overall trend of the gravity field could be fitted accurately whilst the coarse lateral resolution prevented the harvester from fitting small-wavelengths, e.g., in the northwestern part of the modelling area.

2.1.3. Results

2.1.3.1. Starting structural model

The individual depth maps of the major density interfaces and thickness maps of the starting structural model are presented in Figure 2.2. The thickness distribution of the crystalline crust, as obtained from the compiled sediment thickness data and Moho depth, ranges between 70 km along the Andean orogen in the west and 19 km in the northern domain of the modelled area. It is less than 30 km thick along the Transbrasiliano Lineament. The crust east of the Sierras Pampeanas thickens to 42 km and is limited to the west by the boundary between the Pampia terrane and the Río de la Plata craton, which coincide approximately with the Transbrasiliano Lineament in this area.

2.1.3.2. Gravity forward modelling

The calculated gravity field and the gravity residual obtained from the starting model are shown in Figure 2.4. In the foreland, the observed gravity anomaly is characterized by small variations ranging between -100 and 40 mGal. To the contrary, the calculated gravity field shows strong variations of several 100 mGal. The synthetic model resembles the gravity low due to the crustal root of the Central Andes in the northwest between 28 and 22°S, but compared to the observed gravity field, it extends too far towards the east. This is apparent in the gravity residual map (Fig. 2.4b) as well. Negative residuals (blue) in Fig. 2.4b indicate mass
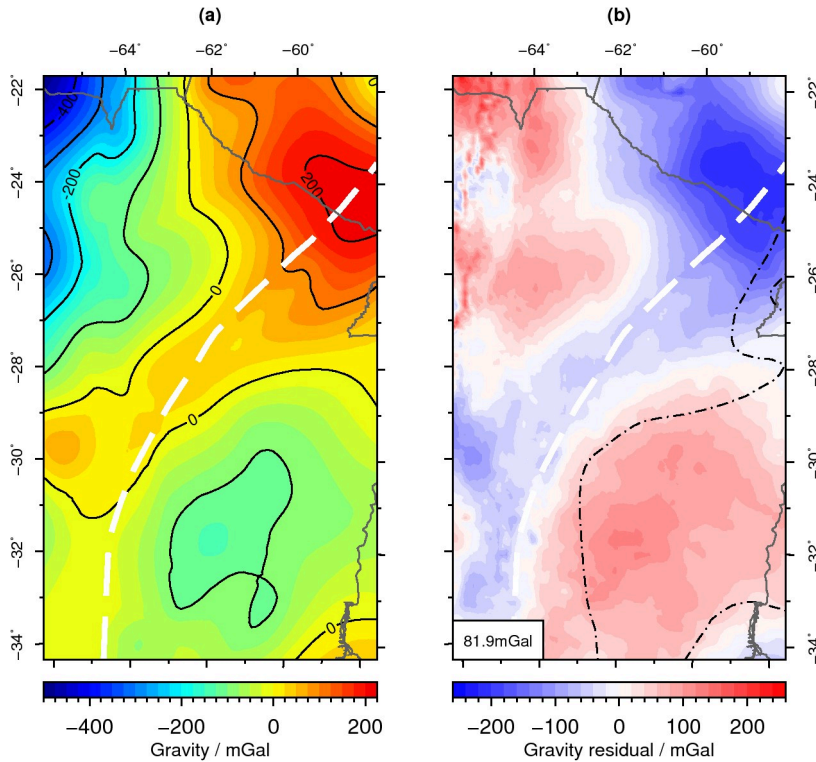
Figure 2.4.: Results of forward modelling: **(a)** calculated Bouguer gravity field, black contours every 100 mGal; **(b)** residual gravity ($g_{obs} - g_{calc}$). The white dashed line represents the Transbrasiliano Lineament (Peri et al., 2015; Ramos et al., 2010), while the dash-dotted line represents the extent of the Serra Geral flood basalts (Pezzi and Mozetic, 1989). The box in the bottom left corner indicates the RMS residual.

excess in the model with respect to the observed gravity field, whereas positive residuals (red) indicate mass deficits. As a result, the forward model exhibits mass excess in the southwest and northeast that is connected via a corridor parallel to the Transbrasiliano Lineament. The existence of this corridor is reflected in the morphology of the Moho (Fig. 2.2c) and indicates that the Moho dominates the synthetic gravity field. Positive residuals in the northwest and southeast indicate mass deficits, whereby the southeastern residual, up to ≈120 mGal, correlates with the extent of Serra Geral flood basalts (dash-dotted line, Fig. 2.4b).

2.1.3.3. Crustal structure

The gravity inversion fitted the residual gravity field (Fig. 2.4b) with an RMS fit of 15.7 mGal (Fig. A.4a). Figures 2.5a and b show the distribution of upper and lower crustal thickness as predicted from the inversion procedure. The thickness of the upper crust reaches up to 39 km and is greatest in the west beneath the eastern Central Andes and the Sierras Pampeanas tectonic province, as well as in the northeast. Upper crust as thin as 5 km is predicted beneath the Silurian-Devonian foreland basin in the north and the Neopaleozoic to Mesozoic basin in the central southeast. Most basins (marked 1, 3, and 4 in Fig. 2.2b) are predicted to be underlain by a lower crust thicker than 15 km, and only the Las Breñas trough is associated with thinner lower crust. Virtually no lower crust is predicted in the northeastern corner of the model. This area coincides with the shallowest parts of the Moho (Fig. 2.2c), which reach depths of 27 to 30 km.

The crustal architecture as derived from gravity inversion can also be treated as a measure of the average density of the crystalline crust (Fig. 2.6a). Analogous to the lower crustal
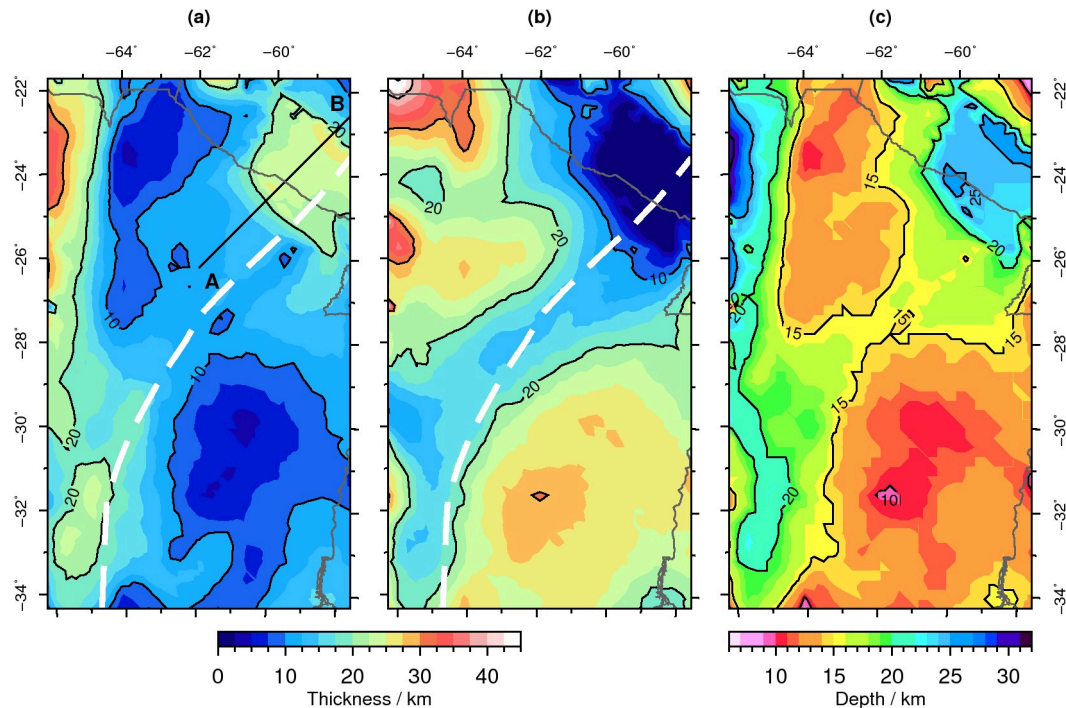
Figure 2.5.: Results of gravity inversion. **(a)** thickness of the upper crust; **(b)** thickness of the lower crust; **(c)** depth at the top of the lower crust. the dashed line indicates the Transbrasiliano Lineament (Peri et al., 2015; Ramos et al., 2010)

thickness distribution, the average crustal density is low along the Transbrasiliano Lineament. The average crustal density lies at a minimum of $2800\,\mathrm{kg\,m^{-3}}$ in the northeast and a maximum of $2930\,\mathrm{kg\,m^{-3}}$ in the northwest.

2.1.3.4. Isostatic topography

Assuming local isostasy, we calculated the isostatic topography of the final structural model (for details, see the Supplement). The reference pressure for the calculation at the equilibrium depth of $200\,\mathrm{km}$ was defined as the average pressure at the model base of $6.423\,\mathrm{GPa}$. The isostatic topography shown in Figure 2.6a predicts high relief in the northwest and shallower relief in the Chaco-Paraná plain, parts of which lie below mean sea level. Compared to the actual topography (Fig. 2.6b), the largest differences are observed in the west close to the Andes and the Sierras Pampeanas, where both larger and smaller values are predicted than observed. These differences are elongated in the north-south direction, characterized by a wavelength of 200 to $300\,\mathrm{km}$ in the east-west direction, and occur in areas of high topographic elevation.

2.1.3.5. Mantle density and thermal structure

Sample maps of obtained average mantle density for the *Xenolith* assemblage are shown in Figs. 2.7a-c. Low densities of approximately $3328\,\mathrm{kg\,m^{-3}}$ in the north are common between the tomographic models of Assumpção et al. (2013) and Schaeffer and Lebedev (2013). A similarly
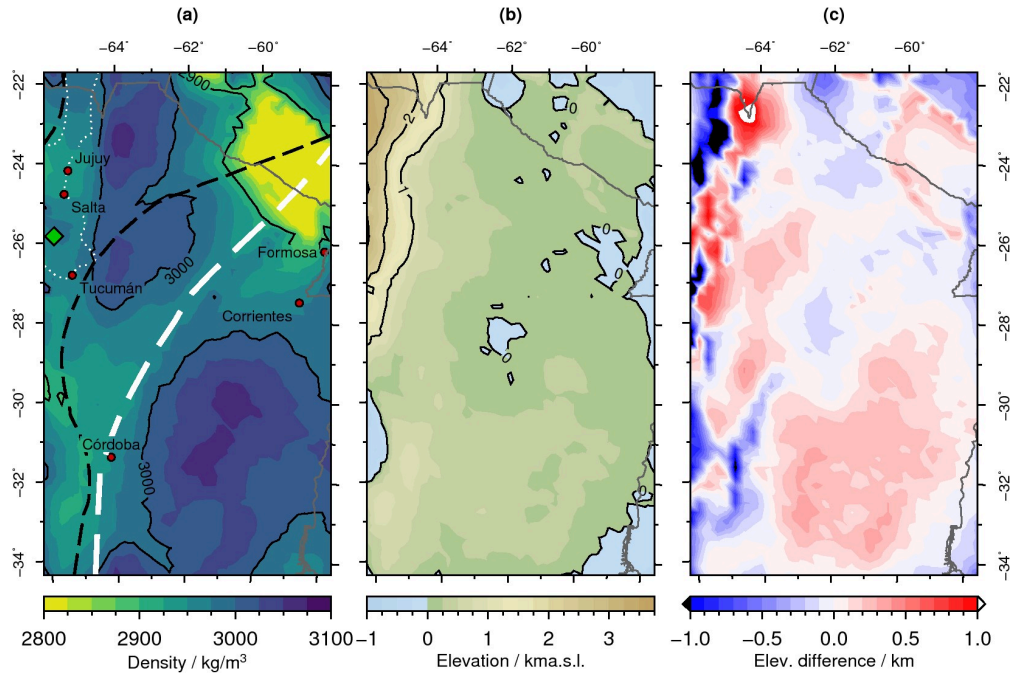
Figure 2.6.: Average crustal density and isostatic response of the final model. The black dashed lines represent terrane boundaries by Chernicoff and Zappettini (2004), while the white dashed line represents the Transbrasilian Lineament (Ramos et al., 2010). **(a)** Average crustal density inferred from the inversion; the green diamond marks the location of lower crustal xenoliths (Lucassen et al., 1999), white dotted line is the present-day extent of the Puncoviscana formation (Escayola et al., 2011); **(b)** topographic elevation for an average pressure of 6.423 GPa at the model base; **(c)** difference to observed topographic elevation; positive values indicate that our model overestimates the topography.

common feature between both models is a density increase towards the south, although the model of Assumpção et al. (2013) yielded considerably higher densities than the model by Schaeffer and Lebedev (2013). Compared to the first two shear wave models, the magnitude of density variation in the model of Debayle et al. (2016) is considerably lower. Nevertheless, this model indicates a trend of increasing densities as well. Furthermore, the models *aVs_2013_Tecto* and *3D2016_03Sv* both show decreasing densities towards the south.

Overall, the converted temperatures at 100 km depth (Figs. 2.7d-f) reflect the trends of the average mantle density distributions. High temperatures are predicted from the models by Assumpção et al. (2013) and Schaeffer and Lebedev (2013), whereas the temperature distribution obtained from Debayle et al. (2016) shows little variation at this depth.

2.1.4. Sensitivity analysis

The input data we used are associated with specific error ranges. Therefore, we tested the sensitivity of our model with respect to variations in sediment density, depth to the top crystalline basement, and mantle density variations.

2.1.4.1. Lithospheric mantle density

We tested the sensitivity of the model to mantle density variations by imposing densities obtained from shear wave velocity models of the uppermost mantle. We then computed the gravity fields of these models with an inhomogeneous mantle and compared them to the gravity field of the model with a homogeneously dense mantle.
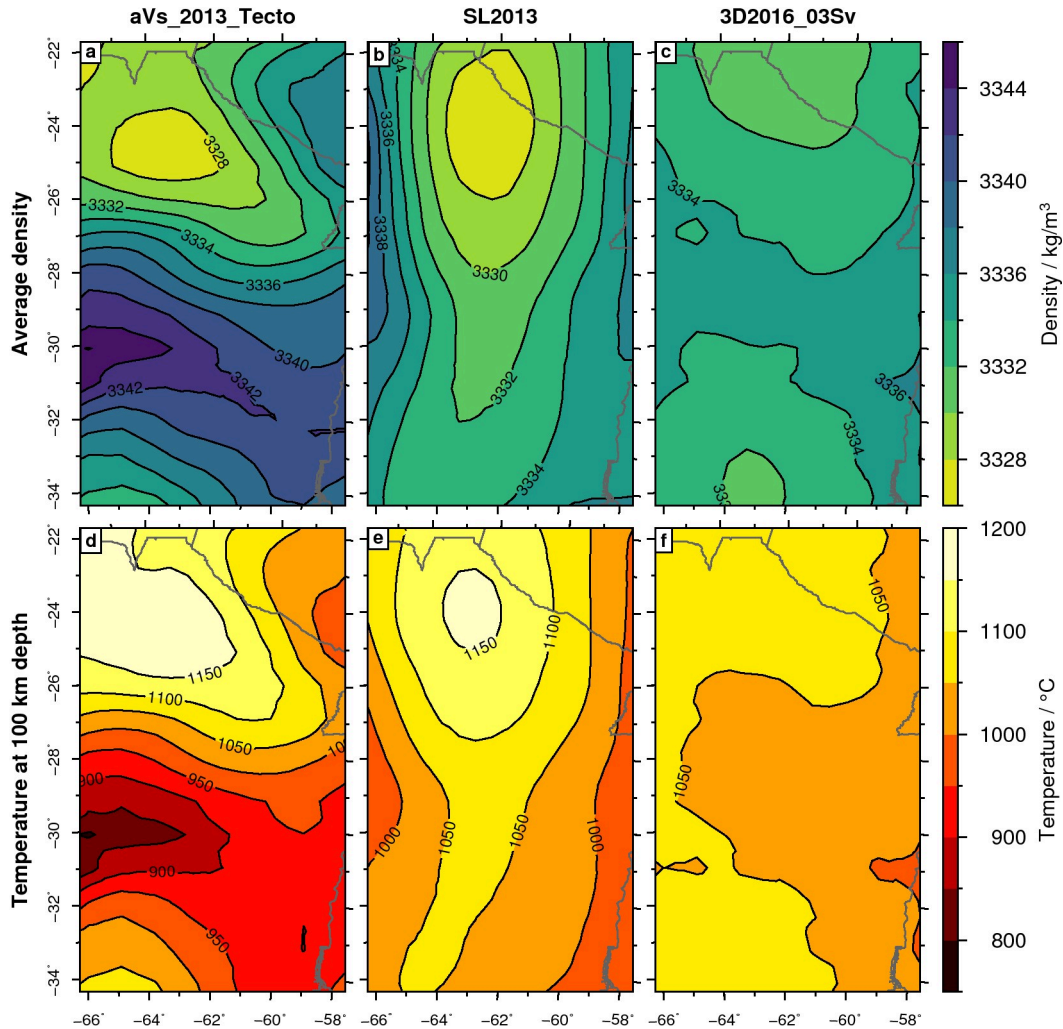
Figure 2.7.: Selected results of the density and temperature conversion using the *Xenolith* assemblage (Table 2.1). **a - c** show the average density of the mantle voxels, **d - f** show the temperature distribution at approximately 100 km depth. *aVs_2013_Tecto* by Assumpção et al. (2013), *SL2013* by Schaeffer and Lebedev (2013), *3D2016_03Sv* by Debayle et al. (2016).

We thus applied the obtained mantle density variations (Sec. 2.1.3.5) in the range from depths of 50 to 200 km and then compared the gravity field with the gravity field of the homogeneous model. Those parts of the tomographic model that fall above the Moho depth, i.e., sectors within the crystalline crust, were excluded. Where the Moho is shallower than 50 km and a volume of lithospheric mantle is not covered by information from the tomographic model, the density of the lithospheric mantle was set to the average voxel density (Fig. A.3).

The difference in the forward-modelled gravity fields between models with homogeneous
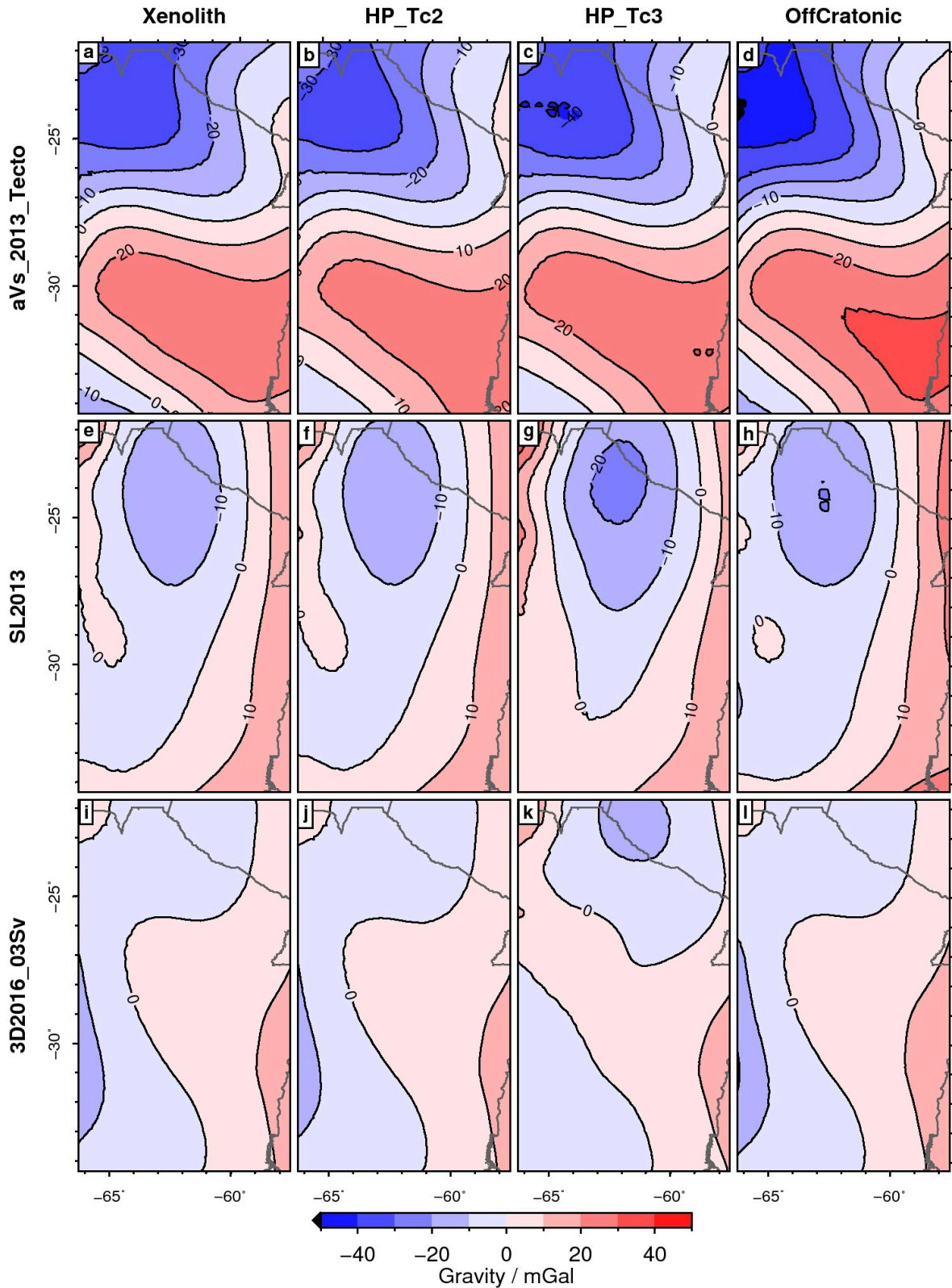
Figure 2.8.: Difference maps illustrating the effect of variations in mineralogical assemblages and shear wave velocity models on the forward modelled gravity field. The difference between the forward modelled gravity field $g_{z,vox}$ of a model and the specified mantle configuration, and the model with a homogeneous mantle $g_{z,hom}$ (Fig. 2.4a) is shown. The mineral assemblages used are provided in Table 2.1.
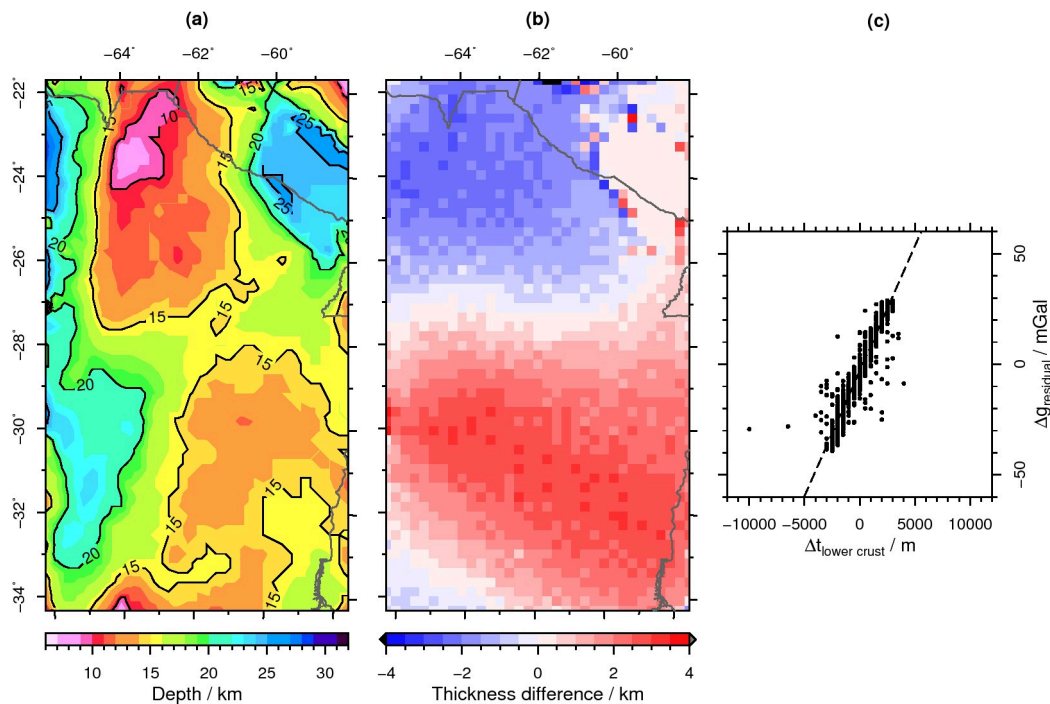
Figure 2.9.: Model sensitivity to mantle density variations: **(a)** Top of the lower crust using the mantle model *aVs_2013_Tecto* and *Xenoltih* assemblage; **(b)** lower crustal thickness change in km, positive numbers indicate that the crustal thickness was reduced in the inhomogeneous mantle model with respect to the homogeneous mantle model; **(c)** cross plot of crustal thickness variations $\Delta t_{lowercrust}$ versus gravity differences in the reference model $\Delta g_{residual}$. The dashed line represents the best fit with $\Delta g_z = 0.01\mathrm{mGal\,m^{-1}} \cdot \Delta t - 3.13\,\mathrm{mGal}$ and determination coefficient $R^2 = 0.91$.

mantle and with mantle voxel is shown in Figure 2.8. The maps show that the shear wave velocity model *aVs_2013_Tecto* (Assumpção et al., 2013) has the largest impact on the calculated gravity field, and that the model *3D2016_Sv* (Debayle et al., 2016) has the least effect. The deviation between the gravity fields of models with homogeneous and inhomogeneous mantle does not exceed $\pm 55\,\mathrm{mGal}$.

To estimate how much these variations influence the resulting lower crustal thickness distribution, we performed an exemplary gravity inversion on *aVs_2013_Tecto* applying the *Xenolith* mineral assemblage. The thickness differences of the lower crust between the homogeneous and inhomogeneous mantle models, as inferred from gravity inversion (Fig. 2.9b), largely range around $\pm 4\,\mathrm{km}$. In the northwest, the crust in the inhomogeneous mantle model is up to 4 km thicker, while it is up to 4 km thinner in the southern half of the model. The thickened crust compensates for the mass loss that results from less-than-average densities within the lithospheric mantle in the northwestern sector covered by the model. A cross plot of mantle gravity and lower crustal thickness variation reveals an expected good linear correlation with $R^2 = 0.91$ (Fig. 2.9c), and indicates that for every 10 mGal variation in the gravity field, the inferred lower crustal thickness changes by 1 km.

We used this linear relationship to quantify the impact of the other tomographic models on the inferred thickness distribution of the lower crust. Although the pattern of induced gravity variation between the individual models is significant (Fig. 2.9) for all of the models, the

lower crustal thickness would be reduced in the northern part of the model. This reduction, however, would be less than 5 km, which is small compared to the total lower crustal thickness (Fig. 2.5b).

In summary, for every 10 mGal introduced to the gravity field by mantle heterogeneities or other objects the inferred lower crustal thickness changes by about 1 km. Here, we varied the lithospheric mantle density by about ± 30 kg m^{-3}, which affects the top of the lower crust by up to ± 4 km (Table 2.3).

2.1.4.2. Crustal density

We imposed density variations of ± 50 kg m^{-3} on the upper crystalline crust and computed the gravity response of the model. The model with the reduced (increased) density obtained a gravity field up to 20 mGal less (more) in the northeast, and up to 53 mGal more (less) along the Central Andes from 28 to 22°S. From the established linear relationship between gravity perturbation and lower crustal thickness variation (Sec. 2.1.4.1, Fig. 2.9c) we reason that the induced thickness variation is in the order of maximum ± 5 km along the Central Andes in the west and up to ± 2km in the northeast of the model area. South of 28°S the possible variation is less than 1 km.

We also tested the sensitivity of the model with respect to variations in the density of the lower crust by varying the density by ± 100 kg m^{-3} (equivalent to a 3 % variation). The inversion fitted the gravity field well for a 3200 kg m^{-3} dense lower crust(RMS = 18.4 mGal, Fig. A.5f). Compared to the thickness of a lower crust at 3100 kg m^{-3}, the thickness was reduced by about 5 km northwest and southeast of the Transbrasiliano Lineament (Appendix, Fig. A.5a) and by about 3 km along the lineament. No variation in thickness was observed in the northeast, where the Moho is shallowest.

In contrast, the inversion was not able to fit the gravity field assuming a 3000 kg m^{-3} dense lower crust (RMS = 20.5 mGal, Fig. A.5e), leaving a misfit of about 50 mGal in the area of the Neopaleozoic to Mesozoic depocentres in the southeast (Fig. 2.2b). In the northwest, the lower crustal thickness increased between 4-8 km and by about 3 km along the Transbrasiliano Lineament, while it showed no variation in the northeast. The misfit in the southeast is due to the fact that the thickness of the lower crust already reached 100% of the total crustal thickness in this area, eliminating the possibility to compensate the remaining missing mass. This inability to fit the gravity field indicates that the lower crustal density must be greater than 3000 kg m^{-3}.

2.1.4.3. Sediment density

We tested the sensitivity of the model with regard to variations in sediment density by running the inversion twice for a variation of ± 50 kg m^{-3} in the sediment density, which is equivalent to a density variation of 2 %. This particular density difference was chosen based on a comparison of the average density of different lithologies that could be expected in the CPB (Table 2.2).

For a density of 2490 kg m^{-3}, the top of the lower crust mostly decreases by 500 to 1000 m.

Table 2.2.: Different lithologies with compaction parameter k and depositional porosity ϕ_0 (Hantschel and Kauerauf, 2009). The average density $\overline{\rho}$ was calculated following Eqn. (A.4) for a maximum thickness of 7.2 km. The density difference in the last column states the difference of the average sediment density to typical sandstone, which was used as lithology for the sediment body.

		k km^{-1}	ϕ_0	ρ_S $kg\,m^{-3}$	$\overline{\rho}$ $kg\,m^{-3}$	Difference $kg\,m^{-3}$
Sandstone	typical	0.31	0.41	2720	2440	0
	clay-rich	0.32	0.40	2760	2480	40
	clay-poor	0.30	0.42	2700	2410	-30
	arkose, typical	0.39	0.33	2730	2540	100
	quartzite	0.30	0.42	2640	2360	-80
Limestone	shaly	0.48	0.50	2730	2490	50
Shale	typical	0.83	0.70	2700	2500	60

A decrease of the sediment density to 2390 kg m^{-3} leads to a slight increase of the top lower crust by about 500 m. Accordingly, the variation in the topography of the top lower crust is strongest in the northwest and southeast where the deepest depocentres are located.

2.1.4.4. Basement depth

The sediment thickness data was presented by Pezzi and Mozetic (1989) as isopachs for different epochs, as well in the form of a cumulative sediment thickness map. The sum of the individual epoch isopachs and the cumulative thickness information, however, are inconsistent and differ non-systematically. Additionally, the isopachs were only presented until the end of the Mesozoic units, without information on the thickness distribution of Cenozoic sediments. Data from Marengo (2015) indicate at least 700 m of additional Cenozoic sediments in the area of the Neopaleozoic-Mesozoic depocentre of the CPB (Fig. 2.2b). This additional thickness is a minimum estimate, since the thickness of the Palermo Member, which is the earliest Cenozoic member of the Chaco Formation, is missing. We quantified the impact of underestimated sediment thickness on the modelling results by rescaling the sediment thickness distribution (Fig. 2.2e). In areas with a thickness in excess of 1 km an additional 10% was added to the thickness at each point, whereas areas with less than 1-km-thick sediments were not edited, as this would have added sediment thickness in areas of outcropping basement. The amount of additional sediment thickness is shown in Fig. 2.10a.

Due to increased sediment thickness, the amount of low-density sediments close to the topography increases whilst the basement, representing the uppermost density contrast in the subsurface, moves farther down. This overall mass reduction at the surface results in more negative gravity anomalies predicted in the areas of greatest sediment thickness (Fig. 2.10b). In contrast, slightly higher anomalies are predicted in areas of thin sedimentary cover. This increase, i.e., the gravity shift, is an effect that is introduced during the calculation of the gravity field. A gravity shift needs to be applied on calculated gravity fields to make it comparable to the measured gravity field. The absolute variation in gravity due to the increased sediment thickness is about 15 mGal.

The difference in the gravity field is in turn reflected by variations in the inverted lower
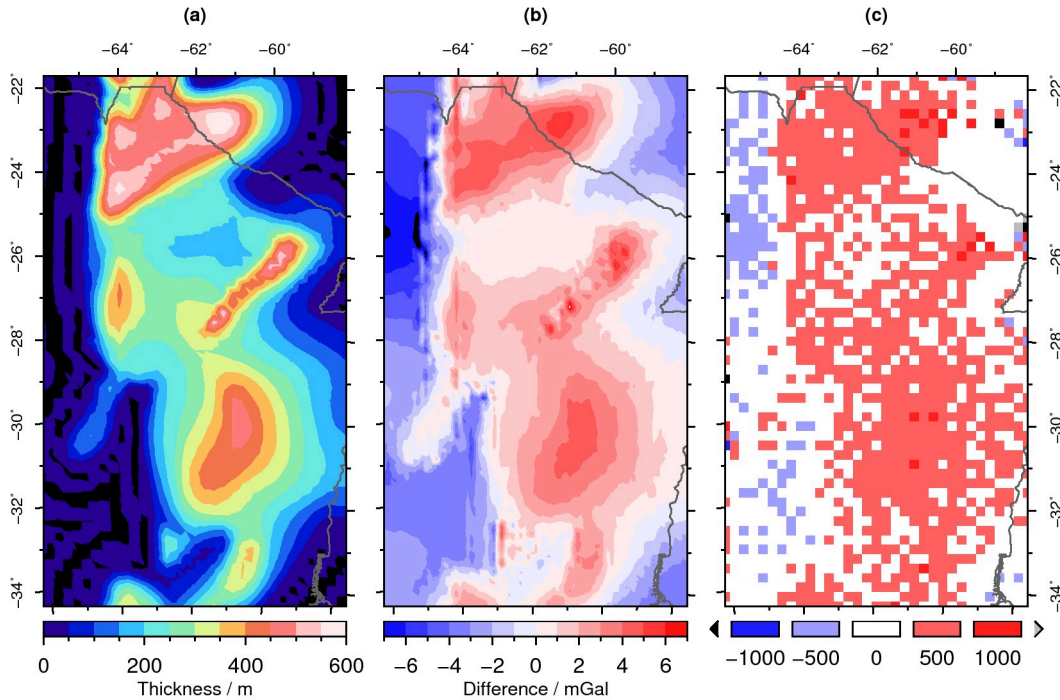
Figure 2.10.: Model sensitivity to basement depth variations: **(a)** sediment thickness difference imposed on the sensitivity model. Sediments in the Neopaleozoic depocentre are about 450 m thicker than in the standard model; **(b)** difference between calculated gravity fields. Negative values indicate mass deficit in the sensitivity model with respect to the standard model; **(c)** difference in inverted lower crustal thickness. Negative values indicate that the lower crust in the sensitivity model is thicker than in the previous models.

crustal thickness (Fig. 2.10c). The pattern of thickness variation appears noisy, which is attributed to the non-unique inversion algorithm and the fact that lower crustal thickness is added in increments of 500 m. However, areas of reduced gravity also correspond to an overall reduction in lower crustal thickness (Fig. 2.10c). This reduction is not larger than 500 m and is restricted to small areas beneath thin sediment cover. Beneath the areas of increased sediment thickness, we observe an increase of lower crustal thickness by 500 m. Only very locally lower crustal thickness increases by 1000 m.

We conclude that inaccurate sediment thickness data impacts the predicted lower crustal thickness by ±500 m. Compared to the absolute thicknesses of several tens of kilometres, this is, however, an acceptable deviation.

2.1.4.5. Moho depth

We performed an exemplary analysis on a profile in the northeast of the modelling area to illustrate the sensitivity of the model results to variations in Moho depth. The profile *A-B* transects an area where the inversion predicts lower crust to be absent, and coincides with the shallowest Moho in the modelling area (Fig. 2.2c). As the Moho depth is very shallow and point constraints are far away, this area seems suitable for testing. For the tests, we subsequently limited the Moho depth to depths of 30, 35, and 40 km and then inverted for the top of the
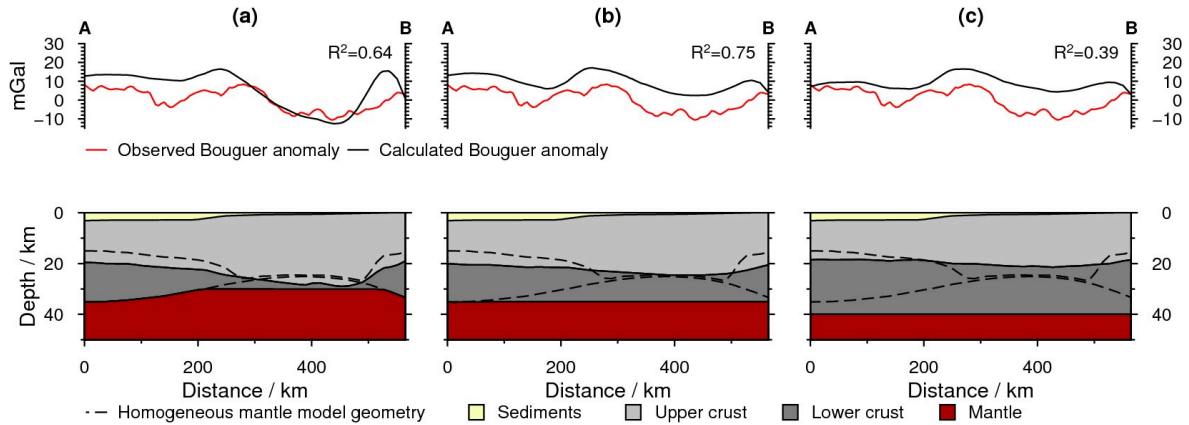
Figure 2.11.: Profiles showing test configurations (below) together with the gravity residuals after the inversion (top). Profile location is provided in Fig. 2.5a. **(a)** Moho capped at 30 km depth; **(b)** Moho capped at 35 km depth; **(c)** Moho capped at 40 km depth. R^2 is the determination coefficient between $g_{z,obs}$ and $g_{z,calc}$.

Table 2.3.: Sensitivity analysis summary of various parameters of the model on the induced variation of the top of the lower crust. The factor f is calculated by dividing the relative variation by the induced variation and is a measure of the extent to which potential errors in the model quantity affect the inferred intra-crustal structure.

	Parameter	Imposed variation Rel.	Abs.	Induced variation	f
		%		km	km/%
z	Basement	10	+0 - 600 m	±0.5	0.05
ρ	Sediments	2	±50 kg m^{-3}	∓1.0	0.5
	Upper crust	2	±50 kg m^{-3}	∓5	2.5
	Lower crust	3	±100 kg m^{-3}	∓5	1.7
	Mantle	1	+30 kg m^{-3}	±4	4.0

lower crust for each depth configuration. The results of the three test models, compared to the homogeneous mantle model, are shown in Figure 2.11. With decreasing Moho depth, the top of the lower crust above the capped Moho gradually increases from about 28 km for the 30 km-deep Moho (Fig. 2.11a), to about 20 km for the 40 km deep Moho (Fig. 2.11c). The calculated gravity fields of the three models is within ±20 mGal of the observed Bouguer gravity field, which indicates that they are approximate equally valid solutions for the subsurface. This example demonstrates that, within the given uncertainty of the provided Moho depth, the crustal configuration can change significantly.

2.1.4.6. Summary of sensitivity analysis

Table 2.3 provides a summary of the sensitivity analyzes conducted. To better compare the impact of the individual model quantities, we calculated a factor f, which we define as the absolute induced variation divided by the relative imposed variation.

The factor is a measure of the variation of the top of the lower crust, or the lower crustal thickness in response to a change in a model parameter; the variation is expressed as a percentage of each parameter. Using this approach small density variations in the upper lithospheric

mantle result in the largest impact on the gravity inversion process in the modelling area. This is owed to the fact that, although the mantle is the deepest body in the model, the mantle volume is the largest component. However, the basement constitutes a major density contrast, and, furthermore is the contrast closest to the gravity stations. Variations in basement depth could be relatively large without altering the main outcomes of this study. Potential variations in Moho depth far away from point constraints exert the largest uncertainty on the model results. However, an increased robustness of the results could only be obtained by more precise depth information on the Moho.

2.1.5. Discussion

2.1.5.1. Model validity

We constrained the density model with geophysical and geological observations and reduced the number of possible solutions by imposing boundary conditions during the inversion. However, a systematic error in our model was introduced by the approximating the Earth's surface as in a flat Cartesian coordinate system. With a simplified model (see Supplement), we show that the error due to this simplification is less than $\pm 5\,\text{mGal}$. This difference would impose thickness changes of about $500\,\text{m}$ to the inferred lower crust, but is not significant enough to change the major trends discovered.

We used the calculated isostatic topography (Fig. 2.6b) as a proxy for the robustness of the results. Therefore, we separated the topographic grids into long and short wavelength components using a Gaussian band-pass filter with a wavelength of $500\,\text{km}$. The inferred topographic map reproduces first-order features ($\lambda \geq 500\,\text{km}$, $R^2 = 0.92$, Fig. A.6e) such as the Central Andes between 28 and 22°S, the Sierras de Córdoba in the southwest and an extensive flood plain in the remaining model area. There are high-amplitude, short-wavelength deviations (Fig. 2.6c) from the observed topography in the foreland of the orogen that are also reflected in gravity residuals after the inversion (Fig. A.4a). This deviation is probably an artifact due to local isostasy, where flexural effects play a dominant role, especially in the area of the Andean thrust wedge. On the other hand, in the southern CPB, an area between 34 to 28°S is predicted to have an elevation up to $300\,\text{m}$ higher than observed, which indicates that the lithospheric column is too light, resulting in additional uplift. A good fit in the gravity residual (Fig. A.4a) and the large wavelength of the uplift indicate that mass differences at depth might cause this deviation. In light of the elevated average mantle densities that were obtained from shear wave models (Figs. 2.7a-c) in the southern part of the model, disregarded masses in the mantle may explain the additional uplift. Optionally, the depth to isostatic equilibrium might be deeper than $200\,\text{km}$ in northern Argentina.

Overall, the good agreement of first-order topographic features between observed and predicted topography argue in favour of the model results. We would like to emphasize that the results of this density model are non-unique and that, given other boundary conditions such as a different Moho depth, the outcome may differ from this model. However, in the following we will discuss the results of our model and highlight differences or deviations from geological

or geophysical observations that allow robust conclusions.

2.1.5.2. Structure and composition of the crystalline crust

We use the predicted average density of the crystalline crust (Fig. 2.6a) as an indicator for lateral partitioning. The map is dominated by two high density provinces ($> 3000 \, \text{kg} \, \text{m}^{-3}$) in the southeast and northwest, that are surrounded by less dense crust (2900 - 2980 $\text{kg} \, \text{m}^{-3}$). We find that these trends agree well with observations on composition and partitioning of the crust and will discuss the details in the following.

Over the whole model area, the trajectory of the Transbrasiliano Lineament (Ramos et al., 2010) coincides with low-density crystalline crust which originates from a shallow Moho (Fig. 2.2c). Ramos et al. (2010) suggested that the Transbrasiliano lineament and location and trend of the early Paleozoic Las Breñas trough might be related to each other, which together with the shallow Moho might be indicative that the thin crust is a relic of ancient crustal thinning. Since thinning of crust and propagation of rifts along sutures is a well-known process, e.g., in the East African Rift (e.g., Hetzel and Strecker, 1994; Smith and Mosley, 1993); therefore, we prefer the location of the Transbrasiliano Lineament by Ramos et al. (2010) over the one proposed by Chernicoff and Zappettini (2004). Accepting the lineament as tectonic boundary, we derive average densities for the Río de la Plata craton of about 3000 $\text{kg} \, \text{m}^{-3}$ and 2970 $\text{kg} \, \text{m}^{-3}$ for the Pampia terrane, excluding the low-density area in the northeast. The Pampia terrane, in addition, seems to be subdivided into a crust with a higher average density to the north (3000 $\text{kg} \, \text{m}^{-3}$) than to the south (2940 $\text{kg} \, \text{m}^{-3}$).

As the greatest part of the Río de la Plata craton in northern Argentina is covered by sedimentary strata of the CPB, its composition is, apart from punctual well data (Rapela et al., 2007; Winn Jr and Steinmetz, 1998), largely unknown. From outcrop and well data in Argentina and Uruguay, Rapela et al. (2007) argued for a rather uniform lithological character of the Río de la Plata craton. Based on the consistently high average crustal density that we obtained east of the Transbrasiliano Lineament (Fig. 2.6a), laterally continuous silica-poor basement rocks throughout the CPB are in agreement with our results.

Observations from outcrops and seismic experiments in the southern Sierras Pampeanas argue for an overall felsic crystalline crust of the Pampia terrane (e.g., Alvarado et al., 2009; Perarnau et al., 2012). At the southern transition between Río de la Plata craton and Pampia terrane (south of 29°S), the average crustal densities in our model decrease from $> 3000 \, \text{kg} \, \text{m}^{-3}$ in the east to about 2920-2960 $\text{kg} \, \text{m}^{-3}$ beneath the Sierras de Córdoba in the west, arguing for a bulk increase of felsic components. The average density decreases to the west as the top of the lower crust is dipping towards this direction (Fig. 2.5c), resulting in an overall thinner lower crust. This deepening beneath the Sierras de Córdoba agrees with the results by Perarnau et al. (2012), but our model underestimates the depth to the lower crust by about 5 km compared to their results. If we regard the inhomogeneous mantle using the model by Assumpção et al. (2013), the difference in the top to the lower crust (Fig. 2.9a) decreases to about 2-3 km, which is in the range of the error of the receiver functions by Perarnau et al. (2012).

For the northern Pampia terrane lower crustal xenoliths have been used to infer an overall felsic composition of the crystalline crust (Lucassen et al., 1999). Our model agrees with this hypothesis as low densities extend northward in a narrow band of about 150 km along the thrust wedge of the Central Andes. Yet, in a laterally restricted province adjacent to the thrust wedge, the average density of the northern Pampia terrane reaches values comparable to the central Río de la Plata craton, possibly indicating a similar mafic crustal composition. Hacker et al. (2011), on the other hand, demonstrated that not only mafic rocks can attain densities above 3000 kg m^{-3} at lower crustal levels; rocks of felsic composition such as pelites or wackes can as well if they were previously exposed to extreme P/T conditions (1050 °C at 3 GPa). Rocks of a similar composition, that is the Puncoviscana formation, were deposited to the west of the crustal high-density province in a peripheral foreland basin at 540 to 524 Ma (Escayola et al., 2011). The authors propose that, during this period, the Puncoviscana formation was deposited on the Arequipa-Antofalla plate, which subsequently subducted beneath the Río de la Plata craton. The sediments of the Puncoviscana could have been exposed to similar P/T conditions during subduction and relaminated to the base of Pampia terrane, a mechanism proposed by Hacker et al. (2011). The present-day extent of the Puncoviscana formation (N of 27°S) argues in favour of this hypothesis, as it coincides with the extent of the high-density crust. Based on the sensitivity analyses, we furthermore eliminate inaccurate basement depth, sediment densities and density variations from the lithospheric mantle as causes for overestimated crustal densities, leaving overestimated Moho depth as an alternative explanation. A bulk change of mineralogy in the crystalline crust could also point to the existence of a still unknown terrane beneath the foreland of the southern Central Andes.

Thick lower crust is predicted beneath the CPB in the southeastern sector of the study area (Fig. 2.5b) that spatially coincides with the extent of Serra Geral flood basalts in the CPB (Fig. 2.1). Since the exact depth level of emplacement and the thickness distribution of the basalts are unknown, an error is introduced to the lower crustal thickness estimate. We estimated the maximum impact of the missing basalt layer ($\rho_{Basalt} \approx 2870$ kg m^{-3}, Christensen and Mooney, 1995) that reaches maximum thickness of $h_{max} = 1.2$ km (Chebli et al., 1999) with $\Delta g \approx 2\pi G h_{max}(\rho_B - \rho_S)$, where G is the gravitational constant and ρ_S the sediment density (Fig. 2.3). This estimate yields a maximum impact of the basalt layer of ≈ 14 mGal on the gravity field, which is about a magnitude lower than the gravity residual in the forward model (100 to 120 mGal). Since for every 10 mGal, the inferred lower crustal thickness changes by about 1 km (Section 2.1.4.1), we conclude that the thickness of the lower crust may be overestimated by 1 to 2 km within the extent of the Serra Geral formation. However, this does not significantly change the observation of thick lower crust beneath the southeastern CPB. Similar accumulations of dense lower crust beneath volcanic centres were observed in seismic refraction studies and gravity constrained models of other areas, such as the Chyulu Hills on the eastern shoulder of the Kenya Rift (Khan et al., 1999; Sippel et al., 2017) or in the Paraná Basin, Brazil (Dragone, 2013). These have been attributed to possible magmatic differentiation and ponding (e.g., Prodehl et al., 1997) of differentiated melts that generated the overlying volcanic provinces. The thickened lower crust may therefore be explained by

differentiation processes at the time of Serra Geral volcanism and may be interpreted as magmatic underplating.

2.1.5.3. Thermal state of the lithosphere

At depths less than 150 km in particular, the selected tomographic models indicate a trend from low velocities at about 24°S to higher velocities south of 28°S (supplement Fig. 10).

At 100 km depth, these velocities translate to temperatures of 1100 - 1200 °C in the north, to 800 - 1050 °C at about 30 °S (Fig. 2.7d-f). The wavelength of this variation is greater than the resolution of tomographic models, and as the different models show similar trends, we argue that the foreland lithosphere of the southern Central Andes could be warmer than beneath the Sierras Pampeanas. At first glance, this observation contradicts the hypothesis of Babeyko and Sobolev (2005), who proposed a cold and strong lithosphere for the southern Central Andes that host the Altiplano, and a warm and weak lithosphere with strong upper crystalline crust for the foreland region that corresponds to the Puna plateau region. However, although the heat input from the lithospheric mantle is important, the heat budget of the crust contributes significantly to the thermal field of the lithosphere, which ultimately affects its strength. Therefore, inferring the rheological state of the lithosphere from tomography-derived temperature maps of the mantle alone would be insufficient.

2.1.5.4. Implications on the rheological behaviour of the lithosphere

From our model results, we derived two principal scenarios for the rheology of the lithosphere in the Andean foreland of northern Argentina. Firstly, if the composition of the high-density crust north of 28°S is of predominantly felsic composition, the thick crystalline crust might add to the heat budget of the lithosphere and therefore lead to further weakening. Alternatively, if the proportion of mafic crust increases, either due to magmatic differentiation or compositional change of the entire crystalline crust, the overall heat budget would be reduced due to the low potential of radiogenic heat produced in mafic rocks (Vilà et al., 2010). The latter scenario might support the hypothesis of Babeyko and Sobolev (2005), as such a thick lower crust could compensate for the high heat input from the lithospheric mantle. However, if the first scenario applies, the foreland of the Bolivian Andes should be weak and easily deformable.

Using the presented 3D model as a basis for assessing the lithospheric-scale thermal field will potentially clarify how temperatures are perturbed by the interaction of the different temperature-controlling factors (i.e., the mantle versus crustal heat contribution). Furthermore, the assessed density configuration of the crust and inferred compositional trends (i.e., mafic versus felsic crust) may be interpreted in terms of rheological trends. Accordingly, the thick lower crust of the Bolivian foreland might be indicative of higher total crustal strengths in this area, given that mafic rocks generally withstand higher deviatoric stresses than felsic rocks before deforming physically (e.g., Carter and Tsenn, 1987). To summarize, our 3D model indicates thermal and compositional variations along-strike the Andean foreland that should be considered when discussing factors responsible for along-strike variations in deformation

styles.

2.1.6. Summary and conclusions

We followed an integrated modelling approach combining forward modelling and inversion to analyse the crustal density structure of the Andean foreland in northern Argentina. The sensitivity of the model was tested in detail with respect to variations in depth and density of individual interfaces and bodies. We find that

1. a model with an upper crust of $2800\,\mathrm{kg\,m^{-3}}$and a lower crust of $3100\,\mathrm{kg\,m^{-3}}$reproduces the observed gravity field.

2. there is evidence for increasing bulk density of the crystalline crust in the foreland north of 28°S, hinting either at a transition to a crust that has a significant proportion of high-density lower crust or a change to a silica-poor bulk composition.

3. although temperatures converted from shear wave velocities argue in favour of a warm lithospheric mantle beneath the Altiplano foreland and colder mantle beneath the Puna Plateau foreland, an increase of mafic components in the crystalline crust north of 28°S may be indicative of lower amounts of radiogenic heat and thus lower crustal temperatures than in the foreland to the east of the Puna plateau.

4. thick high-density lower crust spatially correlates with the extent of Jurassic flood basalts and may represent the product of magma differentiation or possible magmatic underplating associated with these massive volcanic extrusions.

5. extensional processes in the early Paleozoic along the Transbrasiliano Lineament, as proposed by Ramos et al. (2010), might have led to the shallow Moho observed beneath the lineament and the Las Breñas trough.

6. density variations in the upper lithospheric mantle and the thickness variations in the lower crust have the largest impact on the modelling results for this particular study area.

7. the configuration of the Moho is essential to the density configuration of the crystalline crust, and better data coverage in the CPB would enhance the results of this study.

The data for this model are available as supporting information on the journal website for this article.

2.2. Lithospheric control on asthenospheric flow from the Iceland plume: 3D density modelling of the Jan Mayen-East Greenland region, NE Atlantic

2.2.1. Introduction

The Iceland Plume exerts far-field effects on the thermal structure of adjacent mid-ocean ridges, both to the south (Reykjanes Ridge) (e.g. Ito, 2001; Parnell-Turner et al., 2014; White et al., 1995) and to the north of the plume (e.g. Howell et al., 2014; Jones et al., 2002; Pilidou et al., 2005). There is debate as to what extent the spreading ridges channel the flow of plume material (e.g. Ito, 2001; Shorttle et al., 2010). Using observed seismic anisotropy patterns beneath Iceland, Xue and Allen (2005) suggest that there is a ridge-channelled flow of material away from Iceland towards the southern end of the Kolbeinsey Ridge. Based on a regional tomography model and observed gravity field, Marquart et al. (2007) pointed out that the Kolbeinsey Ridge is characterized by a large-scale radial buoyancy plume flux around Iceland, superimposed on the ridge perpendicular spreading. A later examination of geophysical and geochemical data along the Kolbeinsey Ridge, on the other hand, motivated Shorttle et al. (2010) to suggest that the Iceland Plume spreads in a radial, pancake-like fashion. Recent high-resolution 3D thermo-mechanical numerical modelling suggests that flow of the plume material along the Kolbeinsey Ridge is constrained by pre-existing lithosphere structures related to the rifting of the Jan Mayen microcontinent off East Greenland (Koptev et al., 2017).

Several studies suggest that a lateral mantle flow related to the Iceland Plume extends as far north as the West Jan Mayen Fracture Zone (WJMFZ) (Breivik et al., 2008; Howell et al., 2014; Jones et al., 2002), shown by a sub-lithospheric low-velocity layer observed under the study area (Pilidou et al., 2005; Rickers et al., 2013). Similarly, the refraction seismic studies of Hooft et al. (2006) indicate that the Kolbeinsey Ridge (Fig. 2.12) is characterized by shallow mantle melting caused by a hot and less viscous outflow of the Iceland Plume into the asthenosphere under the ridge. Both regional geochemical and seismic studies suggest a decreasing amount of thermal and geochemical plume influence with distance from the centre of the Iceland plume (e.g. Hooft et al., 2006; Klingelhöfer et al., 2000b; Kodaira et al., 1997; Schilling, 1999).

The thermal structure of oceanic lithosphere is controlled by its cooling history so that temperature at a given depth decreases with increasing age and distance from a mid-ocean ridge (e.g. Adam and Vidal, 2010; Doin and Fleitout, 1996; Stein and Stein, 1992). The
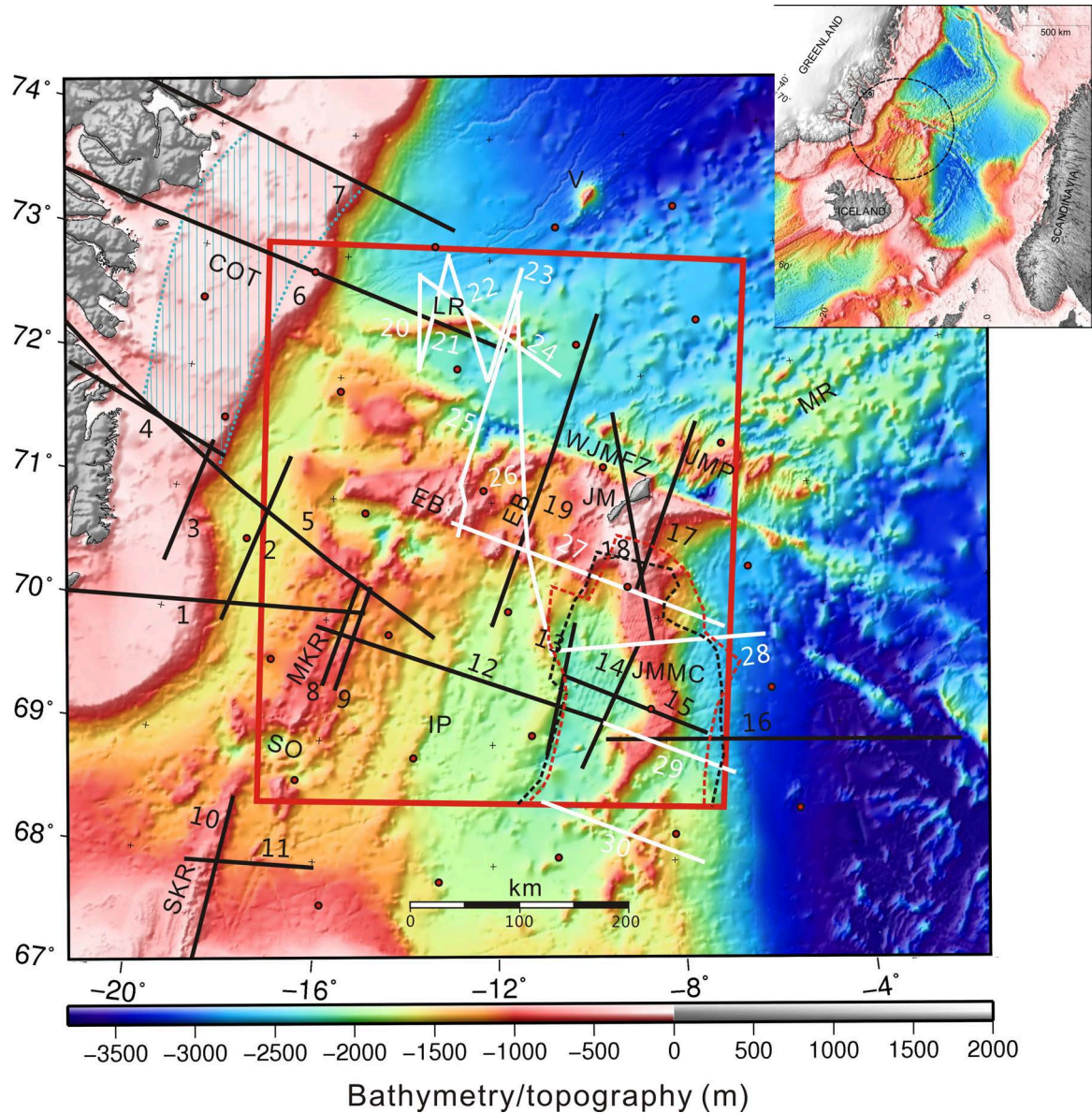
Figure 2.12.: Topography and bathymetry of the study area (IBCAO-3) (Jakobsson et al., 2012). Inserted map (ETOPO 2V2) (National Geophysical Date Center, 2006) shows the location of the study area. The black and white lines show the locations of refraction and reflection seismic lines, respectively (annotations in Table 2.4). The Continent Ocean Transition Zone (COT) is shown in blue dotted lines (Hermann, 2013; Voss and Jokat, 2007), outline of the Jan Mayen Microcontient (JMMC)(black dashed line) is derived from Peron-Pinvidic et al. (2012a,b), while the red dashed line represents the location of the JMMB by (Breivik et al., 2012a) incorporating results from Kandilarov et al. (2012). The red dots represent points sampled from tomography model with a horizontal spacing of 100 km (Rickers et al., 2013). The Eggvin Bank is a topographically anomalous shallow area with scattered volcanic peaks between the Jan Mayen Island and East Greenland (Mertz et al., 2004). EB: Eggvin Bank, IP: Iceland Plateau, JM: Jan Mayen Island, JMP: Jan Mayen Plateau, JMMC: Jan Mayen Microcontinent, LR: Logi Ridge, MKR: Middle Kolbeinsey Ridge, MR: Mohn's Ridge, SO: Spar Offset, SKR: South Kolbeinsey Ridge, V: Vesteris Seamount.

Table 2.4.: Database for the construction of a 3D structural and density model that differentiates the main sedimentary and crustal units.

Label	Line name	Reference	Available information
Input regional seismic reflection and refraction lines (Fig. 2.12)			
1-4	ARK 1988 lines 3-6	Weigel et al. (1995)	V_p model, 2D gravity
5	AWI20090100	Hermann (2013)	V_p model, 2D gravity
6-7	AWI20030400 and AWI 20030500	Voss and Jokat (2007)	V_p model, 2D gravity
8-9	JMKR-95 lines 1-2	Kodaira et al. (1997) and Mjelde et al. (2002)	V_p model, V_s model
10	KRISE line 1	Hooft et al. (2006)	V_p model, 2D gravity,isostasy
11	KRISE line 4	Furmall (2010)	V_p model
12	JMKR-95 lines 3	Kodaira et al. (1998a) and Mjelde et al. (2002)	V_p model, V_s model
13-15	JMKR-95 lines 4-6	Kodaira et al. (1998b) and Mjelde et al. (2007)	V_p model, V_s model, 2D gravity
16	OBS 2000 lines 8-00	Breivik et al. (2012a)	V_p model
17-18	OBS-JM-2006 lines 1-2	Kandilarov et al. (2012) and Kandilarov et al. (2015)	V_p model, V_s model, 2D gravity
19	Profile-1	Tan et al. (2017)	V_p model, V_s model
20-24	Profile2-6	Breivik et al. (2012b)	Reflection seismic
25-27	NPDJM11-004,005,006	Sandstå et al. (2012)	Reflection seismic
28-30	NPD08, Inseis 01, Inseis 06	Peron-Pinvidic et al. (2012a,b)	Reflection seismic

Name	Reference	Comments
Additional constraints		
Crustal models of the Mohn's Ridge	(Klingelhöfer et al., 2000a,b)	Constrain the Moho depth in the Mohn's Ridge for oceanic ages less than 22 Ma (Fig. 2.13c)
Moho depth of NE Atlantic	(Haase et al., 2016)	Derived from 3D gravity inversion modelling; here only used in the NKR where refraction seismics are lacking (Fig. 2.13c)
Sediment thickness of world's ocean and marginal seas	(Divins, 2004)	Grid spacing of 5 arc-minutes by 5 arc-minutes provides additional information on the depth of the basement
CRUST 1.0	(Laske et al., 2013)	1 × 1 degree grid provides additional information on the depth of Moho

question is how the Iceland Plume affects the thermal state of the greater Jan Mayen-East Greenland Region, where different segments of a number of active mid-ocean ridges meet (Fig. 2.12). Haase et al. (2016) published 3D forward-and inverse- gravity modelling of the NE Atlantic, where the temperature-dependent lithospheric mantle densities are derived from the age of the oceanic lithosphere following the approach of Sandwell (2001). We note that their model has a mass excess along the Kolbeinsey Ridge and north of the WJMFZ. This area correlates with an area of low upper mantle seismic S-wave velocities (Rickers et al., 2013), which suggests that the upper mantle densities have been overestimated, and that the gravity misfit in their model could be related to mass anomalies caused by the Iceland plume.

Measured gravity anomalies are the result of the density structure from the shallowest sediments, crust, and upper mantle. Information about the upper mantle density below 50 km can be derived from mantle tomography models, while the crustal structure and sediment distribution is reasonably well known from active source seismic data. We can use variations in the observed gravity field of the greater Jan Mayen-East Greenland Region to derive the density configuration of the upper mantle above 50 km to infer first-order trends of related temperature variations. The seafloor, the top of the basement (interface between sediments and crystalline crustal rocks) and the Moho (crust-mantle boundary) represent the largest density contrasts in the lithosphere. The region is relatively well covered by geological and geophysical observations derived from reflection and refraction seismic data (e.g. Hermann and Jokat, 2016; Kodaira et al., 1998b, 1997), teleseismics (e.g. Rickers et al., 2013) and gravity data (e.g. Gaina et al., 2011) (Fig. 2.12, Tab. 2.4).

The objective of our study is to develop a 3D density model of the study area that is consistent with all available geophysical observations to provide new constraints on the lateral geometry and extent of the shallowest upper mantle domain that is presently most affected by the Iceland Plume.

2.2.2. Geological setting

The research area extends from the Jan Mayen Ridge to the east coast of Greenland, and from the South Kolbeinsey Ridge (SKR) in the south (Spar offset) to the Logi Ridge in the north (Fig. 2.12). With the very slow-spreading Kolbeinsey and Mohn's ridges (full spreading rate less than 20 mm/yr) (Gaina et al., 2009), the anomalously shallow Eggvin Bank, the Jan Mayen Microcontinent (JMMC), and the tectonically active WJMFZ, the region represents one of the most complex areas of the NE Atlantic region.

The rifting of the JMMC off the East Greenland margin occurred around 24-25 Ma due to the spreading axis jump from the Aegir Ridge to the Kolbeinsey Ridge (e.g. Nunns, 1982). The spreading along the Kolbeinsey Ridge is slow (full rate: 16-18 mm/yr) and nearly orthogonal (Appelgate, 1997). It underwent several minor eastwards jumps of the spreading axis (e.g. Appelgate, 1997). The Kolbeinsey Ridge is divided into three different sections (southern, middle and northern part), of which the study area only covers the middle and northern parts. The Middle Kolbeinsey Ridge (MKR) and surrounding Iceland Plateau show abnormally thick

oceanic crust (average 9 km) and shallow bathymetry (Kodaira et al., 1998a, 1997), which is attributed to the thermal influence of the Iceland Plume (Elkins et al., 2011; Kodaira et al., 1998a,b, 1997). The MKR basalts are related to a homogeneously depleted mantle source (e.g. Elkins et al., 2011). In contrast, the basalts from the North Kolbeinsey Ridge (NKR) and nearby Eggvin Bank are enriched in incompatible elements and radiogenic isotopic composition (e.g. Elkins et al., 2016; Haase et al., 2003). The Eggvin Bank is a shallow region surrounding the northern Kolbeinsey Ridge segment. A seismic refraction line across the bank approximately 70 km east of the spreading ridge shows large variations in crustal thickness (from 8 to 13 km) (Tan et al., 2017). The seismic velocities indicate that there could be some thermal Iceland plume influence under the northern Eggvin Bank, while the elevated magmatism in the southern Eggvin Bank may be mostly affected by an enriched mantle source (Tan et al., 2017).

The WJMFZ offsets the adjacent spreading axes right-laterally by about 200 km. North of the fracture zone, opposite of the Jan Mayen Island (Fig. 2.12), spreading takes place on the Mohn's Ridge. The formation of the Mohn's Ridge dates back to the continental breakup between Greenland and Norway in the Early Eocene (54-55 Ma). The rate of spreading is symmetrical having a full rate of 16 mm/yr, and the spreading direction is moderately oblique. It is mostly producing a thin oceanic crust (4 ±0.5 km) (Kandilarov et al., 2012; Klingelhöfer et al., 2000a,b). The thick oceanic crust observed along the East Greenland and conjugate Norwegian margins show that the commencement of the Mohn's Ridge was influenced by the Iceland Plume to increase magma productivity during the earliest spreading phase (e.g. Breivik et al., 2009; Breivik et al., 2014; Voss and Jokat, 2007).

The JMMC has large crustal thickness variations. The maximum thickness is observed at the northern boundary of the JMMC (25 km), while the minimum could be as low as 3 km (Kandilarov et al., 2012; Kodaira et al., 1998b). In addition, the eastern and western sides of JMMC are interpreted as volcanic and non-volcanic rifted margins, respectively (e.g. Breivik et al., 2012a; Kodaira et al., 1998b).

2.2.3. 3D gravity modelling

2.2.3.1. Modelling strategy

Aside from one refraction seismic profile (Hermann and Jokat, 2016), there is a lack of seismic constraints on mantle densities between 50 km (b.s.l.) and the Moho. Hence, the main purpose of performing 3D gravity modelling is to close this observation gap between the crust and mantle densities that can be obtained from mantle tomography. Therefore, we integrate the data-derived densities for the sediments, crust and deeper mantle into an initial 3D density model and adjust the 3D density configuration of the shallowest mantle until the gravity response of the entire 3D model is consistent with the observed gravity anomalies.

First, we calculate the gravity response of an initial 3D density model that includes the data-constrained densities of the sediments, crust and deeper mantle, while including a constant density of 3300 kg m^{-3} for the shallowest unconstrained mantle (forward gravity modelling). As

a result of this step, we obtain the gravity misfit of this initial 3D density model by subtracting the observed gravity from the calculated gravity. A positive gravity misfit then corresponds to a mass excess in the model. In a second step, we use the gravity misfit to invert for the density configuration of the shallowest mantle above 50 km depth (inverse gravity modelling).

For the forward calculations, we use the Interactive Gravity and Magnetic Application System IGMAS+ (Götze and Lahmeyer, 1988; Schmidt and Götze, 1998; Schmidt et al., 2011). IGMAS+ calculates the total gravity response of a predefined 3D density model by combining triangulated model geometries (polyhedrons that geometrically define geological units) with density information attached to voxel cubes. For the inverse gravity modelling step, we make use of a modified version (Meeßen et al., 2018) of the Harvester module (Uieda and Barbosa, 2011), which is part of the open-source code library *fatiando a terra* (for Python 2.7; (Uieda et al., 2013)).

2.2.3.2. Modelling the structure and density of the sediments and crystalline crust

Previous studies, including (i) the interpretation of reflection seismic data (Blischke et al., 2016; Peron-Pinvidic et al., 2012a,b) , (ii) wide-angle refraction seismic data (Breivik et al., 2012a; Hermann and Jokat, 2016; Kandilarov et al., 2012; Kandilarov et al., 2015; Klingelhöfer et al., 2000a,b; Kodaira et al., 1998a, 1997; Tan et al., 2017; Voss and Jokat, 2007; Weigel et al., 1995), and (iii) studies of dredged samples (e.g. Elkins et al., 2016, 2011; Haase et al., 2003; Klingelhöfer et al., 2000b; Mertz et al., 2004; Schilling, 1999), show that the study area is characterized by large variations in terms of crustal structure as well as mantle composition, and mantle melting degree. Table 2.4 and Figure 2.12 provide an overview of the data types and sources used to develop a 3D structural and density model for the crystalline crust and sedimentary cover. Based on the published interpretations, we define 10 sedimentary and crustal layers with characteristic densities for our study area. (left column of Tab. 2.5) and thus be used to construct the elements for the 3D density model.

The Cenozoic sediments are dominated by muds and silts with some additional ice-rafted material from the recent glacial periods (e.g. Blischke et al., 2016; Haase et al., 2003; Thiede and Hempel, 1991). At depths down to 1 km they are estimated to have low densities (2100 kg m^{-3}); higher densities (2400 kg m^{-3}) were assigned to deeper Cenozoic sediments (burial greater than 1 km). The pre-Cenozoic sediment layers, which are only observed in the JMMC, are characterized by relatively high velocities (4.5-5.6 km/s), and thus are modelled with the highest sedimentary densities (2650 kg m^{-3}).

The oceanic crust is divided into two layers, a lower-velocity upper crust (V_p: 2.5-6.6 km/s) and a high-velocity lower crust (V_p: 6.6-7.6 km/s). The upper oceanic crust corresponds to pillow lavas and sheeted dikes (Detrick et al., 1994; Dilek, 1998). It is strongly influenced by fissures and cracks causing higher porosity (Jacobson, 1992), thus it was assigned lower densities (2700 kg m^{-3}). The lower crust is characterized by gabbroic rocks of low porosity and higher density (3000 kg m^{-3}). Dense intruded bodies (3160 kg m^{-3}) are indicated by regional refraction studies in the area of the Greenland continental-ocean transition (COT) (Fig. 2.12)

Table 2.5.: Densities of geological units from publications used to setup the initial 3D density model (last column).

	Density published for the surrounding area / kg m⁻³								Modelled Density / kg m⁻³
	Voss and Jokat (2007)	Weigel et al. (1995)	Peron-Pinvidic et al. (2012a,b)	Mjelde et al. (2007)	Kandilarov et al. (2012)	Hooft et al. (2006)	Hermann (2013)	Haase et al. (2016)	
	East Greenland (Logi Ridge)	East Greenland (MKR)	JMMC	JMMC, Iceland Plateau	JMMC, Jan Mayen	SKR	NE Atlantic (3D modelling)	NE Atlantic (3D modelling)	
Water	1030	1030	1030	1030	1030	1030	1030	1030	1030
Cenozoic upper	2000-2400	2100	2100	2000	2200		1900-2100	2200	2100
Cenozoic lower	2330-2520		2100	2300	2400		2400	2200-2700	2400
Precenozoic	2560-2650	2300-2600	2560	2520-2730	2400		2200-2700	2200-2700	2650
Upper oceanic crust	2600	2800-2900	2750	2840	2850	2850	2900	2850	2700
Lower oceanic crust	2900	3000-3100	3000	3000	2850	2850	2900	2850	3000
Upper continental crust	2720		2740	2700-2820	2750-2950		2700	2750	2700
Lower continental crust	2830-2900		2950	2830-2960	3050		2950	2950	2950
Lower-crustal intrusions	3160						3180	3180	3160
Upper crust (JMMC)					2900			2950	2900
Lower crust (JMMC)					3050			2950	2950
Upper mantle	3240-3310	3200-3300	3300	3200-3400	3200-3400	3240	3220-3310	3200-3300	3050

Note. MKR = Middle Kolbeinsey Rdige; JMMC = Jan Mayen Microcontinent; SKR = South Kolbeinsey Ridge.

(Hermann, 2013; Voss and Jokat, 2007).

The continental crust of the JMMC is divided into an upper layer of lower V_p (4.5-6.5 km/s) and modelled density (2700 kg m^{-3}) and a lower layer of higher V_p (6.5-6.85 km/s) and density (2950 kg m^{-3}). A relatively dense upper (2900 kg m^{-3}) and lower crust (3050 kg m^{-3}) is restricted around the northern boundary of the JMMC where the Moho depth is greatest (Kandilarov et al., 2012; Kandilarov et al., 2015).

The modelled crustal densities are consistent with empirical velocity-density relationships (Barton, 1986) and are within the range of densities from previous studies (Tab. 2.5). The Moho depth is mainly constrained by seismic lines revealing mantle refractions (P_n) and Moho reflections (P_mP). It represents an intra-lithospheric boundary with a large density contrast, which is characterized by an increase in P-wave velocity to values greater than 7.6 km/s.

We used QGIS (QGIS Devlopment Team, 2009) to georeference all the seismic constraints into a consistent coordinate system (UTM 28N). Since seismic profiles do not cover the entire area, we have implemented additional constraints (Tab. 2.4). These are (i) a crustal model of the Mohn's Ridge (Greenland Basin) covering the region of oceanic ages of less than 22 Ma (Klingelhöfer et al., 2000b); (ii) Moho depths of the NE Atlantic as derived by 3D gravity inversion (Haase et al., 2016), that were only used in the western NKR domain where refraction seismic data are lacking; (iii) a global model of oceanic sediment thickness (Divins, 2004) and (iv) crustal thickness (CRUST 1.0) (Laske et al., 2013) (Tab. 2.4, Fig. 2.13c). These models provide additional information on the depth of basement and the Moho, which we use to fill the gaps between the original seismic constraints.

The results from seismic lines and additional constraints listed in Table 2.12 were jointly interpolated with Petrel (by Schlumberger 1998–2013) using the *Minimum Tension Gridding* algorithm to create regular grids of interfaces. In case of the WJMFZ, due to the sharp changes across the fracture zone, we first interpolate between seismic lines north of the WJMFZ to create regular grids, then we interpolate between seismic lines south of the WJMFZ, and finally we combine these two grids together. The dimensions of the final modelling area are 420 km in north-south direction and 500 km in east-west direction. The model has a horizontal node spacing of 10 km in both northing and easting directions. The vertical spacing (down to Moho depth) corresponds to the thickness of the different geological units. The chosen model node spacing preserves the main structural trends derived from the seismic refraction and reflection lines.

Figure 2.13 shows the two key horizons (top basement and Moho), as well as sediment and crustal thickness. The basement depth in the oceanic domain increases with increasing distance from the spreading centres (Fig. 2.13a). In addition, wide parts of the Kolbeinsey Ridge, Iceland Plateau and Eggvin Bank are high standing areas. Here, the depth of the basement is almost equal to the seafloor bathymetry, while a thin layer of sediments (< 2 km) is observed in the western domain of the MKR. In the Greenland Basin (north of the WJMFZ), the sediments are only Cenozoic with a thickness of less than 500 m around the Mohn's spreading ridge, increasing to 7000 m towards the continent-ocean boundary off Greenland (Fig. 2.13b). The JMMC is covered by sediments varying in thickness from 0 to 7000 m (Fig. 2.13b). The
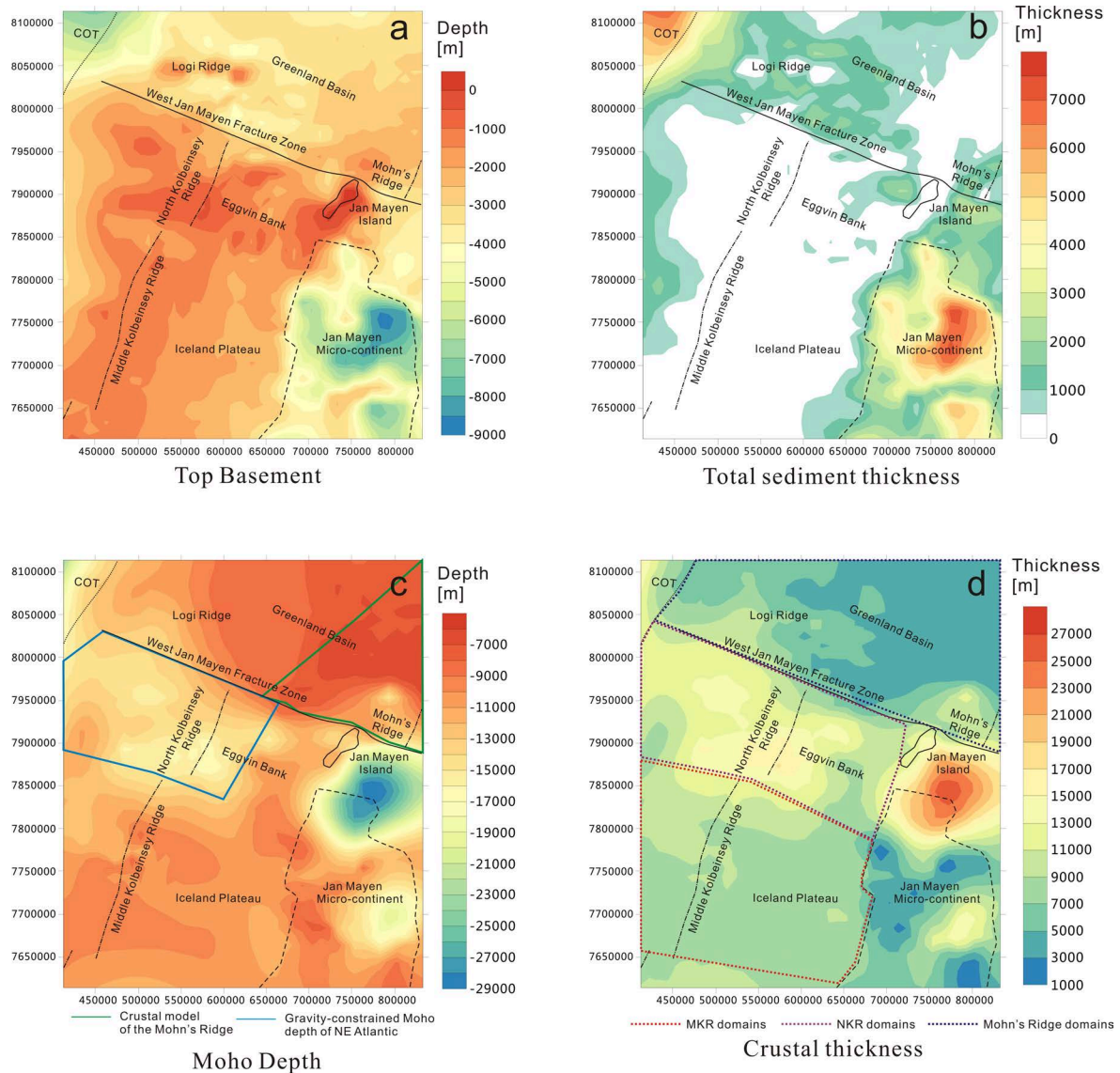
Figure 2.13.: Major structural elements of the crust. Locations of three present day spreading axis are derived from regional magnetic anomaly data (Olesen et al., 2007). **(a)** Depth to the top of the crystalline crust (basement), **(b)** Total sediment thickness, **(c)** Depth to the crust-mantle boundary (Moho) as mostly constrained by seismic data (Fig. 2.12), the area constrained by the crustal model of the Mohn's Ridge (Klingelhöfer et al., 2000a) and gravity-constrained Moho depth of the NE Atlantic (Haase et al., 2016) are presented by green and blue lines, respectively. **(d)** Thickness of the crystalline crust; the colour-coded dotted lines outline three different domains (MKR, NKR, and Mohn's Ridge) used for further analysis (see main text).

sedimentary section is thickest along the eastern margin of the JMMC (Fig. 2.13b).

In the Greenland Basin, the Mohn's Ridge shows a shallow Moho depth of approx. 7 km, while the Moho depth increases to 19 km towards the continent-ocean boundary off Greenland (Fig. 2.13c). The average crystalline crustal thickness is around 8.5 km along the MKR and adjacent Iceland Plateau, and increases to around 12-15 km over the Eggvin Bank in the NKR domain (Fig. 2.13d). In the JMMC, the Moho depth varies strongly with the shallowest depths beneath the western edge of the JMMC (Jan Mayen Basin) (8.5 km), moderate depths beneath the eastern edge of the JMMC (Jan Mayen Ridge) (18 km), and largest depths around the northern part of the JMMC (27 km) (Fig. 2.13d). The western margin of the JMMC shows an abrupt transition from thin continental crust (5 km) to a thick oceanic crust (9 km) in the Iceland Plateau (Fig. 2.13d).

2.2.3.3. Density configuration of the mantle at depths below 50 km (b.s.l.)

This chapter has been shortened. Please refer to Appendix B.1 for more detailed information.

We have utilised the tomographic model of the North Atlantic by Rickers et al. (2013) to obtain the density distribution in the lithospheric mantle. Due to the vertical resolution of 10 km in the uppermost 350 km, and the largest Moho depth of 28 km, we suggest that velocities are not accurately imaged at depths shallower than 50 km. To obtain the density distribution in the mantle at depths greater than 50 km, we first converted the shear wave velocities to temperatures using the approach suggested by Priestley and McKenzie (2006), see Appendix B.1.1. In a second step, we converted these temperatures to densities (Appendix B.1.2) using relationships between temperature and density proposed by Bai et al. (2014). These density estimates consider temperature- and pressure-dependent thermal expansion coefficients and bulk moduli of the mantle rocks.

2.2.3.4. Gravity response of the initial 3D density model

In order to avoid edge effects during the gravity modelling, we have extended the model horizontally by 300 km in all directions. The extended area is mainly constrained by regional seismic refraction studies (Brandsdóttir et al., 2015; Furmall, 2010; Hermann, 2013; Hooft et al., 2006; Klingelhöfer et al., 2000b; Voss and Jokat, 2007; Weigel et al., 1995) (Fig. 2.12), the global map of oceanic sediment thickness (Divins, 2004), and the model CRUST 1.0 (Laske et al., 2013).

We performed the gravity modelling covering an area of 1020 × 1100 km (extended region) for the density configurations of the sediments, crust, and mantle above 250 km (regular 10 km × 10 km grids). The 3D density model in IGMAS+ is built upon a series of parallel vertical 2D planes, where the 3D structure is obtained by triangulating polyhedrons between planes. In this study, the gravity model contains 56 parallel working planes running in east-west direction at 20 km intervals. Thus, the 2D planes are approximately perpendicular to the mainly N-S directed major structural elements, crossing the most important gravity lows and
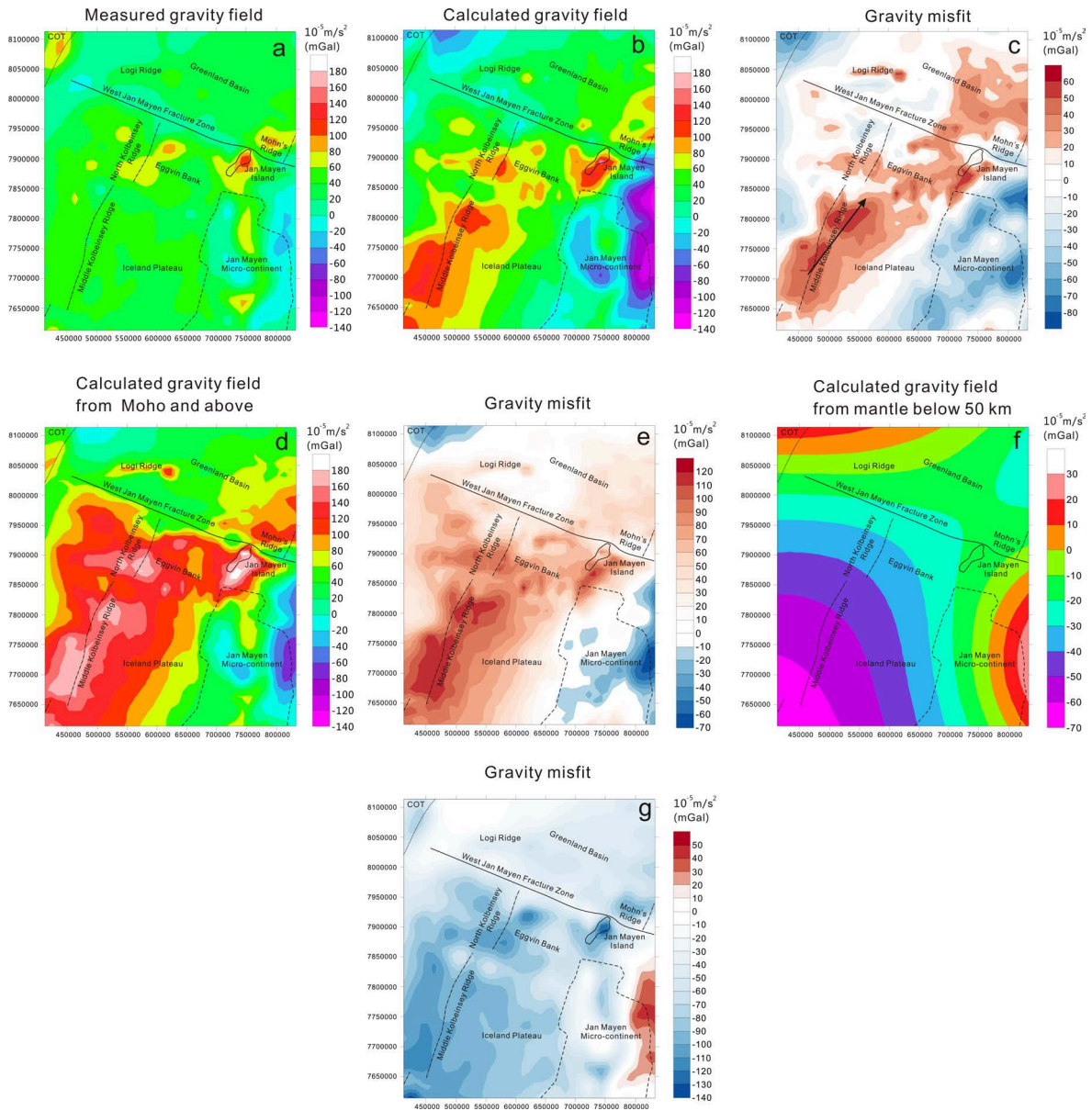
Figure 2.14.: (a) Observed gravity field; free air gravity anomaly offshore and the Bouguer anomaly for the Jan Mayen Island (Gaina et al., 2011). **(b)** Gravity field calculated for the initial 3D density model with homogeneous mantle density (3300 kg m⁻³) between Moho and 50 km. **(c)** The gravity misfit is the calculated field subtracted the observed field. Blue colours indicate a mass deficit in the model, while the red areas show mass excess. The black arrow indicates the NE-SW axis of maximum positive gravity anomalies. **(d,e)**: The calculated gravity response induced only by masses located above the Moho, and the gravity misfit made by subtracting the observed field from it. **(f,g)**: The calculated gravity field from the mantle below 50 km, and the gravity misfit made by subtracting the observed field from it.

highs (Fig. 2.14a).

To each sedimentary and crustal model unit, a homogeneous density is assigned (Tab. 2.5). The mantle density is constant (3300 kg m^{-3}) between the Moho and 50 km, while the S wave-derived density configuration of the mantle between 50 and 250 km depth is modelled by a voxel grid with a regular spacing of 10 km in both horizontal and vertical directions.

The gravity field data that we have chosen to use is CAMP-G, a recently published Arctic gravity field model (10×10 km grid resolution) containing free-air gravity anomalies offshore and Bouguer anomalies onshore (Jan Mayen Island) (Gaina et al., 2011) (Fig. 2.14a). It is an expansion of the ArcGP free air gravity published by Kenyon et al. (2008) by compiling regional gridded data, and merging that with a hybrid satellite/surface measurement based gravity model (EIGEN GL04C) (Förste et al., 2008) for the long wavelengths. There is a gravity low over the eastern margin of the JMMC and Jan Mayen Basin. The gravity field over the Eggvin Bank, Jan Mayen Island, and Jan Mayen Ridge show pronounced high gravity. In addition, the WJMFZ is characterized by a narrow gravity low bounded by positive gravity anomalies on both sides. The gravity over most parts of the Mohn's Ridge and the MKR reveal moderately positive anomalies, ranging from 20 to 40 mGal.

Figure 2.14c shows the gravity misfit (Root Mean Square (RMS): 34.24 mGal) calculated as the gravity response of the initial density model (Fig. 2.14b) minus the observed gravity (Fig. 2.14a). Any negative gravity misfit implies a mass deficit in that particular area of the model. The initial gravity misfit is characterized by a NE-SW striking, positive (up to 60 mGal) misfit trending from MKR to the Mohn's Ridge. At MKR, this anomaly runs slightly east from the spreading axis, where the gravity misfits are gradually decreasing away from this trend. The JMMC is dominated by short-wavelength negative misfits, while short-wavelength positive misfit anomalies are observed at the Eggvin Bank. In addition, we calculated gravity response induced by masses located above the Moho (Fig. 2.14d) and mantle below 50 km (Fig. 2.14f), and their corresponding gravity misfit anomaly fields (Fig. 2.14e,g), in order to reveal how they contributed to the gravity modelling.

2.2.3.5. Gravity inversion: mantle density shallower than 50 km

The gravity misfit calculated for the initial 3D density model (Fig. 2.14c) provides the boundary condition for the inversion step: To minimize the gravity misfit of the forward model, we use the Harvester algorithm (Uieda and Barbosa, 2011; Uieda et al., 2013) to stepwise modify the density distribution of the mantle at depths < 50 km. This algorithm propagates initial density perturbations – the *seeds* – through a mesh of rectangular prisms with a defined reference density – the *medium* –, repeated until the corresponding forward gravity field reaches the prescribed boundary condition. In the present study, the *seeds* initially form a 1 km thick layer of which (i) the base is situated at a depth of 50 km and (ii) the density distribution is equal to the one at 50 km depth as derived from the V_{SH} constraints (Fig. B.2b). The minimum top depth is constrained by the Moho. The *seeds* replace the *medium* in the upward direction, where the *medium* is assigned a constant density of 3300 kg m^{-3} (a mantle density

value typical at the depth of the Moho). The final thicknesses of the *seeds* and the *medium* (obtained when the gravity misfit is minimized) define the average bulk density of the shallowest mantle. Hence, we have calculated the vertically averaged density of the mantle at depth of < 50 km, by weighting the density of a *seed* and its overlying *medium* by their relative thicknesses for each column:

$$\rho_{average} = (t_m \cdot 3300 kg/m^3 + t_s \cdot \rho_s)/(t_m + t_s) \qquad (2.1)$$

where $\rho_{average}$ and ρ_s represent the average mantle density at depths shallower than 50 km and the density of *seeds*, while the t_m and t_s corresponds to the thickness of *medium* and *seeds*, respectively.

Figure 2.15a presents the resulting average mantle density for depths shallower than 50 km. This configuration shows lower densities of <3220 kg m^{-3}under the MKR and in an area close to Mohn's Ridge spreading axis, but significantly higher density (3250-3270 kg m^{-3}) in the middle northern part of the study area (red line in Fig. 2.15a). Then, we modified the initial 3D density model by substituting the homogeneous density of the shallowest mantle by the inverted average densities (Fig. 2.15a) and recalculated the gravity response of the entire model (using IGMAS+). This calculation results in the new gravity misfit field shown by Figure 2.15b.

The gravity misfit map (Fig. 2.15b; RMS: 20.37 mGal) shows that the middle northern parts of the study area are characterized by a large positive gravity misfit (up to 70 mGal), which indicates mass excess in this domain of the model. Because the density reduction of the upper 50 km of the mantle is restricted by the density of the seed, this prevents the uppermost mantle to obtain arbitrarily low densities, and thus there can still be a gravity misfit after this first inversion step. This area of model mass excess is observed within the area of temperatures lower than 900 °C (outlined by the red line in Fig. 2.15b), where the conversion to temperature and density has the largest uncertainties (Priestley and McKenzie, 2013). These uncertainties allow for changing the starting conditions for a second inversion run. In order to reduce the mass excess, the seed density was lowered from the 3210-3280 kg m^{-3}range to a uniform 3210 kg m^{-3}for this region, corresponding to 900 °C at 50 km depth.

The average mantle density distribution from the second inversion run is shown in Figure 2.15c, and the corresponding misfit in Figure 2.15d. As reflected in the initial gravity misfit field (Fig. 2.14c), the mantle density below the MKR is characterized by a NE-SW trending anomaly of low density (3180-3200 kg m^{-3}) with densities gradually increasing perpendicular to this virtual axis. Interestingly, the NE-SW elongated mantle anomaly does not, however, coincide entirely with the NNE-SSW striking ridge axis. The NKR domain is characterized by intermediate mantle densities (3200-3240 kg m^{-3}). In the region of the Greenland basin, close to the Mohn's Ridge spreading axis, the average mantle density is around 3220 kg m^{-3}, slightly increasing to 3240 kg m^{-3}away from the spreading axis, with a sharp increase to 3280 kg m^{-3}at the COT. In addition, some relatively high mantle densities (3250 kg m^{-3}) are observed around the WJMFZ.
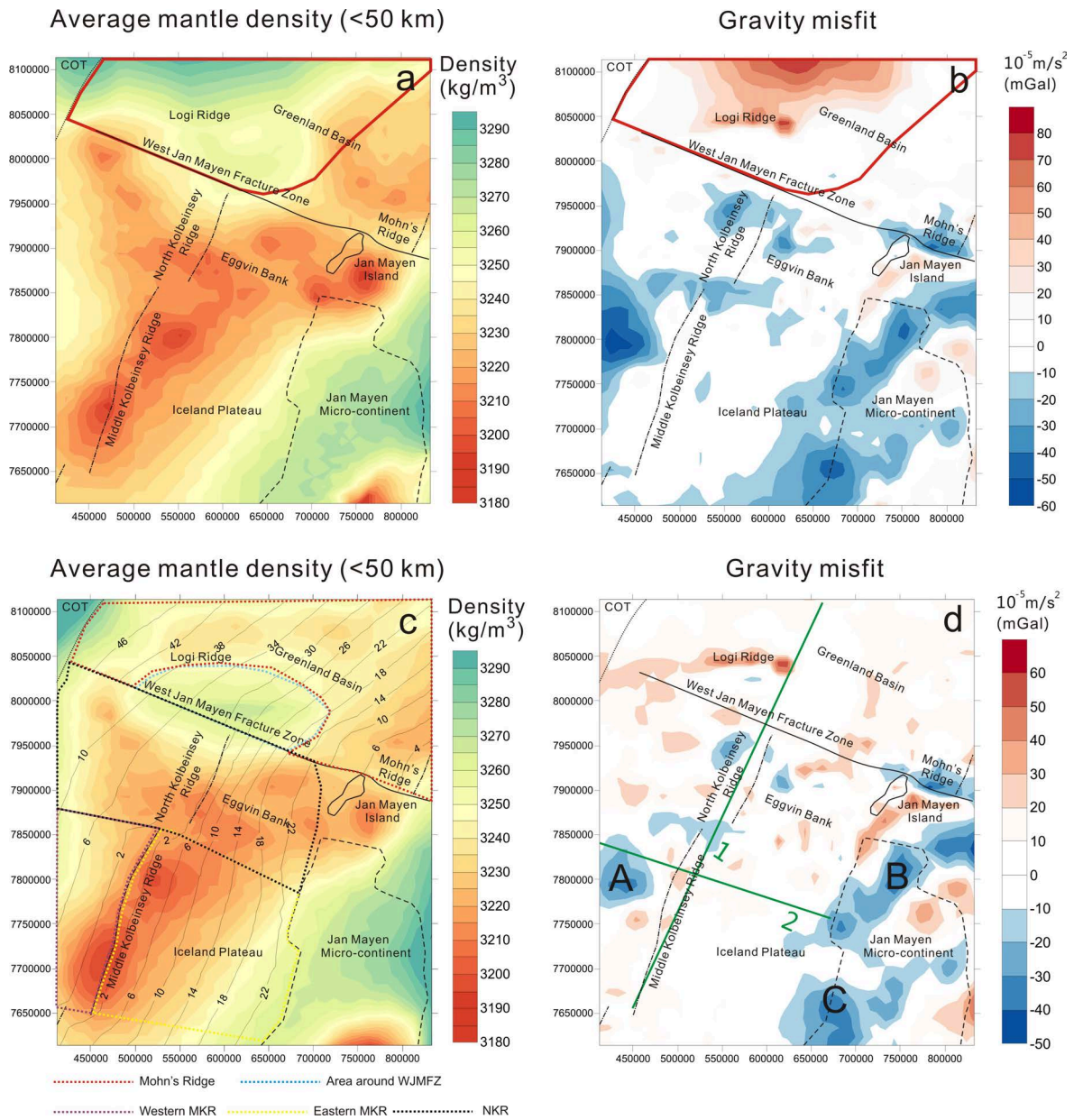
Figure 2.15.: **(a, b)** Results of first gravity inversion run. Average mantle density between the Moho and 50 km depth (a), and gravity misfit (modelled gravity minus observed gravity) (b). For this inversion run, the density configuration of the *seeds* layer has been set equal to the V_s derived densities at 50 km depth (Fig. B.2b). The red line delineates the area for which the estimated mantle temperature at 50 km depth is less than 900 °C (Fig. B.2a). **(c, d)** Results of second gravity inversion run. Average mantle density between Moho and 50 km depth (c), and gravity misfit (d). For the second inversion run, the maximum density of the "seed" layer has been set to 3210 kg m^{-3} which leads to a modification of the density model in the northern parts of the study area (red line in Fig. 2.15a). The solid gray lines with numbers show the oceanic seafloor ages (Müller et al., 2008). Five different domains (Mohn's Ridge, area around WJMFZ, western MKR, eastern MKR, and NKR) are shown by colour coded dotted lines. Two green lines show positions of the sections of Figs. 2.19-2.18. Points A-C represent the main anomaly misfits.

Table 2.6.: Sensitivity analysis of various parameters of the sedimentary and crustal model on the gravity response and induced variation of the uppermost mantle density

	Parameter	Imposed variations	Gravity response differences / mGal			Uppermost mantle density variations / kg m^{-3}		
			MKR	NKR	Mohn's	MKR	NKR	Mohn's
Z	Basement	Equal to bathymetry	2	2	10	<10	<10	<10
	Basement	+1.5 km	2	2	3	<10	<10	<10
	Top of lower oceanic crust	±1.5 km	∓20	∓20	∓20	<±10	<±10	<±10
	Top of lower oceanic crust*	±3 km		∓30			±20	
	Moho	±1.5 km	∓15	∓12	∓15	±10	±10	<±10
	Moho*	±3.0 km		∓20			±15	
ρ	Sediment	Assigned 2650 kg m^{-3}	1	2	10	<10	<10	<10
	Upper oceanic crust	+20 kg m^{-3}	20	20	15	10	10	<10
	Upper oceanic crust	-10 kg m^{-3}	-10	-10	-8	<10	<10	<10
	Lower oceanic crust	±10 kg m^{-3}	±25	±35	± 12	∓15	∓25	<∓10

Note. MKR = Middle Kolbeinsey Ridge; NKR = North Kolbeinsey Ridge. * These parameters have been tested for two different values, respectively, to reflect the larger depth uncertainty in the less-constrained western part of the NKR.

The obtained gravity response of the density model shows a good fit with measured gravity , having a Root Mean Square deviation of 15.34 mGal (Fig. 2.15d). In the oceanic crustal domains, the long-wavelength NE-SW gravity misfit (Fig. 2.14c) as well as the large positive gravity misfit in the north (Fig. 2.15b) have been removed, and the majority of the final gravity misfits range between ± 10 mGal (Fig. 2.15d). However, some short-wavelength negative misfits (up to -30 mGal) are found in the northwestern parts of the MKR (Fig. 2.15d, point A). In addition, the northern (Fig. 2.15d, point B) and southwestern margins of the JMMC (Fig. 2.15d, point C) have negative misfits up to -40 mGal.

2.2.3.6. Sensitivity analysis

For the sedimentary and crustal layers, the resolution of the model is controlled by the coverage of constraints of the model layers. Areas where the initial sedimentary and crustal model derived its structure from interpolation and extrapolation across large distances have the greatest uncertainties. Thus, the most uncertain areas are the western part of the NKR domain, while the MKR domain and Mohn's Ridge are better constrained. Compared to previous 3D gravity/seismic studies (Funck et al., 2016; Haase et al., 2016; Hermann, 2013), recently published seismic refraction and reflection results allowed for some improvements with regard to the distribution of sediment around the Logi Ridge (Breivik et al., 2012b) and the deep structure of the crystalline crust over the eastern part of the Eggvin Bank within the NKR domain (Tan et al., 2017).

We tested the sensitivity of the gravity response of the entire model with regard to both density and layer thickness variations. Our analyses focus on the differences between the three domains: MKR, NKR, and Mohn's Ridge (Fig. 2.15c). Table 2.6 gives an overview of the models tested and respective parameters changed. Concerning the depth of the oceanic basement (which is relatively well constrained due to the small amounts of sediments and

good seismic coverage), we have tested the effects of (i) setting it equal to the bathymetry and (ii) shifting it downwards by 1.5 km. With the value chosen, we are testing an extreme scenario given that the uncertainty of this parameter typically is much smaller. For the top of the lower crust and the depth of the Moho, the Moho depth uncertainty of the western part of the NKR domain (not covered by seismic data) is given as ± 3.0 km, while for the remaining parts it is ± 1.5 km (Haase et al., 2016). We have assumed the same uncertainty values for the top of the lower crust. Concerning the density of sediments, we have tested an unrealistic endmember scenario by assuming a largely compacted sediment sequence with a density of 2650 kg m^{-3}. For the sub-sedimentary crustal units, we have tested extreme density values as derived from literature values (Tab. 2.5).

For each of the models tested, we have calculated the gravity response and the difference with respect to our preferred model. These "gravity response differences" are represented by their average values in Table 2.6. Although we have tested extreme values for the different parameters, the overall range of response differences obtained is significantly smaller compared to the gravity misfit distribution calculated for a homogeneous mantle at depths < 50 km (Fig. 2.14c). In addition, changing the input parameters would result in the inverted upper-mantle densities to be changed by generally less than 10 kg m^{-3}. However, in the western NKR domain, the crust structure is less constrained and changes in lower crustal density and Moho depth might result in mantle density changes of up to 25 kg m^{-3}. Thus, there are some uncertainties for the density in the uppermost mantle beneath the western part of the NKR domain. This uncertainty will be further discussed in relation to interpretation of results in section B.1.

In the MKR domain, the modelled uppermost mantle density anomaly increasingly deviates to the east of the spreading axis northwards (Fig. 2.15c). Checkerboard tests (Fig. B.3) show that the anomalously low density is reasonably well resolved down to the dimensions we observe. These tests suggest that the density anomalies may be underestimated as the dimensions become smaller, but there is no lateral displacement involved in the inversion process. In addition, the initial maximum gravity misfit (Fig. 2.14c) runs slightly east from the spreading axis, indicating lower density there. A forward gravity modelling test shows that if we shift the low density zone in the model back underneath the spreading axis, it will result in ~ 30 mGal gravity misfit. Thus, we believe that the anomalously low density in the uppermost mantle is not an artefact of the gravity inversion process.

Figure. 2.14f shows that mantle density variations at depth of > 50 km mainly result in a long-wavelength gravity response, so that the change of the deeper mantle density would not remove the smaller scale anomalies in the upper 50 km. Also, the initial gravity misfit (Fig. 2.14c) does not spatially correlate with any of the subdomains (Fig. 2.13d). Therefore, treating the subdomains differently in terms of composition or temperature-density relation would not improve the overall fit.

2.2.4. Discussion

2.2.4.1. Model assessment

2.2.4.1.1. Density configuration of the sediments and crust Compared to the final density configuration of the shallowest mantle (Fig. 2.15c), the gravity misfits are of shorter wavelengths (Fig. 2.15d), which point to heterogeneities within the crust that are not resolved by the data constraints (Table. 2.5). A short-wavelength gravity misfit low (up to -40 mGal) is observed in the northwestern part of the MKR (point A; Fig. 2.15d). This is consistent with observed high-velocity lower crust (with densities of 3050-3100 kg/m^3) underlying this area (Hermann and Jokat, 2016; Weigel et al., 1995). However, since the spatial constraints of this high density layer are limited, it cannot be adequately traced, and is not incorporated into the model.

In addition, one negative short-wavelength gravity misfit (point B; Fig. 2.15d) could potentially be explained by mafic intrusions into the JMMC, also not in the model (e.g. Blischke et al., 2016; Kandilarov et al., 2012; Kodaira et al., 1998b; Peron-Pinvidic et al., 2012a,b). Another negative misfit is restricted to the southwestern boundary of the JMMC, where there are no seismic constraints (point C; Fig. 2.15d). Pre-breakup formation of the MKR is characterized by a long rifting period with significant conductive heat loss and accordingly not much magmatism generated (Kodaira et al., 1998a; Mjelde et al., 2008). The strong extension along the western boundary of the JMMC might have resulted in shallower Moho depths than used in the crustal model (Fig. 2.13d), which if implemented would improve the gravity fit there.

2.2.4.1.2. Gravity constrained mantle density between Moho and 50 km depth There are some published 2D gravity models in the area based on seismic crustal constraints, and a few also have additional velocity measurements of the uppermost mantle (Hermann and Jokat, 2016; Kandilarov et al., 2012; Kandilarov et al., 2015; Peron-Pinvidic et al., 2012a,b; Voss and Jokat, 2007; Weigel et al., 1995). However, none of these studies constrain the deeper velocity and hence the density of the mantle lithosphere, and thus cannot be directly compared to our modelling results. The 3D model by Haase et al. (2016) solved the density structure of the lithosphere by forward temperature models based on lithospheric age, and miss some of the plume-induced temperature variations that are clearly present.

In this study, the mantle density at depths <50 km is a result of gravity inversion, while mantle density at depths >50 km is derived from S-wave velocities. Despite the different types of constraints on density, there should be a positive correlation between the two. We have plotted average mantle density between 50 and 90 km (ρ_{50-90}) against the gravity-constrained density of the shallowest mantle for the entire oceanic domain (Fig. 2.16a). The MKR domain has significantly lower ρ_{50-90} compared to the Mohn's Ridge, indicating the Iceland plume influence there. Despite the independence of constraints (S-wave velocity, respectively gravity) and the artificial, methodologically imposed separation of the two mantle domains, there is a strong correlation between the two for the areas near the Mohn's Ridge (green points) (Fig. 2.16a), where the correlation coefficient (R) is 0.84. MKR and NKR domains have a
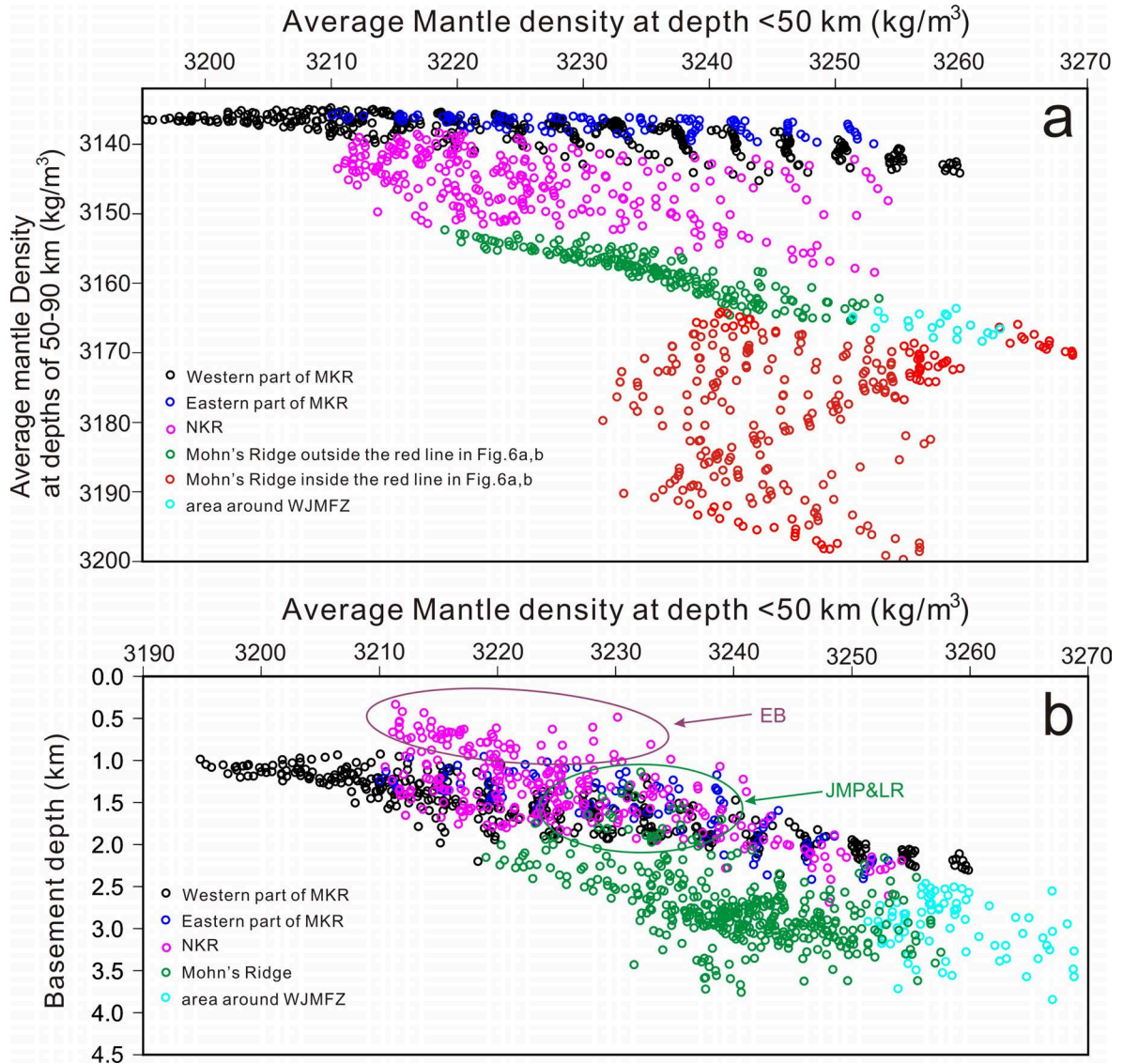
Figure 2.16.: **(a)** Comparison of mantle density derived for different depths levels (<50 km and 50-90 km (ρ_{50-90}), respectively) with colours showing different sub-domains of the study area. Under the Mohn's Ridge, red dots represent ρ_{50-90} within the area of less than $900°C$ at 50 km depth (red line in Fig. 2.15a, b), while green dots indicate the ρ_{50-90} outside this sub-domain. **(b)** Comparison of gravity-constrained mantle density (<50 km) and basement depth (corrected for sediments loading). Arrows indicate local geological features departing from the expected trends: Eggvin Bank (EB), Jan Mayen Plateau (JMP) and Logi Ridge(LR) (Fig. 2.12).

weaker correlation with a correlation coefficient of 0.69 and 0.54 respectively. However, for the northwestern Mohn's Ridge subregion (red points) where derived mantle temperatures at 50 km depth are $<900°$C and the accuracy of the V_s-to-T conversion is reduced (Priestley and McKenzie, 2006, 2013), there is a poor correlation (R=0.20). Accordingly, the gravity-inverted densities are associated with larger uncertainties in this region.

In terms of density and temperature, the NKR takes an intermediate position between the MKR and the Mohn's Ridge, but the linear correlation between the shallow and deep mantle densities is much less pronounced. Therefore, factors other than temperature might control

density variations in the NKR. A recent seismic study shows that the anomalously shallow NKR domain relates to thick crust (Tan et al., 2017). Apart from this study, the crustal model in the western part of the NKR domain is not well constrained, as it is derived from previous gravity inversion (Haase et al., 2016). Therefore, both the less-constrained crustal model and a heterogeneous mantle source under the NKR domain (e.g. Haase et al., 2003) could contribute to a weaker correlation (R=0.54) between ρ_{50-90} and average mantle density at depths <50 km.

Basement depth and topography/bathymetry are isostatically controlled by variations in the crustal thickness, upper mantle densities and sediment load (Stein and Stein, 1992). To calculate basement depth corrected for sediment loading (B_s), a standard Airy isostatic correction (Le Douaran and Parsons, 1982) was applied:

$$B_s = B + (\frac{\rho_w - \overline{\rho_s}}{\rho_a - \rho_w})Z_s \tag{2.2}$$

where B is the depth to the top basement (Fig. 2.13a), ρ_a is the density of asthenospheric mantle (3200 kg/m^3), ρ_w is the density of water (1030 kg/m^3), and Z_s is the thickness of the sediment units (Fig. 2.13b). The average density of the sedimentary column ($\overline{\rho_s}$) is calculated based on our crustal density model (Table 2.5).

Except for some oceanic islands and plateaus (e.g. Eggvin Bank, Logi Ridge), crustal thickness is relatively uniform within each of the three different domains (MKR: 8-9.5 km, NKR: 10-11 km, Mohn's Ridge: 3-5 km) (Fig. 2.13). Thus, we can discuss basement depths as being mostly controlled by mantle density variations within each domain. We have plotted corrected basement depth against gravity-constrained average mantle density at depths <50 km (Fig. 2.16b). Not surprisingly, the oceanic domain overall shows a positive correlation indicating that the study area is locally in isostatic equilibrium. Some deviations from the main trends (marked in the Fig. 2.16b) indicate local geological features with shallower bathymetry and thicker crust.

Basement depth of the oceanic plate corrected for sediment loading has a linear relation with the square root of the sea-floor age ($Myr^{1/2}$) if subsidence is controlled by passive thermal cooling only (e.g. Adam and Vidal, 2010; Stein and Stein, 1992). Linear regression shows a trend at the Mohn's Ridge of 300 m/$Myr^{1/2}$ (Fig. 2.17a), which is comparable to normal seafloor subsidence rate at 320 m/$Myr^{1/2}$ (Korenaga, 2008). However, the eastern MKR younger than 10 Ma shows a subsidence rate of about 230 m/$Myr^{1/2}$, while the subsidence rate for oceanic ages older than 10 Ma increases to around 390 m/$Myr^{1/2}$. The youngest western MKR has a subsidence rate of about 200 m/$Myr^{1/2}$, but increases to 490 m/$Myr^{1/2}$ for oceanic ages older than 4 Ma (Fig. 2.17a). Thus, the observed trends show a substantial deviation in mantle thermal structure compared to the theoretical half-space cooling model. The poor correlation between the basement depth and oceanic ages observed under the NKR domain is on the other hand, most likely related to large crustal thickness variations as mapped in the eastern NKR by Tan et al. (2017).

Similarly, the average mantle density < 50 km depth derived from the half-space cooling
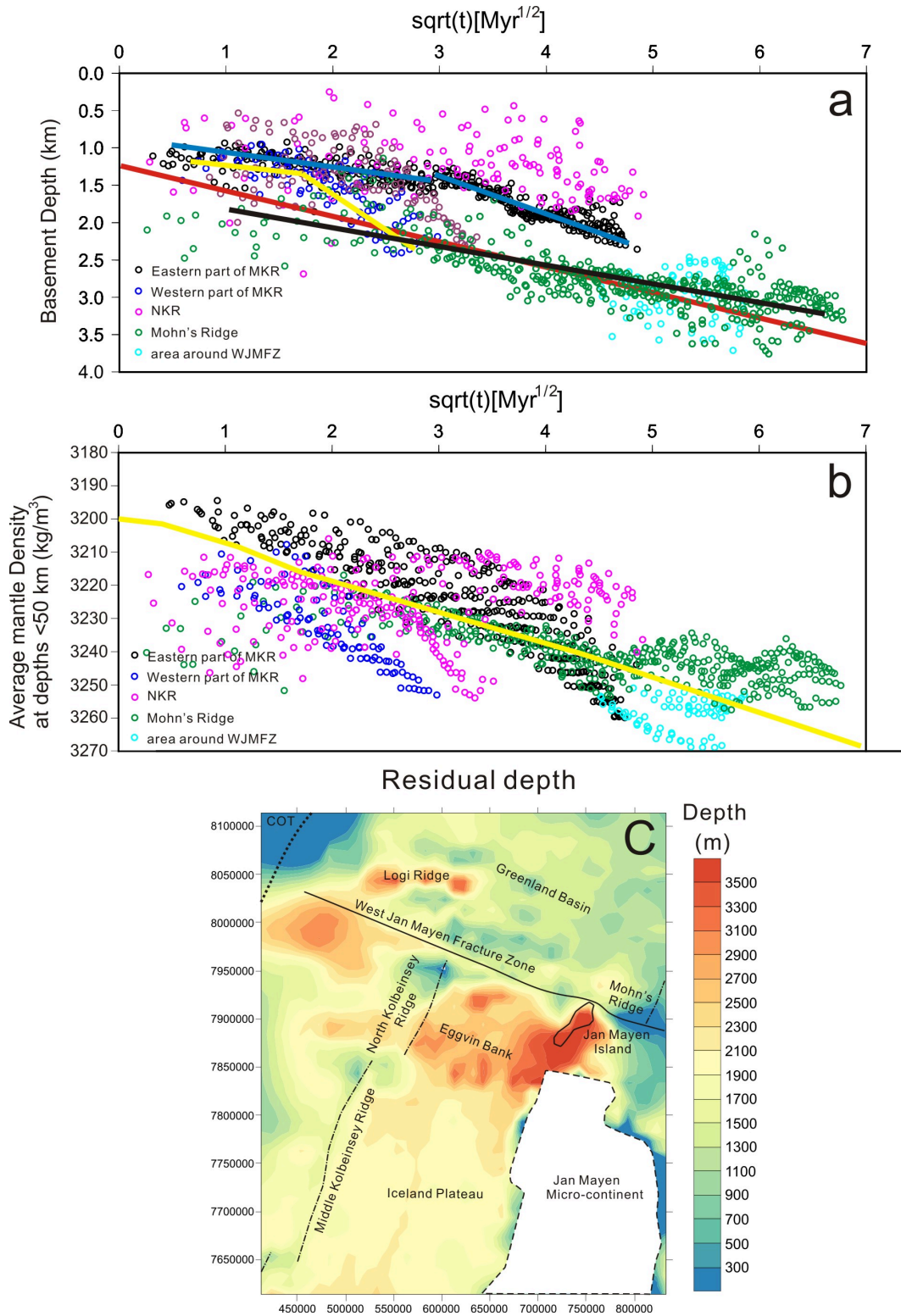
Figure 2.17.: (a) Observed basement depth (corrected for sediment load) against the square root of sea-floor age (Müller et al., 2008)) for different sub-domains of the study area. Red solid line: a normal seafloor subsidence rate of $320\,\mathrm{m/Myr^{1/2}}$ (Korenaga, 2008), blue line: eastern MKR, yellow line: western MKR, black line: Mohn's Ridge. **(b)** Mantle density at depths $< 50\,\mathrm{km}$ against the square root of sea-floor age for different sub-domains of the study area. The yellow line illustrates the age-dependent average mantle density ($< 50\,\mathrm{km}$) based on Sandwell (2001). **(c)** Residual basement depth is corrected for sediment loading and subsidence with seafloor age using a seafloor subsidence rate at $320\,\mathrm{m/Myr^{1/2}}$ and a spreading axis depth at $2600\,\mathrm{m}$ (Stein and Stein, 1992).
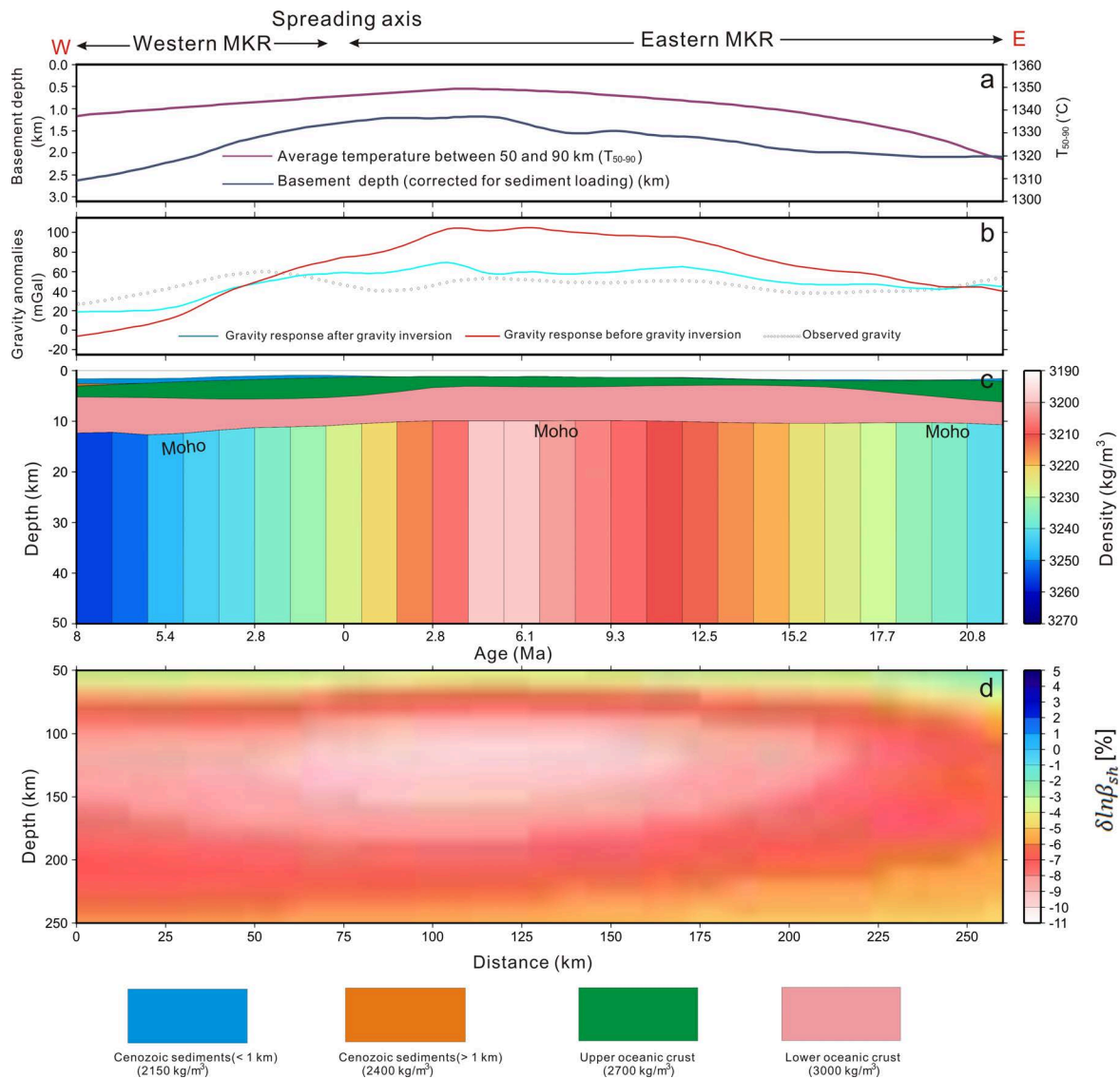
Figure 2.18.: Results of the 3D gravity modelling along a W-E directed section through the study area (green line 2 in Fig. 2.15d). **(a)** Basement depth and average mantle temperature (T_{50-90}) between 50 and 90 km depth (Fig. B.2c). **(b)** The corresponding observed and calculated gravity before and after gravity inversion. **(c)** Vertical section through the 3D model with vertical average mantle density configuration between the Moho and 50 km depth (Fig. B.2d). **(d)** S-wave relative velocity perturbations ($\delta ln\beta_{sh}$ (%)) in the deeper mantle from Rickers et al. (2013). MKR: Middle Kolbeinsey Ridge.

model shows a positive trend with the square root of the sea-floor age (Myr$^{1/2}$) (Fig. 2.17b) (Sandwell, 2001). However, under the MKR domain the density distribution of the upper mantle (< 50 km) differs somewhat from that, and is asymmetric with lower density east of the spreading axis (Figs. 2.17b, 2.18). Consistent with the thermal subsidence deviation, the mantle density at eastern MKR domain for seafloor ages less than 10 Ma is slightly lower than expected from the half-space cooling model (yellow line in Fig. 2.17b). The yellow line shows the age-dependent average mantle density (<50 km) based on lithospheric thermal structure from Sandwell (2001) and conversion of these temperatures to density following the method in section B.1.2. A sharp increase in mantle density is observed for seafloor ages older than 10 Ma (Fig. 2.17b). On the other hand, the density distribution of the Mohn's Ridge at age between 6 and 25 Ma follows the half-space cooling model, but shows slightly less density older than 25 Ma and higher for younger than 6 Ma. This is consistent with little impact from the Iceland plume near the spreading zone. The mantle density under the NKR domain has large variations and there is no correlation between the density and oceanic age (Fig. 2.17b). The lack of correlation is most likely related to a complex development where off-axis magmatic intrusions affect seafloor depth and crustal thickness (Tan et al., 2017). Uncertainty in the crustal thickness in the western NKR also make upper mantle densities less well constrained, and could contribute to this.

In order to address this uncertainty, we show a map of basement depth corrected for sediment loading and age-controlled subsidence (assuming subsidence rate at 320 m/Myr$^{1/2}$ and depth of the spreading axis at 2600 m (Stein and Stein, 1992)) (Fig. 2.17c). The result shows that the residual basement of Mohn's Ridge has almost no variations, while in the northern parts of the MKR, the residual basement of the eastern part of the spreading ridge is about 300 m shallower than the remaining MKR domain, consistent with Figure 2.17b. Similarly, the eastern NKR is 600 m shallower than western part. The regions of shallow depths (< 2000 m) do largely correlate with regions of low calculated average mantle density < 3250 kg m^{-3} at depths less than 50 km (Fig. 2.15c).

An anomalously deeper residual basement of the western NKR allows for a colder mantle or a thinner crust. Isostatic analysis shows that 600 m deeper basement can be balanced by an increase of uppermost mantle density by 25 kg m^{-3}. This is consisted with our gravity-derived uppermost mantle density, where the difference between the average uppermost mantle density between the eastern (3220 kg m^{-3}) and western NKR (3240 kg m^{-3}) is 20 kg m^{-3}. Alternatively, the deeper residual basement could be caused by crustal thickness variations, where a 600 m deeper basement of the western NKR can be balanced by a decrease of Moho depth of about 1 km. However, a decrease of Moho depth of 1 km gives a decrease of uppermost mantle density < 10 kg m^{-3} (Tab. 2.6). In this case, the eastern NKR still needs less dense mantle compared to western part. A sensitivity test shows that if the Moho depth of western NKR domain is decreased by 3 km, then this would make the uppermost mantle density more symmetrical over the NKR. However, with a symmetrical low-density distribution, the present magmatism along the NKR would show melting under elevated mantle temperature, but this is inconsistent with geochemical studies (e.g. Elkins et al., 2016; Haase et al., 2003). Also, the eastern displacement

of the negative uppermost mantle density anomaly under the NKR is continuous with that of the better constrained MKR domain to the south, as well as to that of the southern Mohn's Ridge to the north, suggesting that our preferred model is reasonable. Nevertheless, additional seismic surveys around the NKR would be needed to better constrain the development of this area, and to determine to what extent the influence of the Iceland plume has varied over time at the northern tip of the Kolbeinsey Ridge.

2.2.4.1.3. Density configuration of the deeper mantle (>50 km) The mantle temperature estimated from V_s has uncertainties, since the empirical relationship was derived from observations in the Pacific Ocean (Priestley and McKenzie, 2006). However, this relationship is comparable to that of a recent study of Schoonman et al. (2017), who postulate an empirical relationship between observed surface residual elevation, temperature and shear wave velocity for the mantle of northern Britain and western Norway. In addition, the V_s-derived temperature configuration (T_{50-90}; Fig. B.2c) is indirectly validated by the observed crustal thickness (Fig. 2.13d). Accordingly, the crustal thickness difference between the present-day spreading axis of the MKR and Mohn's Ridge (4–4.5 km) (Fig. 2.13d) indicates that the mantle potential temperature under the MKR is elevated by about 75 °C (Ito and Lin, 1995). This is consistent with the difference in the T_{50-90} around the present-day spreading axis of MKR (1350 °C) and Mohn's Ridge (1270 °C) which is 80 °C (Fig. B.2c).

Our Vs-temperature-density calculations are based on the assumption that the mantle composition is homogeneous. There appears to be a homogeneous, depleted mantle source under the MKR (e.g. Elkins et al., 2011) and Mohn's Ridge (e.g. Klingelhöfer et al., 2000b) but a heterogeneous enriched mantle under the NKR (e.g. Haase et al., 2003). A variation of the mantle composition below the melt zone could affect V_s, producing discrepancies in derived mantle temperature, and accordingly mantle density estimates (Goes and van der Lee, 2002). Several studies (Priestley and McKenzie, 2006, 2013; Schutt and Lesher, 2006), however, suggest that the mantle composition variations are difficult to resolve from seismic tomography. Moreover, the velocity anomalies caused by compositional changes are unlikely to exceed 1% (Priestley and McKenzie, 2006; Schutt and Lesher, 2006). A change in V_s of 0.04 km/s would result in a 40 °C and 6 kg m^{-3} difference at a temperature of 1300 °C (Fig. B.1). Sensitivity tests performed for the 3D density model presented here shows that a decrease of the mantle density at depth between 50 and 90 km by 1% under the MKR domain results in a gravity response with average 14 mGal difference. This indicates that the derived density heterogeneities at greater mantle depths (> 50 km) exert minor control on the gravity field compared to shallower mantle and crustal structure.

The upper oceanic mantle density is also affected by melt extraction from the mantle beneath spreading ridges, causing chemical depletion of the residual solid (e.g. Jha et al., 1994; Oxburgh, 1977; Schutt and Lesher, 2006; Scott and Stevenson, 1989). However, the part of the mantle that has undergone the highest melt degree by ascent through the whole melt zone is located in the shallowest part, and will mostly fall within the region where we invert for density, and the effect should therefore be incorporated in the modelling results.

Another uncertainty is the potential presence of a melt fraction within the mantle. Priestley and McKenzie (2006) argue that the fraction is generally small ($< 0.1\%$) and has little effect on the V_s to temperature conversion. While some authors argue that the low seismic velocities observed in the upper asthenosphere can be adequately explained without much melt (e.g. Stixrude and Lithgow-Bertelloni, 2005), other observations indicate that some unmobilized melt up to a few percent could be present locally (Naif et al., 2013; Rychert and Shearer, 2009). The V_s model has low resolution, was sampled at a 100 km grid, and will not delineate the spreading ridges well. However, we note that the V_s distribution is reasonably well centered on the spreading ridges (Fig. B.2a,c), which may be a combined effect of melt and elevated temperature. However, it is not obvious that a small melt fraction should affect the V_s significantly. The formation of melt would extract water from the mantle, which will increase the velocity of the solid. With fractional melting, the net effect could be a slight velocity increase in total (e.g. Karato and Jung, 1998). That the modelled low-density anomaly shows an increasing discrepancy from the spreading ridge position to the north, and correlates well with anomalously low seafloor subsidence (Fig. 2.17), suggests that it is not an artefact of the V_s to temperature conversion assumptions. The V_s-derived mantle density gives a long-wavelength density distribution (Fig. 2.14f) that cannot be predicted from the age of the oceanic lithosphere alone, and should improve the inversion results considerably. Absolute densities may be affected near the spreading ridges if retained melt changes the V_s-temperature relationship, but the trend of the uppermost mantle low density anomaly that we find should be robust.

2.2.4.2. Plume-lithosphere interaction

The WJMFZ represents a main mantle temperature contrast (Fig. B.2c). North of the WJMFZ, the Greenland Basin is characterized by thinner crust, larger basement depth, higher mantle density, and lower mantle temperature compared to the NKR domain (Fig. 2.19). This is illustrated by calculating lithospheric thickness from the age-grid of Müller et al. (2008) using the approach of Zhang and Lay (1999) (Fig. 2.20). There is a significant thickness increase from the NKR to the Greenland Basin to the north. Approximately midway between the northern tip of the Kolbeisney Ridge and Jan Mayen, the lithospheric thickness is predicted to be similar on both sides of the WJMFZ. Farther to the east, the lithoshere should be thinnest north of the WJMFZ, close to the Mohn's Ridge. Such steps in the lithosphere-asthenosphere boundary have been postulated to control the emplacement of plume material (*plume ponding*, (Sleep, 1997)), and could potentially accumulate plume material from a northwards flow out from the Iceland plume under the Eggvin Bank, if the flow was strongly directed by the spreading ridge.

E.g. Elkins et al. (2016) and Schilling (1999) argue that excess magmatism in the NKR domain is caused by a putative Jan Mayen plume. However, Mertz et al. (2004) argue that the plume does not follow a simple time-transgressive track and cannot explain the radiogenic Nd-Pb isotope compositions of basalts from the NKR. The Eggvin Bank excess magmatism appears not to be governed by elevated temperature (Haase et al., 2003), but by an enriched
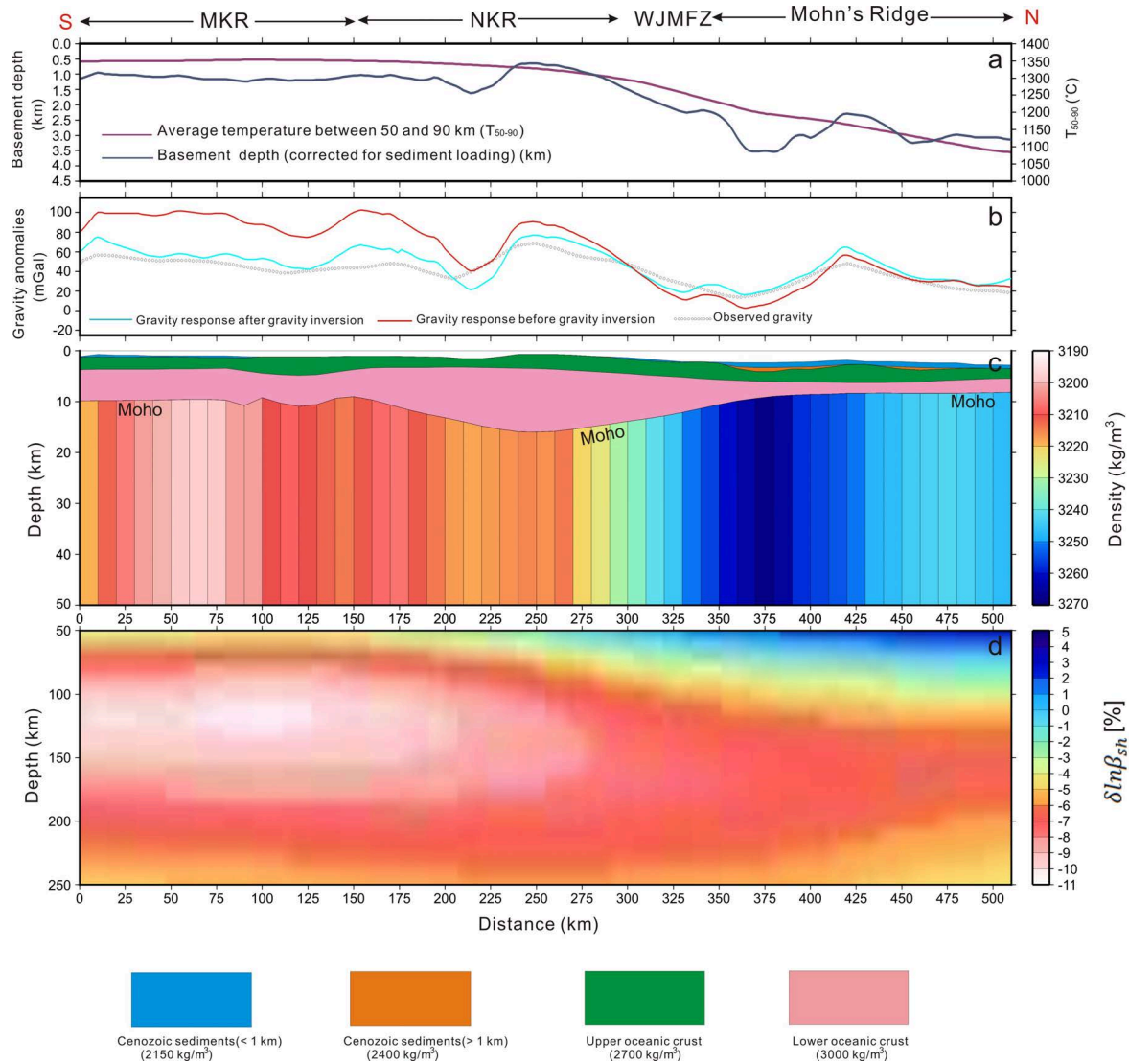
Figure 2.19.: Results of the 3D gravity modelling along a N-S directed section through the study area (green line 1 in Fig. 2.15d). **(a)** Basement depth and average mantle temperature (T_{50-90}) between 50 and 90 km depth (Fig. B.2c). **(b)** The corresponding observed and calculated gravity before and after gravity inversion. **(c)** Vertical section through the 3D model with vertical average mantle density configuration between the Moho and 50 km depth (Fig. B.2d). **(d)** S-wave relative velocity perturbations ($\delta ln\beta_{sh}$ (%)) in the deeper mantle from Rickers et al. (2013). MKR: Middle Kolbeinsey Ridge, NKR: North Kolbeinsey Ridge, WJMFZ: Western Jan Mayen Fracture Zone.
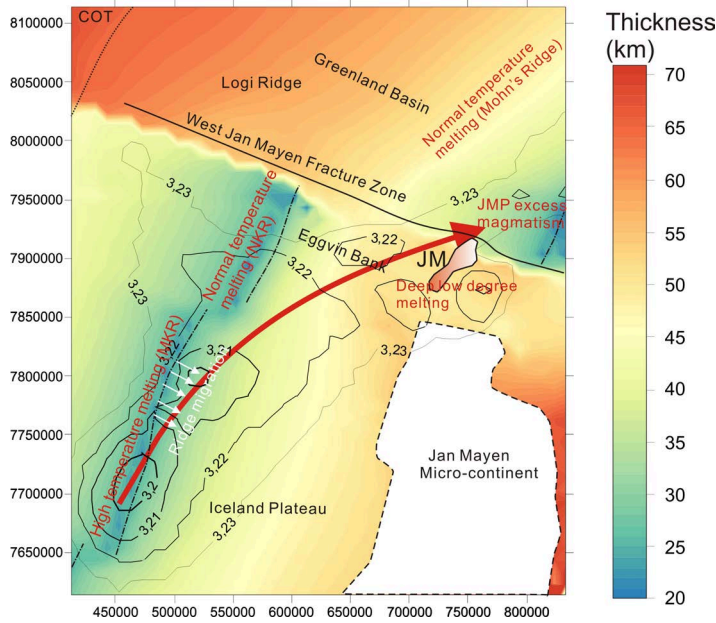
Figure 2.20.: Estimated oceanic lithosphere thickness for the study area based on the crustal age model of Müller et al. (2008) using the approach of Zhang and Lay (1999). The solid black lines with numbers show contours of the uppermost mantle densities less than $3.23\,\mathrm{g/cm^3}$, where thicker lines correspond to lower densities (Fig. 2.15c). JM: Jan Mayen, JMP: Jan Mayen Plateau.

mantle component, probably over some time (Tan et al., 2017), and at least does not require a thermal mantle plume. Jones et al. (2002) document V-shaped ridges along the Kolbeinsey Ridge up to the end of the middle Kolbeinsey Ridge segment, taken to indicate transport of mantle zones with variable temperature from the Iceland plume. It shows an apparent propagation speed that is still quite high in the northernmost part (100–150 mm/Ma) and a counter flow from a potential Jan Mayen plume is therefore not expected there.

South of the WJMFZ, a tomography model shows a strong low-velocity anomaly located in the upper mantle (90–150 km) beneath the MKR domain (Fig. 2.19, 2.18). Velocity perturbations here reach between -9% and -11%, indicating high-temperature and reduced asthenospheric density there. The shallower mantle depth between 50 and 90 km resembles this, where our density model shows a high temperature ($T_{50-90} > 1340\,°\mathrm{C}$; Fig. B.2c) and a low-density ($\rho_{50-90} < 3140\,\mathrm{kg\,m^{-3}}$; Fig. B.2d) anomaly at a broad region. However, the shallow mantle density anomaly at depths of < 50 km is much narrower (Fig. 2.15c). In the south, the uppermost mantle density anomaly lies underneath the spreading ridge, and should reflect the cooling of the lithosphere as it moves away from the ridge. Judging from the 9–11 km oceanic crustal thickness south of our study area, it is also affected by hot plume material in the axial zone (Hooft et al., 2006). However, the centre of the low-density anomaly increasingly deviates to the east of the spreading ridge northwards. We interpret this deviation to be the effect of lithospheric heating from plume flow in the upper asthenosphere below (not resolved by the tomography model). In this sense, it represents thermal erosion of the lithosphere that will make the temperature structure and thickness deviate from what is expected from a passive cooling model based on age, as shown in Fig. 2.17. The obtained density model for the mantle shallower than 50 km will mostly encompass the lithosphere, and show this thermal influence. The lowest mantle densities from the model are contoured on top of the age-based lithospheric thickness grid in Fig. 2.20. The zone of lowest density passes under Jan Mayen

towards the southern tip of the Mohn's Ridge. Thus, judging from the distribution of the lowest upper-mantle density, the asthenospheric flow below appears to avoid the lithospheric thickness increase north of the Kolbeinsey Ridge, and is instead redirected farther east towards the region where there is no obstacle in lithospheric thickness, as indicated by the red arrow in Fig. 2.20. The eastward deviation of the uppermost asthenospheric flow may have existed for some time, as it correlates with other geological observations. In the south, the MKR axis underwent eastward ridge migration since approximately 5.5 Ma (Appelgate, 1997), following this deviation. Thus, the thermal erosion of the lithosphere on the east side of the MKR could be the driving force behind the eastwards axial relocations (Fig. 2.20). This redirection of the plume flow could also help to explain why the present spreading at the NKR does not appear to be influenced by elevated mantle temperature. Rather, it is known to be sourced from an enriched mantle component different from the MKR (e.g. Elkins et al., 2016, 2011; Haase et al., 2003). Thus, neither geochemical data, nor our results can confirm a model where ponding of northwards plume flow occurs against a lithospheric thickness increase at the northern end of the Kolbeinsey Ridge. While the upper asthenospheric plume flow appears to be influenced by spreading ridge location to some degree, it responds on a slightly larger, more regional scale, where it is determined by the change of lithospheric thickness north of the WJMFZ. Finally, we note that the flow passes underneath the presently volcanically active Jan Mayen island, probably supplying the extra heat for a small degree of deep mantle melting to occur (Trønnes et al., 1999) (Fig. 2.20). Also the oceanic crust around the southern tip of the Mohn's Ridge across the WJMFZ is thicker than normal, adjacent to the island on the same trend (Kandilarov et al., 2012) (Figs. 2.12,2.20).

2.2.5. Summary and conclusions

A three-dimensional structural and density model of the crust and upper mantle is developed for the greater Jan Mayen-East Greenland region, in order to determine the influence of the Iceland mantle plume on the area. We obtain the 3D density structure of the sedimentary cover and the crust down to the Moho mainly from regional reflection and refraction seismic lines. The deeper mantle temperature and density structure (>50 km) is derived from an S-wave mantle tomography model (Rickers et al., 2013), while the shallower mantle density (<50 km) is determined by 3D gravity inversion. The V_s derived mantle temperature and density show large variations at depths between 50 and 90 km. Based on present day spreading axis segmentation, we divided the study area into Middle Kolbeinsey Ridge (MKR), North Kolbeinsey Ridge (NKR), and Mohn's Ridge regions (Fig. 2.13d). In general, the model shows trends of decreasing average mantle temperature (T_{50-90}) and increasing density (ρ_{50-90}) between 50 and 90 km from MKR to NKR and to the Mohn's Ridge in the direction away from the plume.

Compared to the MKR domain, the greater basement depth, denser shallowest mantle, and cooler mantle temperature (T_{50-90}) under the Mohn's Ridge, show much reduced plume influence here. The NKR, including the shallow Eggvin Bank, is bounded by two ridge offsets,

where the WJMFZ has a long offset of 200 km, and represent a major lithospheric thickness contrast. Beneath the Kolbeinsey region, the uppermost mantle density shows a NE-SW elongated density anomaly. In the south, it coincides well with the spreading ridge, but rotates clockwise away from the northern MKR and the NKR, towards the Mohn's Ridge when approaching the WJMFZ. This anomaly is interpreted to be the result of the Iceland plume flow to a large degree interacting with the base lithosphere topography on a regional scale. To some extent, the flow follows the spreading axis, but the large offset of the WJMFZ appears to form an obstacle since the lithospheric thickness increases to the north of the tip of the Kolbeinsey Ridge. Instead, the flow is deviated eastwards toward the Mohn's Ridge, where the lithospheric thickness is similar or less to the north of the WJMFZ. This results in a marked east-west asymmetry across the northern MKR, where the western domain has higher mantle densities (< 50 km) and a deeper top basement, which indicates lower lithospheric mantle temperature there. Under the eastern MKR domain, the low mantle density anomaly lies east of the present day ridge axis. This results in a significant departure from the half-space cooling model, and the plume-flow induced thermal erosion on the east side of the ridge may be the cause for several eastwards ridge relocations in the past 5.5 Ma (Appelgate, 1997). Also, the plume flow appears to deviate eastwards of the NKR, consistent with the present lack of elevated mantle temperature in the melt zone underneath the ridge (e.g. Haase et al., 2003). Furthermore, it passes under the volcanically active Jan Mayen island, across the WJMFZ and towards the thick oceanic crust surrounding the southern tip of the Mohn's Ridge, and it is the likely cause for both.

3. The validity of the steady-state assumption in retroarc foreland basins

3.1. How do first-order controlling factors of subduction zones affect the thermal field of retroarc foreland basins?

3.1.1. Introduction

Retroarc foreland basins form as a consequence of non-collisional subduction (DeCelles and Giles, 1996). They are basins significant for hydrocarbon generation and migration, and they constitute relevant sedimentary archives that yield information on the complex interplay between the tectonic evolution of the adjacent mountain belts and ensuing changes in atmospheric circulation, rainfall, and erosion patterns (e.g. DeCelles, 2012; Hain et al., 2011). As such they are premier targets for integrated studies to decipher the role of different forcing factors concerning mountain building, basin subsidence, erosion and the thermal evolution of the paired orogen-foreland system.

Studies involving thermal assessments of basins, e.g. the characterisation of rheological conditions, rely on the accurate simulation of subsurface temperatures utilising models of the geological structure of the specific area that is considered (e.g. Noack et al., 2010; Sippel et al., 2017). A common assumption in many of the thermal models in these studies is that the present-day temperature distribution is close to steady-state conditions. This assumption has been proven useful in many occasions and particularly enables to identify the principal controlling factors of the thermal field of sedimentary basins (e.g. Scheck-Wenderoth et al., 2014).

At non-collisional continental margins, the subduction of a cold oceanic slab alters the thermal field of the entire lithosphere on time scales of several ten to hundred millions of years (Molnar and England, 1990). Shear heating along the subduction interface, faulting and ductile deformation further modify the thermal field in the continental plate (e.g. Babeyko et al., 2002; Peacock, 1996; Turcotte and Schubert, 1973). The presence of these transient processes suggests that the thermal field in a retroarc foreland basin may not be in a steady-state. For the thermal assessment of these basins, it is therefore essential to understand if, and at which time during its evolution, it can be considered to be in a thermal steady-state. The validity, and its extend, of steady-state conditions in such geological settings has not been addressed so far in the literature. As a first step to address this problem, it is important to understand the impact of first-order controlling factors of subduction on the thermal field of

retroarc foreland basins.

Several previous studies have analysed the influence of various geodynamic factors in subduction settings on the thermal fields of the overlying plate, the mantle wedge and the subducting slab itself (e.g. Abers et al., 2006; Hall, 2012; Kneller et al., 2007; Molnar and England, 1990; Syracuse et al., 2010). These studies have shown that the following factors exert a control on the thermal field of the subduction system: the age and dip of the oceanic slab, the plate-convergence rate, the shear-stress magnitude, the thickness of oceanic and continental lithosphere, geodynamic processes in the mantle wedge, as well as the physical properties of the rocks. Most of the studies, however, are based on the assumption of steady-state or near steady-state conditions and did not analyse how the aforementioned factors affect the temporal evolution of the thermal field in the foreland.

In conductive thermal models, steady-state is easily defined by setting time-dependent factors of the heat equation to zero. As to when a transient computation reaches a steady-state, however, is not trivial. Peacock (1996) assumed that the thermal field of a subducting plate reaches a steady state when the relative temperature changes at the slab interface are less than $1\% \, \mathrm{Myrs^{-1}}$, which corresponds to approximately $10°\mathrm{C} \, \mathrm{Myrs^{-1}}$. For temperatures around $500°\mathrm{C}$ at the Moho, this rate would correspond to $5°\mathrm{C} \, \mathrm{Myrs^{-1}}$. Such a rate, although decreasing over time, might accrue temperature changes over several Myr that are significant for some geodynamic properties, such as estimates of the lithospheric strength. In this study we strive to shed light on the differences between alternative formulations of this steady-state criterion.

Our principal aim is to assess the impact of first-order controlling factors of subduction in space and time on the thermal state of the continental plate. Therefore, we performed a sensitivity analysis on a set of controlling factors (slab age, convergence rate, slab dip, shear-stress, continental plate thickness) within geologically and geophysically probable bounds. These bounds define a parameter space that we can efficiently scan by reducing the problem to predominantly thermal conductive processes and by approximating shear heating as an internal boundary condition. Using numerical modelling, we computed the transient thermal field until near steady-state of a large number of models that sufficiently cover the input parameter space in terms of geologically probable combinations. The simulated thermal fields were subsequently analysed in order to quantify the time to reach steady-state conditions in the continental crust, and to assess how much of the continental crust is potentially influenced by the subduction-zone processes.

In this study, we review our results in the context of the South American convergent plate margin. The Andean foreland basin, running more than $7000 \, \mathrm{km}$ along the eastern flank of the Andes of South America (DeCelles, 2012) is the modern archetype of a retroarc foreland basin. A convergent plate regime has been prevailing along the South American plate margin since the Cambrian (Charrier et al., 2015; Ramos et al., 1986). Since the Late Cretaceous, non-collisional subduction progressively led to the rise of the Andes and the evolution of the associated foreland basins (Charrier et al., 2015; Mpodozis and Ramos, 1990). The continuity of the subduction, the well known slab geometry, and the extensive foreland basin system along the Andes allows the transfer of the results of this studies.
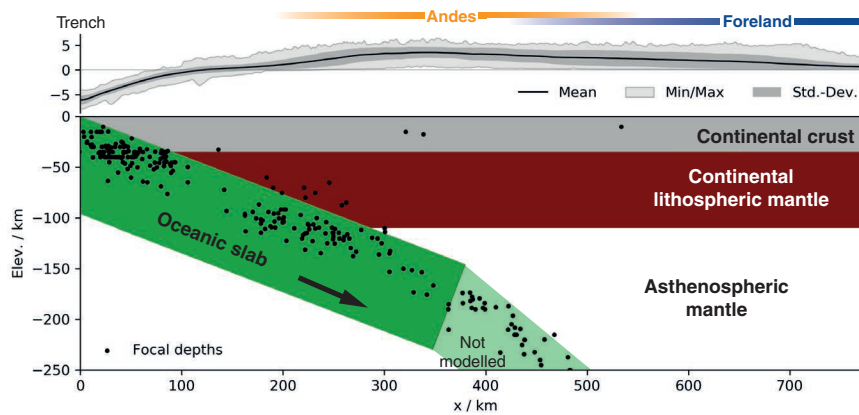
Figure 3.1.: Simplified geometry of a non-collisional subduction zone that depicts the Andean setting between 20 to 24°S. Black dots represent projected earthquake focal depths in the foreland of the southern Central Andes between 20 to 24°S latitude (Storchak et al., 2013) for comparison with data observations. Topography represents a vertically exaggerated swath profile along subduction direction between 5 to 40°S using ETOPO1 (Amante and Eakins, 2009).

3.1.2. Approach

The model geometry that we consider in this study encompasses the two fundamental bodies of a subduction zone: the oceanic and the continental plate (Fig. 3.1). The latter is represented by continental crust and lithospheric mantle. As the asthenospheric mantle is characterised by convective heat transport and a low geothermal gradient we consider the lithosphere asthenosphere boundary (LAB) as a lower boundary condition with depth-dependent temperature. Each of the modelled bodies is assumed to be homogeneous in its properties that are relevant for heat transport, i.e. density, radiogenic heat production, bulk heat capacity and bulk thermal conductivity.

The input properties slab age, slab dip and continental plate thickness sufficiently define the model geometry. Plate-convergence rate and shear-stress add the transient component to the models. By sampling a normal-distributed parameter space with 3000 models we homogeneously cover the input space and ensure that each model is unique in its configuration.

We started the computation of the transient models from initial conditions representing an undisturbed thermal steady-state with a constant depth LAB (Fig. 3.2a). The first time step was set to 0.1 Myr, while successive steps were adapted to ensure efficient computation. By running each model until 350 Myr we allow that the propagation of the temperature perturbation in the continental crust can attain its maximum value (see supplements, Fig. A.4).

To assess different formulations of steady-state conditions, we analysed the relative temperature change over time in the continental crust using $1\,\%\,\mathrm{Myr}^{-1}$ used by Peacock (1996), and a more strict criterion of $0.1\,\%\,\mathrm{Myr}^{-1}$ (for definition see Section 3.1.3). Furthermore, to understand the potential impact into the foreland, we analyse the horizontal propagation distance x of temperature perturbations that are induced in the continental crust by the subduction process.

We simulated the transient conductive thermal field on 2D triangle meshes using the LYNX
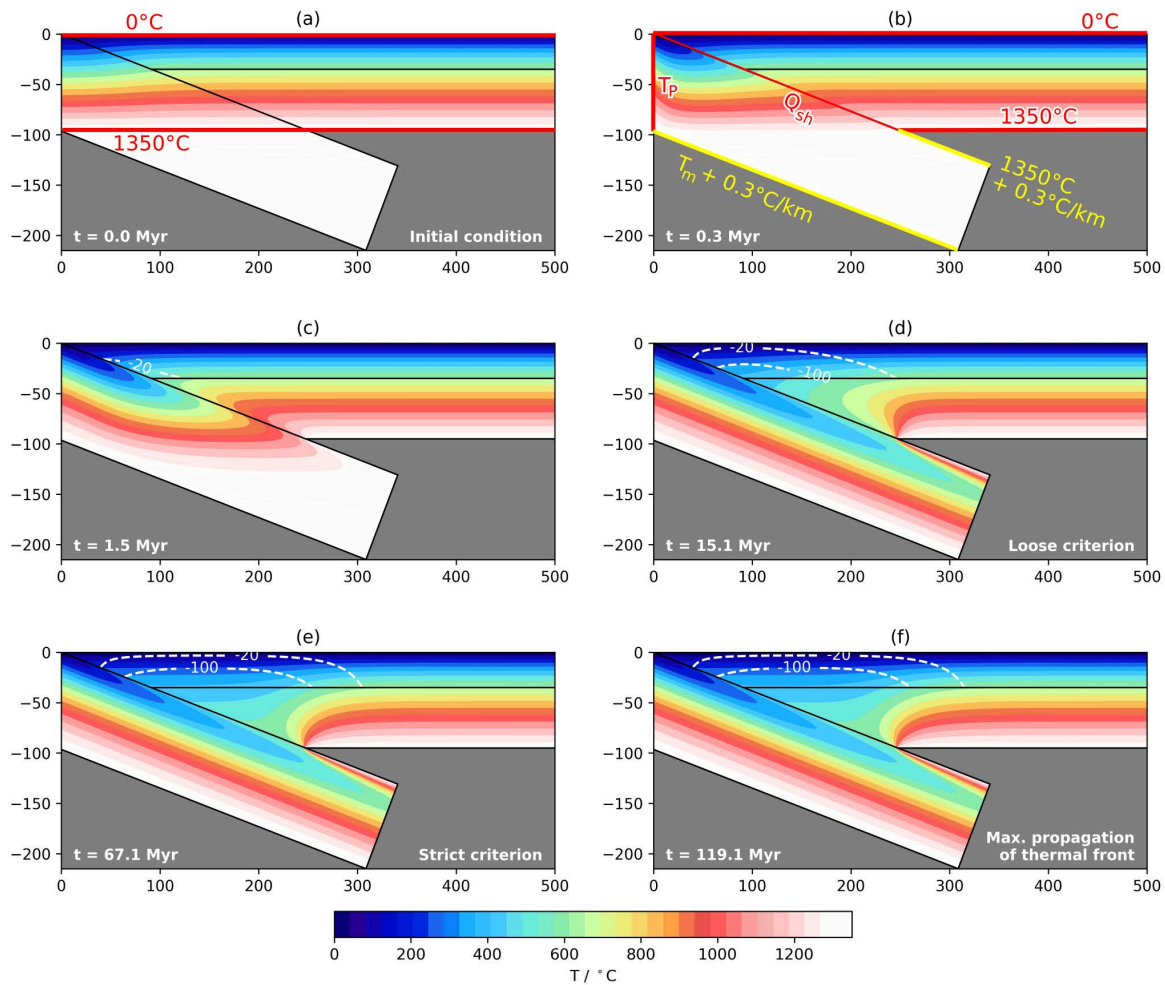
Figure 3.2.: Exemplary thermal model result at different time steps. Model scenario with slab dip = 19°, LAB depth = 105 km, slab age = 45 Ma, subduction velocity = 54 mm yr⁻¹ and shear-stress = 48 MPa. Figures are cropped at x=500 km. White dashed lines represent the thermal front where the model cooled by 20 °C or 100 °C with respect to initial conditions. **(a)** initial condition, boundary conditions indicated; **(b)** 0.3 Myr, transient boundary conditions indicated, Q_{sh} is shear heating, T_P the temperature profile of the *plate* model (Hasterok, 2013) and T_m is the temperature at the base of the *plate* model; **(c)** 1.5 Myr, the 20 °C cooling thermal front starts to propagate; **(d)** 15.1 Myr, the time when the loose criterion (1 % Myr⁻¹) applies in the continental crust (see main text for details); **(e)** 67.1 Myr, the time where the strict criterion (0.1 %̇Myr⁻¹) applies; **(f)** 237.7 Myr, time when the propagation of the thermal front in the continental crust ceases.

Table 3.1.: Parameter space. References a) Lallemand et al. (2005), b) Artemieva (2006), c) Priestley and McKenzie (2013), d) Rychert and Shearer (2009), e) Molnar and England (1990).

Parameter		Min.	Max.	Unit
Slab age [a]	a	25	150	Myr
Slab dip [a]	α	10	45	°
Convergence rate [a]	v	1	100	mm yr^{-1}
Continental LAB [b-d]	z_{lab}	80	110	km
shear-stress [e]	τ	0	100	MPa

simulator developed by Jacquey and Cacace (2018). A convergence test proving the robustness of the computation is provided in the supplements.

3.1.2.1. Model geometry

Lallemand et al. (2005) showed that the slab dip generally correlates with the nature of the slab (continental vs. oceanic) and the velocity of the overriding plate with respect to a fixed hotspot reference frame. They did not report any correlation between dip and (a) the age of the slab, (b) the relative convergence rate between upper plate and slab, nor (c) the dip direction. Cruciani et al. (2005) also concluded that slab age and dip are not causally related. These results allow us to assume slab dip, slab age and relative convergence rate as independent input parameters of the model. Based on the dataset of Lallemand et al. (2005) we selected values for slab age, dip and velocity (Tab. 3.1) that cover at least 85% of the values observed at present day subduction systems (see supplements, Fig. A.1). We modelled slab dips less than 45°, as larger values are thought to result in trench rollback and back-arc spreading (Lallemand et al., 2005). The thickness of the continental lithosphere was limited to within 80 and 110 km, which is representative for non-cratonic areas (Artemieva, 2006; Priestley and McKenzie, 2013; Rychert and Shearer, 2009). The only geometrical parameter which remained constant in all model runs was the thickness of the crystalline continental crust with 35 km. To analyse the thermal impact on the foreland, we prescribed the model to extend 500 km to the right from the triple-point of oceanic crust, lithospheric mantle and asthenosphere (Fig. 3.1).

We defined the geometric and physical properties of the oceanic slab following the *plate* model by Hasterok (2013). This model is based on the plate model by McKenzie (1967), and was calibrated with respect to a global collection of heat flow data, where data points in area with vigorous hydrothermal circulation had been removed. We took the properties determined by Hasterok (2013) and set the thickness of the oceanic slab to 95 km. The slab was then rotated by the amount of prescribed slab dip, and the remaining model geometry calculated accordingly.

We then discretised the models using the meshing software Gmsh (Geuzaine and Remacle, 2009), using triangle elements with an average of 0.2 triangles per km^2.

3.1.2.2. Governing equations

We solve for conductive heat transport in the continental and oceanic crust, as well as the heat transported by the moving oceanic slab, described by

$$\frac{\partial T}{\partial t} + \nabla \cdot \left(v_s T - \frac{\lambda}{(\rho C)_b} \nabla T \right) = \frac{Q_R}{(\rho C)_b} + \frac{Q_{sh}}{(\rho C)_b} \tag{3.1}$$

where T is the temperature, λ the thermal conductivity, $(\rho C)_b$ the bulk specific heat, v_s the subduction velocity, Q_R the radiogenic heat production and Q_{sh} the heat produced by shear heating. We represent the subduction shear zone in the models as a line source of heat, where the heat input can be approximated as the product of subduction velocity and shear-stress (Turcotte and Schubert, 1973). This assumption is valid if the model operates at time scales larger than 10^5 years (Peacock, 1992).

3.1.2.3. Boundary conditions

For the initial steady-state thermal field, Dirichlet boundary conditions were set to 0°C at the top (Earth's surface) and 1350°C (Turcotte and Schubert, 2014) at the lower boundary of the continental lithosphere (Fig. 3.2a).

During the transient computation, the boundary conditions (Fig. 3.2b) were set differently: at the left boundary (oceanic slab) we applied the temperature profile T_P (see C.1.1) for the respective slab age according to the *plate* model (Hasterok, 2013). At the bottom of the oceanic slab we prescribed a linear temperature increase (see C.1.2) with the mantle adiabat (Turcotte and Schubert, 1982).

Shear heating is expressed as the product between shear-stress and convergence rate (Turcotte and Schubert, 1973); this was implemented as a Neumann boundary condition along the slab interface (Q_{sh} in Fig. 3.2b). Assuming that shear heating occurs only at temperatures below the brittle-ductile transition (Peacock, 1996), we express Q_{sh} as

$$Q_{sh} = \frac{\tau v_s}{2} \left[1 - \mathrm{erf} \left(\frac{T - T_{BD}}{s} \right) \right] \tag{3.2}$$

where τ is the shear-stress at the plate interface and T_{BD} the temperature of the brittle-ductile transition. The error function erf was used to gradually deactivate shear heating at T_{BD} using a shape factor s of 30 K (see supplements Fig. A.2).

3.1.2.4. Physical properties

Table 3.1 contains a complete list of the upper and lower bounds for the input parameters that determine model geometry, subduction velocity, and shear-stress. Shear-stresses along the subduction interface are difficult to estimate due to the inaccessibility of the system. Many authors (Duarte et al., 2015; Kneller et al., 2007; Molnar and England, 1990; Peacock, 1992; Schellart, 2004) have tried to estimate the magnitude of shear-stress in subduction settings, with the largest estimates reaching up to 500 MPa (Kneller et al., 2007). This estimate is

Table 3.2.: Constant physical properties of the modelled bodies. References a) Christensen and Mooney (1995), b) Vilà et al. (2010), c) Schön (2015), d) Stein and Stein (1992).

Body	Density	Thermal conductivity	Radiogenic heat prod.	Heat capacity
	ρ	λ	Q_R	C_b
	kg m^{-3}	W m^{-1} K^{-1}	µW m^{-3}	J kg^{-1} K^{-1}
Continental crust	2835 [a]	2.55 [b]	1.03 [b]	960 [c]
Lithospheric mantle	3330 [d]	3.50 [d]	0.0 [d]	1171 [d]
Slab	3330 [d]	3.50 [d]	0.0 [d]	1171 [d]

based on the assumption that viscous forces balance the slab-pull force. However, as up to 90% of the negative buoyancy of the slab is being dissipated by replacing the asthenospheric mantle (Schellart, 2004), a more realistic estimate of the largest possible shear-stress is one magnitude smaller and would be in the order of 50 MPa (Duarte et al., 2015). These authors proposed a feedback loop between hydration of the forearc mantle and subduction velocity, which results in shear-stresses of less than 35 MPa – a value they suggest that may generally be valid for all subduction zones.

Due to the broad range of estimates, we varied the shear-stress at the plate interface between 0 and 100 MPa. This range respects the slab buoyancy dissipation and covers most values used in previous studies. The upper limit of the shear-stress agrees with the largest estimates by Molnar and England (1990) for the Japan subduction zone.

The characteristic properties for conductive heat transport (Tab. 3.2) were constant in all models. We set the density of the continental crust to the global average of 2835 kg m^{-3} (Christensen and Mooney, 1995). Radiogenic heat production, 1.03 µW m^{-3}, and thermal conductivity, 2.55 W m^{-1} K^{-1}, also represent average continental crustal values (Vilà et al., 2010), whereas the heat capacity of 960 J kg^{-1} K^{-1} was measured for granite (Schön, 2015). The physical properties of the subducting slab and lithospheric mantle were entirely adopted from the plate-cooling model of Stein and Stein (1992), assuming no radiogenic heat production.

3.1.3. Results

The distribution of the uniform, randomly chosen input parameters (see supplements Fig. A.3) shows no fall offs, thereby indicating a good coverage of the input parameter space for all 3000 models. Fig. 3.2 depicts the temperature distribution of one model at different time steps, beginning with the initial condition at 0 Myr (Fig. 3.2a). As subduction is initiated, the boundary conditions change: shear heating acts on the slab-interface (Q_{sh} in Fig. 3.2b) and the geothermal profile of the slab (Eq. C.1, T_P in Fig. 3.2b) is transported along the subduction channel. The subducting slab starts to heat up whilst the continental crust begins to cool down (Fig. 3.2c). Towards later time steps, a broad thermal depression develops on top of the slab (Fig.3.2 d-f).

For the evaluation of proximity to steady-state, we analysed the relative absolute temperature change in K per unit of time in the continental crust for two individual steady-state
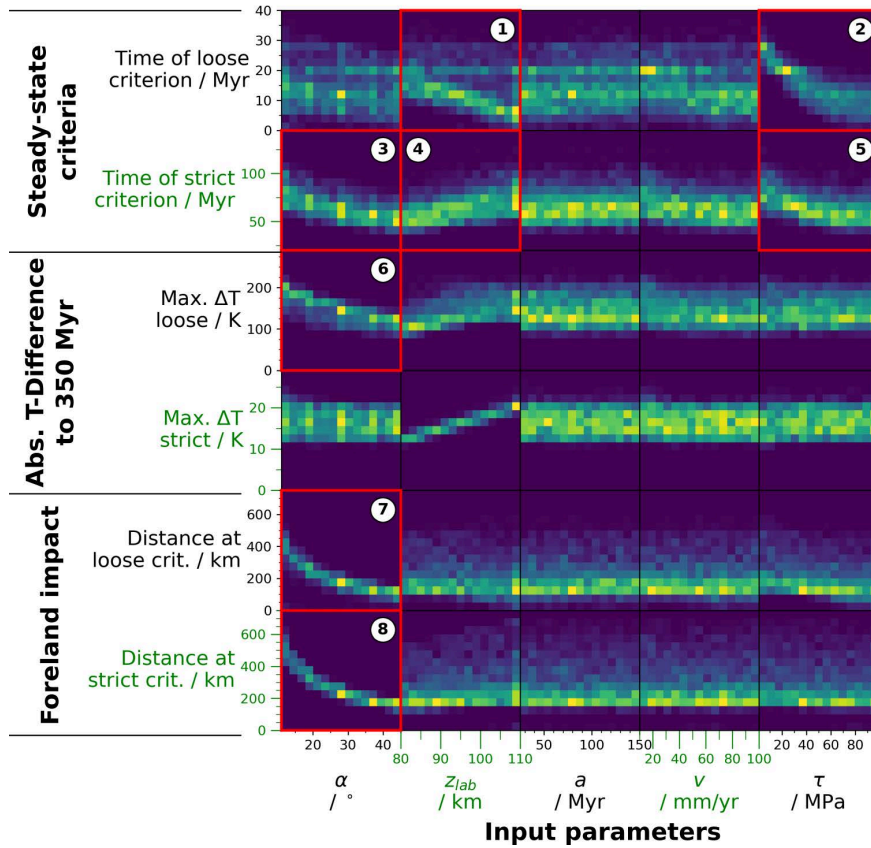
Figure 3.3.: Kernel density matrix between input and output parameters for the 3000 calculated models. The input parameters are slab dip α, continental LAB depth z_{lab}, age a of the subducting slab, slab convergence rate v and shear stress τ. The colour scales in each plot are normalised to one, with bright colours indicating high hit count within the area of the corresponding pixel. Red framed boxes are correlations referred to in text. Max. ΔT is the largest temperature difference that is observed between the temperature at 350 Myr and the loose or strict criteria. Distances to loose and strict criteria refer to the trench, where x equals zero.

criteria. For each model the rate was calculated at all time steps n in the continental crust:

$$\frac{dT}{dt} = \frac{T_n - T_{n-1}}{T_{n-1}\,(t_n - t_{n-1})} \tag{3.3}$$

where T is the absolute temperature in K and t is time. First, we used a relative temperature change of $1\%\,\mathrm{Myr^{-1}}$, a value which was previously used by Peacock (1996) to characterise steady-state conditions along shear zones of subduction zones. However, we find that when this criterion is reached in the continental crust, the thermal field is still subject to significant changes (see below). We therefore additionally analysed the results based on a stricter criterion of $0.1\%\,\mathrm{Myr^{-1}}$. The two criteria are referred to as loose and strict criteria, respectively.

To qualitatively assess dependencies between the input and output parameters, we present the results as kernel density plots (Fig. 3.3). The first two rows in this figure illustrate how much time the models required to attain a state that satisfies the loose ($1\%\,\mathrm{Myr^{-1}}$) and the strict criterion ($0.1\%\,\mathrm{Myr^{-1}}$) for steady-state. Here, slab dip, thickness of the continental plate and shear-stress magnitude determine how long the system requires to reach the criteria. The
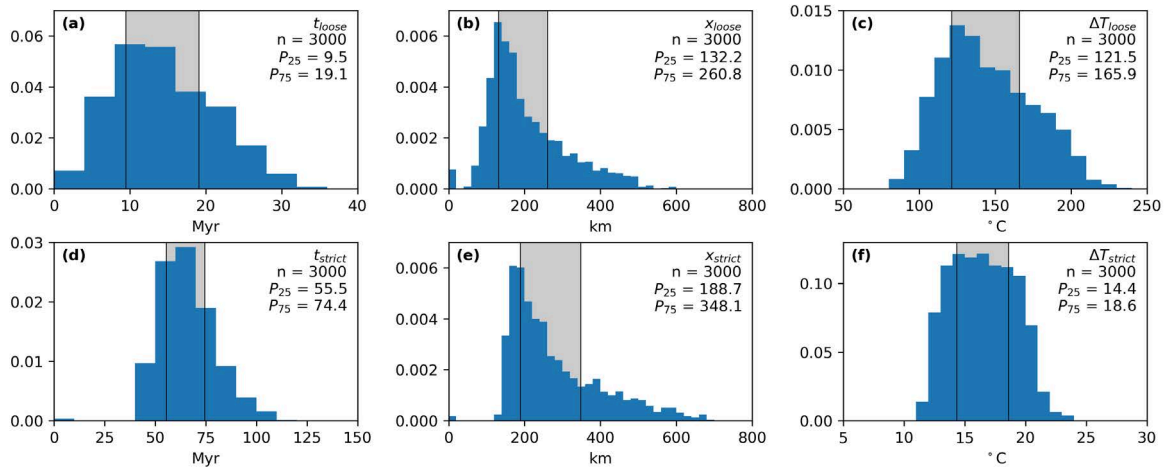
Figure 3.4.: Histograms of key parameters extracted from all modelled scenarios and over all time steps. Number of models indicated by n, grey areas mark the 25 to 75% percentile range given by P25 and P75. **(a)** time t_{loose} until loose equilibration criterion is reached; **(b)** thermal front propagation distance at t_{loose}; **(c)** largest temperature difference between last time step (350 Myr) and t_{loose}; **(d)** time t_{strict} until strict criterion is reached; **(e)** thermal front propagation distance at t_{strict}; **(f)** largest temperature difference between last time step and t_{strict}.

comparison of the temperature in the continental crust at the final time step, which we regard as steady-state, and the temperatures at the steady-state criteria reveals that temperatures might differ by up to 200°C. Finally, we observe that the temperature perturbation that originated from the subduction of the slab (rows 5 and 6) may affect the continental lithosphere laterally by up to 600 km at shallow dips.

3.1.3.1. Time required to reach the steady-state criteria

Most models reached the loose criterion in the continental crust between 9 and 20 Myr after subduction initiation (Fig. 3.4a). We observe a negative correlation between the loose criterion and continental LAB depth (No. 1 in Fig. 3.3), since the equilibration time decreases with increasing thickness of the continental lithosphere. A similar negative correlation applies to increasing shear-stress (No. 2 in Fig. 3.3). The dip angle correlates only to a limited degree with the loose criterion.

After 55 to 75 Myr, the continental crust in most models reached a state corresponding to the strict criterion (Fig. 3.4d). The time to reach this criterion correlates with the slab dip, where greater dips result in faster thermal equilibration (No. 3 in Fig. 3.3). Additionally, a positive correlation with the thickness of the continental lithosphere (4 in Fig. 3.3) was observed. For values above 30 MPa, shear-stress did not significantly influence the time until the strict criterion was reached (No. 5 in Fig. 3.3).

3.1.3.2. Impact on the foreland

The subduction of the oceanic slab transports cold material along the slab interface and therefore cools the adjacent continental lithosphere (Fig. 3.2). To measure the horizontal impact
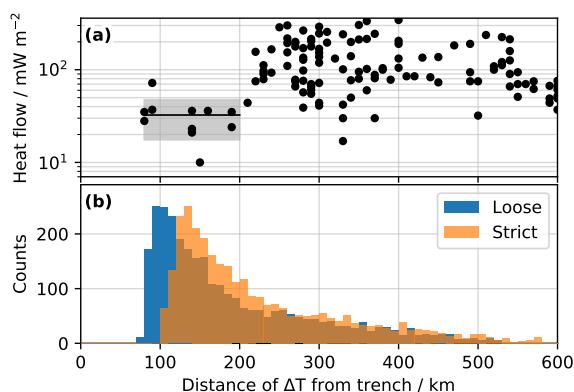
Figure 3.5.: Surface heat flow observed versus distance of largest temperature differences ΔT between final time step and the steady-state criteria. **(a)** surface heat flow observed above the subduction zone of the South American plate (Hamza and Muñoz, 1996; Uyeda and Watanabe, 1982), with distances measured parallelly to the plate motion vectors of the Nazca plate (details in Fig. 3.6a). The black line indicates the mean surface heat flow of $32\,\text{mW}\,\text{m}^{-2}$ for trench distances less than $200\,\text{km}$, the grey box represents the standard deviation of $14\,\text{mW}\,\text{m}^{-2}$; **(b)** distribution of largest ΔT observed between final time step and the loose/strict criteria (Fig. 3.4 c and f).

distance x, we analysed the spatial and temporal evolution of the cooling thermal front that marks a decrease of $20 \pm 1\,°\text{C}$ with respect to the initial thermal field at $0\,\text{Myr}$ in the continental crust (Fig. 3.2 d-f). Therefore, we computed the temperature difference at each point in the model between the time step when the criteria are reached, and the initial time step. This computation yields a temperature difference profile of the model at the time of the loose and strict criteria. We then determined in both difference profiles the point with the largest horizontal distance from the trench that is $20 \pm 1\,°\text{C}$ cooler than at $0\,\text{Myr}$.

The distances measured and shown in rows 5 and 6 of Fig. 3.3 refer to the largest horizontal distance from the trench where x equals zero. At the time of achieved loose and strict criteria, we observe a clear correlation with the slab dip, where steeper dips result in shorter propagation distances. Slab age, velocity and shear-stress do not significantly correlate with the strict criterion. Overall, the horizontal impact distances in most of our models range between 100 to $230\,\text{km}$ for the loose criterion (Fig. 3.4b) and 180 to $320\,\text{km}$ for the strict criterion (Fig. 3.4e).

3.1.4. Discussion

3.1.4.1. Impact of the steady-state criteria on evaluation of temperature-dependent processes

We aim to assess how precisely the loose and strict criteria determine the time when a model reaches a thermal steady-state, and how the different criteria influence analyses of temperature-dependent processes. Since the propagation of the thermal front in all models ceased before the last time step at $350\,\text{Myr}$ (see supplements Fig. A.4), we assume that at this time the simulation attained a thermal state that is representative for a steady-state. Thus, we quantify in all models the largest absolute temperature difference in the continental crust between the last time step and the time steps of the respective criteria. For the loose criterion,

Table 3.3.: Rheological properties used to compute the strength profiles in Fig. 3.7 and Fig. 3.8.

Body	Friction coefficient f_f	Pore fluid factor f_p	Type rheology	Density ρ kg m^{-3}	Pre-exponential scaling factor A_p Pa^{-n} s^{-1}	Power law exponent n	Activation energy Q_p kJ mol^{-1}
Crust	0.75	0.35	Dry diorite[a]	2800	$5.2 \cdot 10^{-18}$	2.4	219
Mantle	0.75	0.35	Dry olivine[b]	3300	$7 \cdot 10^{-14}$	3.0	510

a) Burov et al. (1998), b) Goetze and Evans (1979); Dorn's law parameters for the mantle are $\sigma_d = 8.5$ GPa, $Q_d = 535$ kJ mol^{-1} and $A_d = 5.7 \cdot 10^{11}$ s^{-1}.

the largest temperature differences to steady state in the continental crust are on the order of 120 to 166°C (Fig. 3.4c), and between 14 to 19°C for the strict criterion (Fig. 3.4f).

A closer analysis reveals that 70 per cent of these temperature differences occur at distances less than 200 km from the trench (Fig. 3.5b). This distance corresponds to the fore-arc region of the South American Andes (Fig. 3.6a) and is characterised by an average heat flow of 32 ± 14 mW m^{-2} (Fig. 3.5a). In the models, these observed temperature differences typically occur at the base of the continental crust because the cooling source, i.e. the subducting slab, is structurally located below the continental crust (Fig. 3.2d-f). Assuming that the temperature difference increases linearly with depth, the resulting change in surface heat flow[1] between loose criterion and 350 Myr would be in the order of 14 mW m^{-2}. Between strict criterion and 350 Myr, the differences would be in the order of 2 mW m^{-2}. Although the heat flow difference at the loose criterion is significant with respect to the observed average in the Andean fore-arc region, it is on the same magnitude as the observed standard deviation. Accordingly, we cannot determine a significant difference in the surface heat flow between the different steady-state formulations. As surface heat flow is representative for the shallow, near-surface thermal field, these results imply that models assessing shallow thermal processes may rely on the steady-state assumption if subduction had been active and constant for around 20 Myr. This time scale depends on the thickness of the continental lithosphere (No. 1 in Fig. 3.3) and shear stress magnitude (No. 2 in Fig. 3.3).

Creep, on the other hand, is a process that is important at greater depths and depends exponentially on temperature. Assessments of those processes might be significantly biased depending on which criterion of the thermal field was chosen to define the steady-state. Such assessments are necessary, e.g., for strength analyses of the lithosphere performed to investigate observed deformation patterns, or geodynamic models that start with an initial state as derived from a transient model.

To analyse the impact of the steady-state criteria on rheological estimates, we computed the integrated crustal strength for a model with a particularly high temperature difference between the strict and the loose criterion. The kernel density distribution number 6 in Figure 3.3 indicates that shallow dips produce higher temperature differences than greater dips. We therefore analyse the impact on creep by computing the integrated crustal strength of a

---

[1]Surface heat flow difference $\Delta Q_s = \Delta T \lambda z^{-1}$ where $\lambda = 2.5$ W m^{-1} K^{-1}, ΔT is the temperature difference in the time steps between the surface ($T = 0$ °C) and $z = 35$ km, the base of the continental crust.
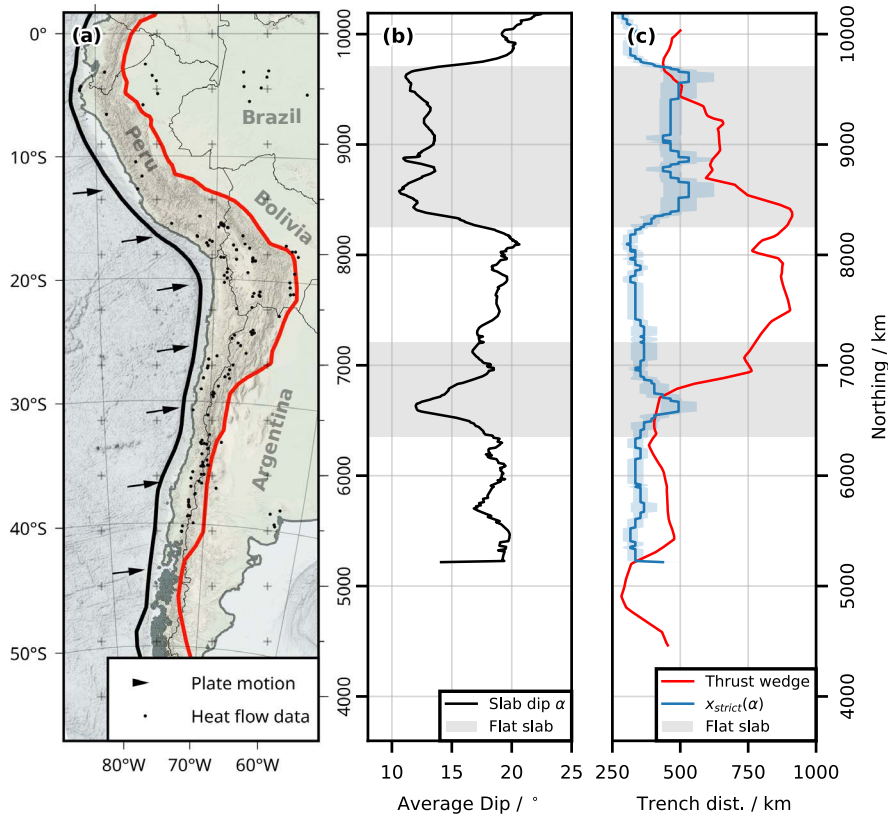
Figure 3.6.: Distance between the trench and the foreland-facing edge of the thrust-wedge in South America (DeCelles et al., 2011). Plate motion vectors (Kreemer et al., 2014) are relative to the South American plate. **(a)** map showing location of the trench (black line), the western limit of the foreland basins (red), plate motion vectors, and location of heat flow data points (Hamza and Muñoz, 1996; Uyeda and Watanabe, 1982) used in Fig. 3.5; **(b)** average dip α of the subducting Nazca plate between 0 and 110 km depth (Hayes et al., 2012), grey boxes indicate latitudes of flat-slabs (Kley et al., 1999); **(c)** distance between trench and limit of the foreland basins (thrust wedge distance; red line), and propagation distance of the thermal front at strict criterion derived from the average slab dip α in b and our model results. The blue shaded area represents the standard deviation. Distances were measured from the trench parallelly to the plate motion vectors, every 10 km between 50° and 0°S latitude.
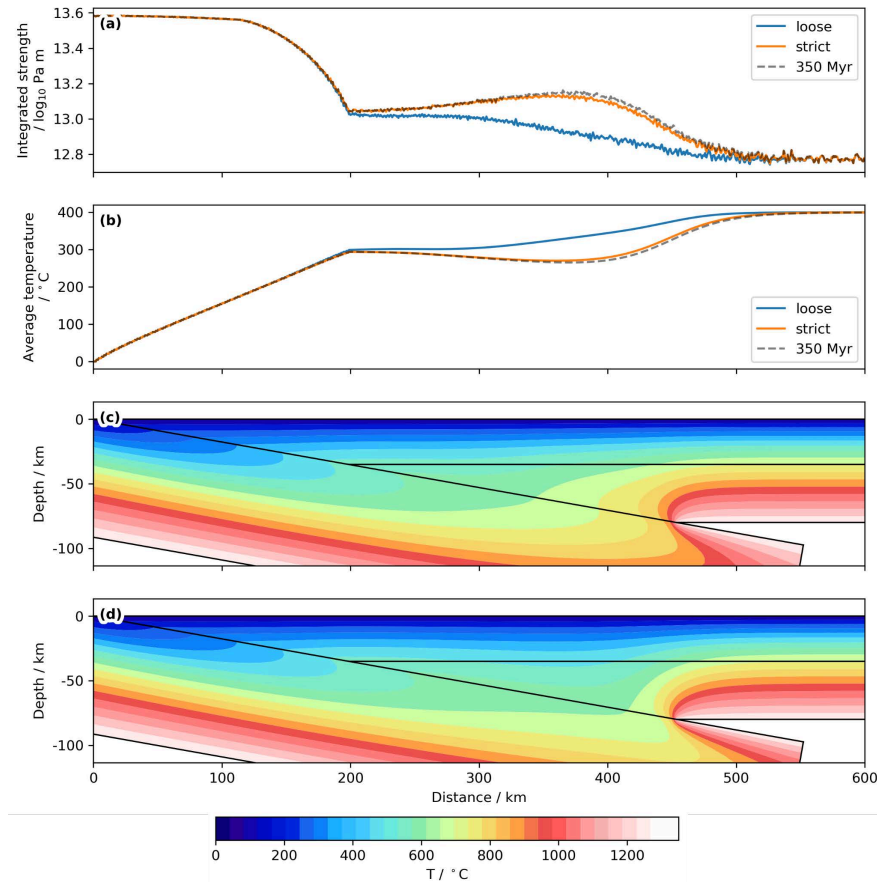
Figure 3.7.: Example for the impact of the steady-state criteria on the integrated strength of the continental crust. The model is characterised by a dip of 10°, a subduction velocity of $10\,\mathrm{mm\,yr^{-1}}$, a shear-stress of $61\,\mathrm{MPa}$, a continental LAB depth of $80\,\mathrm{km}$; the age of the oceanic slab is $61\,\mathrm{Myr}$. **(a)** integrated strength from 0 to $35\,\mathrm{km}$ depth. Note that between trench and $200\,\mathrm{km}$ trench distance, the strength is integrated over the oceanic slab and continental crust. At the strict criterion, the integrated strength of the continental crust between 300 to $450\,\mathrm{km}$ from the trench is up to $0.5\log_{10}\mathrm{Pa\,m}$ stronger than at the earlier loose criterion. Details on the computation of the strength are given in the supplements; **(b)** average temperature in the continental crust over the depth range from 0 to $35\,\mathrm{km}$; **(c)** temperature profile at time of the loose criterion $(1\,\%\,\mathrm{Myr^{-1}})$; **(d)** temperature at the time of the strict criterion $(0.1\,\%\,\mathrm{Myr^{-1}})$.
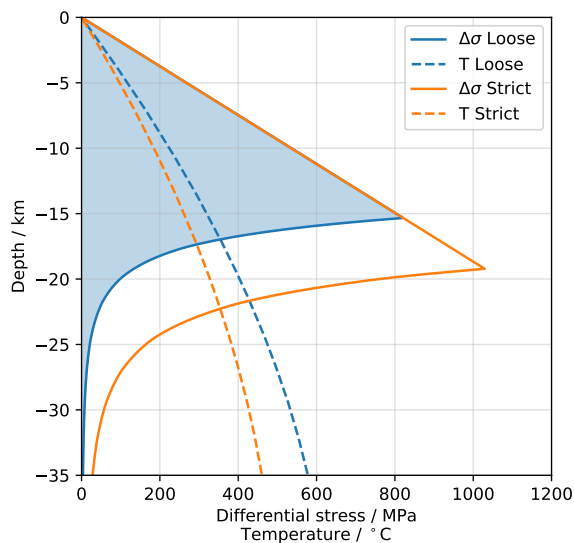
Figure 3.8.: Strength profile trough the continental crust of the model in Figure 3.7 for compression at $x = 180\,km$ and strain rate $10^{-15}\,s^{-1}$. In between the loose and strict criterion, the brittle ductile transition changes by about 4 km.

model with a dip of 10° (Fig. 3.7), using Byerlee's law for brittle deformation, and dislocation creep for ductile deformation (for details see Appendix D.1). The parameters used to compute the strength, representative for dry diorite in the crust (Burov et al., 1998) and dry olivine (Goetze and Evans, 1979) in the mantle, are given in Table 3.3.

The integrated strength profile (Fig. 3.7a) illustrates that at a distance of up to 450 km from the trench the crustal strength between the time steps varies by up to $0.5\log_{10}\text{Pa}\,\text{m}$. The increased strength at the time of the strict criterion is caused by overall decreased crustal temperatures (Fig. 3.7b) and results in a shift of the brittle-ductile transition of up to 4 km (Fig. 3.8). With respect to integrated global crustal strength estimates varying by a factor of about $1.0\log_{10}\text{Pa}\,\text{m}$ (e.g. Tesauro et al., 2012), this difference is substantial. As a consequence, we suggest to assume steady-state conditions for rheological studies on the upper plate if the characteristic parameters of the subduction system satisfy the strict criterion.

3.1.4.2. Thermal impact on the retroarc foreland

We assessed the impact of subduction on the thermal field of the upper plate in a subduction system by the propagation distance of the 20 °C thermal front that originates from the cooling of the upper plate due to the subducting slab. At the time of the strict criterion in the continental crust, the thermal front in most models propagated between 188 to 349 km from the trench (Fig. 3.4e).

We compare the model output with the present-day configuration of the Andean foreland basin system. Therefore, we determine the lateral distance between the trench and the foreland facing thrust wedge between 0 to 45°S latitude in South America by measuring parallelly to the Nazca plate motion vectors (Fig. 3.6a). From the Slab 1.0 model by Hayes et al. (2012) we obtain the average dip α of the Nazca plate between 0 and 130 km depth (Fig. 3.6b). Finally,

we obtain $x_{strict}(\alpha)$, the predicted propagation distance of the 20°C thermal front at the time of the strict criterion (Fig. 3.6b, Fig. 3.4e), at each section of the subducted Nazca slab (Fig. 3.6c). The comparison of x_{strict} and the distance between trench and foreland thrust wedge shows that large parts of the foreland east of the thrust wedge are thermally not influenced by the subduction process itself. Only in those areas with shallow dips in Peru and Argentina, i.e. where flat-slab subduction occurs (Kley et al., 1999), subduction processes more strongly affect the thermal field of the foreland. Flat-slab subduction, a process that is assumed to cause cooling in the upper mantle below 1300 °C and therefore resulting in increased coupling with the upper plate (e.g. Marot et al., 2014), however, cannot be analysed with our models as it would require slab geometries with variable dip. Due to the decreased upper mantle temperatures between the base of the continental crystalline crust and the top of the subducting slab we can expect that in cases of flat-slab subduction the impact on the thermal field reaches farther into the retroarc foreland than predicted in our models (with a homogeneous slab dip). To what extent this hypothesis is valid should be targeted by future studies.

Modelling studies (Babeyko et al., 2002; Sobolev et al., 2006) provide evidence that additional geodynamic processes such as crustal delamination, magmatism, active deformation of the upper plate, or thrusting of the orogenic wedge onto the continental lithosphere may significantly perturb the thermal field. Especially in the case of strong shortening, e.g. 300 km over 35 Myr in the Central Andes (Sobolev et al., 2006), those additional geodynamic processes contribute significantly to the thermal field of the continental plate. For small amounts of shortening, e.g. 40 km over 35 Myr in the southern Andes (Sobolev et al., 2006), however, the thermal field is much less affected . This implies that the conclusions suggested in our study are more applicable in foreland basin settings with low amounts of shortening, such as the southern Andes than in settings that are characterised by greater shortening, such as the Central Andes.

3.1.4.3. Controlling factors

Depending on the criterion, different factors govern the amount of time that the continental crust requires to attain a state of thermal equilibrium. To reach the loose criterion, primarily shear-stress and to a lesser extent the thickness of the continental lithosphere are relevant factors (1,2 in Fig. 3.3). Shear-stresses above 50 MPa effectively heat the plate interface and thereby insulate the upper plate from the cold subducting slab, which leads to a faster equilibration time. This also holds for the strict criterion (5 in Fig. 3.3); however, dip and continental plate thickness are equivalently important controlling factors. In conclusion, the main factors controlling the time required to attain steady-state conditions are the subducting plate dip, the continental plate thickness and the shear-stress. The age of the subducting slab at the trench and the convergence rate are subordinate factors.

3.1.5. Conclusions

We have aimed to better understand the controlling factors of the thermal field at subduction zones, with special emphasis on retro and retroarc foreland basins. With regard to purely conductive processes our results support that most subduction systems acquire a near steady-state (less than 0.1% temperature change per Myr) between 55 to 75 Myr after the onset of subduction. This length of time is primarily controlled by the dip of the oceanic slab, the thickness of the continental lithosphere, and shear heating. The magnitude of shear stress along the plate interface, although having a significant impact on the heat distribution in the system, only influences the time scale of attaining steady-state conditions when below $\approx 50\,\mathrm{MPa}$. For shear-stresses in excess of $50\,\mathrm{MPa}$, the system will equilibrate with respect to the the strict criterion in less than $75\,\mathrm{Myr}$.

The cooling thermal front, in this study $-20\,°\mathrm{C}$, can horizontally propagate up to $600\,\mathrm{km}$ through the continental crust. This distance is primarily governed by the dip of the oceanic slab. The application of our findings on the South American plate margin indicates that the thermal field in modern retroarc foreland basins is not altered significantly if only the influence of the subducting cold slab is considered and the basins are located above "normally" dipping slabs. In cases of flat-slab subduction, the impact into the foreland might be higher due to a cooler upper mantle and increased coupling between the subducting slab and the upper plate.

These conclusions can be applied for settings with low amounts of shortening between trench and foreland, comparable to the southern Andean foreland basins. Foreland basins with associated orogens that were subject to larger amounts of shortening, e.g. similar to the Central Andes, are probably overprinted by additional geodynamic processes such as magmatism, thrusting or delamination. Further efforts should be made towards a quantification as to how these additional geodynamic processes may affect the thermal field with respect to an hypothetical steady state.

3.2. Differences between transient and steady-state thermal fields in the central Andean foreland

3.2.1. Introduction

In Chapter 3.1 it was shown that subduction itself is not capable to modify the thermal field of a foreland basin by thermal conduction. Orogens, however, arise through the deformation of the lithosphere and therefore potentially affect the thermal state of the associated foreland basins.

Particularly the thermal boundary conditions in steady state conductive thermal models are based on snapshots at present time of the state of the lithosphere. Yet the Earth is a dynamic system and these temperature snapshots do not contain information on the temporal variability of temperatures in the conductive lithosphere. It must therefore be assumed that the conductive steady-state thermal field of a model deviates from the actual transient state. How big are the differences between the modelled steady-state temperatures and the present-day transient temperatures?

I aim to answer this question by utilising the results of a coupled thermo-mechanical model of the Central Andes (Sobolev et al., 2006). The results of such coupled numerical models may not be an exact representation of the actual geological processes. However, the higher physical complexity of a coupled transient model compared to a purely conductive steady-state model should allow to draw some conclusions how well a steady-state model predicts the thermal field in a retroarc foreland. Therefore, the selected model allows to isolate the differences between a transient and a steady-state thermal field of the a region, because all relevant parameters for the thermal field are known at each time step: model geometry, rock composition, thermal properties and temperatures.

The model by Sobolev et al. (2006) aims to depict the evolution of the Central Andes and the foreland region on a 2D profile from 35 Ma until present day, at latitudes of the Altiplano plateau. It is one possible scenario for the complete evolution from a horizontally layered geometry (Fig. 3.9 a) to the full orogen-foreland system (Fig. 3.9 b). Sobolev et al. (2006) modelled Maxwell visco-elastic bodies with stress-dependent viscosity and Mohr-Coulomb failure criterion. Viscous deformation mechanisms include dislocation, diffusion and Peierl's creep. They furthermore included the transformation of gabbro to eclogite in the oceanic crust at 700°C and in the continental crust at 800°C, neglecting volume changes and latent heat. The spatial resolution of 4 km did not allow the authors to solve for partial melting and magmatism-related convection in the continental crust (Babeyko et al., 2002). They emulated these convective effects by a ten-fold increase of the thermal conductivity of felsic crustal rocks that are warmer than 750 °C.

The initial model geometry at 35 Ma (Fig. 3.9) encompasses bodies for the oceanic and continental lithosphere. The continental lithosphere is laterally subdivided into a thinner ($\approx$ 75 km thick) section representing weak lithosphere of a back-arc mobile belt (Hyndman et al., 2005), and a thicker ($\approx$ 125 km thick) section depicting the margin of the Brazilian
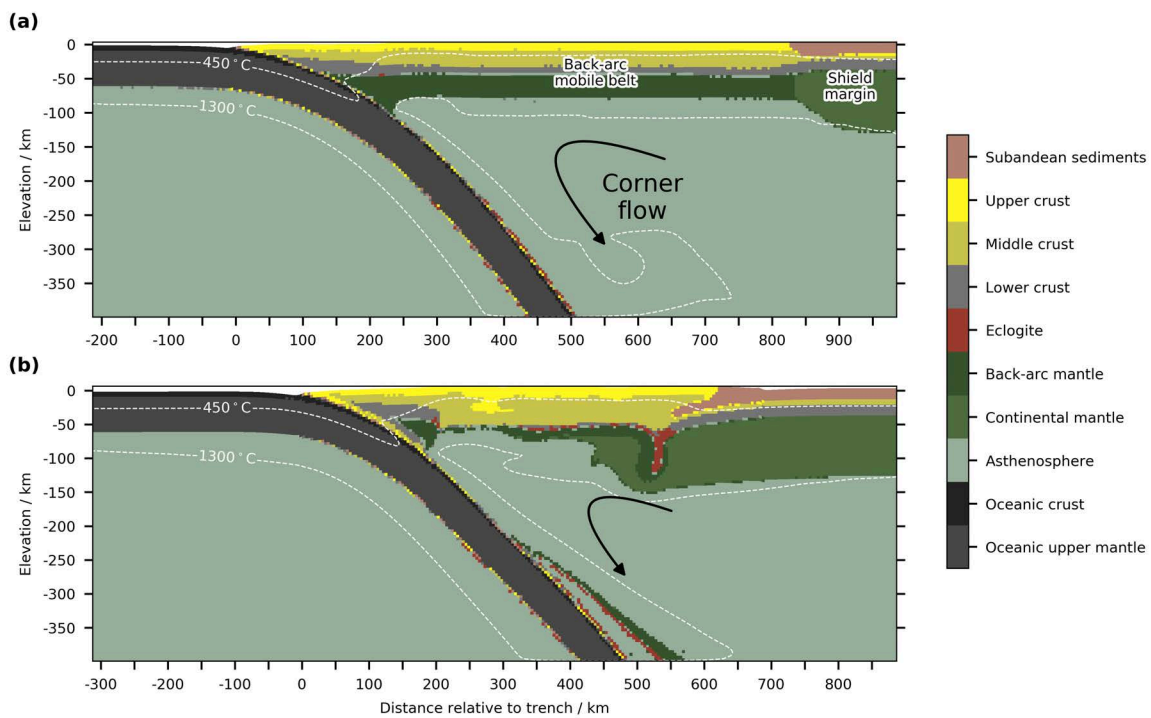
Figure 3.9.: Snapshots of the model representing the evolution of the Central Andes at latitudes of the Altiplano-Plateau by Sobolev et al. (2006). **(a)** First time step, and after **(b)** 35 Myr of simulation time.

continental shield to the east. The section representing the back-arc mobile belt contains a three-layered crystalline crust, where the lower crust is thinned out. On top of the Brazilian shield margin a sedimentary basin is prescribed.

3.2.2. Methods

For the analysis I chose four different time steps where I compared the transient coupled thermal field to the corresponding steady-state thermal field. The first selected time step, at 0.45 Myr, is the first simulation time step. The second step, after 7.25 Myr was chosen because this is the time step before the first delamination of lower crust. The second delamination occurs after the third selected time step of 26.0 Myr. Finally the fourth selected time step is the last time step after 35.0 Myr that represents the present-day configuration. The steady-state thermal field was computed in 2D using the steady-state heat flux equation and LYNX (Jacquey and Cacace, 2018).

3.2.2.1. Computation of the steady-state conductive thermal field

The results of the coupled model were available as quadrilateral grid stored as a Tecplot (©Tecplot, Inc.) ASCII file. At each grid node information about density, phase, temperature and coordinate were available. Each of the phases listed in Fig. 3.9 is represented by a natural ($\mathbb{N}$) number. As the nodes in the coupled model track material properties, the phase

Table 3.4.: Thermal and rheological properties of the modelled bodies. Properties are adopted from Sobolev et al. (2006).

	Body	Heat cond. λ $\mathrm{W\,m^{-1}\,K^{-1}}$	Rad. heat prod. Q_R $\mathrm{\mu W\,m^{-3}}$	Type rheology	Density ρ $\mathrm{kg\,m^{-3}}$	n	A_p $\mathrm{Pa^{-n}\,s^{-1}}$	Q_p $\mathrm{kJ\,mol^{-1}}$
	Subandean sediments	2.50	1.30	Quartzite, wet [1]	2650	4.0	$1 \cdot 10^{-28}$	223
	Upper crust	2.50 [a]	1.30	Quartzite, wet [1]	2700	4.0	$1 \cdot 10^{-28}$	223
	Middle crust	2.50 [a]	1.30	Quartzite, wet [1,b]	2800	4.0	$1 \cdot 10^{-27}$	223
	Lower crust	2.50	0.20	Plagioclase, wet [2]	2950	3.0	$4 \cdot 10^{-16}$	356
	Back-arc mantle	3.30	0.00	Peridotite, dry [3]	3280	3.5	$5 \cdot 10^{-15}$	515
	Continental mantle	3.30	0.00	Peridotite, dry [3]	3280	3.5	$5 \cdot 10^{-17}$	535
	Asthenosphere	3.30	0.00	Peridotite, dry [3]	3300	3.5	$5 \cdot 10^{-15}$	515

[a] Temperature dependent conductivity according to Eqn. 3.4; [b] weakened quartzite where $A_p \cdot 0.1$ with respect to unmodified rheology. Creep properties: [1] Gleason and Tullis (1995); [2] Rybacki and Dresen (2000); [3] Hirth and Kohlstedt (2004), Dorn's law parameters $A_D = 5.8 \cdot 10^{11}\,\mathrm{s^{-1}}$, $Q_D = 545\,\mathrm{kJ\,mol^{-1}}$, $\sigma_D = 8.5\,\mathrm{GPa}$ from Kameyama et al. (1999).

information is not tied to these natural numbers exclusively. Instead, with progressive phase mixing at body interfaces or due to phase changes, the phases along these interfaces may adopt positive real numbers ($\mathbb{R}^{>0}$). For example, a particle representing a mixture of 90 per cent of a phase 1, and 10 per cent of phase 2, would attain a phase of 1.1. The method I used here to compute the steady-state thermal field does not support material fractions for the individual elements. Therefore, in the process of data transformation, I rounded the phase IDs back to natural numbers. At body interfaces, this approach results in inaccurate representation of the materials. However, since the amount of elements that are affected by rounding is small compared to the total number of elements, the introduced error is small.

For each steady-state model to be tested, I extracted a subset of the coupled model between the surface and about 80 km depth. Note that the depth to the lower boundary is not constant since the coupled numerical model by Sobolev et al. (2006) used a Lagrangian mesh. At the selected depth, temperatures in the coupled model do not exceed 1300 °C (Figs. 3.9 and 3.10). This ensures that exclusively convective processes were excluded from the steady-state model. The model extent was limited to the west by the top of the oceanic slab which I excluded because the heat transport within the slab, and at the slab interface had been subject to the previous chapter.

The thermal properties of the involved bodies (Tab. 3.4) were adopted from Sobolev et al. (2006). To mimic the increase of thermal conductivity in the felsic continental crust, I defined

the temperature dependent conductivity as

$$\lambda\left(T\right) = \lambda_0 \left[1 + \frac{f_m - 1}{2}\left(1 + \mathrm{erf}\left(\frac{T - T_L}{f_s}\right)\right)\right] \tag{3.4}$$

where λ_0 is the initial conductivity below the transition temperature $T_L = 750\,°\mathrm{C}$, $f_m = 10$ the multiplicator, $f_s = 10$ a shape factor defining the steepness of the step, and erf the error function. The shape factor must be defined in order to avoid numerical instabilities that would result from a steep transition. I applied Dirichlet boundary conditions at the upper ($0\,°\mathrm{C}$) and lower boundary of the steady-state model. The temperature for the lower boundary condition was extracted from the nodes at the corresponding time step in the coupled model.

3.2.2.2. Computation of lithospheric strength

To assess the impact of the temperature difference between the coupled and the steady state models, I computed the yield strength of the models. Based on shortening estimates in the central Andes, the strain rate used for this computation was set to $5{\cdot}10^{-16}\,\mathrm{s}^{-1}$ (details see Appx. D.1). This strain rate also agrees with the overall strain rate in the coupled model, given an initial width of $\approx 1000\,\mathrm{km}$ and total shortening of $350\,\mathrm{km}$ within $35\,\mathrm{Myr}$ (Sobolev et al., 2006).

I computed the maximum differential stress as an indicator of the in-situ yield strength of the rock at the centre of each element, i.e. within each model element the yield strength is homogeneous. This approach is required, as the vertices of the elements may be situated at the boundaries of two different materials. At these vertices it is impossible to compute the yield strength because they cannot be assigned unique material properties. Thus, I computed the average temperature and the centre of each element, and used these values to compute the yield strength according to equations D.1 and D.6.

3.2.3. Results

At 0.45 Myr (Fig. 3.10a), the layers in the lithosphere are parallelly stratified and undeformed. The temperatures in the steady-state thermal field are underestimated for distances less than $350\,\mathrm{km}$ from the trench by more than $60\,°\mathrm{C}$. Farther away from the trench, the temperatures between transient and steady-state model agree within $\pm 20\,°\mathrm{C}$.

Until 7.25 Myr (Fig. 3.10b), a gravitational instability at $350\,\mathrm{km}$ trench distance developed in the lower crust and the back-arc mantle. At this location, the first delamination of lower crustal material will occur in the following time steps. Due to the corner flow in the mantle wedge (Fig. 3.9b), the lithospheric mantle and parts of the lower continental root are dragged towards the trench. The temperatures in the steady-state model at less than $350\,\mathrm{km}$ trench distance are now underestimated by about 60 to $80\,°\mathrm{C}$. Between 300 to $500\,\mathrm{km}$ a zone developed where temperatures are overestimated by up to $160\,°\mathrm{C}$ in the upper crust, and about $80\,°\mathrm{C}$ in the back-arc mantle. The remaining areas of the the steady-state model agree by $\pm 20\,°\mathrm{C}$ with the temperatures of the transient coupled model.
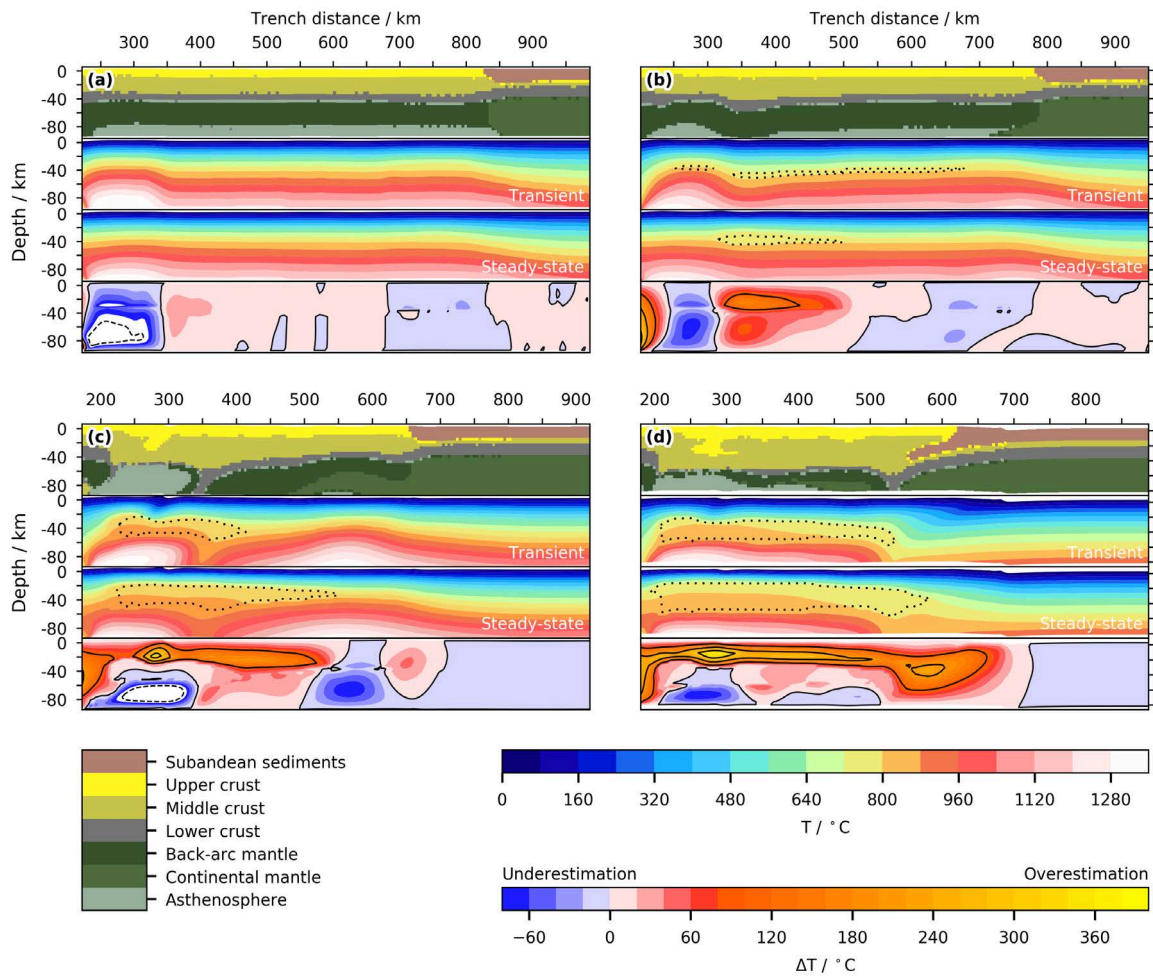
Figure 3.10.: Comparison of transient and steady-state thermal fields at the selected time steps. Each sub figure shows from top to bottom: structure, coupled model thermal field, steady-state thermal field, temperature difference steady-state minus coupled model. The dotted areas in the absolute temperature plots indicate the area where the thermal conductivity of the crystalline crust is increased ten-fold. Bold contours in the temperature difference profiles plot every 100 °C. **(a)** 0.45 Myr; **(b)** 7.25 Myr; **(c)** 26.0 Myr; **(d)** 35.0 Myr.

The complexity of the model geometry as well as the temperature differences increased at 26 Myr (Fig. 3.10c). As a result of the delamination of parts of the lower crust and back-arc mantle at 350 km distance from the trench, asthenospheric mantle is in direct contact with the felsic crystalline crust. At this time step, the second delamination event is imminent at ca. 350 km. The sedimentary basin, however, is not yet affected by deformation. In the upper crust, a wide zone up to 550 km from the trench developed that is characterised by overestimated temperatures in the steady-state model. Bound within this region, between 250 to 300 km, temperatures are overestimated by more than 200 °C. This region is underlain by a broader region of underestimated temperatures. Between 600 to 700 km temperatures are slightly overestimated by 40 to 60 °C. Temperatures in the foreland lithosphere further than 700 km from the trench largely agree between the steady-state and transient models.

At the final time step of 35 Myr (Fig. 3.10d), the deformational front has reached the sedi-
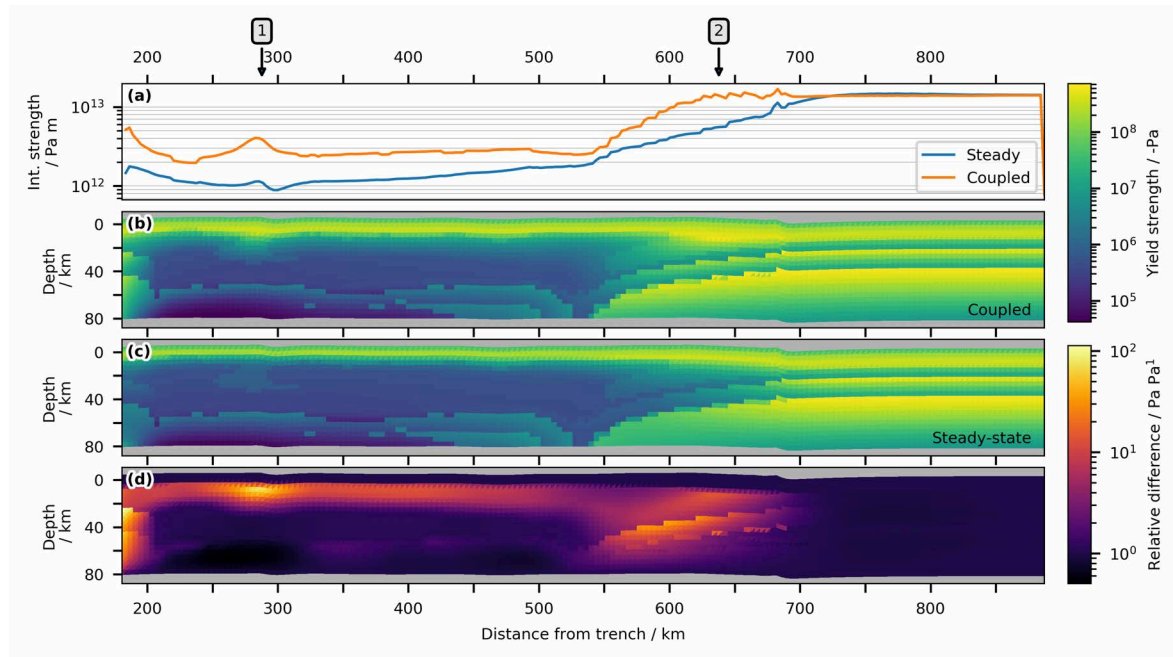
Figure 3.11.: Yield strength of the whole model at the last time step (35 Myr) for a strain rate of $5 \cdot 10^{-16} s^{-1}$. **(a)** integrated strength between surface and 75 km depth for steady and coupled model. Numbered arrows indicate locations of yield strength envelopes, (1) Fig. 3.14a, (2) Fig. 3.14b; **(b)** yield strength of the coupled model; **(c)** yield strength of the steady-state model; **(d)** relative difference between coupled and steady-state model. Bright areas indicate where the coupled model is stronger than the steady-state model. The yield strength of the lithosphere beneath the foreland wedge in the coupled model is up to 100 times stronger than in the steady-state model.

mentary basin and a thrust wedge developed between 550 to 700 km. Furthermore, lower crust and continental mantle in the orogen have been significantly removed by delamination. The temperatures in the crust continue to be overestimated in the steady-state model by more than 200 °C in a large region up to 500 km from the trench. Within the thrust wedge between 550 to 700 km, the temperatures are overestimated by more than 200 °C as well. The foreland temperatures further away than 700 km do not differ significantly from those in the coupled model.

3.2.3.1. Analysis of lithospheric strength

The temperature differences in the thrust wedge and foreland are the largest at the final time step. As the creep laws are sensitive to temperature, the largest strength differences between steady-state and transient occur at this time step.

The integrated strength between surface and 75 km depth in the coupled and steady-state model at 35 Myr (Fig. 3.11a) varies between 10^{12} Pa m in the Altiplano plateau, to about $1.5 \cdot 10^{13}$ Pa m in the undeformed foreland. Within the foreland, the integrated strength is about equal between both models, although the steady-state model is slightly stronger between 725 to 850 km trench distance. Between 200 to 550 km, in the area that represents the Altiplano plateau, the difference between both models is up to $\approx 2.5 \cdot 10^{12}$ Pa m. The largest strength differences occur within the thrust wedge, between 550 to 700 km, which are up to $\approx 8 \cdot 10^{12}$ Pa m.
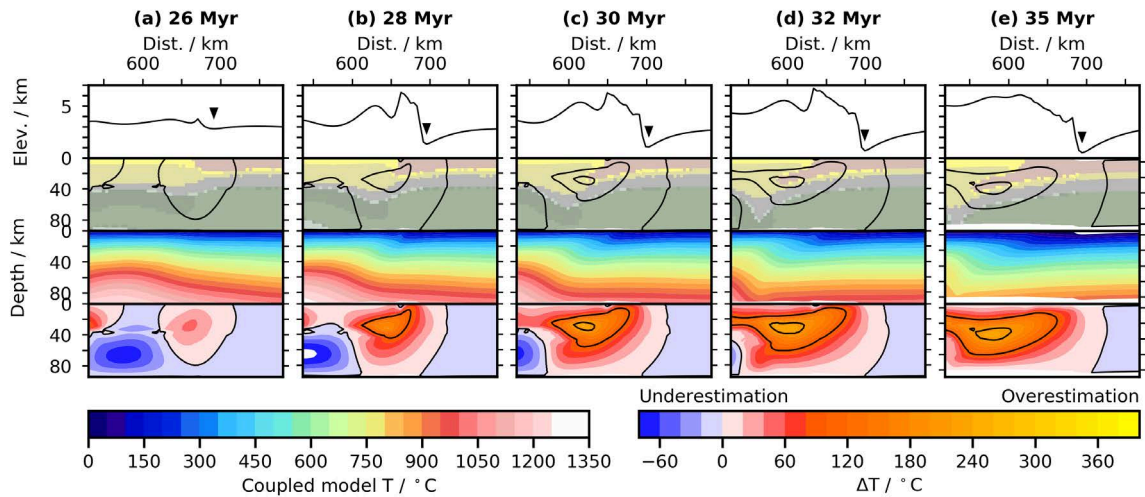
Figure 3.12.: Evolution of the thrust wedge and foredeep. First row plots the topographic elevation where the arrow marks the boundary between the orogenic wedge (left) and the foredeep (right). Distances are relative to the trench. The second row depicts the structure as in Fig. 3.10. Black contours indicate temperature difference in steps of 100 °C as plotted in the last row. Third row plots the absolute temperature in the coupled model. Last row shows the temperature difference between steady state model and coupled model. Blue colours indicate that the steady state model underestimates temperatures in this area. **(a)** 26 Myr; **(b)** 28 Myr; **(c)** 30 Myr; **(d)** 32 Myr; **(e)** 34 Myr.

Overall, the coupled model is characterised by a greater integrated strength in the uppermost 75 km of the lithosphere at 35 Myr.

The yield strength plots of the coupled (Fig. 3.11b) and steady-state model (Fig. 3.11c) show s similar characteristic pattern. The crystalline crust in the Central Andes, which is dominated by material with a 10-fold increased thermal conductivity (Fig. 3.10d), is weak ($< 200\,\text{MPa}$)in both models. The foreland lithosphere, on the other hand, is strong and reaches a peak strength of 800 MPa at the top of the lower crust. In both models, the underthrusted units of the Subandean sediments are well distinguished as a positive strength contrast with respect to the surrounding rocks. Due to the large variation in yield strength magnitude, I compared the relative yield strength between the coupled and steady-state model in Fig. 3.11d. The plot illustrates that the coupled model is up to 100 times stronger in the thrust wedge and the underlying continental crust. Similarly, the shallow crystalline crust in the plateau region of the coupled model is 10 to 100 times stronger as well.

3.2.4. Discussion

3.2.4.1. Cause for deviations between transient- and steady-state thermal fields

As expected, the results show that in actively deforming areas the steady-state model does not reproduce the temperatures of the coupled model. A more precise analysis of the evolution of the thermal field within the thrust wedge (Fig. 3.12), from initial thrusting at 26 Myr, to the final time step, reveals that the displacement of the isotherms is already distinct after 2 Myr of thrusting (Fig. 3.12b). This displacement in the thrust wedge is not reproduced in the steady-

state model, and temperatures are overestimated by up to 200 °C (t = 28 Myr, Fig. 3.12b) at 30 km depth, and 100 °C at 10 km depth. Whilst during progressive thrusting, the width and magnitude of the zone with overestimated temperatures grows, the peak of this zone remains constant at the lower tip of the wedge top, between depths of 30 to 40 km. Notably, during the whole evolution, the steady-state temperatures in the foredeep and forebulge provinces agree within ±20 °C with the transient thermal field of the coupled model.

The appearance of the step between orogenic wedge and foreland lithosphere suggests that diffusive time scale is greater than the advective time scale. To estimate the time that is required to obtain a steady-state in the foreland wedge, I utilise the characteristic time scale for diffusion. The characteristic time for diffusion is obtained by replacing the partial differentials in the heat equation with finite differences, and solving for the time Δt. In a 1D case, the characteristic time is expressed as

$$\Delta t = \left(\frac{\kappa}{\Delta x^2} + \frac{Q_R}{\rho_b C_p \Delta T} \right)^{-1} \tag{3.5}$$

where ρ_b is bulk rock density, C_p the bulk specific heat capacity, κ the thermal diffusivity, Q_R the radiogenic heat production and Δx a distance where a temperature difference ΔT is applied to. Radiogenic heat production is relevant for large Δx or small ΔT, and neglecting it provides an upper limit for the diffusive time scale (Fig. D.5a). In the foreland system of the coupled model, the thickness of the orogenic wedge is equivalent to Δx. The thrust wedge attains its maximum thickness of about 40 km at the final time step (Fig. 3.10d). At this time step, the wedge is characterised by temperature differences ΔT between the topography and its base of up to ≈ 600 °C. The corresponding characteristic time scale for such a setting is about 30 Myr (Fig. D.5a). This time scale is longer than the time of thrusting in the model (9 Myr), supporting that diffusion is not capable to re-equilibrate the thermal field in the continental lithosphere. Sobolev et al. (2006) also modelled dissipative processes, which could contribute to the observed differences. However, the subhorizontal isotherms to the east and west of the thrust zone suggest that there is no significant contribution to the thermal field by dissipation. Therefore, I conclude that the observed difference between steady-state and transient thermal field is attributed to heat advection by thrusting.

Based on this case study, the steady-state assumption can be assumed as valid in the foredeep, forebulge and backbulge provinces of retroarc foreland basins. Within the orogenic wedge, however, heat advection alters the transient thermal field in a manner that it cannot be reproduced in steady-state thermal models. Therefore, the steady-state assumption may not be applicable in such settings.

The 2D geometry of the models discussed in this chapter raises the question whether the results are transferable to a 3D scenario. Cacace and Scheck-Wenderoth (2016) pointed out that the transient thermal field of intracontinental basins, modelled in two dimensions, diverges from the field of equivalent 3D studies. In their study, the authors found that the sedimentary cover in their 3D models has a greater potential of retarding the cooling of the crystalline crust than in a complementary 2D model. Foreland basins, however, differ in their
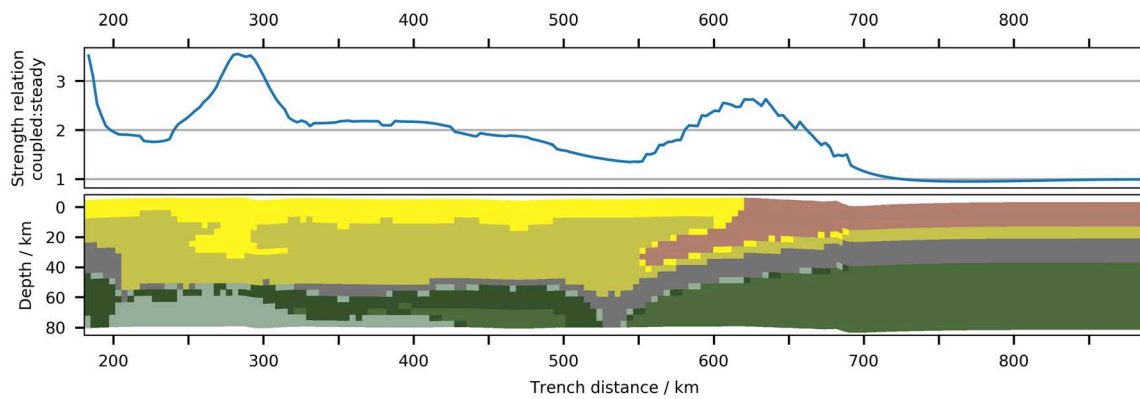
Figure 3.13.: Relation between integrated strength (Fig. 3.11) of the coupled model versus steady-state model at the last time step, along with a structural plot. Generally, the integrated strength of the coupled model is at least twice as large as in the steady-state model. The deviations are largest in areas where thrusting occurs. Only in the undeformed foreland, more than 700 km away from the trench, the strength estimates are approximately equal.

characteristics from intracontinental basins: foreland basins are elongated features running parallelly to their adjacent mountain belts whereas intracontinental basins are typically bowl-shaped. Furthermore, foreland basins generate accumulation space through the load of the advancing thrust wedge and associated sedimentation rather than by cooling of the underlying lithosphere and sedimentation. It is therefore necessary to direct more effort towards understanding how the steady-state thermal field in foreland basins differs from its transient state in three dimensions.

3.2.4.2. Implications of steady-state for the strength of the lithosphere

The integrated strength within the orogen is generally about two times larger in the transient coupled model compared to the steady-state model (Fig. 3.13). In areas with thrusting, especially in the orogenic wedge, the transient model is up to 3.5 times stronger.

Although the temperatures deviate significantly between the steady-state and the coupled model, the patterns of the strength distribution are comparable. In the central Andes, slight deviations are observed only in the shallow crystalline crust at depths of about 5 km bmsl. Figure 3.14a illustrates a yield strength envelope at a lateral distance of about 290 km from the trench, situated in the Andean Plateau. At this location, thrusting occurred in the upper crust (Fig. 3.10b-d), which resulted in an overall temperature depression down to 40 km depth. As the steady-state model cannot reproduce this feature, the difference in the integrated strength within the Andean Plateau is largest at this point (Fig. 3.11a). From the yield strength envelope it emerges that the bulk difference in integrated strength derives from a weakened uppermost crust as predicted by the steady-state model. The elevated temperatures in the steady-state model result in shallower activation of dislocation creep mechanisms. Below 25 km depth, the temperature differences, and hence strength differences, between the models are small. Although in the shallow crust the temperature differences between steady-
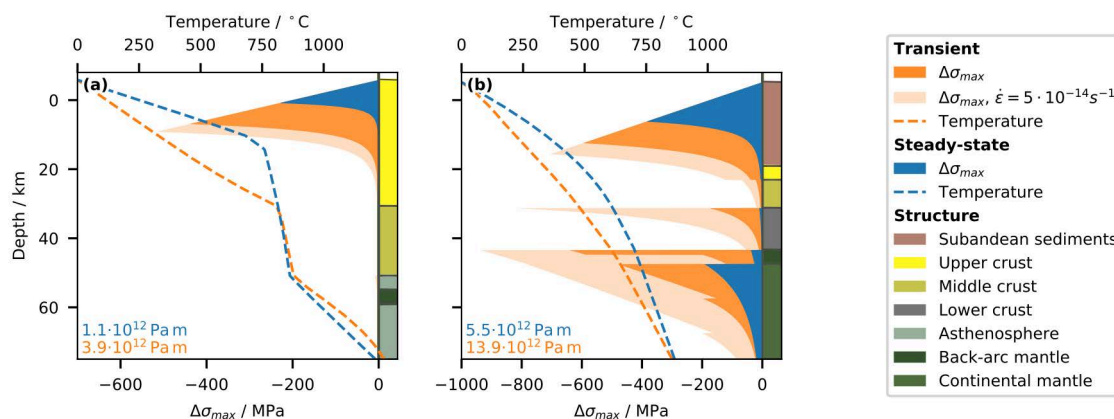
Figure 3.14.: Yield strength envelopes for compression at 35 Myr and **(a)** 290 km distance from the trench, representative for the Altiplano; **(b)** 640 km distance from the trench, in the thrust wedge, representative for the Eastern Cordillera. See Fig. 3.11a for locations. The coloured numbers in the lower left corner indicate the integrated strength for the appropriate profile.

state and coupled model are mostly larger than 150 °C (Fig. 3.10d), this difference does not alter the overall rheological characteristic of this area that can be described as the classical *crème brûlée* type model (Burov and Watts, 2006). This classification is robust also for a ten-fold increase of the strain rate (dotted line in Fig. 3.14a). However, the elastic thickness of the lithosphere changes significantly from 18.2 km in the coupled model to 9.6 km in the steady-state model (details on the computation of elastic thickness, see Appx. D.2).

At a first glance, these results suggest that under the given geometrical and physical configuration, rheological models, based on a steady-state conductive thermal field, will underestimate the crustal strength within the Central Andean plateaus. However, this outcome has to be taken with care as the temperature dependent conductivity implemented to mimic convective heat transport by magmatism (Eqn. 3.4, Tab. 3.4) effectively modifies the structural configuration of the model. This condition increases the zone of the high geothermal gradient that is associated to the high thermal conductivity (Fig. 3.10d, Fig. 3.14a). Thus, the temperatures of shallow crustal rocks less than 10 km bmsl are overestimated. I therefore assume that the observed strength difference marks the upper limit of possible variation.

The aforementioned limitation due to modified thermal conductivities is not relevant in the area of the thrust wedge, at lateral distances greater than 550 km from the trench (Fig. 3.10d). Thus, within this area I could derive better estimates on the potential impact of the steady-state assumption on strength estimates in the Central Andean foreland basins. Figure 3.14b plots the yield strength envelopes for the steady-state and coupled model in the centre of the thrust wedge, a position that is equivalent to the Eastern Cordillera. The yield strength envelope for the coupled model can be classified as *jelly sandwich* (Burov and Watts, 2006) with three decoupled layers. Although the yield strength envelope for the steady-state model also satisfies the *jelly sandwich* model, the amount of decoupled layers reduced to two. With an integrated strength of $13.9 \cdot 10^{12}$ Pa m, the lithosphere in the coupled model is about 2.2 times stronger than the lithosphere in the steady-state model ($5.5 \cdot 10^{12}$ Pa m). This is attributed to

the fact that the steady-state model overestimates the temperatures especially at those depths where dislocation creep is the dominant deformation process.

3.2.5. Conclusions

In this chapter I analysed how much a modelled steady-state conductive thermal field may deviate from its actual transient representation using a specific example of a 2D coupled model by Sobolev et al. (2006). This particular example stresses the importance of geodynamic processes on the state of the thermal field in convergent tectonic settings. It illustrates that mass transport, specifically the growth of the thrust wedge and associated flexural subsidence of the foredeep crust, is capable to significantly deviate the thermal field from its steady-state. This is evident although temperatures are below 1300 °C, the commonly assumed upper limit where conduction is thought to be the dominant heat transport mechanism. In this specific case, models that assume a steady-state conductive thermal field are influenced by mountain building processes as far as the foredeep. The foreland-facing parts of the foredeep, as well as the forebulge and more distal provinces of the foreland are not significantly influenced by these processes, i.e. steady-state can be assumed in retroarc foreland basins but not in the orogen. Overall, this analysis predicts that within the orogenic wedge the integrated lithospheric strength derived from steady-state thermal models might be two to three times below the actual integrated strength.

Although the lithosphere in the coupled model is up to 3.5 times stronger compared to the corresponding steady-state, the yield strength contrasts did not differ significantly. In both, steady-state and coupled models, the stratification in the orogen classifies as *crème brûlée*, and the foreland as *jelly sandwich* type models.

Further effort is required to fully understand the error magnitude introduced in the application of the steady-state assumption in dynamic settings. First, the temperature dependent thermal conductivity in the studied model effectively modifies the physical and therefore structural configuration of the steady-state model. This modification impedes the interpretation of the study results in the orogen. Therefore, models with higher resolution should be computed in order properly image intracrustal melt movement. Second, erosion and sedimentation alter the isostatic response of the plate and modify the thermal field. The role these processes play with respect to steady-state thermal fields needs to be further analysed. Third, the transferability of the results to the 3D cases may be difficult due to the 2D model geometry. Thus, by studying the 3D transient and steady-state thermal field, it should be possible to determine whether or not is is correct to assume thermal steady-state conditions in a retroarc foreland basin.

4. The present-day thermal and rheological state of the Chaco-Paraná basin

The outcomes of the previous chapters provide the basis for the assessment of the rheological state of the lithosphere in northern Argentina. In this chapter, I aim to analyse the steady-state thermal field of the CPB and assess the impact on the rheological state of the lithosphere. Since the sparse data availability in northern Argentina does not allow to constrain a unique thermal lower boundary condition, I analyse two scenarios of this lower boundary condition. Therefore, I selected two temperature slices at a constant depth in the uppermost lithospheric mantle that were derived from tomographic shear-wave velocity models (Chapter 2.1). The temperatures were obtained assuming a mineral assemblage for the lithospheric mantle following the approach by Goes et al. (2000) and the code published in Meeßen (2017). One of the scenarios depicts large lateral temperature variation, whereas the other one predicts rather uniform temperatures in the upper lithospheric mantle. With these lower boundary conditions, I can predict possible ranges of steady-state conductive thermal fields, and use those to estimate the rheological stratification of the lithosphere.

4.1. Introduction

In the introduction I addressed the question about the controlling factors of the thin- and thick-skinned deformation styles in the northern Argentinian foreland basins. The assessment of the internal density structure in Chapter 2, together with the analysis of how geodynamic processes affect the retroarc thermal field in Chapter 3, enables to assess the rheological characteristics of the Chaco-Paraná foreland basin.

Therefore, the conductive steady-state thermal field must be estimated and rheological characteristics of the lithosphere throughout the model domain. Generally, for the compilation and assessment of the conductive thermal model I require data on the thermal boundary conditions as well as independent temperature data for the model verification. Both, boundary conditions and data for verification, are problematic in the modelling area.

The upper boundary condition is commonly defined as the long-term averaged surface temperature of the modelled region, which is available from global datasets. The lower boundary, however, is often taken as the depth to the LAB, respective the 1300 to 1350 °C isotherm, see Chapter 3.1.2.3, because at greater depths convection is the dominant heat transport (e.g. Eaton et al., 2009). Some data on the LAB depth was acquired using S receiver functions in the central Andes by Heit et al. (2007) and Heit et al. (2014), as well as in southern Paraguay

and the the province Buenos Aires, Argentina (Heit et al., 2007). First, these data are sparse and do not cover the model area. Second, the vertical accuracy of S receiver functions is low and requires additional constraints on the vertical velocity structure (Eaton et al., 2009). Third, mantle convection in the corner between the subducting Nazca plate and the South American plate distorts isotherms both in cases of "normal" subduction and "flat-slab" subduction (Abers et al., 2006; Hall, 2012; Marot et al., 2014). Fourth, the LAB depth estimates do not agree with temperature estimates derived from tomographic shear wave models. These four main problems impede the mere interpolation of the available data to a consistent and continuous lower boundary condition. Thus, the definition of the lower boundary condition in the modelling area is non-trivial and cannot be solved with sufficient accuracy. Additionally, data to verify the thermal field from well data is not available in Northern Argentina.

Due to the above circumstances, I aimed to analyse two different thermal models that allow to delimit possible magnitudes of strength variation in the CPB. Therefore, I utilised the temperature distributions obtained from seismic tomography in Chapter 2.1 as lower boundary conditions. Note that these lower boundary conditions are slices at constant depths in the upper lithospheric mantle that do not represent the LAB. I selected the tomographic models *aVs_2013_Tecto* (Assumpção et al., 2013) and *3D2016_03Sv* (Debayle et al., 2016) to obtain the lower boundary condition. The model by Assumpção et al. (2013), dubbed *Assumpção*, represents an scenario with strong lateral temperature variations in the upper mantle. Accordingly, the mantle temperatures are characterised by pronounced high temperatures below the northern foreland between 22–27°S, and cold temperatures south of 27°S. The other model (Debayle et al., 2016) depicts a scenario with less pronounced lateral temperature variations, is represented by the model of. This model is characterised by much smaller lateral gradients and is referred to as *Debayle*.

4.2. Setup of the thermal and rheological model

I used the model results of the gravity inversion in Chapter 2.1 with minor modifications to the configuration of the upper crystalline crust. The inverted average crustal density indicates that to the west of the Transbrazilian Lineament, the crust is characterised by a rather felsic rheology (Fig. 2.6a). This is supported by average v_p between 5.8 to 6.0 km s^{-1} and v_p/v_s ratios below 1.75 (Alvarado et al., 2009). Felsic rocks differ in their thermal properties from mafic rocks (Vilà et al., 2010). I therefore subdivide the upper crust of the model area along the Transbrazilian Lineament suggested by Ramos et al. (2010) and supported by Meeßen et al. (2018) (Fig. 2.1) into a more felsic domain, the Pampia terrane, and into the more mafic Río de la Plata craton. Finally, I cut the model at a constant depth of ≈ 100 km, the depth where the temperature maps were obtained (Fig. 2.7).

The structural model was populated with properties and compiled using the in-house GFZ software *Geo Modelling System* (*GMS*) and stored in a regular structured mesh format. This structural model was then used to compute the steady-state conductive thermal field in *GOLEM* (Cacace and Jacquey, 2017; Jacquey and Cacace, 2017). Due to the structured mesh

geometry, computed temperatures are stored on the layer interfaces. Since geotherms inside bodies with radiogenic heat production are not linear but curved, temperature-dependent creep processes would not be correctly represented if temperatures are stored only on the layer interfaces. Therefore, I vertically refined each body by a factor of 5 to 10 (Tab. 4.2) in *GMS* before computing the steady-state thermal field in *GOLEM*. This ensures that temperatures can be reasonably well approximated by linear interpolation in between the surfaces for the computation of the rheology. The rheology was computed and visualised in *pyGMS*, a Python 3.7 module written for this study (Meeßen, 2019b).

4.2.1. Governing equations and thermal boundary conditions

The 3D steady-state conductive thermal field was computed using Fourier's law of heat conduction (e.g. Turcotte and Schubert, 2014):

$$0 = -\nabla \left(\lambda \cdot \nabla T \right) + Q_R \tag{4.1}$$

where λ is the bulk thermal conductivity and Q_R is the radiogenic heat production. I applied Dirichlet boundary conditions to the surface and the lower boundary of the model. At the surface, the Dirichlet boundary condition is set to the mean annual surface temperature from 1961 to 1990 (Fig. 4.1a) by New et al. (2002). At the lower boundary, I applied the temperatures that were obtained in Chapter 2.1.2.3.3 for the upper lithospheric mantle (Fig. 4.1).

The lithospheric strength was computed using a strain rate of $5 \cdot 10^{-16} \text{s}^{-1}$, following the procedure described in Appendix D.1.

4.2.2. Thermal and rheological parametrisation

I parametrised the individual bodies of the models according to their prevailing lithological characteristics. The sedimentary infill of the CPB is predominantly sandstone and siliciclastic material (Chapter 2.1.1.1), with the average density of 2440 kg m^{-3}. The thermal conductivity of sandstone depends on the rock density and corresponding to the modelled density, I used $2.1 \text{ W m}^{-1} \text{ K}^{-1}$ (Cermak et al., 1982). The radiogenic heat production, 0.9 µW m^{-3}, is an average value for sandstones Vilà et al. (2010). The type rheology was chosen in accordance with Sobolev et al. (2006) and the rheology used in Chapter 3.2.

Wells that reached the basement of the Río de la Plata craton predominantly encountered mafic rocks (Fig. 2.1; Rapela et al., 2007; Winn Jr and Steinmetz, 1998). The lithologies of the encountered basements were gabbros, granodiorites, norites (Winn Jr and Steinmetz, 1998) and olivine-gabbros (Rapela et al., 2007). Table 4.1 lists the range of thermal properties of the encountered lithologies. I assigned a thermal conductivity of $2.5 \text{ W m}^{-1} \text{ K}^{-1}$ which corresponds to gabbro or norite. The radiogenic heat production of 0.5 µW m^{-3} is taken in order to account for the presence of the slightly more silicic granodiorites. As type rheology I assigned dry diabase (Carter and Tsenn, 1987; Sippel et al., 2017).

For the Pampia terrane, Alvarado et al. (2009) reported average crustal v_p between 5.8
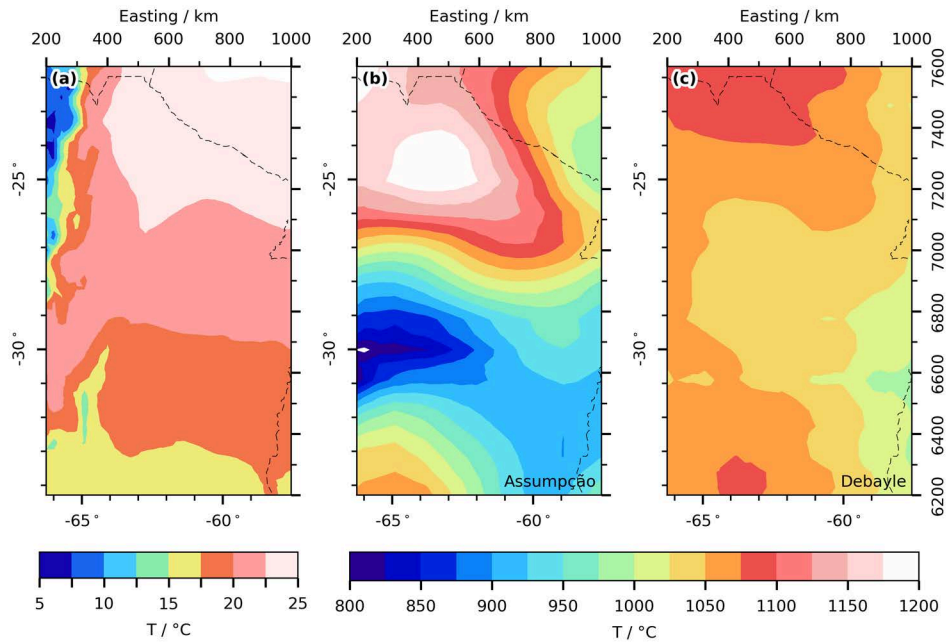
Figure 4.1.: Thermal boundary conditions to compute the steady-state conductive thermal field. **(a)** upper thermal boundary condition, the 60-year mean annual surface temperature (New et al., 2002); **(b)** lower boundary condition at 102 km depth for the high-enthalpy model, temperatures obtained from conversion of the *Assumpção* model by Assumpção et al. (2013); **(c)** lower boundary condition at 102 km for the low-enthalpy model, converted from the model *Debayle* by Debayle et al. (2016).

Table 4.1.: Thermal properties of rock types found in the upper crust of the study area.

Pampia terrane			Río de la Plata craton		
Rock type	λ W m^{-1} K^{-1}	Q_R µW m^{-3}	Rock type	λ W m^{-1} K^{-1}	Q_R µW m^{-3}
Quartzite	3.0–8.7 [a,c]	0.8 [a]	Gabbro	2.6 [a]	0.3 [a]
Gneiss	2.4 [a]	1.9 [a]	Olivine-gabbro	1.9 [a]	-
Granite-gneiss	3.0 [a]	0.4-3.3 [a]	Granodiorite	2.7 [a]	1.7 [a]
Schist	3.1 [a]	1.5 [a]	Norite	2.7 [a]	0.1 [a]
L/M metamorphic	-	1.7 [b]			
L/M igneous	-	1.3 [b]			
L/M metasediment	-	2.0 [b]			
H metamorphic	-	1.5 [b]			

[a] Cermak et al. (1982) [b] Vilà et al. (2010) [c] Davis et al. (2007). L/M = low to medium grad metamorphism, H = high-grade metamorphism.

Table 4.2.: Thermal and rheological properties used for the computation of the steady-state conductive thermal field and the lithospheric strength.

Property	Unit	Sediments	Río de la Plata craton	Pampia terrane	Lower crust	Lithospheric mantle
λ	$\mathrm{W\,m^{-1}\,K^{-1}}$	2.1	2.5	3.1	2.0	3.0
Q_R	$\mathrm{\mu W\,m^{-3}}$	0.9	0.5	1.5	0.15	0.01
Type rheology		Quartzite, wet [a]	Diabase, dry [b]	Quartzite, wet [a]	Plagioclase, wet [c]	Peridotite, dry [d]
ρ	$\mathrm{kg\,m^{-3}}$	2440	2800	2800	3100	3300
n		4.0	3.05	4.0	3.0	3.5
A_P	$\mathrm{Pa^{-n}\,s^{-1}}$	$1\cdot10^{-28}$	$6.31\cdot10^{-20}$	$1\cdot10^{-28}$	$4\cdot10^{-16}$	$5\cdot10^{-15}$
Q_P	$\mathrm{kJ\,mol^{-1}}$	223.0	276.0	223.0	356.0	535.0
Refinement		5	10	10	10	10

For all units $f_f = 3.0$ and $f_p = 0.35$ [a] Gleason and Tullis (1995)   [b] Carter and Tsenn (1987) [c] Rybacki and Dresen (2000)   [d] Hirth and Kohlstedt (2004).

to $6\,\mathrm{km\,s^{-1}}$ and v_p/v_s less than 1.75. According to the authors, these values correspond to more felsic crustal lithologies. After Christensen and Mooney (1995), the observed average velocities may correspond to quartzite ($5.9\,\mathrm{km\,s^{-1}}$) or granite-gneiss ($6.1\,\mathrm{km\,s^{-1}}$) at a depth of 20 km. Furthermore, the basement outcrops in the Sierras de Córdoba are dominated by felsic rock types, including gneisses, schists, as well as granitic and tonalitic intrusions (Martino, 2003; Perarnau et al., 2012, and references therein). Although average crustal velocities suggest quartzite as the dominant rheology, the wide range and overall high values for thermal conductivity (Tab. 4.1) appear inappropriate with respect to the variety of lithologies outcropping in the Sierras de Córdoba. I therefore assigned a thermal conductivity of $3.1\,\mathrm{W\,m^{-1}\,K^{-1}}$, a value respecting the quartzitic components but also also agrees with the values of schists and granite-gneisses. Given the observed lithologies, radiogenic heat production may vary between 0.8 to $3.3\,\mathrm{\mu W\,m^{-3}}$. Regarding the metamorphic grade of the rocks, the compilation by Vilà et al. (2010) suggests values between 1.3 to $2.0\,\mathrm{\mu W\,m^{-3}}$. Accordingly, I assigned a value of $1.5\,\mathrm{\mu W\,m^{-3}}$ to the upper crust of the Pampia terrane. In agreement with the properties of the upper crust in Sobolev et al. (2006) and the model in Chapter 3.2, I prescribed wet quartzite as the type rheology.

The nature of the lower crust is, apart from its density of $3100\,\mathrm{kg\,m^{-3}}$, not precisely determined. Based on the high density, I assumed mafic granulites as the representative lithological type. These rocks are characterised by an average thermal conductivity of $2.0\,\mathrm{W\,m^{-1}\,K^{-1}}$ (Cermak et al., 1982) and radiogenic heat production of $0.15\,\mathrm{\mu W\,m^{-3}}$ (Vilà et al., 2010). The type rheology of wet plagioclase for the lower crust was adopted from Chapter 3.2.

The thermal conductivity of the lithospheric mantle, $3.0\,\mathrm{W\,m^{-1}\,K^{-1}}$, was taken from McKenzie et al. (2005), and the radiogenic heat production of $0.01\,\mathrm{\mu W\,m^{-3}}$ from Vilà et al. (2010). As type rheology, dry peridotite was taken from the appropriate model in Chapter 3.2, regarding Dorn's Law for σ_b greater than 200 MPa.
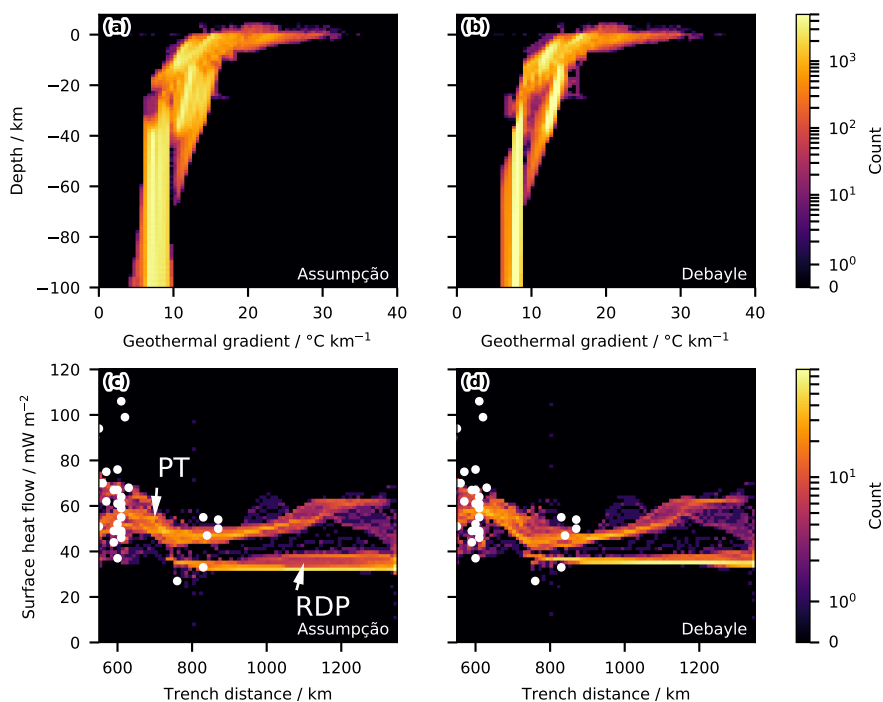
Figure 4.2.: Geothermal gradients and surface heat flow of the models. Upper panels: Kernel density plots of the geothermal gradients in every cell ($25\,\text{km} \times 25\,\text{km}$) of the models for **(a)** *Assumpção*; **(b)** *Debayle*. Lower panels: Kernel density plots of computed surface heat flow plotted against distance from the Nazca plate trench. White dots are surface heat flow measurements in South America (Hamza and Muñoz, 1996; Uyeda and Watanabe, 1982), see Figs. 3.5 and 3.6a. The Pampia terrane (PT) has a generally higher surface heat flow than the Río de la Plata craton (RDP); **(c)** *Assumpção*, **(d)** *Debayle*.

4.3. Results

4.3.1. End-member thermal fields of the Chaco-Paraná basin

As a first proxy for the geothermal field I computed the geothermal gradients in the model. Each individual gradient was computed for 1000 equally spaced points between the surface and the base of the model. This procedure was repeated for each grid cell on the model surface, i.e. for a rectangular point grid with a lateral spacing of 25 km. Figure 4.2a and b show kernel density plots for the geothermal gradients plotted against depth in model *Assumpção* and *Debayle* respectively. In both models, the gradients at shallow depths range between 20 to $35\,°\text{C}\,\text{km}^{-1}$, and decrease to 5 to $10\,°\text{C}\,\text{km}^{-1}$ for depths greater than 60 km.

Both models do not significantly differ in the computed surface heat flow (Fig. 4.2c,d). Due to the higher upper crustal thermal conductivity (Tab. 4.2), the Pampia terrane is characterized by higher overall surface heat flow (40 - $60\,\text{mW}\,\text{m}^{-2}$) than the Río de la Plata craton (35 - $40\,\text{mW}\,\text{m}^{-2}$). The heat flow was computed for the uppermost geothermal gradient value of the geotherms described above. Surface heat flow measurements for the modelling area were not available. Therefore I compared the data to the measurements of South America (Hamza and Muñoz, 1996; Uyeda and Watanabe, 1982) with distances relative to the pacific plate trench
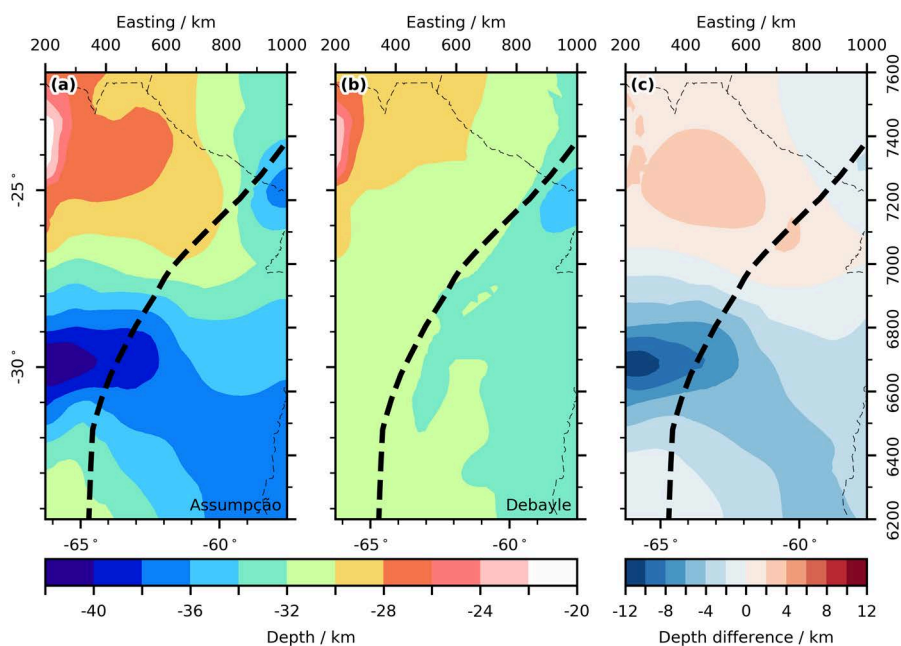
Figure 4.3.: Depth to the 450 °C isotherms for **(a)** model *Assumpção*; **(b)** model *Debayle*; **(c)** difference *Assumpção-Debayle*.

(Fig. 3.6, p. 72). The computed surface heat flow does not significantly deviate from the values observed across the South American continent.

I characterised the effect of the different lower boundary conditions on the thermal field by analysing the depth to the 450 °C isotherm. This isotherm has been suggested by Chen and Molnar (1983) as the lower bound for seismicity in continental interiors and is often used as a proxy for the brittle-ductile transition in the continental crust (e.g. Fujinawa et al., 1999; Mall and Sharma, 2009; Olsen, 1995; Simpson, 2001). As this isotherm is roughly centred in between the upper and lower temperature bounds of the model, its depth distribution is a good proxy for the overall thermal field.

The depth to the 450 °C isotherm in the model *Assumpção* (Fig. 4.3a) is characterised by a large gradient from north to south. North of 27°S the isotherm is less than 30 km deep, with the shallowest values situated north of 25°S, where it reaches depths less than 22 km. Around 30°S the depth is largest with up to 42 km at the western boundary of the model. In comparison, the 450 °C isotherm in the model *Debayle* (Fig. 4.3b) exhibits weaker horizontal gradients and is slightly tilted towards east-south-east. Only in the northwestern area, north of 25°S, it reaches up to 22 km depth. Overall, the difference between both isotherms (Fig. 4.3c) is less than 4 km north of 27°S, but up to 12 km around 30°S.

4.3.2. Implications for the lithospheric strength

I computed the strength of the lithosphere under compression for the given strain rate of $5 \cdot 10^{-16} \, \mathrm{s}^{-1}$ (details see Appendix D.1), and analysed both the integrated lithospheric strength and yield-strength profiles through areas of of thin-skinned and thick-skinned deformational
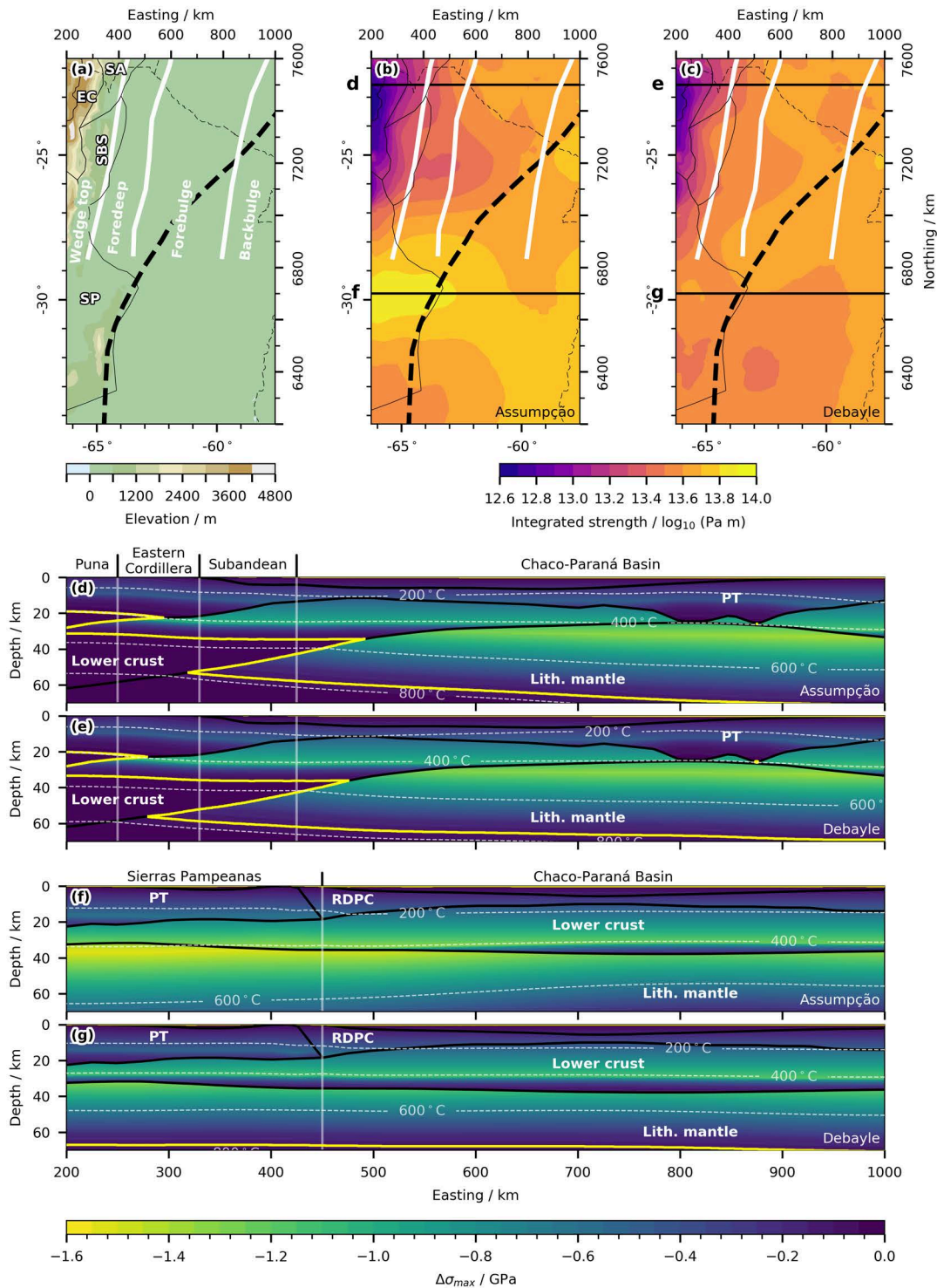
Figure 4.4.: Resoluts of the rheological models for the study area. **(a)** Morphotectonic (Jordan et al., 1983) and flexural (Menegazzo et al., 2016) provinces in the study area, bold black dashed line is the Transbrasilian Lineament (Meeßen et al., 2018; Ramos et al., 2010) that separates the Río de la Plata craton (RDPC) from the Pampia terrane (PT); **(b)** integrated lithospheric strength model *Assumpção* (Fig. 4.1b); **(c)** integrated lithospheric strength for model *Debayle* (Fig. 4.1c); **(d − g)** show yield strength profiles through locations depicted in (b) and (c). Dashed white lines indicate temperature in steps of 200 °C, the yellow lines indicate the limits of mechanically competent bodies (Appx. D.2).

styles. Effects due to flexural stresses were neglected in this study. Such stresses are relevant in areas where plate curvature is high, which is particularly the case in the forebulge and the backbulge provinces of retroarc foreland basins. The locus of these provinces in northern Argentina is still a matter of debate (e.g. Menegazzo et al., 2016), which hampers estimates on flexural stresses. However, beneath the orogenic wedge and the foredeep the flexure of the plate should be small and have little impact on the results.

The lithosphere in both models *Assumpção* (Fig. 4.4b), and *Debayle* (Fig. 4.4c) is weakest below the Eastern Cordillera and Puna-Plateau. Within these provinces, the integrated strengths is below $13 \log_{10}(\text{Pa m})$, being slightly weaker in model *Assumpção* than in *Debayle*.

The locations of the strongest areas in the lithosphere, however, differ between the two endmembers. In model *Debayle*, the lithosphere is strongest in the eastern part of the study area, and along the Transbrazilian Lineament east of 64°W (Fig. 4.4c). Along the Transbrazilian Lineament, the Moho has an anticlinal geometry (Fig. 2.2c, p. 11), that results in significant contribution to the lithospheric strength by the upper mantle. In the other model, *Assumpção*, the strongest domain is situated in the Sierras Pampeanas, between 31 to 29°S. Here, the lithospheric mantle is cold and strong due to a lower boundary condition that is below 900 °C (Fig. 4.1b).

To gain information on the vertical strength distribution, brittle-ductile transitions and coupling, I analysed two yield strength envelope profiles located in the thin-skinned and thick-skinned provinces of the model area. The profiles in Fig. 4.4d and Fig. 4.4e are situated in the northern CPB, crossing the thin-skinned Subandean fold-and-thrust belt. For the given configuration it emerges that the 400 °C and the 250 °C isotherms correspond to the peak-strength, i.e. the brittle-ductile transition, in the lower and upper crust, respectively. Although the temperature at the lower boundary condition beneath the Puna to Subandean provinces is about 100 °C warmer in *Assumpção* compared to *Debayle* (Fig. 4.1b,c), the thermal field in the crystalline crust does not significantly differ between both models (compare also isotherm depths in Fig. 4.4d, e). Accordingly, the predictions of the vertical yield strength distribution beneath these provinces do not diverge much between the two models, although the lithospheric mantle is slightly stronger in *Debayle*. The models predict that the rheological stratification beneath the Puna and Eastern Cordillera correspond to a *crème brûlée* model (Burov and Watts, 2006). Together with an eastward rising Moho, the lithospheric mantle increasingly dominates the strength profile, and a two-layered *jelly sandwich* (Burov and Watts, 2006) establishes in the Subandean ranges. The stratification within the northern CPB is dominated by a fully coupled, competent lithosphere up to 60 km depth..

The yield strength profiles at about 30°S (Fig. 4.4f,g) are crossing the strongest areas of the Sierras Pampeanas. In model *Debayle*, the lower crust is ductile at the Moho, whereas in *Assumpção* it behaves brittle beneath the Pampia terrane and ductile beneath the Río de la Plata craton. Despite these differences, crust and lithospheric mantle are fully coupled in both models and both models therefore predict a *jelly sandwich* type rheology in the Sierras Pampeanas and the adjacent CPB.

4.4. Discussion

Validation of thermal models is usually performed by comparing model-independent data, e.g. borehole temperatures and/or surface flow measurements, with the corresponding results of the model. These data are not accessible in the model area and a validation of the results is therefore difficult. However, it is possible to check the results for plausibility by analysing the complete sets of geothermal gradients and computed surface heat flow (Fig. 4.2). Neither geothermal gradients nor the computed surface heat flow significantly deviate from values that would be expected in a foreland basin (Allen and Allen, 2013; Hamza and Muñoz, 1996; Uyeda and Watanabe, 1982). Therefore, both models are possible representations of the thermal field. Further verification on the model, in terms of temperature and structure, could be achieved by comparing earthquake focal depths with the rheological structure of the model.

Although the end-member models are characterised by significant differences in the lower thermal boundary condition, up to 100 °C in the north, and 250 °C in the south, the resulting thermal fields agree well in the northern part of the model area. Only in the southern section, the thermal fields differ significantly, with up to 10 km difference in the 450 °C isotherm. The corresponding integrated strength maps (Fig. 4.4b,c) reflect the thermal configuration. It is important to note that the strength is likely overestimated in the forebulge and backbulge zones (Fig. 4.4b,d). Within these zones, the differential stress distribution is reduced due alteration in the vertical stress distribution as a result of the flexural deflection of the lithosphere (Burov and Diament, 1995).

4.4.1. Relation between rheology and surface deformation

In the thin-skinned foreland, the models predict a *crème brûlée* in the orogen and the orogenic wedge, that transitions into a fully coupled *jelly sandwich* in the CPB. The fully coupled rheology and high yield strength (>1 GPa) of the CPB lithosphere does not allow the localisation of new faults by externally applied tectonic stresses that reach values of only 100 to 600 MPa (e.g. Burov, 2011; Cloetingh and Wortel, 1986; Molnar and Lyon-Caen, 1988). Therefore, the observed shortening must be accommodated along fault zones within the orogen or the orogenic wedge. Here, the ductile sections of the crystalline crust (Fig. 4.4d,e and Fig. 4.5a) allow the development of shear zones that connect via transfer faults to the décollements in the fold-and-thrust belts. The locus of these transfer faults might be influenced by inherited weak zones such as foliation or crustal scale discontinuities (Fig. 4.5a). Since deformation may distribute over a wider area if the CPB lithosphere would be a weak *crème brûlée*, I suggest, that thin-skinned deformation requires a strong lithosphere in continental foreland and weak lithosphere in the orogen. This hypothesis agrees with the model for thin-skinned deformation as proposed by Mouthereau et al. (2013). Moreover, we observed the same conditions in a gravity-constrained 3D geodynamic model of the central Andes and the foreland in **ibarra_3d_inreview**. Here, we found that surface deformation predominantly occurs where the lithospheric strength gradients are largest which is particularly the case when a *crème brûlée* stratification changes to a *jelly sandwich*.
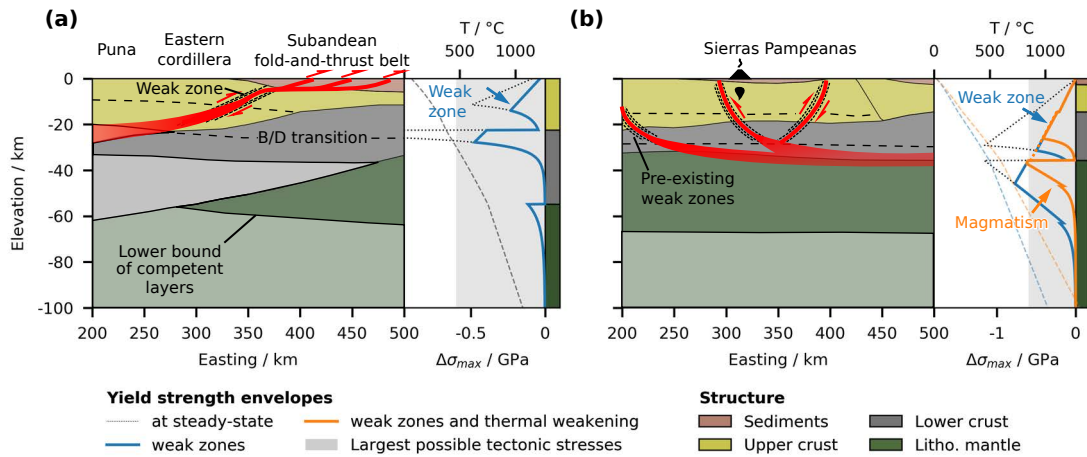
Figure 4.5.: Interpretation relating surface deformation to the rheological structure of northern Argentina. **(a)** interpretation for the Subandean fold-and-thrust belt where shear-zones evolve within weak decoupled mid-crustal layers. The décollements of the Subandean thrust belts may be connected to those shear zones via reverse faults that developed within inherited weak zones; **(b)** interpretation for the Sierras Pampeanas. Due to full coupling, deformation can most easily be accommodated by reactivating pre-existing weak zones. Such weak zones ($f_f = 0.8$ in this example), however, might not be sufficient to lower differential stresses to reactivate the weak zones. Additional magmatism (here linear increase with $100\,°C$ at the Moho) could further decrease the yield strength and result in the reactivation of the weak zones.

Thick-skinned deformation, in contrast to thin-skinned deformation, is thought to be primarily related to pre-existing, high-angle weak zones within the crust. The existence of such weak zones are well documented in the Sierras Pampeanas in terms of sutures. There is consensus that these sutures are being reactivated and act as interfaces along which basement blocks are uplifted (e.g. Ramos, 1988; Ramos et al., 2002). These high-angle crustal-scale discontinuities are thought to be rooted in subhorizontal shear zones at mid- to lower crustal depths; Perarnau et al. (2012) found evidence that these shear zones might juxtapose the Moho, therefore potentially reaching to even greater depths. As the CPB lithosphere further north, coupling and differential stresses up to $1.6\,GPa$ in the Sierras Pampeanas, let the lithosphere sustain high applied stresses without creating new faults. The sutures might therefore be the key factors that weaken the lithosphere in a manner that they can be reactivated by tectonic forces. Although the lithosphere is coupled in the thick-skinned foreland, ductile sections within the crystalline crust of the Pampia terrane and Río de la Plata craton (Fig. 4.5b) may then provide the space for subhorizontal detachments. Assuming a Byerlee friction coefficient of 0.8 for these sutures (derivation see Appendix D.1; Behnsen and Faulkner, 2012; Behr and Platt, 2014), the yield strength within narrow zones could indeed be significantly reduced (Fig. 4.5b). The resulting reduced yield strength envelope in this example still represents a coupled lithosphere, and the mantle is still capable to sustain differential stresses greater than $600\,MPa$. Given that the chosen friction coefficient is at the lower end of what is thought to be possible, the sutures likely do not weaken the lithosphere sufficiently for a reactivation – particularly at greater depth where increasing temperatures and pressures allow the healing of fractures.

Ramos et al. (2002) reported a spatio-temporal correlation between magmatism and basement block uplift in the Sierras Pampeanas. The authors found that several uplift events occurred within 4.0 to 2.6 Myr after the occurrence of magmatism in the foreland. If magmatism occurs in proximity to a weak zone, the temperature increase in the surrounding lithosphere could have additionally weakened the rock (Fig. 4.5b). Rothstein and Manning (2003), however, showed that the impact of instantaneous plutonism on the geothermal field is laterally restricted to within less than 20 km. Accounting that the volcanism reported by Ramos et al. (2002) might be of smaller scale in the subsurface than plutonism, this implies that magmatic intrusions must occur along or in the direct vicinity of the crustal weak zones in order to reactivate them. The friction coefficient of the crustal discontinuities might be further lowered by fluids that could be released during the cooling of the residual magmatic bodies, and that lubricate the preexisting weak zones. Both, the heating of the ambient rocks and the release of lubricating fluids are delayed with respect to the volcanism which may explain the dilation between volcanism and basement uplift that had been reported by Ramos et al. (2002). Whether the mechanisms proposed here are able to explain the thick-skinned tectonics and a delay between volcanism an uplift, should be the topic of further investigations.

The hypotheses I suggest here, relating lithospheric rheology and surface deformation, agree well with the results of coupled numerical models by Cloetingh et al. (1999): the authors inferred that the wavelength of folding and faulting of lithosphere under compression depends on thicknesses of the competent and weak layers. In their numerical models, a *crème brûlée* stratification generated small scale folds and faults, whereas *jelly sandwich* models generated larger undulations. The rheological models presented here provide data-based evidence that the lithosphere deforms by thin-skinned style of deformation in the presence of a *crème brûlée* stratification. In contrast, thick-skinned deformation occurs if the underlying lithosphere is characterised by an overall strong *jelly sandwich* stratification.

4.5. Conclusion

In this chapter I discussed two possible thermal fields and their implications on the rheological stratification of the lithosphere. The steady-state conductive thermal fields were computed using different lower boundary conditions that were obtained from two shear-wave velocity models. Despite the fact that the thermal models could not be validated using independent measurements, the observed ranges of the geothermal gradients and surface heat flow classify the geothermal fields as potential representations of the present-day steady-state thermal field in the study area.

The rheological analysis indicates that the lithosphere at latitudes of the Sierras Pampeanas is fully coupled and could withstand differential stresses greater than 1.5 GPa. Such stress magnitudes are probably not reached within the lithosphere. Inherited weak zones, as suggested by many studies, therefore play a key role in the accommodation of shortening as their reactivation requires less stress than faulting of the crust. However, my results suggest that these discontinuities are not be able to sufficiently weaken the generally strong and fully

coupled lithosphere in the Sierras Pampeanas. Hence, I suggest that magmatism in the Sierras Pampeanas is the decisive process that allows the reactivation of inherited weak zones primarily by thermal weakening the crustal-scale discontinuities. In order to cause a weakening, this magmatism has to occur in direct vicinity of these discontinuities. The ductile lower crust beneath the Río de la Plata craton, and possibly also beneath most of the Sierras Pampeanas, might provide a locus for subhorizontal detachments that connect to the high-angle faults at shallower crustal levels.

Towards the northern study area, these ductile zones disappear in the east due to the rising Moho. Beneath the Puna and the Subandean ranges, my models predict a *crème brûlée* type of stratification that transitions into a fully coupled *jelly sandwich* towards the CPB. The decoupled upper crust beneath the Puna and Eastern cordillera allows for the localisation of a detachment at mid- and lower-crustal levels. Via transfer faults within the upper crystalline crust, deformation is transferred towards the décollement surface of the Subandean fold-and-thrust belt.

Due to the scarce data coverage, I suggest to direct further efforts into the analysis of the present-day rheological state. These efforts should include the verification of the thermal field, e.g. with borehole data and focal depths, and a better structural model. The latter would benefit from receiver functions better depicting the structure of the crystalline crust in northwestern Argentina, especially at the transition between the Subandean ranges and the foreland.

5. Discussion

## 5.1. Impact of the steady-state assumption on the strength estimates

In Chapter 3.2, I concluded that models that assume a steady-state conductive thermal field may overestimate temperatures in the wedge top and foredeep by up to 200 °C. I utilise these results to obtain an estimated transient thermal field that is based on the steady-state thermal field computed in Chapter 4. Therefore, I reduced the temperature in particular 1D profiles of the steady-state model by an amount that was predicted at the final time step in corresponding regions of the 2D model (Fig. 3.12e, p. 83). This yields a "corrected" geotherm that aims at representing the present-day transient thermal field, and that I use to obtain a better estimate of the rheological behaviour.

The Subandean ranges constitute the wedge top of the thin-skinned foreland. At a position equivalent to the wedge top in the 2D study (see Fig. D.6, p. 147), the temperatures between transient and steady-state diverge by up to 90 °C at 20 km depth (Fig. 5.1a). The corresponding yield strength envelopes (Fig. 5.1b) illustrate that the corrected model is stronger, and that the ductile part of the upper crust is now brittle. In the Subandes, the rheological estimate of the steady-state model should therefore be robust with respect to the processes studied in Chapter 3.2.

At locations equivalent to the Puna and Eastern Cordillera in the 2D model (Fig. D.6), the estimated transient thermal state is about 200°C cooler at depths between 20 to 40 km. Accordingly, the strength of the crystalline crust is significantly affected, which results in a stronger coupling between upper and lower crust (Fig. D.6b,d). The estimate for the Eastern Cordillera (Fig. D.6d) suggests a crystalline crust that can sustain differential stresses greater than 600 MPa. As elaborated in Chapter 4.4, this implies that tectonic forces should not be able to generate faults in the crust. These faults, however, are required for the strain transfer from the ductile lower crust beneath the Puna (Fig. D.6b) to the basal décollements in the fold-and-thrust belts. As a consequence, inherited weak zones within the uppermost crust of the orogenic wedge, such as foliation or faults, should play a significant role in the localisation of the transfer faults and the evolution of thin-skinned fold-and-thrust belts.

5.2. Relation between surface deformation and elastic thickness

A property that is commonly used to relate the rheological state of the lithosphere to deformation styles is the effective elastic thickness T_e. In numerous studies, T_e was estimated for the Central Andes and surrounding areas (e.g. García et al., 2018; Pérez-Gussinyé et al., 2007;
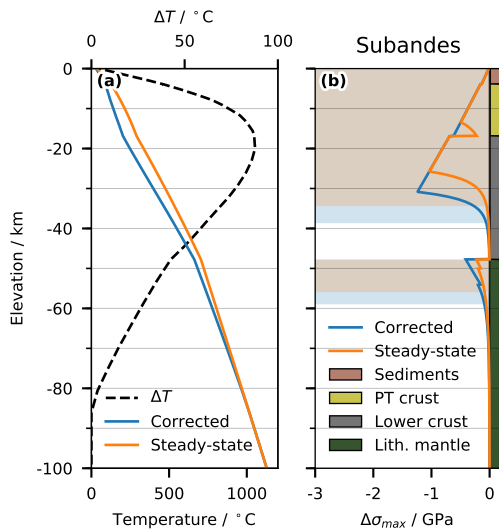
Figure 5.1.: Estimated difference between steady-state model and present-day transient state in the Subandean fold-and-thrust belt, based on the results from Chapters 3.2 and 4. The profiles were extracted from model *Assumpção* at 380 km Easting of the profile in Fig. 4.4d. See Figure D.6 (p. 147) for location of the profile in the coupled model by Sobolev et al. (2006). **(a)** Steady-state (orange) and inferred (blue) transient geotherms. The inferred transient geotherm was computed by subtracting the temperature differences ΔT (black dashed line) from the steady-state geotherm; **(b)** Strength-profiles for compression using the steady-state and corrected geotherms from (a), coloured areas represent the mechanical thicknesses of the layers (Appendix D.2).

Tassara, 2005; Tassara et al., 2007; Watts et al., 1995). Watts et al. (1995) used gravity anomalies and an infinite plate flexural model to estimate effective elastic thicknesses T_e across several profiles through the Central Andes and their foreland basins. They found that T_e correlates with both style and magnitude of shortening since the Late Miocene: thin-skinned fold-and-thrust belts correlate with regions characterised by large T_e, and thick-skinned regimes with regions of low T_e. They concluded that the lithosphere is strongest in the Brazilian craton, becoming successively weaker towards the southwest. This conclusion had been supported by Stewart and Watts (1997), who used a broken flexural plate model instead of an infinite plate as Watts et al. (1995). Studies utilising wavelet spectral analysis of gravity fields (Tassara et al., 2007) achieve similar observations although absolute values of T_e differ. Similarly, Mouthereau et al. (2013) argue that deformation styles relate to the thermotectonic age of the lithosphere which is expressed by its effective elastic thickness.

There are, however, studies that challenge this proposed relationship between T_e and surface deformation. For example, García et al. (2018) published a study on the relation between effective elastic thickness and surface deformation styles in the Central Andes. For their estimates, the authors made use of a 2D infinite-plate flexural model and inverted T_e from a Moho which was inverted from low-pass filtered Bouguer gravity anomaly maps. Their high-resolution T_e estimates indicate a weak lithosphere in the northern Sierras Pampeanas, the Santa-Barbara System ($T_e < 20$ km) and the southeastern Eastern Cordillera. In contrast, the effective elastic thickness in the thin-skinned Subandean belt in Bolivia, ranges between 20 to 60 km on the foreland-facing side, to more than 90 km at the boundary to the Altiplano.

The effective elastic thicknesses for the rheological models in Chapter 4 are computed using the differential stress distribution in the model and the definition of Burov and Diament (1995) (see Appx. D.3). Overall, I observe that the effective elastic thicknesses predicted by the thermal models *Assumpção* and *Debayle* (Fig. 5.2a,c) are between 20 km in the Eastern Cordillera, to 80 - 100 km in the Sierras Pampeanas. In both models, the minimum T_e occur in the Eastern Cordillera (EC in Fig. 5.2) and increase towards the east and south. The trend
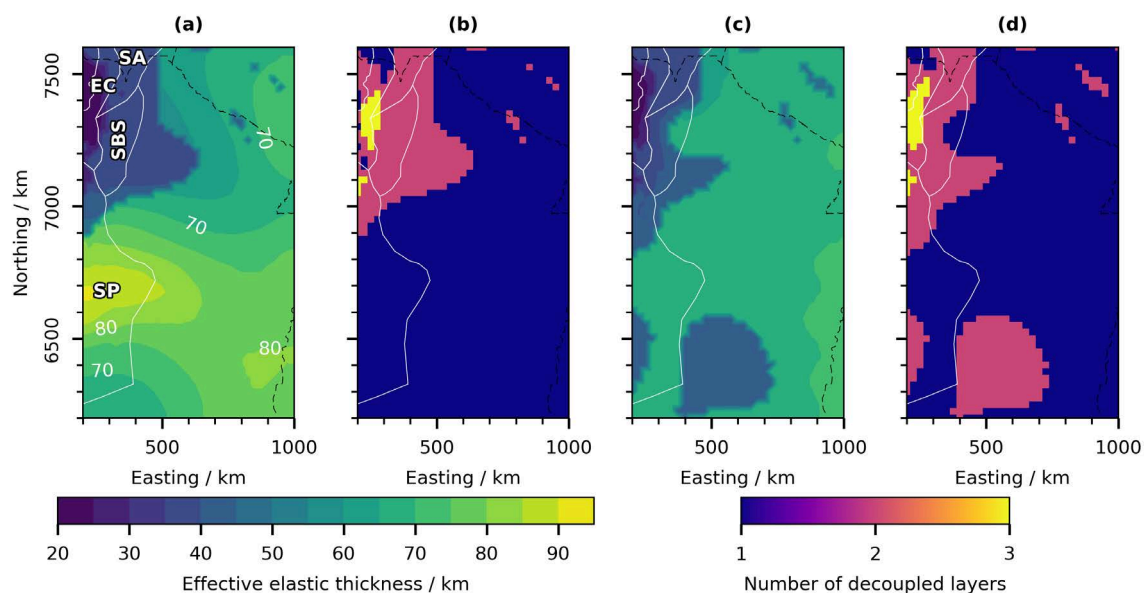
Figure 5.2.: Effective elastic thickness and rheological stratification of the end-member models, computed for $\dot{\epsilon} = 5 \cdot 10^{-16}\,\mathrm{s}^{-1}$. See Appendix D.2 for more details. **(a)** T_e of *Assumpção*; **(b)** number of decoupled layers in (a); **(c)** T_e of end-member *Debayle*; **(d)** number of decoupled layers in (c). Provinces after Jordan et al. (1983), SA = Subandean, EC = Eastern Cordillera, SBS = Santa-Bárbara System, SP = Sierras Pampeanas.

from low T_e in the north to higher values in the south reflects the surface deformation styles in a sense that the spatial distance of the thrusts increases from low to high T_e, as shown by Cloetingh et al. (1999).

This conclusion contradicts the hypothesis proposed by Mouthereau et al. (2013) who suggested a relation between the thermotectonic age of the lithosphere, equivalently T_e, at the time of collision and the style of deformation. The authors found that lithosphere older than 1 Ga accommodates shortening by thin-skinned deformation. The last two major thermotectonic events of the Pampia terrane in northern Argentina were rifting with the development of the Puncoviscana basin between 850 to 600 Ma, followed by a convergent phase which ended with the closure of this basin and the emplacement of granitoids around 540 to 530 Ma (Ramos, 2008). Considering that the thermotectonic age of the Subandean lithosphere was reset with the collision during the early Paleozoic, thick-skinned deformation should be expected here according to Mouthereau et al. (2013). To invert the relation between the T_e values predicted by the models of Chapter 4, the lower boundary conditions would have to be altered by several 100°C (Fig. D.7). The models presented here therefore provide robust evidence that T_e correlates differently with surface deformation styles than proposed by Mouthereau et al. (2013). Therefore, I suggest that high T_e result in thick-skinned deformation, whereas thin-skinned deformation requires a strength contrast from high T_e in the foreland to a low T_e in the orogen and the orogenic wedge.

To better test this hypothesis, the workflow presented in this dissertation should be applied to an expanded modelling area, and additionally supported by coupled numerical models.

This expanded area should include the Chaco plain in Bolivia, and also extend farther into the Andes. The expected results would benefit from the extension into the Chaco plain in particular, because extensive thin-skinned deformation prevails within the Subandean ranges. An additional benefit by extending the study are is the available data sources in Bolivia (Hamza and Muñoz, 1996) that allow the validation of the thermal field.

5.3. The influence of terranes in the density model

In Chapter 2.1 we have derived the average density distribution of the crust in the CPB. Because of the ambiguous trajectory of the TBL, we treated the upper crust as a homogeneously dense body and did not differ between the Pampia terrane and the Río de la Plata craton. However, as stated in Chapter 4.2.2, the crystalline crust of the Pampia terrane is felsic. Due to the predominantly mafic composition of the Río de la Plata craton (see Chapter 2.1.1.1), we should expect that its overall density is higher than the density of the adjacent Pampia terrane. To test the impact this spatial differentiation of tectonic domains into areas of different composition and its potential impact on crustal structure, thermal field and lithospheric strength, I performed the complete workflow from gravity inversion to thermal modelling. During this test I took into account the lateral variations of the tectonic terranes as depicted in Fig. 2.1. As in Chapter 2.1.2.4, the gravity model was setup covering the map area of Fig. 2.1. Prevailing lithologies and the densities assigned are given in the Appendix D.3.

Although the density differences between the models with and without individual crustal domains are not significantly different (Fig. D.3), the thickness distribution of the lower crust changes in response to the decreased density of the Pampia terrane. In the Pampia terrane, west of 64°W, the depth increases by 5 to 10 km (Fig. D.2), whilst it does not significantly change east of this longitude. On the contrary, in the realm of the Río de la Plata craton, the top of the lower crust decreases rather homogeneously by 2 to 3 km. This new configuration, with a thicker and more extensive lower crust in the Pampia terrane, does not alter the conclusions drawn in Chapter 2.1.6, since the fundamental features that can be observed are still observed.

Due to the increased crustal thickness in the Pampia terrane, a larger portion of lower crust in the north-western CPB (between 200–400 km Easting in Fig. D.4d) is subject to brittle deformation than in the previous model. However, since a significant competent mantle is not present in this area, the conclusion of a *crème brûlée* type model (Burov and Watts, 2006) that had been drawn in Chapter 4.5 is robust. Neither, the *jelly sandwich* stratification in the southern CPB (Fig. D.4f) in this model.

5.4. Methodological improvements

This study relies on published data that is available in the CPB and a major disadvantage is that the main structural interfaces in this study are poorly constrained. That is, the depth to the top of the lower crust and the depth to the Moho. The thickness distribution

of the sedimentary infill is devoid of the complete Cenozoic strata (Marengo, 2015), encompassing only Mesozoic and Paleozoic units (Pezzi and Mozetic, 1989). Whilst we could show in Chapter 2.1.4.4 that the main conclusions are not affected much by the missing Cenozoic strata, it is desirable from the modelling perspective to represent the main interfaces as good as it is possible. Second, the depth to the Moho in large fractions of the study area is constrained by inversion of a tomographic shear wave model (Assumpção et al., 2013) with local point constraints from receiver functions. Whilst in proximity to the point constraints, the accuracy of the Moho depth is high, its uncertainty increases significantly in those areas where point constraints are absent. This is especially the case for the anticlinal Moho-high that strikes southwest-northeast in the central and north-eastern study area (Fig. 2.2c). To estimate potential uncertainties of the gravity-derived density model, we performed a sensitivity analysis on the relevant parameters (Chapter 2.1.4). However, this sensitivity analysis only yields uncertainties for this specific model configuration. For each possible configuration of the Moho, this sensitivity analysis would have to be carried out again. Therefore, such sensitivity analyses do not allow to draw more general conclusions that would enable us to predict probability distributions of interface configurations.

In future data-constrained density models, a Bayesian approach should be implemented to enable the probabilistic analysis of structural models (e.g. Wellmann et al., 2010). With the development of *GemPy*, a first step towards integrated Bayesian inversion in structural modelling has been taken by de la Varga et al. (2019). However, during the development of this dissertation, there was no workflow available to integrate the data-constrained structural interfaces of this model into *GemPy*. A challenge that is owed to the fundamentally different way *GemPy* handles input data and represents the subsurface structure. Contrary to the common practice of using interfaces that were interpolated from data sources, *GemPy* utilises the raw data together with their associated uncertainty. This allows *GemPy* to modify the shape of the interfaces within the bounds prescribed by the uncertainties. In future studies it is therefore required to refrain the current practice of computing models that were constructed with interpolated data and instead utilise the fundamental data sources.

Such fundamental data sources also include seismic travel times. The joint inversion of gravity and travel times had been established by Simmons et al. (2010, 2006, 2009), to study the structure of the mantle. In their studies, however, the authors constrain the crustal structure from global models, e.g. CRUST1.0 (Laske et al., 2013). The accuracy of such globally interpolated models however is poorly estimated. In a joint Bayesian approach it should therefore be aimed to implement the fundamental data constraints and associated each data point with an individual uncertainty. A non-complete list of such constraints includes travel times, gravity anomalies, borehole data, receiver functions or refraction seismic data. Finally, the application of the Bayesian inversion should yield more reliable information on the subsurface structure.

6. Conclusions

The overall aim of this dissertation was to connect the rheological state of the lithosphere to surface deformation styles by means of 3D structural, density, thermal and rheological modelling. The main outcomes of my study are:

1. A new method to automatically obtain density distributions of the crystalline crust using *fatiando a terra* (Uieda and Barbosa, 2012; Uieda et al., 2016b) was successfully established. It has been shown that this method is furthermore applicable to the uppermost mantle, resolving density trends with lateral dimensions up to 125 km half-wavelength. This method therefore provides an important tool to close the data gap between the Moho and depths where tomographic studies can be used to obtain density distributions.

2. The impact of tested mantle density variations on the modelled gravity field can be on the order of up to ±40 mGal.

3. The density-model of the CPB supports the location of the Transbrasilian Lineament as suggested by Peri et al. (2015, 2013) and Ramos et al. (2010)

4. With regard to purely thermal conductive processes, subduction is capable to deviate the thermal field of the overlying continental plate from its steady-state at distances of up to 600 km from the trench. This relation depends on the dip of the slab, which is why the thermal field of most foreland regions along the Andes should not be affected by subduction. However, gently dipping (<15°) or flat-slabs could indeed affect the thermal field of the overlying continental plate.

5. The assumption of a thermal steady-state in the foredeep, forebulge and backbulge provinces of the central Andean retroarc foreland basins is valid.

6. Evidence from 2D thermal models suggest that the steady-state assumption is not applicable in the orogenic wedge. When assuming steady-state conditions in an active retroarc foreland basin, the thermal field in the orogenic wedge might be overestimated by more than 200 °C at 30 to 40 km depth.

7. Although the thermal fields between transient- and steady-state models might deviate significantly, the rheological stratifications (*crème brûlée* vs. *jelly sandwich*) in the modelled scenarios were not affected.

8. Thin-skinned deformation in the study area correlates with a *crème brûlée* type of stratification in the orogen and the orogenic wedge, and a stronger *jelly sandwich* continental lithosphere. The transient estimate of the rheological stratification suggests that the stress transfer from the ductile crust in the orogen to the basal décollement in the fold-and-thrust wedge strongly depends on inherited weak zones within the crust of the orogenic wedge.

9. Thick-skinned deformation in the Sierras Pampeanas is related to a fully coupled *jelly sandwich* lithosphere and high effective elastic thickness. Here, crust and mantle are able to sustain differential stresses larger than 600 MPa. In the Sierras Pampeanas, the existing crustal discontinuities do not lower the yield strength of the lithosphere sufficiently to cause a reactivation of these structures. The spatio-temporal correlation of magmatism and uplift in the Sierras Pampeanas therefore suggests that magmatism is the key factor for basement block uplift in this region. Magmatism, if it occurs in the vicinity of the inherited weak zones, may lubricate and thermally weaken the discontinuities, effectively lowering the yield strength to values that can be reached by tectonically applied stresses.

Bibliography

Abers, G. A., P. E. van Keken, E. A. Kneller, A. Ferris and J. C. Stachnik (2006). 'The Thermal Structure of Subduction Zones Constrained by Seismic Imaging: Implications for Slab Dehydration and Wedge Flow'. In: *Earth and Planetary Science Letters* 241.3-4, pp. 387–397. ISSN: 0012821X. DOI: 10.1016/j.epsl.2005.11.055.

Adam, C. and V. Vidal (2010). 'Mantle Flow Drives the Subsidence of Oceanic Plates'. In: *Science* 328.5974, pp. 83–85.

Allen, P. A. and J. R. Allen (2013). *Basin Analysis: Principles and Application to Petroleum Play Assessment*. Wiley. ISBN: 978-1-118-45030-7.

Allmendinger, R. W., T. E. Jordan, S. M. Kay and B. L. Isacks (1997). 'The Evolution of the Altiplano-Puna Plateau of the Central Andes'. In: *Annual Review of Earth and Planetary Sciences* 25.1, pp. 139–174. DOI: 10.1146/annurev.earth.25.1.139.

Allmendinger, R. W., V. A. Ramos, T. E. Jordan, M. Palma and B. L. Isacks (1983). 'Paleogeography and Andean Structural Geometry, Northwest Argentina'. In: *Tectonics* 2.1, pp. 1–16. ISSN: 1944-9194. DOI: 10.1029/TC002i001p00001.

Allmendinger, R. W., M. Strecker, J. E. Eremchuk and P. Francis (1989). 'Neotectonic Deformation of the Southern Puna Plateau, Northwestern Argentina'. In: *Journal of South American Earth Sciences* 2.2, pp. 111–130. ISSN: 0895-9811. DOI: 10.1016/0895-9811(89)90040-0.

Almeida, F. F. M. de, B. B. de Brito Neves and C. Dal Ré Carneiro (2000). 'The Origin and Evolution of the South American Platform'. In: *Earth-Science Reviews* 50.1–2, pp. 77–111. ISSN: 0012-8252. DOI: 10.1016/S0012-8252(99)00072-0.

Alvarado, P., S. Beck and G. Zandt (2007). 'Crustal Structure of the South-Central Andes Cordillera and Backarc Region from Regional Waveform Modelling'. In: *Geophysical Journal International* 170.2, pp. 858–875. ISSN: 0956540X, 1365246X. DOI: 10.1111/j.1365-246X.2007.03452.x.

Alvarado, P., M. Pardo, H. Gilbert, S. Miranda, M. Anderson, M. Saez and S. Beck (2009). 'Flat-Slab Subduction and Crustal Models for the Seismically Active Sierras Pampeanas Region of Argentina'. In: *Geological Society of America Memoirs* 204.0, pp. 261–278. ISSN: 0072-1069. DOI: 10.1130/2009.1204(12).

Amante, C. and B. W. Eakins (2009). *ETOPO1 1 Arc-Minute Global Relief Model: Procedures, Data Sources and Analysis*. URL: https://doi.org/10.7289/V5C8276M (visited on 18/10/2016).

Appelgate, B. (1997). 'Modes of Axial Reorganization on a Slow-Spreading Ridge: The Structural Evolution of Kolbeinsey Ridge since 10 Ma'. In: *Geology* 25, pp. 431–434.

Arriagada, C., P. Roperch, C. Mpodozis and P. R. Cobbold (2008). 'Paleogene Building of the Bolivian Orocline: Tectonic Restoration of the Central Andes in 2-D Map View'. In: *Tectonics* 27.6, TC6014. ISSN: 1944-9194. DOI: 10.1029/2008TC002269.

Artemieva, I. M. (2006). 'Global 1°×1° Thermal Model TC1 for the Continental Lithosphere: Implications for Lithosphere Secular Evolution'. In: *Tectonophysics*. The Heterogeneous Mantle 416.1, pp. 245–277. ISSN: 0040-1951. DOI: 10.1016/j.tecto.2005.11.022.

Assumpção, M. (1992). 'The Regional Intraplate Stress Field in South America'. In: *Journal of Geophysical Research: Solid Earth* 97.B8, pp. 11889–11903. ISSN: 2156-2202. DOI: 10.1029/91JB01590.

Assumpção, M., M. Feng, A. Tassara and J. Julià (2013). 'Models of Crustal Thickness for South America from Seismic Refraction, Receiver Functions and Surface Wave Tomography'. In: *Tectonophysics*. Moho: 100 Years after Andrija Mohorovicic 609, pp. 82–96. ISSN: 0040-1951. DOI: 10.1016/j.tecto.2012.11.014.

Athy, L. F. (1930). 'Density, Porosity, and Compaction of Sedimentary Rocks'. In: *AAPG Bulletin* 14.1, pp. 1–24. ISSN: 0149-1423. URL: http://archives.datapages.com/data/bulletns/1917-30/data/pg/0014/0001/0000/0001.htm (visited on 01/12/2016).

Babeyko, A. Y., S. V. Sobolev, R. B. Trumbull, O. Oncken and L. L. Lavier (2002). 'Numerical Models of Crustal Scale Convection and Partial Melting beneath the Altiplano–Puna Plateau'. In:

Earth and Planetary Science Letters 199.3, pp. 373–388. ISSN: 0012-821X. DOI: 10.1016/S0012-821X(02)00597-6.

Babeyko, A. Y. and S. V. Sobolev (2005). 'Quantifying Different Modes of the Late Cenozoic Shortening in the Central Andes'. In: *Geology* 33.8, pp. 621–624. URL: http://geology.gsapubs.org/content/33/8/621.short (visited on 12/10/2015).

Bai, Y., S. E. Williams, R. D. Müller, Z. Liu and M. Hosseinpour (2014). 'Mapping Crustal Thickness Using Marine Gravity Data: Methods and Uncertainties'. In: *Geophysics* 79.2, G27–G36.

Barthelmes, F. and W. Köhler (2012). 'International Centre for Global Earth Models (ICGEM)'. In: *Journal of Geodesy*. The Geodesists Handbook 86.10, pp. 932–934. URL: http://icgem.gfz-potsdam.de/ICGEM/ (visited on 23/11/2015).

Barton, P. J. (1986). 'The Relationship between Seismic Velocity and Density in the Continental Crust – A Useful Constraint?' In: *Geophys. J. R. Astron. Soc.* 87, pp. 195–208.

Bauville, A. and S. M. Schmalholz (2015). 'Transition from Thin- to Thick-Skinned Tectonics and Consequences for Nappe Formation: Numerical Simulations and Applications to the Helvetic Nappe System, Switzerland'. In: *Tectonophysics* 665, pp. 101–117. ISSN: 0040-1951. DOI: 10.1016/j.tecto.2015.09.030.

Behnsen, J. and D. R. Faulkner (2012). 'The Effect of Mineralogy and Effective Normal Stress on Frictional Strength of Sheet Silicates'. In: *Journal of Structural Geology* 42, pp. 49–61. ISSN: 0191-8141. DOI: 10.1016/j.jsg.2012.06.015.

Behr, W. M. and J. P. Platt (2014). 'Brittle Faults Are Weak, yet the Ductile Middle Crust Is Strong: Implications for Lithospheric Mechanics'. In: *Geophysical Research Letters* 41.22, pp. 8067–8075. ISSN: 1944-8007. DOI: 10.1002/2014GL061349.

Blischke, A., C. Gaina, J. R. Hopper, G. Péron-Pinvidic, B. Brandsdóttir, P. Guarnieri, Ö. Erlendsson and K. Gunnarsson (2016). 'The Jan Mayen Microcontinent: An Update of Its Architecture, Structural Development and Role during the Transition from the Ægir Ridge to the Mid-Oceanic Kolbeinsey Ridge'. In: *Geol. Soc. London Spec. Publ.* 447. DOI: http://doi.org/10.1144/SP447.5.

Bossi, G. E., S. M. Georgieff, I. J. C. Gavriloff, L. M. Ibañez and C. M. Muruaga (2001). 'Cenozoic Evolution of the Intramontane Santa María Basin, Pampean Ranges, Northwestern Argentina'. In: *Journal of South American Earth Sciences* 14.7, pp. 725–734. ISSN: 0895-9811. DOI: 10.1016/S0895-9811(01)00058-X.

Brandsdóttir, B., E. E. E. Hooft, R. Mjelde and Y. Murai (2015). 'Origin and Evolution of the Kolbeinsey Ridge and Iceland Plateau, N-Atlantic'. In: *Geochem. Geophys. Geosyst.* 16, pp. 612–634.

Breivik, A. J., J. I. Faleide and R. Mjelde (2008). 'Neogene Magmatism Northeast of the Aegir and Kolbeinsey Ridges, NE Atlantic: Spreading Ridge – Mantle Plume Interaction?' In: *Geochem. Geophys. Geosyst.* 9.Q02004. DOI: 10.1029/2007GC001750.

Breivik, A. J., J. I. Faleide, R. Mjelde and R. Flueh (2009). 'Magma Productivity and Early Seafloor Spreading Rate Correlation on the Northern Vøring Margin, Norway – Constraints on Mantle Melting'. In: *Tectonophysics* 468, pp. 206–223. DOI: 10.1016/j.tecto.2008.09.020.

Breivik, A. J., R. Mjelde, J. I. Faleide and Y. Murai (2012a). 'The Eastern Jan Mayen Microcontinent Volcanic Margin'. In: *Geophys. J. Int.* 188, pp. 798–818. DOI: 10.1111/j.1365-246X.2011.05307.x.

Breivik, A. J., R. Mjelde, A. K. Rai and A. Frassetto (2012b). 'Geophyical Survey of the Eggvin Bank and Logi Ridge-Greenland Sea'. In: *Eos Trans. AGU* 93.52. Fall Meet. Suppl., Abstract T31B-2598.

Breivik, A., R. Mjelde, J. I. Faleide, E. Flueh and Y. Murai (2014). 'Magmatic Development of the Outer Vøring Margin from Seismic Data'. In: *J. Geophys. Res.* 119, pp. 6733–6755. DOI: 10.1002/2014JB011040.

Burov, E. B. (2011). 'Rheology and Strength of the Lithosphere'. In: *Marine and Petroleum Geology* 28.8, pp. 1402–1443. ISSN: 02648172. DOI: 10.1016/j.marpetgeo.2011.05.008.

Burov, E. B. and M. Diament (1995). 'The Effective Elastic Thickness (T e) of Continental Lithosphere: What Does It Really Mean?' In: *Journal of Geophysical Research: Solid Earth* 100.B3, pp. 3905–3927. ISSN: 2156-2202. DOI: 10.1029/94JB02770.

Burov, E. B., C. Jaupart and J. C. Mareschal (1998). 'Large-Scale Crustal Heterogeneities and Lithospheric Strength in Cratons'. In: *Earth and Planetary Science Letters* 164.1–2, pp. 205–219. ISSN: 0012-821X. DOI: 10.1016/S0012-821X(98)00205-2.

Burov, E. B. and A. Watts (2006). 'The Long-Term Strength of Continental Lithosphere: "Jelly Sandwich" or "Crème Brûlée"?' In: *GSA Today* 16.1, p. 4. ISSN: 1052-5173. DOI: 10.1130/1052-5173(2006)016<4:TLTSOC>2.0.CO;2.

Byerlee, J. (1978). 'Friction of Rocks'. In: *pure and applied geophysics* 116.4-5, pp. 615–626. ISSN: 0033-4553, 1420-9136. DOI: 10.1007/BF00876528.

Cacace, M. and M. Scheck-Wenderoth (2016). 'Why Intracontinental Basins Subside Longer: 3-D Feedback Effects of Lithospheric Cooling and Sedimentation on the Flexural Strength of the Lithosphere'. In: *Journal of Geophysical Research: Solid Earth* 121.5, 2015JB012682. ISSN: 2169-9356. DOI: 10.1002/2015JB012682.

Cacace, M. and A. B. Jacquey (2017). 'Flexible Parallel Implicit Modelling of Coupled Thermal–Hydraulic–Mechanical Processes in Fractured Rocks'. In: *Solid Earth* 8.5, pp. 921–941. ISSN: 1869-9529. DOI: 10.5194/se-8-921-2017.

Cahill, T. and B. L. Isacks (1992). 'Seismicity and Shape of the Subducted Nazca Plate'. In: *Journal of Geophysical Research: Solid Earth* 97.B12, pp. 17503–17529. ISSN: 2156-2202. DOI: 10.1029/92JB00493.

Cammarano, F. and M. Guerri (2017). 'Global Thermal Models of the Lithosphere'. In: *Geophys. J. Int.* 210.1, pp. 56–72.

Cammarano, F., S. Goes, P. Vacher and D. Giardini (2003). 'Inferring Upper-Mantle Temperatures from Seismic Velocities'. In: *Physics of the Earth and Planetary Interiors* 138.3-4, pp. 197–222. ISSN: 00319201. DOI: 10.1016/S0031-9201(03)00156-0.

Capitanio, F. A., C. Faccenna, S. Zlotnik and D. R. Stegman (2011). 'Subduction Dynamics and the Origin of Andean Orogeny and the Bolivian Orocline'. In: *Nature* 480.7375, pp. 83–86. ISSN: 0028-0836. DOI: 10.1038/nature10596.

Carpenter, B. M., C. Marone and D. M. Saffer (2011). 'Weakness of the San Andreas Fault Revealed by Samples from the Active Fault Zone'. In: *Nature Geoscience* 4.4, pp. 251–254. ISSN: 1752-0908. DOI: 10.1038/ngeo1089.

Carpenter, B. M., D. M. Saffer and C. Marone (2012). 'Frictional Properties and Sliding Stability of the San Andreas Fault from Deep Drill Core'. In: *Geology* 40.8, pp. 759–762. ISSN: 0091-7613. DOI: 10.1130/G33007.1.

Carter, N. L. and M. C. Tsenn (1987). 'Flow Properties of Continental Lithosphere'. In: *Tectonophysics* 136.1-2, pp. 27–63. URL: http://www.sciencedirect.com/science/article/pii/0040195187903337 (visited on 08/03/2017).

Cermak, V., H.-G. Huckenholz, L. Rybach, R. Schmid, J. R. Schopper, M. Schuch, D. Stöffler and J. Wohlenberg (1982). 'Physikalische Eigenschaften Der Gesteine Teilband a'. In: *LANDOLDT-BÖRNSTEIN Zahlenwerte Und Funktionen Aus Naturwissenschaften Und Technik*. Ed. by G. Angenheister. Red. by K.-H. Hellwege. Vol. Band 1. Gruppe V: Geophysik Und Weltraumforschung. Berlin: Springer Verlag, pp. 305–371. ISBN: 9783 5401 033 32.

Charrier, R., V. A. Ramos, F. Tapia and L. Sagripanti (2015). 'Tectono-Stratigraphic Evolution of the Andean Orogen between 31 and 37 S (Chile and Western Argentina)'. In: *Geological Society, London, Special Publications* 399.1, pp. 13–61. ISSN: 0305-8719, 2041-4927. DOI: 10.1144/SP399.20.

Chase, C. G., A. J. Sussman and D. D. Coblentz (2009). 'Curved Andes: Geoid, Forebulge, and Flexure'. In: *Lithosphere* 1.6, pp. 358–363. ISSN: 1941-8264, 1947-4253. DOI: 10.1130/L67.1.

Chebli, G. A., M. E. Mozetic, E. A. Rossello, M. Bühler and R. Caminos (1999). 'Cuencas Sedimentarias de La Llanura Chacopampeana'. In: *Geología Argentina*. Ed. by R. Caminos. Anales 29. Buenos Aires, pp. 627–644.

Chen, W.-P. and P. Molnar (1983). 'Focal Depths of Intracontinental and Intraplate Earthquakes and Their Implications for the Thermal and Mechanical Properties of the Lithosphere'. In: *Journal of Geophysical Research: Solid Earth* 88.B5, pp. 4183–4214. ISSN: 0148-0227. DOI: 10.1029/JB088iB05p04183.

Chernicoff, C. J. and E. O. Zappettini (2004). 'Geophysical Evidence for Terrane Boundaries in South-Central Argentina'. In: *Gondwana Research* 7.4, pp. 1105–1116. ISSN: 1342-937X. DOI: 10.1016/S1342-937X(05)71087-X.

Christensen, N. I. and W. D. Mooney (1995). 'Seismic Velocity Structure and Composition of the Continental Crust: A Global View'. In: *Journal of Geophysical Research: Solid Earth* 100.B6, pp. 9761–9788. ISSN: 01480227. DOI: 10.1029/95JB00259.

Cloetingh, S., E. Burov and A. Poliakov (1999). 'Lithosphere Folding: Primary Response to Compression? (From Central Asia to Paris Basin)'. In: *Tectonics* 18.6, pp. 1064–1083. ISSN: 02787407. DOI: 10.1029/1999TC900040.

Cloetingh, S. and R. Wortel (1986). 'Stress in the Indo-Australian Plate'. In: *Tectonophysics*. Intraplate Deformation: Characteristics, Processes, and Causes 132.1, pp. 49–67. ISSN: 0040-1951. DOI: 10.1016/0040-1951(86)90024-7.

Comin-Chiaramonti, P., G. Demarchi, V. A. V. Girardi, F. Princivalle and S. Sinigoi (1986). 'Evidence of Mantle Metasomatism and Heterogeneity from Peridotite Inclusions of Northeastern Brazil and Paraguay'. In: *Earth and Planetary Science Letters* 77.2, pp. 203–217. ISSN: 0012-821X. DOI: 10.1016/0012-821X(86)90161-5.

Cordani, U. G., M. M. Pimentel, C. E. G. D. Araújo, M. A. S. Basei, R. A. Fuck and V. A. V. Girardi (2013). 'Was There an Ediacaran Clymene Ocean in Central South America?' In: *American Journal of Science* 313.6, pp. 517–539. ISSN: 0002-9599, 1945-452X. DOI: 10.2475/06.2013.01.

Cordani, U. G. and K. Sato (1999). 'Crustal Evolution of the South American Platform, Based on Nd Isotopic Systematics on Granitoid Rocks'. In: *Episodes-Newsmagazine of the International Union of Geological Sciences* 22.3, pp. 167–173. URL: http://www.episodes.org/index.php/epi/article/download/62772/48971 (visited on 26/10/2016).

Cruciani, C., E. Carminati and C. Doglioni (2005). 'Slab Dip vs. Lithosphere Age: No Direct Function'. In: *Earth and Planetary Science Letters* 238.3, pp. 298–310. ISSN: 0012-821X. DOI: 10.1016/j.epsl.2005.07.025.

Davis, M. G., D. S. Chapman, T. M. V. Wagoner and P. A. Armstrong (2007). 'Thermal Conductivity Anisotropy of Metasedimentary and Igneous Rocks'. In: *Journal of Geophysical Research: Solid Earth* 112.B5. ISSN: 2156-2202. DOI: 10.1029/2006JB004755.

De la Varga, M., A. Schaaf and F. Wellmann (2019). 'GemPy 1.0: Open-Source Stochastic Geological Modeling and Inversion'. In: *Geoscientific Model Development* 12.1, pp. 1–32. ISSN: 1991-9603. DOI: 10.5194/gmd-12-1-2019.

Debayle, E., F. Dubuffet and S. Durand (2016). 'An Automatically Updated S-Wave Model of the Upper Mantle and the Depth Extent of Azimuthal Anisotropy'. In: *Geophysical Research Letters* 43.2, 2015GL067329. ISSN: 1944-8007. DOI: 10.1002/2015GL067329.

DeCelles, P. G., B. Carrapa, B. K. Horton and G. E. Gehrels (2011). 'Cenozoic Foreland Basin System in the Central Andes of Northwestern Argentina: Implications for Andean Geodynamics and Modes of Deformation: ANDEAN FORELAND BASIN'. In: *Tectonics* 30.6, n/a–n/a. ISSN: 02787407. DOI: 10.1029/2011TC002948.

DeCelles, P. G. and K. A. Giles (1996). 'Foreland Basin Systems'. In: *Basin Research* 8.2, pp. 105–123. ISSN: 1365-2117. URL: http://www.earthdoc.org/publication/publicationdetails/?publication=62646 (visited on 10/10/2016).

DeCelles, P. G. (2012). 'Foreland Basin Systems Revisited: Variations in Response to Tectonic Settings'. In: *Tectonics of Sedimentary Basins. Recent Advances. Wiley–Blackwell, Oxford*, pp. 405–426. URL: http://www.geo.arizona.edu/sites/www.geo.arizona.edu/files/12-decelles-tsb.pdf (visited on 10/10/2016).

DeCelles, P. G. and B. K. Horton (2003). 'Early to Middle Tertiary Foreland Basin Development and the History of Andean Crustal Shortening in Bolivia'. In: *Geological Society of America Bulletin* 115.1, pp. 58–77. ISSN: 0016-7606, 1943-2674. DOI: 10.1130/0016-7606(2003)115<0058:ETMTFB>2.0.CO;2.

Detrick, R., J. Collins, R. Stephen and S. Swift (1994). 'In Situ Evidence for the Nature of the Seismic Layer 2/3 Boundary in Oceanic Crust'. In: *Nature* 370, pp. 288–290.

Dilek, Y. (1998). 'Structure and Tectonics of Intermediate-Spread Oceanic Crust Drilled at DSDP/ODP Holes 504B and 896A, Costa Rica Rift, in Geolocial Evolution of Ocean Basin: Results From the Ocean Drilling Program, Edited by A. Cramp et Al.' In: *Geol. Soc. Spec. Publ.* 131, pp. 179–197.

Divins, D. L. (2004). 'Total Sediment Thickness of the World's Oceans and Marginal Seas'. In: World Data Cent. for Mar. Geol. and Geophys., Natl. Geophys. Data Cent., Boulder, Colo.

Doin, M. P. and L. Fleitout (1996). 'Thermal Evolution of the Oceanic Lithosphere: An Alternative View'. In: *Earth Planet. Sci. Lett* 142.1-2, pp. 121–136.

Dragone, G. N. (2013). 'ESTRUTURA CRUSTAL DA BACIA DO CHACO-PARANÁ A PARTIR DE DADOS GRAVIMÉTRICOS'. DISSERTAÇÃO DE MESTRADO. São Paulo: Universidade de São Paulo.

Duarte, J. C., W. P. Schellart and A. R. Cruden (2015). 'How Weak Is the Subduction Zone Interface?' In: *Geophysical Research Letters* 42.8, pp. 2664–2673. ISSN: 1944-8007. DOI: 10.1002/2014GL062876.

Eaton, D. W., F. Darbyshire, R. L. Evans, H. Grütter, A. G. Jones and X. Yuan (2009). 'The Elusive Lithosphere–Asthenosphere Boundary (LAB) beneath Cratons'. In: *Lithos*. Continental Lithospheric Mantle: The Petro-Geophysical Approach 109.1, pp. 1–22. ISSN: 0024-4937. DOI: 10.1016/j.lithos.2008.05.009.

Elkins, L. J., C. Hamelin, J. Blichert-Toft, S. R. Scott, K. W. W. Sims, I. A. Yeo, C. W. Devey and R. B. Pedersen (2016). 'North Atlantic Hotspot-Ridge Interaction near Jan Mayen Island'. In: *Geochem. Persp. Lett.* 2, pp. 55–67.

Elkins, L. J. et al. (2011). 'Understanding Melt Generation beneath the Slow-Spreading Kolbeinsey Ridge Using 238U, 230Th, and 231Pa Excesses'. In: *Geochim. Cosmochim. Acta.* 75, pp. 6300–6329.

Escayola, M. P., C. R. van Staal and W. J. Davis (2011). 'The Age and Tectonic Setting of the Puncoviscana Formation in Northwestern Argentina: An Accretionary Complex Related to Early Cambrian Closure of the Puncoviscana Ocean and Accretion of the Arequipa-Antofalla Block'. In: *Journal of South American Earth Sciences* 32.4, pp. 438–459. ISSN: 08959811. DOI: 10.1016/j.jsames.2011.04.013.

Exxon (1985). *Tectonic Map of the World*. Tulsa, OK, USA: Exxon Production Research.

Feng, M., S. van der Lee and M. Assumpção (2007). 'Upper Mantle Structure of South America from Joint Inversion of Waveforms and Fundamental Mode Group Velocities of Rayleigh Waves'. In: *Journal of Geophysical Research: Solid Earth* 112.B4, B04312. ISSN: 2156-2202. DOI: 10.1029/2006JB004449.

Fichtner, A. and J. Trampert (2011). 'Resolution Analysis in Full Waveform Inversion'. In: *Geophys. J. Int.* 187.3, pp. 1604–1624.

Flemings, P. B. and T. E. Jordan (1989). 'A Synthetic Stratigraphic Model of Foreland Basin Development'. In: *Journal of Geophysical Research* 94.B4, pp. 3851–3866. URL: http://www.geo.arizona.edu/geo5xx/geos517/pdfs/flemingsjordan-1989.pdf (visited on 12/10/2015).

Förste, C., S. L. Bruinsma, O. Abrikosov, J. M. Lemoine, J. C. Marty, F. Flechtner, G. Balmino, F. Barthelmes and R. Biancale (2014). 'EIGEN-6C4 The Latest Combined Global Gravity Field Model Including GOCE Data up to Degree and Order 2190 of GFZ Potsdam and GRGS Toulouse'. In: *GFZ German Research Center for Geosciences.* DOI: 10.5880/icgem.2015.1.

Förste, C., R. Schmidt, R. Stubenvoll, F. Flechtner, U. Meyer, R. König, H. Neumayer, R. Biancale, J. Lemoine, S. Bruinsma et al. (2008). 'The GeoForschungsZentrum Potsdam/Groupe de Recherche de Geodesie Spatiale Satellite-Only and Combined Gravity Field Models: EIGEN-GL04S1 and EIGEN-GL04C'. In: *J. Geodesy* 82.6, pp. 331–346.

Fowler, C. M. R. (1990). *The Solid Earth: An Introduction to Global Geophysics*. Cambridge University Press. ISBN: 0-521-38590-3.

Fujinawa, Y., N. Kawakami, J. Inoue, T. H. Asch, S. Takasugi and Y. Honkura (1999). '2-D Georesistivity Structure in the Central Part of the Northeastern Japan Arc'. In: *Earth, Planets and Space* 51.10, pp. 1035–1046. ISSN: 1343-8832, 1880-5981. DOI: 10.1186/BF03351577.

Funck, T., W. H. Geissler, G. S. Kimbell, S. Gradmann, Erlendsson, Ö, Mcdermott, K. and U. K. Petersen (2016). 'Moho and Basement Depth in the NE Atlantic Ocean Based on Seismic Refraction Data and Receiver Functions'. In: *Geol. Soc. Spec. Pub.* 477. DOI: 10.1144/SP447.1.

Furmall, A. V. (2010). 'Melt Production and Ridge Geometry over the Past 10 Myr on the Southern Kolbeinsey Ridge, Iceland'. USA: University of Oregon.

Gaina, C., L. Gernigon and P. Ball (2009). 'Palaeocene–Recent Plate Boundaries in the NE Atlantic and the Formation of the Jan Mayen Microcontinent'. In: *J. Geol. Soc.* 166, pp. 601–616. DOI: 10.1144/0016-76492008-112.

Gaina, C., S. C. Werner, R. Saltus, S. Maus and T. C.-G. GROUP (2011). 'Circum-Arctic Mapping Project: New Magnetic and Gravity Anomaly Maps of the Arctic.' In: *J. Geol. Soc.* 35, pp. 39–48.

García, H. P. A., G. M. Gianni, M. N. Lupari, M. A. Sánchez, S. R. Soler, F. Ruiz and F. G. Lince Klinger (2018). 'Effective Elastic Thickness in the Central Andes. Correlation to Orogenic Deformation Styles and Lower Crust High-Gravity Anomaly'. In: *Journal of South American Earth Sciences.* South American Tectonics 87, pp. 232–246. ISSN: 0895-9811. DOI: 10.1016/j.jsames.2017.11.021.

Geuzaine, C. and J.-F. Remacle (2009). 'Gmsh: A 3-D Finite Element Mesh Generator with Built-in Pre- and Post-Processing Facilities'. In: *International Journal for Numerical Methods in Engineering* 79.11, pp. 1309–1331. ISSN: 1097-0207. DOI: 10.1002/nme.2579.

Gleason, G. C. and J. Tullis (1995). 'A Flow Law for Dislocation Creep of Quartz Aggregates Determined with the Molten Salt Cell'. In: *Tectonophysics* 247.1-4, pp. 1–23. ISSN: 00401951. DOI: 10.1016/0040-1951(95)00011-B.

Goes, S., R. Govers and P. Vacher (2000). 'Shallow Mantle Temperatures under Europe from P and S Wave Tomography'. In: *Journal of Geophysical Research: Solid Earth* 105.B5, pp. 11153–11169. ISSN: 2156-2202. DOI: 10.1029/1999JB900300.

Goes, S. and S. van der Lee (2002). 'Thermal Structure of the North American Uppermost Mantle Inferred from Seismic Tomography'. In: *Journal of Geophysical Research: Solid Earth* 107.B3, ETG 2–1. ISSN: 2156-2202. DOI: 10.1029/2000JB000049.

Goetze, C. and J. P. Poirier (1978). 'The Mechanisms of Creep in Olivine [and Discussion]'. In: *Philosophical Transactions of the Royal Society of London A: Mathematical, Physical and Engineering Sciences* 288.1350, pp. 99–119. ISSN: 1364-503X, 1471-2962. DOI: 10.1098/rsta.1978.0008.

Goetze, C. and B. Evans (1979). 'Stress and Temperature in the Bending Lithosphere as Constrained by Experimental Rock Mechanics'. In: *Geophysical Journal International* 59.3, pp. 463–478. ISSN: 0956-540X. DOI: 10.1111/j.1365-246X.1979.tb02567.x.

Götze, H. .-.-J. and B. Lahmeyer (1988). 'Application of Three-Dimensional Interactive Modeling in Gravity and Magnetics'. In: *GEOPHYSICS* 53.8, pp. 1096–1108. URL: http://geophysics.geoscienceworld.org/content/gsgpy/53/8/1096.full.pdf (visited on 05/07/2017).

Griffin, W. L., S. Y. O'Reilly, J. C. Afonso and G. C. Begg (2009). 'The Composition and Evolution of Lithospheric Mantle: A Re-Evaluation and Its Tectonic Implications'. In: *Journal of Petrology* 50.7, pp. 1185–1204. ISSN: 0022-3530. DOI: 10.1093/petrology/egn033.

Grose, C. J. and J. C. Afonso (2013). 'Comprehensive Plate Models for the Thermal Evolution of Oceanic Lithosphere'. In: *Geochemistry, Geophysics, Geosystems* 14.9, pp. 3751–3778. ISSN: 1525-2027. DOI: 10.1002/ggge.20232.

Haase, C., J. Ebbing and T. Funck (2016). 'A 3D Crustal Model of the NE Atlantic Based on Seismic and Gravity Data'. In: *Geol. Soc. Spec. Pub.* 447.

Haase, K. M., C. W. Devey and M. Wieneke (2003). 'Magmatic Processes and Mantle Heterogeneity beneath the Slow-Spreading Northern Kolbeinsey Ridge Segment, North Atlantic'. In: *Contrib. Mineral. Petrol.* 144, pp. 428–448.

Hacker, B. R., P. B. Kelemen and M. D. Behn (2011). 'Differentiation of the Continental Crust by Relamination'. In: *Earth and Planetary Science Letters* 307.3, pp. 501–516. ISSN: 0012-821X. DOI: 10.1016/j.epsl.2011.05.024.

Hain, M. P., M. R. Strecker, B. Bookhagen, R. N. Alonso, H. Pingel and A. K. Schmitt (2011). 'Neogene to Quaternary Broken Foreland Formation and Sedimentation Dynamics in the Andes of NW Argentina (25°S): SALTA FORELAND FRAGMENTATION'. In: *Tectonics* 30.2, n/a–n/a. ISSN: 02787407. DOI: 10.1029/2010TC002703.

Hall, P. S. (2012). 'On the Thermal Evolution of the Mantle Wedge at Subduction Zones'. In: *Physics of the Earth and Planetary Interiors* 198-199, pp. 9–27. ISSN: 00319201. DOI: 10.1016/j.pepi.2012.03.004.

Hamza, V. M. and M. Muñoz (1996). 'Heat Flow Map of South America'. In: *Geothermics* 25.6, pp. 599–646. URL: http://www.sciencedirect.com/science/article/pii/S0375650596000259 (visited on 12/10/2015).

Hantschel, T. and A. I. Kauerauf (2009). *Fundamentals of Basin and Petroleum Systems Modeling*. Springer Science & Business Media. ISBN: 3-540-72318-8.

Hasterok, D. (2013). 'A Heat Flow Based Cooling Model for Tectonic Plates'. In: *Earth and Planetary Science Letters* 361, pp. 34–43. ISSN: 0012-821X. DOI: 10.1016/j.epsl.2012.10.036.

Hayes, G. P., D. J. Wald and R. L. Johnson (2012). 'Slab1.0: A Three-Dimensional Model of Global Subduction Zone Geometries: SLAB1.0 3D SUBDUCTION GEOMETRY'. In: *Journal of Geophysical Research: Solid Earth* 117.B1, n/a–n/a. ISSN: 01480227. DOI: 10.1029/2011JB008524.

Heine, C., L. G. Yeo and R. D. Müller (2015). 'Evaluating Global Paleoshoreline Models for the Cretaceous and Cenozoic'. In: *Australian Journal of Earth Sciences*, pp. 1–13. ISSN: 0812-0099, 1440-0952. DOI: 10.1080/08120099.2015.1018321.

Heine, C., J. Zoethout and R. D. Müller (2013). 'Kinematics of the South Atlantic Rift'. In: *Solid Earth* 4.2, pp. 215–253. ISSN: 1869-9510. DOI: 10.5194/se-4-215-2013.

Heit, B., M. Bianchi, X. Yuan, S. M. Kay, E. Sandvol, P. Kumar, R. Kind, R. N. Alonso, L. D. Brown and D. Comte (2014). 'Structure of the Crust and the Lithosphere beneath the Southern

Puna Plateau from Teleseismic Receiver Functions'. In: *Earth and Planetary Science Letters* 385 (Supplement C), pp. 1–11. ISSN: 0012-821X. DOI: 10.1016/j.epsl.2013.10.017.

Heit, B., F. Sodoudi, X. Yuan, M. Bianchi and R. Kind (2007). 'An S Receiver Function Analysis of the Lithospheric Structure in South America'. In: *Geophysical Research Letters* 34.14. ISSN: 0094-8276. DOI: 10.1029/2007GL030317.

Hermann, T. (2013). 'The Northeast Greenland Margin-Tectonic Evolution'. University of Jena.

Hermann, T. and W. Jokat (2016). 'Crustal Structure off Kong Oscar Fjord, East Greenland: Evidence for Focused Melt Supply along the Jan Mayen Fracture Zone'. In: *Tectonophysics* 691, pp. 110–119.

Hetzel, R. and M. R. Strecker (1994). 'Late Mozambique Belt Structures in Western Kenya and Their Influence on the Evolution of the Cenozoic Kenya Rift'. In: *Journal of Structural Geology* 16.2, pp. 189–201. ISSN: 0191-8141. DOI: 10.1016/0191-8141(94)90104-X.

Hirth, G. and D. Kohlstedt (2004). 'Rheology of the Upper Mantle and the Mantle Wedge: A View from the Experimentalists'. In: *Inside the Subduction Factory*. Ed. by J. Eiler. American Geophysical Union, pp. 83–105. ISBN: 978-1-118-66857-3. DOI: 10.1029/138GM06. URL: http://onlinelibrary.wiley.com/doi/10.1029/138GM06/summary (visited on 05/12/2017).

Holland, T. J. B. and R. Powell (1998). 'An Internally Consistent Thermodynamic Data Set for Phases of Petrological Interest'. In: *Journal of Metamorphic Geology* 16.3, pp. 309–343. ISSN: 1525-1314. DOI: 10.1111/j.1525-1314.1998.00140.x.

Hooft, E. E. E., B. Brandsdóttir, R. Mjelde, H. Shimamura and Y. Murai (2006). 'Asymmetric Plume Ridge Interaction around Iceland: The Kolbeinsey Ridge Iceland Seismic Experiment'. In: *Geochem. Geophys. Geosyst.* 7.5, pp. 1–26.

Howell, S. M., G. Ito, A. J. Breivik, A. Rai, R. Mjelde, B. Hanan, K. Sayit and P. Vogt (2014). 'The Origin of the Asymmetry in the Iceland Hotspot along the Mid-Atlantic Ridge from Continental Breakup to Present-Day'. In: *Earth Planet. Sci. Lett.* 392, pp. 143–153.

Huck, H. (2012). 'The Road to Open Source: Sharing a Ten Years Experience in Building OpendTect, the Open Source Seismic Interpretation Software'. In: *74th EAGE Conference and Exhibition-Workshops*.

Hyndman, R. D., C. A. Currie and S. Mazzotti (2005). 'Subduction Zone Backarcs, Mobile Belts, and Orogenic Heat'. In: *GSA TODAY* 15.2, p. 7. DOI: 10:1130/1052-5173(2005)015<4:SZBMBA>2.0.CO;2.

Isacks, B. L. (1988). 'Uplift of the Central Andean Plateau and Bending of the Bolivian Orocline'. In: *Journal of Geophysical Research: Solid Earth* 93.B4, pp. 3211–3231. ISSN: 2156-2202. DOI: 10.1029/JB093iB04p03211.

Ito, G. (2001). 'Reykjanes V-Shaped Ridges Originating from a Pulsing and Dehydrating Mantle Plume'. In: *Nature* 411, pp. 681–684.

Ito, G. T. and J. Lin (1995). 'Mantle Temperature Anomalies along the Past and Paleoaxes of the Galápagos Spreading Center as Inferred from Gravity Analyses'. In: *J. Geophys. Res.* 100.B3, pp. 3733–3745.

Jacobson, R. S. (1992). 'Impact of Crustal Evolution on Changes of the Seismic Properties of the Uppermost Oceanic Crust'. In: *Rev. Geophys.* 30.1, pp. 23–42.

Jacquey, A. B. and M. Cacace (2017). *GOLEM, a MOOSE-Based Application v1.0*. Zenodo. DOI: 10.5281/zenodo.999401. URL: https://zenodo.org/record/999401 (visited on 25/03/2019).

– (2018). 'How a State- and Rate-Dependent Friction and Its Coupling to Porosity Evolution Influence the Deformation Dynamics of the Lithosphere'. In: *Proceedings GeoMod2018 v1.0*. GeoMod2018 Barcelona. Barcelona, Spain, pp. 80–81. URL: http://www.ub.edu/geomod2018/Program_files/Abstracts_book_v1.0_LR.pdf (visited on 01/02/2019).

Jakobsson, M. et al. (2012). 'International Bathymetric Chart of the Arctic Ocean (IBCAO) Version 3.0'. In: *Geophys. Res. Lett.* 39.L12609. DOI: 10.1029/2012GL052219.

Jammes, S. and R. S. Huismans (2012). 'Structural Styles of Mountain Building: Controls of Lithospheric Rheologic Stratification and Extensional Inheritance: CRUSTAL STRENGTH AND MOUNTAIN BUILDING'. In: *Journal of Geophysical Research: Solid Earth* 117.B10. ISSN: 01480227. DOI: 10.1029/2012JB009376.

Jha, K., E. M. Parmentier and J. P. Morgan (1994). 'The Role of Mantle-Depletion and Melt-Retention Buoyancy in Spreading-Center Segmentation'. In: *Earth. Planet. Sci. Lett.* 125.1-4, pp. 221–234.

Johnston, A. C. and E. S. Schweig (1996). 'THE ENIGMA OF THE NEW MADRID EARTHQUAKES OF 1811–1812'. In: *Annual Review of Earth and Planetary Sciences* 24.1, pp. 339–384. ISSN: 0084-6597, 1545-4495. DOI: 10.1146/annurev.earth.24.1.339.

Jones, S. M., N. White and J. Maclennan (2002). 'V-Shaped Ridges around Iceland: Implications for Spatial and Temporal Patterns of Mantle Convection'. In: *Geochem. Geophys. Geosyst.* 3.10, 1059. DOI: 10.1029/2002GC000361.

Jordan, T. E., B. L. Isacks, R. W. Allmendinger, J. A. Brewer, V. A. Ramos and C. J. Ando (1983). 'Andean Tectonics Related to Geometry of Subducted Nazca Plate'. In: *Geological Society of America Bulletin* 94.3, pp. 341–361. ISSN: 0016-7606, 1943-2674. DOI: 10.1130/0016-7606(1983)94<341: ATRTGO>2.0.CO;2.

Kameyama, M., D. A. Yuen and S.-I. Karato (1999). 'Thermal-Mechanical Effects of Low-Temperature Plasticity (the Peierls Mechanism) on the Deformation of a Viscoelastic Shear Zone'. In: *Earth and Planetary Science Letters* 168.1, pp. 159–172. ISSN: 0012-821X. DOI: 10.1016/S0012-821X(99)00040-0.

Kandilarov, A., R. Mjelde, R. B. Pedersen, B. Hellevang, C. Papenberg, C. J. Petersen, L. Planert and E. Flueh (2012). 'The Northern Boundary of the Jan Mayen Microcontinent, North Atlantic Determined from Ocean Bottom Seismic, Multichannel Seismic, and Gravity Data'. In: *Mar. Geophys. Res.* 33.1, pp. 55–76.

Kandilarov, A., R. Mjelde, E. Flueh and R. B. Pedersen (2015). 'Vp/Vs-Ratios and Anisotropy on the Northern Jan Mayen Ridge, North Atlantic, Determined from Ocean Bottom Seismic Data'. In: *Polar Science* 9.3, pp. 293–310. ISSN: 1873-9652. DOI: 10.1016/j.polar.2015.06.001.

Karato, S. and H. Jung (1998). 'Water, Partial Melting and the Origin of the Seismic Low Velocity and High Attenuation Zone in the Upper Mantle'. In: *Earth Planet. Sci. Lett.* 157, pp. 193–207.

Karato, S.-i. and P. Wu (1993). 'Rheology of the Upper Mantle: A Synthesis'. In: *Science* 260.5109, pp. 771–778. ISSN: 0036-8075. JSTOR: 2881160.

Kennett, B. L. N., E. R. Engdahl and R. Buland (1995). 'Constraints on Seismic Velocities in the Earth from Traveltimes'. In: *Geophysical Journal International* 122.1, pp. 108–124. ISSN: 0956-540X, 1365-246X. DOI: 10.1111/j.1365-246X.1995.tb03540.x.

Kenyon, S., R. Forsberg and B. Coakley (2008). 'New Gravity Field for the Arctic'. In: *Eos, Transactions American Geophysical Union* 89.32, pp. 289–290.

Khan, M. A. et al. (1999). 'The Lithospheric Structure of the Kenya Rift as Revealed by Wide-Angle Seismic Measurements'. In: *Geological Society, London, Special Publications* 164.1, pp. 257–269. ISSN: 0305-8719, 2041-4927. DOI: 10.1144/GSL.SP.1999.164.01.13.

Kirchner, A. (1997). '3D-Dichtemodellierung zur Anpassung des Schwere- und des Schwerepotentialfeldes der zentralen Anden'. In: *Berliner geowissenschaftliche Abhandlungen*. Berliner geowissenschaftliche Abhandlungen 25.B. ISSN: 0722-687X.

Kley, J. (1999). 'Geologic and Geometric Constraints on a Kinematic Model of the Bolivian Orocline'. In: *Journal of South American Earth Sciences* 12.2, pp. 221–235. URL: http://www.sciencedirect.com/science/article/pii/S0895981199000152 (visited on 07/06/2017).

Kley, J., C. R. Monaldi and J. A. Salfity (1999). 'Along-Strike Segmentation of the Andean Foreland: Causes and Consequences'. In: *Tectonophysics* 301.1–2, pp. 75–94. ISSN: 0040-1951. DOI: 10.1016/S0040-1951(98)90223-2.

Kley, J. and C. R. Monaldi (2002). 'Tectonic Inversion in the Santa Barbara System of the Central Andean Foreland Thrust Belt, Northwestern Argentina: INVERSION TECTONICS, NW ARGENTINA'. In: *Tectonics* 21.6, pp. 11-1-11–18. ISSN: 02787407. DOI: 10.1029/2002TC902003.

Klingelhöfer, F., L. Géli, L. Matias, N. Steinsland and J. Mohr (2000a). 'Crustal Structure of a Super-Slow Spreading Centre: A Seismic Refraction Study of Mohns Ridge, 72°N'. In: *Geophys. J. Int.* 141, pp. 509–526.

Klingelhöfer, F., L. Géli and R. S. White (2000b). 'Geophysical and Geochemical Constraints on Crustal Accretion at the Very-Slow Spreading Mohns Ridge'. In: *Geophys. Res. Lett.* 27.10, pp. 1547–1550.

Kneller, E. A., P. E. van Keken, I. Katayama and S. Karato (2007). 'Stress, Strain, and B-Type Olivine Fabric in the Fore-Arc Mantle: Sensitivity Tests Using High-Resolution Steady-State Subduction Zone Models'. In: *Journal of Geophysical Research: Solid Earth* 112.B4. ISSN: 2156-2202. DOI: 10.1029/2006JB004544.

Kodaira, S., R. Mjelde, K. Gunnarsson, H. Shiobara and H. Shimamura (1998a). 'Evolution of Oceanic Crust on the Kolbeinsey Ridge, North of Iceland, over the Past 22 Myr'. In: *Terra Nova* 10, pp. 27–31.

– (1998b). 'Structure of the Jan Mayen Microcontinent and Implication for Its Evolution'. In: *Geophys. J. Int.* 132, pp. 383–400.

Kodaira, S., R. Mjelde, H. Shimamura, K. Gunnarsson and H. Shiobara (1997). 'Crustal Structure of the Kolbeinsey Ridge, N. Atlantic, Obtained by Use of Ocean Bottom Seismographs'. In: *J. Geophys. Res.* 102.B2, pp. 3131–3151.

Koptev, A., S. Cloetingh, E. Burov, T. François and T. Gerya (2017). 'Long-Distance Impact of Iceland Plume on Norway's Rifted Margin'. In: *Sci. Rep.* 7.

Korenaga, J. (2008). 'Urey Ratio and the Structure and Evolution of Earth's Mantle'. In: *Rev. Geophys.* 46.2.

Kreemer, C., G. Blewitt and E. C. Klein (2014). 'A Geodetic Plate Motion and Global Strain Rate Model'. In: *Geochemistry, Geophysics, Geosystems* 15.10, pp. 3849–3889. ISSN: 15252027. DOI: 10.1002/2014GC005407.

Kroll, H., A. Kirfel, R. Heinemann and B. Barbier (2012). 'Volume Thermal Expansion and Related Thermophysical Parameters in the Mg, Fe Olivine Solid-Solution Series'. In: *Eur. J. Mineral.* 24.6, pp. 935–956.

Lallemand, S., A. Heuret and D. Boutelier (2005). 'On the Relationships between Slab Dip, Back-arc Stress, Upper Plate Absolute Motion, and Crustal Nature in Subduction Zones'. In: *Geochemistry, Geophysics, Geosystems* 6.9. ISSN: 1525-2027. DOI: 10.1029/2005GC000917.

Laske, G., G. Masters, Z. Ma and M. Pasyanos (2013). 'Update on CRUST 1.0- A 1-Degree Global Model of Earth's Crust.' In: *Geophys. Res. Abstracts* 15. Abstract EGU2013-2658.

Le Douaran, S. and B. Parsons (1982). 'A Note on the Correction of Ocean Floor Depths for Sediment Loading'. In: *J. Geophys. Res. Solid Earth* 87.B6, pp. 4715–4722.

Liu, M., Y. Yang, S. Stein, Y. Zhu and J. Engeln (2000). 'Crustal Shortening in the Andes: Why Do GPS Rates Differ from Geological Rates?' In: *Geophysical Research Letters* 27.18, pp. 3005–3008. ISSN: 1944-8007. DOI: 10.1029/2000GL008532.

Lucassen, F., R. Becchio, R. Harmon, S. Kasemann, G. Franz, R. Trumbull, H.-G. Wilke, R. L. Romer and P. Dulski (2001). 'Composition and Density Model of the Continental Crust at an Active Continental Margin—the Central Andes between 21 and 27 S'. In: *Tectonophysics* 341.1, pp. 195–223. URL: http://www.sciencedirect.com/science/article/pii/S0040195101001883 (visited on 11/04/2016).

Lucassen, F., S. Lewerenz, G. Franz, J. Viramonte and K. Mezger (1999). 'Metamorphism, Isotopic Ages and Composition of Lower Crustal Granulite Xenoliths from the Cretaceous Salta Rift, Argentina'. In: *Contributions to Mineralogy and Petrology* 134.4, pp. 325–341. ISSN: 0010-7999, 1432-0967. DOI: 10.1007/s004100050488.

Mall, D. M. and S. R. Sharma (2009). 'Tectonics and Thermal Structure of Western Satpura, India'. In: *Journal of Asian Earth Sciences* 34.3, pp. 450–457. ISSN: 1367-9120. DOI: 10.1016/j.jseaes.2008.07.004.

Marengo, H. (2015). *Neogene Micropaleontology and Stratigraphy of Argentina: The Chaco-Paranense Basin and the Península de Valdés*. Springer. ISBN: 3-319-12814-0.

Marot, M., T. Monfret, M. Gerbault, G. Nolet, G. Ranalli and M. Pardo (2014). 'Flat versus Normal Subduction Zones: A Comparison Based on 3-D Regional Traveltime Tomography and Petrological Modelling of Central Chile and Western Argentina (29°–35°S)'. In: *Geophysical Journal International* 199.3, pp. 1633–1654. ISSN: 0956-540X, 1365-246X. DOI: 10.1093/gji/ggu355.

Marquart, G., H. Schmeling and O. Čadek (2007). 'Dynamic Models for Mantle Flow and Seismic Anisotropy in the North Atlantic Region and Comparison with Observations'. In: *Geochem. Geophys. Geosyst.* 8.2.

Martino, R. D. (2003). 'Las fajas de deformación dúctil de las Sierras Pampeanas de Córdoba: Una reseña general'. In: Revista de la Asociación Geológica Argentina 58.4, pp. 549–571.

McKenzie, D. P. (1967). 'Some Remarks on Heat Flow and Gravity Anomalies'. In: *Journal of Geophysical Research (1896-1977)* 72.24, pp. 6261–6273. ISSN: 2156-2202. DOI: 10.1029/JZ072i024p06261.

McKenzie, D. P., J. Jackson and K. Priestley (2005). 'Thermal Structure of Oceanic and Continental Lithosphere'. In: *Earth and Planetary Science Letters* 233.3-4, pp. 337–349. ISSN: 0012821X. DOI: 10.1016/j.epsl.2005.02.005.

Meeßen, C. (2017). *VelocityConversion*. Version v1.0.1. DOI: 10.5880/GFZ.6.1.2017.001. URL: http://pmd.gfz-potsdam.de/panmetaworks/showshort.php?id=escidoc:2301889.

– (2019a). *Data repository to "The thermal and rheological state of the Northern Argentinian foreland basins"*. Version v1.0. DOI: 10.5281/zenodo.3562215. URL: https://doi.org/10.5281/zenodo.3562215.

Meeßen, C., J. Sippel, M. Scheck-Wenderoth, C. Heine and M. R. Strecker (2018). 'Crustal Structure of the Andean Foreland in Northern Argentina: Results From Data-Integrative Three-Dimensional Density Modeling'. In: *Journal of Geophysical Research: Solid Earth* 123.2, pp. 1875–1903. ISSN: 2169-9356. DOI: 10.1002/2017JB014296.

Meeßen, C. (2019b). *pyGMS: lithosphere-scale rheological analyses of GMS models in Python*. Version v1.0.0. DOI: 10.5281/zenodo.3338066. URL: https://doi.org/10.5281/zenodo.3338066.

Menegazzo, M. C., O. Catuneanu and H. K. Chang (2016). 'The South American Retroarc Foreland System: The Development of the Bauru Basin in the Back-Bulge Province'. In: *Marine and Petroleum Geology* 73, pp. 131–156. ISSN: 0264-8172. DOI: 10.1016/j.marpetgeo.2016.02.027.

Mertz, D. F., W. D. Sharp and K. M. Haase (2004). 'Volcanism on the Eggvin Bank (Central Norwegian-Greenland Sea, Latitude 71°N): Age, Source, and Relationship to the Iceland and Putative Jan Mayen Plumes'. In: *J. Geodyn.* 38, pp. 57–83. DOI: 10.1016/j.jog.2004.03.003.

Milani, E. J. and P. V. Zalan (1999). 'An Outline of the Geology and Petroleum Systems of the Paleozoic Interior Basins of South America'. In: *Episodes* 22, pp. 199–205. URL: http://www.episodes.co.in/index.php/epi/article/download/62777/48976 (visited on 12/10/2015).

Mjelde, R., R. Aurvåg, S. Kodaira, H. Shimamura, K. Gunnarsson, A. Nakanishi and H. Shiobara (2002). 'Vp/Vs-Ratios from the Central Kolbeinsey Ridge to the Jan Mayen Basin, North Atlantic; Implications for Lithology, Porosity and Present-Day Stress Field'. In: *Mar. Geophys. Res.* 23.2, pp. 123–145.

Mjelde, R., I. Eckhoff, S. Solbakken, S. Kodaira, H. Shimamura, K. Gunnarsson, A. Nakanishi and H. Shiobara (2007). 'Gravity and S-Wave Modeling across the Jan Mayen Ridge, North Atlantic; Implications for Crustal Lithology and Continental Break-up Processes'. In: *Mar. Geophys. Res.* 28, pp. 27–41. DOI: 10.1007/s11001-006-9012-3.

Mjelde, R., T. Raum, A. J. Breivik and J. I. Faleide (2008). 'Crustal Transect across the North Atlantic'. In: *Mar. Geophys. Res.* 29, pp. 73–87. DOI: 10.1007/s11001-008-9046-9.

Molnar, P. and P. England (1990). 'Temperatures, Heat Flux, and Frictional Stress near Major Thrust Faults'. In: *Journal of Geophysical Research: Solid Earth* 95.B4, pp. 4833–4856. ISSN: 0148-0227. DOI: 10.1029/JB095iB04p04833.

Molnar, P. and H. Lyon-Caen (1988). 'Some Simple Physical Aspects of the Support, Structure, and Evolution of Mountain Belts'. In: *Geological Society of America Special Papers*. Vol. 218. Geological Society of America, pp. 179–208. ISBN: 978-0-8137-2218-4. DOI: 10.1130/SPE218-p179. URL: https://pubs.geoscienceworld.org/books/book/356/chapter/3796610/ (visited on 16/04/2019).

Mon, R. (1979). 'Esquéma Estructural Del Noroeste Argentino'. In: *Revista de la Asociacíon Geológica Argentina* 35, pp. 53–60.

Mon, R. and J. A. Salfity (1995). 'M 62: Petroleum Basins of South America'. In: AAPG. URL: http://archives.datapages.com/data/specpubs/memoir62/12monsal/0269.htm?aoai=I8X%2Faahs42dgYRhpbI8mK9soO7GKaylz50SQd%2F%2FZ4ALMUumsRZ1TxpjMs5zl%2FPyB.

Mouthereau, F., A. B. Watts and E. Burov (2013). 'Structure of Orogenic Belts Controlled by Lithosphere Age'. In: *Nature Geoscience* 6.9, pp. 785–789. ISSN: 1752-0908. DOI: 10.1038/ngeo1902.

Mpodozis, C. and V. A. Ramos (1990). 'The Andes of Chile and Argentina'. In: *Geology of the Andes and Its Relation to Hydrocarbon and Mineral Resources*. URL: http://archives.datapages.com/data/circ_pac/0012/0059_f.htm (visited on 25/10/2016).

Müller, R. D., M. Sdrolias, C. Gaina and W. R. Roest (2008). 'Age, Spreading Rates, and Spreading Asymmetry of the World's Ocean Crust'. In: *Geochemistry, Geophysics, Geosystems* 9.4, Q04006. ISSN: 1525-2027. DOI: 10.1029/2007GC001743.

Naif, S., K. Key, S. Constable and R. L. Evans (2013). 'Melt-Rich Channel Observed at the Lithosphere-Asthenosphere Boundary'. In: *Nature* 495, pp. 356–359. DOI: 10.1038/nature11939.

National Geophysical Date Center (2006). '2-Minute Gridded Global Relief Data (ETOPO2) v2. National Geophysical Data Center, NOAA'. In: DOI: 10.7289/V5J1012Q.

New, M., D. Lister, M. Hulme and I. Makin (2002). 'A High-Resolution Data Set of Surface Climate over Global Land Areas'. In: *Climate Research* 21.1, pp. 1–25. DOI: 10.3354/cr021001.

Nilfouroushan, F., R. Pysklywec, A. Cruden and H. Koyi (2013). 'Thermal-Mechanical Modeling of Salt-Based Mountain Belts with Pre-Existing Basement Faults: Application to the Zagros Fold and Thrust Belt, Southwest Iran: MODELING OF SALT-BASED MOUNTAIN BELTS'. In: *Tectonics* 32.5, pp. 1212–1226. ISSN: 02787407. DOI: 10.1002/tect.20075.

Noack, V., Y. Cherubini, M. Scheck-Wenderoth, B. Lewerenz, T. Höding, A. Simon and I. Moeck (2010). 'Assessment of the Present-Day Thermal Field (NE German Basin)—Inferences from 3D Modelling'. In: *Chemie der Erde - Geochemistry* 70, pp. 47–62. ISSN: 00092819. DOI: 10.1016/j.chemer.2010.05.008.

Nunns, A. (1982). 'The Structure and Evolution of the Jan Mayen Ridge and Surrounding Regions'. In: *Studies in Continental Margin Geology*. Ed. by J. S. Watkins and C. L. Drake. Vol. 34. Tulsa, Oklahoma, USA: Am. Assoc. Petrol. Geol., pp. 193–208.

Nürnberg, D. and R. D. Müller (1991). 'The Tectonic Evolution of the South Atlantic from Late Jurassic to Present'. In: *Tectonophysics* 191.1–2, pp. 27–53. ISSN: 0040-1951. DOI: 10.1016/0040-1951(91)90231-G.

Olesen, O., J. Ebbing, E. Lundin, E. Mauring, J. R. Skilbrei, T. H. Torsvik, E. K. Hansen, T. Henningsen, P. Midbøe and M. Sand (2007). 'An Improved Tectonic Model for the Eocene Opening of the Norwegian-Greenland Sea: Use of Modern Magnetic Data'. In: *Mar. Petrol. Geol.* 24, pp. 53–66. DOI: 10.1016/j.marpetgeo.2006.10.008.

Olsen, K. H. (1995). *Continental Rifts: Evolution, Structure, Tectonics*. Elsevier. 511 pp. ISBN: 978-0-08-052983-7.

Otamendi, J. E., G. I. Vujovich, J. D. de la Rosa, A. M. Tibaldi, A. Castro, R. D. Martino and L. P. Pinotti (2009). 'Geology and Petrology of a Deep Crustal Zone from the Famatinian Paleo-Arc, Sierras de Valle Fértil and La Huerta, San Juan, Argentina'. In: *Journal of South American Earth Sciences*. Magmatism, Crustal Evolution, and Metallogenesis of Carajás and Adjacent Provinces 27.4, pp. 258–279. ISSN: 0895-9811. DOI: 10.1016/j.jsames.2008.11.007.

Oxburgh E. R.and Parmentier, E. M. (1977). 'Compositional and Density Stratification in Oceanic Lithosphere-Causes and Consequences'. In: *J. Geol. Soc., London* 133.4, pp. 343–355.

Padula, E. and A. Mingramm (1963). 'The Fundamental Geological Pattern of the Chaco-Parana Basin (Argentina) in Relation to Its Oil Possibilities'. In: *World Petroleum Congress*, pp. 293–310. URL: https://www.onepetro.org/conference-paper/WPC-10019.

Parnell-Turner, R., N. White, T. Henstock, B. Murton, J. Maclennan and S. M. Jones (2014). 'A Continuous 55-Million-Year Record of Transient Mantle Plume Activity beneath Iceland'. In: *Nat. Geosci.* 7.12, pp. 914–919.

Peacock, S. M. (1992). 'Blueschist-Facies Metamorphism, Shear Heating, and P-T-t Paths in Subduction Shear Zones'. In: *Journal of Geophysical Research: Solid Earth* 97.B12, pp. 17693–17707. ISSN: 2156-2202. DOI: 10.1029/92JB01768.

– (1996). 'Thermal and Petrologic Structure of Subduction Zones'. In: *Subduction Top to Bottom*. Ed. by G. E. Bebout, D. W. Scholl, S. H. Kirby and J. P. Platt. American Geophysical Union, pp. 119–133. ISBN: 978-1-118-66457-5. DOI: 10.1029/GM096p0119. URL: http://onlinelibrary.wiley.com/doi/10.1029/GM096p0119/summary (visited on 20/09/2017).

Pearson, D. M., P. Kapp, P. G. DeCelles, P. W. Reiners, G. E. Gehrels, M. N. Ducea and A. Pullen (2013). 'Influence of Pre-Andean Crustal Structure on Cenozoic Thrust Belt Kinematics and Shortening Magnitude: Northwestern Argentina'. In: *Geosphere* 9.6, pp. 1766–1782. URL: http://geosphere.gsapubs.org/content/9/6/1766.short (visited on 14/02/2017).

Perarnau, M., H. Gilbert, P. Alvarado, R. Martino and M. Anderson (2012). 'Crustal Structure of the Eastern Sierras Pampeanas of Argentina Using High Frequency Local Receiver Functions'. In: *Tectonophysics* 580, pp. 208–217. ISSN: 0040-1951. DOI: 10.1016/j.tecto.2012.09.021.

Pérez-Gussinyé, M., A. R. Lowry and A. B. Watts (2007). 'Effective Elastic Thickness of South America and Its Implications for Intracontinental Deformation: ELASTIC THICKNESS'. In: *Geochemistry, Geophysics, Geosystems* 8.5, n/a–n/a. ISSN: 15252027. DOI: 10.1029/2006GC001511.

Peri, V. G., H. Barcelona, M. C. Pomposiello and A. Favetto (2015). 'Magnetotelluric Characterization through the Ambargasta-Sumampa Range: The Connection between the Northern and Southern Trace of the Río de La Plata Craton – Pampean Terrane Tectonic Boundary'. In: *Journal of South American Earth Sciences* 59, pp. 1–12. ISSN: 08959811. DOI: 10.1016/j.jsames.2015.01.003.

Peri, V. G., M. C. Pomposiello, A. Favetto, H. Barcelona and E. A. Rossello (2013). 'Magnetotelluric Evidence of the Tectonic Boundary between the Río de La Plata Craton and the Pampean

Terrane (Chaco-Pampean Plain, Argentina): The Extension of the Transbrasiliano Lineament'. In: *Tectonophysics* 608, pp. 685–699. ISSN: 00401951. DOI: 10.1016/j.tecto.2013.08.012.

Peron-Pinvidic, G., L. Gernigon, C. Gaina and P. Ball (2012a). 'Insights from the Jan Mayen System in the Norwegian-Greenland Sea-I. Mapping of a Microcontinent'. In: *Geophys. J. Int.* 191, pp. 385–412.

– (2012b). 'Insights from the Jan Mayen System in the Norwegian-Greenland Sea-II. Architecture of a Microcontinent'. In: *Geophys. J. Int.* 191, pp. 413–435.

Pezzi, E. E. and M. E. Mozetic (1989). 'Cuencas Sedimentarias de La Region Chacoparanense'. In: *Cuencas Sedimentarias Argentinas*, pp. 65–78.

Pfiffner, O. A. (2017). 'Thick-Skinned and Thin-Skinned Tectonics: A Global Perspective'. In: *Geosciences* 7.3, p. 71. DOI: 10.3390/geosciences7030071.

Pilidou, S., K. Priestley, E. Debayle and O. Gudmundsson. (2005). 'Rayleigh Wave Tomography in the North Atlantic: High Resolution Images of the Iceland, Azores and Eifel Mantle Plumes'. In: *Lithos.* 79, pp. 453–474.

Prezzi, C. B., H.-J. Götze and S. Schmidt (2009). '3D Density Model of the Central Andes'. In: *Physics of the Earth and Planetary Interiors* 177.3–4, pp. 217–234. ISSN: 0031-9201. DOI: 10.1016/j.pepi.2009.09.004.

– (2014). 'Andean Foreland Evolution and Flexure in NW Argentina: Chaco–Paraná Basin'. In: *Tectonophysics* 628, pp. 228–243. ISSN: 00401951. DOI: 10.1016/j.tecto.2014.04.041.

Priestley, K. and D. P. McKenzie (2006). 'The Thermal Structure of the Lithosphere from Shear Wave Velocities'. In: *Earth and Planetary Science Letters* 244.1–2, pp. 285–301. ISSN: 0012-821X. DOI: 10.1016/j.epsl.2006.01.008.

– (2013). 'The Relationship between Shear Wave Velocity, Temperature, Attenuation and Viscosity in the Shallow Part of the Mantle'. In: *Earth and Planetary Science Letters* 381, pp. 78–91. ISSN: 0012-821X. DOI: 10.1016/j.epsl.2013.08.022.

Prodehl, C., K. Fuchs and J. Mechie (1997). 'Seismic-Refraction Studies of the Afro-Arabian Rift System — a Brief Review'. In: *Tectonophysics* 278.1-4, pp. 1–13. ISSN: 00401951. DOI: 10.1016/S0040-1951(97)00091-7.

QGIS Devlopment Team (2009). *QGIS Geographic Information System.* URL: http://qgis.osgeo.org.

Ramos, V. A. (1988). 'Late Proterozoic-Early Paleozoic of South America-a Collisional History'. In: *Episodes* 11.3, pp. 168–174.

– (1999). 'Las Provincias Geológicas Del Territorio Argentino'. In: *Geología Argentina*. Ed. by R. Caminos. Anales 29. Buenos Aires: SEGEMAR, pp. 41–96. URL: http://aviris.gl.fcen.uba.ar/Bibliografia/Cap_03_PROVINCIAS_GEOLOGICAS.pdf (visited on 25/10/2016).

– (2008). 'The Basement of the Central Andes: The Arequipa and Related Terranes'. In: *Annual Review of Earth and Planetary Sciences* 36.1, pp. 289–324. DOI: 10.1146/annurev.earth.36.031207.124304.

Ramos, V. A. and R. N. Alonso (1995). 'El Mar Paranense En La Provincia de Jujuy'. In: *Rev.Geol. Jujuy* 10, pp. 73–80.

Ramos, V. A., E. O. Cristallini and D. J. Pérez (2002). 'The Pampean Flat-Slab of the Central Andes'. In: *Journal of South American Earth Sciences*. Flat-Slab Subduction in the Andes 15.1, pp. 59–78. ISSN: 0895-9811. DOI: 10.1016/S0895-9811(02)00006-8.

Ramos, V. A., T. E. Jordan, R. W. Allmendinger, C. Mpodozis, S. M. Kay, J. M. Cortés and M. Palma (1986). 'Paleozoic Terranes of the Central Argentine-Chilean Andes'. In: *Tectonics* 5.6, pp. 855–880. ISSN: 1944-9194. DOI: 10.1029/TC005i006p00855.

Ramos, V. A., G. Vujovich, R. Martino and J. Otamendi (2010). 'Pampia: A Large Cratonic Block Missing in the Rodinia Supercontinent'. In: *Journal of Geodynamics*. Supercontinents and Crustal Evolution 50.3–4, pp. 243–255. ISSN: 0264-3707. DOI: 10.1016/j.jog.2010.01.019.

Rapela, C. W., R. J. Pankhurst, C. Casquet, C. M. Fanning, E. G. Baldo, J. M. González-Casado, C. Galindo and J. Dahlquist (2007). 'The Río de La Plata Craton and the Assembly of SW Gondwana'. In: *Earth-Science Reviews* 83.1, pp. 49–82. ISSN: 0012-8252. DOI: 10.1016/j.earscirev.2007.03.004.

Rickers, F., A. Fichtner and J. Trampert (2013). 'The Iceland Jan Mayen Plume System and Its Impact on Mantle Dynamics in the North Atlantic Region: Evidence from Full-Waveform Inversion.' In: *Earth Planet. Sci. Lett* 367, pp. 39–51.

Ritsema, J., H. J. van Heist and J. H. Woodhouse (1999). 'Complex Shear Wave Velocity Structure Imaged beneath Africa and Iceland'. In: *Science* 286, pp. 1925–1928.

Rosa, M. L., B. Collaço, M. Assumpção, N. Sabbione and G. Sánchez (2016). 'Thin Crust beneath the Chaco-Paraná Basin by Surface-Wave Tomography'. In: *Journal of South American Earth Sciences* 66, pp. 1–14. ISSN: 0895-9811. DOI: 10.1016/j.jsames.2015.11.010.

Rothstein, D. A. and C. E. Manning (2003). 'Geothermal Gradients in Continental Magmatic Arcs; Constraints from the Eastern Peninsular Ranges Batholith, Baja California, Mexico'. In: *Special Paper 374: Tectonic Evolution of Northwestern Mexico and the Southwestern USA*. Vol. 374. Geological Society of America, pp. 337–354. ISBN: 978-0-8137-2374-7. DOI: 10.1130/0-8137-2374-4.337. URL: https://pubs.geoscienceworld.org/books/book/521/chapter/3801401/ (visited on 18/04/2019).

Rudnick, R. L. and D. M. Fountain (1995). 'Nature and Composition of the Continental Crust: A Lower Crustal Perspective'. In: *Reviews of Geophysics* 33.3, pp. 267–309. ISSN: 1944-9208. DOI: 10.1029/95RG01302.

Rybacki, E. and G. Dresen (2000). 'Dislocation and Diffusion Creep of Synthetic Anorthite Aggregates'. In: *Journal of Geophysical Research: Solid Earth* 105.B11, pp. 26017–26036. ISSN: 2156-2202. DOI: 10.1029/2000JB900223.

Rychert, C. A. and P. M. Shearer (2009). 'A Global View of the Lithosphere-Asthenosphere Boundary'. In: *Science* 324.5926, pp. 495–498. ISSN: 0036-8075, 1095-9203. DOI: 10.1126/science.1169754. pmid: 19390041.

Sandstå N, R., R. B. Pedersen, R. Williams, D. Bering, M. Magnus, M. Sand and H. Brekke (2012). 'Submarine Fieldwork on the Jan Mayen Ridge: Integrated Seismic and ROV-Sampling. Norwegian Petroleum Directorate, Stavanger, Norway'. In: URL: http://www.npd.no/Global/Norsk/3-Publikasjoner/%20Presentasjoner/Submarine-fieldwork-on-the-Jan-Mayen-Ridge-%202012.pdf.

Sandwell, D. T. (2001). *Cooling of the Oceanic Lithosphere and Ocean Floor Topography*. URL: http://topex.ucsd.edu/geodynamics/07cooling.pdf (visited on 07/12/2017).

Schaeffer, A. J. and S. Lebedev (2013). 'Global Shear Speed Structure of the Upper Mantle and Transition Zone'. In: *Geophysical Journal International* 194.1, pp. 417–449. ISSN: 0956-540X, 1365-246X. DOI: 10.1093/gji/ggt095.

Scheck-Wenderoth, M., M. Cacace, Y. P. Maystrenko, Y. Cherubini, V. Noack, B. O. Kaiser, J. Sippel and L. Björn (2014). 'Models of Heat Transport in the Central European Basin System: Effective Mechanisms at Different Scales'. In: *Marine and Petroleum Geology*. Fluid-Rock-Tectonics Interactions in Basins and Orogens 55, pp. 315–331. ISSN: 0264-8172. DOI: 10.1016/j.marpetgeo.2014.03.009.

Schellart, W. P. (2004). 'Quantifying the Net Slab Pull Force as a Driving Mechanism for Plate Tectonics'. In: *Geophysical Research Letters* 31.7. ISSN: 1944-8007. DOI: 10.1029/2004GL019528.

Schenk, C. J., R. J. Viger and C. P. Anderson (2000). *Maps Showing Geology, Oil and Gas Fields, and Geologic Provinces of the South America Region*. USGS. URL: http://pubs.usgs.gov/of/1997/ofr-97-470/OF97-470D/.

Schilling, J. (1999). 'Dispersion of the Jan Mayen and Iceland Mantle Plumes in the Arctic: A He-Pb-Nd-Sr Isotope Tracer Study of Basalts from the Kolbeinsey, Mohns, and Knipovich Ridges'. In: *J. Geophys. Res.* 104, pp. 10543–10569.

Schmidt, S. and H. J. Götze (1998). 'Interactive Visualization and Modification of 3-D Models Using GIS Functions.' In: *Phys. Chem. Earth* 23, pp. 289–296.

Schmidt, S., C. Plonka, H.-J. Götze and B. Lahmeyer (2011). 'Hybrid Modelling of Gravity, Gravity Gradients and Magnetic Fields'. In: *Geophys. Prospect.* 59.6, pp. 1046–1051.

Schmitz, M. and J. Kley (1997). 'The Geometry of the Central Andean Backarc Crust: Joint Interpretation of Cross-Section Balancing and Seismic Refraction Data'. In: *Journal of South American Earth Sciences* 10.1, pp. 99–110. ISSN: 0895-9811. DOI: 10.1016/S0895-9811(97)00009-6.

Schön, J. H. (2015). *Physical Properties of Rocks: Fundamentals and Principles of Petrophysics*. Elsevier. 514 pp. ISBN: 978-0-08-100423-4.

Schoonman, C. M., N. J. White and D. Pritchard (2017). 'Radial Viscous Fingering of Hot Asthenosphere within the Icelandic Plume beneath the North Atlantic Ocean'. In: *Earth Planet. Sci. Lett.* 468, pp. 51–61.

Schutt, D. L. and C. E. Lesher (2006). 'Effects of Melt Depletion on the Density and Seismic Velocity of Garnet and Spinel Iherzolite'. In: *J. Geophys. Res.* 111, B05401.

Scott, D. R. and D. Stevenson (1989). 'A Self-Consistent Model of Melting, Magma Migration and Buoyancy-Driven Circulation beneath Mid-Ocean Ridges'. In: *J. Geophys. Res.* 94.B3, pp. 2973–2988.

Segerstrom, K. and J. C. M. Turner (1972). *A Conspicuous Flexure in Regional Structural Trend in the Puna of Northwestern Argentine*. Geological Survey Professional Paper 800B:205-9. USGS, B205–B209.

Shapiro, N. M. and M. H. Ritzwoller (2004). 'Thermodynamic Constraints on Seismic Inversions'. In: *Geophysical Journal International* 157.3, pp. 1175–1188. ISSN: 0956540X, 1365246X. DOI: 10.1111/j.1365-246X.2004.02254.x.

Sheffels, B. M. (1990). 'Lower Bound on the Amount of Crustal Shortening, in the Central Bolivian Andes'. In: *Geology* 18.9, pp. 812–815. ISSN: 0091-7613. DOI: 10.1130/0091-7613(1990)018<0812: LBOTAO>2.3.CO;2.

Shorttle, O., J. Maclennan and S. M. Jones (2010). 'Control of the Symmetry of Plume-Ridge Interaction by Spreading Ridge Geometry'. In: *Geochem. Geophys. Geosyst.* 11.7.

Simmons, N. A., A. M. Forte, L. Boschi and S. P. Grand (2010). 'GyPSuM: A Joint Tomographic Model of Mantle Density and Seismic Wave Speeds'. In: *Journal of Geophysical Research* 115.B12. ISSN: 0148-0227. DOI: 10.1029/2010JB007631.

Simmons, N. A., A. M. Forte and S. P. Grand (2006). 'Constraining Mantle Flow with Seismic and Geodynamic Data: A Joint Approach'. In: *Earth and Planetary Science Letters* 246.1, pp. 109–124. ISSN: 0012-821X. DOI: 10.1016/j.epsl.2006.04.003.

– (2009). 'Joint Seismic, Geodynamic and Mineral Physical Constraints on Three-Dimensional Mantle Heterogeneity: Implications for the Relative Importance of Thermal versus Compositional Heterogeneity'. In: *Geophysical Journal International* 177.3, pp. 1284–1304. ISSN: 0956540X, 1365246X. DOI: 10.1111/j.1365-246X.2009.04133.x.

Simpson, C., R. D. Law, L. Gromet, R. Miro and C. Northrup (2003). 'Paleozoic Deformation in the Sierras de Cordoba and Sierra de Las Minas, Eastern Sierras Pampeanas, Argentina'. In: *Journal of South American Earth Sciences* 15.7, pp. 749–764. ISSN: 08959811. DOI: 10.1016/S0895-9811(02)00130-X.

Simpson, F. (2001). 'Fluid Trapping at the Brittle–Ductile Transition Re-Examined'. In: *Geofluids* 1.2, pp. 123–136. ISSN: 1468-8123. DOI: 10.1046/j.1468-8123.2001.00011.x.

Sippel, J., C. Meeßen, M. Cacace, J. Mechie, S. Fishwick, C. Heine, M. Scheck-Wenderoth and M. R. Strecker (2017). 'The Kenya Rift Revisited: Insights into Lithospheric Strength through Data-Driven 3-D Gravity and Thermal Modelling'. In: *Solid Earth* 8.1, pp. 45–81. ISSN: 1869-9510. DOI: 10.5194/se-8-45-2017.

Sleep, N. H. (1997). 'Lateral Flow and Ponding of Starting Plume Material'. In: *J. Geophys. Res.* 102.B5, pp. 10001–10012.

Smith, M. and P. Mosley (1993). 'Crustal Heterogeneity and Basement Influence on the Development of the Kenya Rift, East Africa'. In: *Tectonics* 12.2, pp. 591–606. ISSN: 1944-9194. DOI: 10.1029/92TC01710.

Snoke, J. A. and D. E. James (1997). 'Lithospheric Structure of the Chaco and Paraná Basins of South America from Surface-Wave Inversion'. In: *Journal of Geophysical Research: Solid Earth* 102.B2, pp. 2939–2951. ISSN: 2156-2202. DOI: 10.1029/96JB03180.

Sobolev, S. V., A. Y. Babeyko, I. Koulakov and O. Oncken (2006). 'Mechanism of the Andean Orogeny: Insight from Numerical Modeling'. In: *The Andes: Active Subduction Orogeny*. Ed. by O. Oncken, G. Chong, G. Franz, P. Giese, H.-J. Götze, V. A. Ramos, M. R. Strecker and P. Wigger. Frontiers in Earth Sciences. Berlin, Heidelberg: Springer Berlin Heidelberg, pp. 513–535. ISBN: 978-3-540-48684-8. DOI: 10.1007/978-3-540-48684-8_25. URL: https://doi.org/10.1007/978-3-540-48684-8_25 (visited on 19/09/2018).

Sobolev, S. V., H. Zeyen, G. Stoll, F. Werling, R. Altherr and K. Fuchs (1996). 'Upper Mantle Temperatures from Teleseismic Tomography of French Massif Central Including Effects of Composition, Mineral Reactions, Anharmonicity, Anelasticity and Partial Melt'. In: *Earth and Planetary Science Letters* 139.1–2, pp. 147–163. ISSN: 0012-821X. DOI: 10.1016/0012-821X(95)00238-8.

Stein, C. A. and S. Stein (1992). 'A Model for the Global Variation in Oceanic Depth and Heat Flow with Lithospheric Age'. In: *Nature* 359.6391, p. 123. ISSN: 1476-4687. DOI: 10.1038/359123a0.

Stewart, J. and A. B. Watts (1997). 'Gravity Anomalies and Spatial Variations of Flexural Rigidity at Mountain Ranges'. In: *Journal of Geophysical Research: Solid Earth* 102.B3, pp. 5327–5352. ISSN: 0148-0227. DOI: 10.1029/96JB03664.

Stixrude, L. and C. Lithgow-Bertelloni (2005). 'Mineralogy and Elasticity of the Oceanic Upper Mantle: Origin of the Low-Velocity Zone'. In: *J. Geophys. Res.* 110.B03204. DOI: 10.1029/2004JB002965.

Storchak, D. A., D. D. Giacomo, I. Bondár, E. R. Engdahl, J. Harris, W. H. K. Lee, A. Villaseñor and P. Bormann (2013). 'Public Release of the ISC–GEM Global Instrumental Earthquake Catalogue (1900–2009)'. In: *Seismological Research Letters* 84.5, pp. 810–815. ISSN: 0895-0695. DOI: 10.1785/0220130034.

Strecker, M. R., P. Cerveny, A. L. Bloom and D. Malizia (1989). 'Late Cenozoic Tectonism and Landscape Development in the Foreland of the Andes: Northern Sierras Pampeanas (26°–28°S), Argentina'. In: *Tectonics* 8.3, pp. 517–534. ISSN: 1944-9194. DOI: 10.1029/TC008i003p00517.

Strecker, M. R., G. E. Hilley, B. Bookhagen and E. R. Sobel (2011). 'Structural, Geomorphic, and Depositional Characteristics of Contiguous and Broken Foreland Basins: Examples from the Eastern Flanks of the Central Andes in Bolivia and NW Argentina'. In: *Tectonics of Sedimentary Basins*. Ed. by C. Busby and A. Azor. John Wiley & Sons, Ltd, pp. 508–521. ISBN: 978-1-4443-4716-6. URL: http://onlinelibrary.wiley.com/doi/10.1002/9781444347166.ch25/summary (visited on 26/10/2015).

Syracuse, E. M., P. E. van Keken and G. A. Abers (2010). 'The Global Range of Subduction Zone Thermal Models'. In: *Physics of the Earth and Planetary Interiors*. Special Issue on Deep Slab and Mantle Dynamics 183.1, pp. 73–90. ISSN: 0031-9201. DOI: 10.1016/j.pepi.2010.02.004.

Tan, P., A. J. Breivik, R. G. Trønnes, R. Mjelde, R. Azuma and S. Eide (2017). 'Crustal Structure and Origin of the Eggvin Bank West of Jan Mayen, NE Atlantic'. In: *J. Geophys. Res: Solid Earth*. 122. 2016JB013495, pp. 43–62. ISSN: 2169-9356. DOI: 10.1002/2016JB013495.

Tan, P., J. Sippel, A. J. Breivik, C. Meeßen and M. Scheck-Wenderoth (2018). 'Lithospheric Control on Asthenospheric Flow From the Iceland Plume: 3-D Density Modeling of the Jan Mayen-East Greenland Region, NE Atlantic'. In: *Journal of Geophysical Research: Solid Earth* 123.10, pp. 9223–9248. ISSN: 2169-9356. DOI: 10.1029/2018JB015634.

Tassara, A. (2005). 'Interaction between the Nazca and South American Plates and Formation of the Altiplano–Puna Plateau: Review of a Flexural Analysis along the Andean Margin (15°–34°S)'. In: *Tectonophysics*. Andean Geodynamics: 399.1, pp. 39–57. ISSN: 0040-1951. DOI: 10.1016/j.tecto.2004.12.014.

– (2006). 'Factors Controlling the Crustal Density Structure underneath Active Continental Margins with Implications for Their Evolution: CONTINENTAL MARGIN CRUSTAL DENSITY'. In: *Geochemistry, Geophysics, Geosystems* 7.1, n/a–n/a. ISSN: 15252027. DOI: 10.1029/2005GC001040.

Tassara, A. and A. Echaurren (2012). 'Anatomy of the Andean Subduction Zone: Three-Dimensional Density Model Upgraded and Compared against Global-Scale Models: Anatomy of the Andean Subduction Zone'. In: *Geophysical Journal International* 189.1, pp. 161–168. ISSN: 0956540X. DOI: 10.1111/j.1365-246X.2012.05397.x.

Tassara, A., C. Swain, R. Hackney and J. Kirby (2007). 'Elastic Thickness Structure of South America Estimated Using Wavelets and Satellite-Derived Gravity Data'. In: *Earth and Planetary Science Letters* 253.1-2, pp. 17–36. ISSN: 0012821X. DOI: 10.1016/j.epsl.2006.10.008.

Tesauro, M., M. K. Kaban and S. A. P. L. Cloetingh (2012). 'Global Strength and Elastic Thickness of the Lithosphere'. In: *Global and Planetary Change*. Coupled Deep Earth and Surface Processes in System Earth: Monitoring, Reconstruction and Process Modeling 90-91, pp. 51–57. ISSN: 0921-8181. DOI: 10.1016/j.gloplacha.2011.12.003.

Thiede, J. and G. Hempel (1991). 'Die Expedition ARKTIS-VII/1 Mit FS "Polarstern"'. In: *Rep. Polar. Res.*, pp. 1–137.

Trønnes, R. G., S. Planke, B. Sundvoll and P. Imsland (1999). 'Recent Volcanic Rocks from Jan Mayen: Low-Degree Melt Fractions of Enriched Northeast Atlantic Mantle'. In: *J. Geophys. Res.* 104.B4, pp. 7153–7168.

Turcotte, D. L. and G. Schubert (1973). 'Frictional Heating of the Descending Lithosphere'. In: *Journal of Geophysical Research* 78.26, pp. 5876–5886. ISSN: 2156-2202. DOI: 10.1029/JB078i026p05876.

– (1982). *Geodynamics: Applications of Continuum Physics to Geological Problems*. Wiley. ISBN: 978-0-471-06018-5.

– (2014). *Geodynamics*. third. Cambridge: Cambridge University Press. ISBN: 978-0-521-18623-0.

Uba, C. E., C. Heubeck and C. Hulka (2006). 'Evolution of the Late Cenozoic Chaco Foreland Basin, Southern Bolivia'. In: *Basin Research* 18.2, pp. 145–170. ISSN: 1365-2117. DOI: 10.1111/j.1365-2117.2006.00291.x.

Uieda, L. and V. C. F. Barbosa (2011). '3D Gravity Inversion by Planting Anomalous Densities'. In: *SBGf 2011 Expanded Abstracts*.

Uieda, L., V. Barbosa and C. Braitenberg (2016a). 'Tesseroids: Forward-Modeling Gravitational Fields in Spherical Coordinates'. In: *GEOPHYSICS* 81.5, F41–F48. ISSN: 0016-8033. DOI: 10.1190/geo2015-0204.1.

Uieda, L. and V. C. F. Barbosa (2012). 'Robust 3D Gravity Gradient Inversion by Planting Anomalous Densities'. In: *GEOPHYSICS* 77.4, G55–G66. ISSN: 0016-8033, 1942-2156. DOI: 10.1190/geo2011-0388.1.

Uieda, L., V. C. Oliveira Jr and V. C. Barbosa (2013). 'Modeling the Earth with Fatiando a Terra'. In: *Proceedings of the 12th Python in Science Conference (SciPy 2013)*, pp. 96–103. URL: http://conference.scipy.org/proceedings/scipy2013/html/pdfs/uieda.pdf (visited on 17/10/2016).

Uieda, L. et al. (2016b). *Fatiando a Terra v0.5: Modeling and Inversion in Geophysics*. Zenodo. DOI: 10.5281/zenodo.157746. URL: https://zenodo.org/record/157746#.WVyeXSdpz0M (visited on 05/07/2017).

Uyeda, S. and T. Watanabe (1982). 'Terrestrial Heat Flow in Western South America'. In: *Tectonophysics*. Terrestrial Heat Flow 83.1, pp. 63–70. ISSN: 0040-1951. DOI: 10.1016/0040-1951(82)90007-5.

Vilà, M., M. Fernández and I. Jiménez-Munt (2010). 'Radiogenic Heat Production Variability of Some Common Lithological Groups and Its Significance to Lithospheric Thermal Modeling'. In: *Tectonophysics* 490.3–4, pp. 152–164. ISSN: 0040-1951. DOI: 10.1016/j.tecto.2010.05.003.

Voss, M. and W. Jokat (2007). 'Continent-Ocean Transition and Voluminous Magmatic Underplating Derived from P-Wave Velocity of the East Greenland Continental Margin'. In: *Geophys. J. Int.* 170, pp. 580–604. DOI: 10.1111/j.1365-246X.2007.03438.x.

Watts, A. B., S. H. Lamb, J. D. Fairhead and J. F. Dewey (1995). 'Lithospheric Flexure and Bending of the Central Andes'. In: *Earth and Planetary Science Letters* 134.1–2, pp. 9–21. ISSN: 0012-821X. DOI: 10.1016/0012-821X(95)00095-T.

Weigel, W. et al. (1995). 'Investigations of the East Greenland Continental Margin between 70° and 72°N by Deep Seismic Sounding and Gravity Studies'. In: *Mar. Geophys.* 17, pp. 167–199.

Wellmann, J. F., F. G. Horowitz, E. Schill and K. Regenauer-Lieb (2010). 'Towards Incorporating Uncertainty of Structural Data in 3D Geological Inversion'. In: *Tectonophysics* 490.3–4, pp. 141–151. ISSN: 0040-1951. DOI: 10.1016/j.tecto.2010.04.022.

White, R. S., J. W. Bown and J. R. Smallwood (1995). 'The Temperature of the Iceland Plume and Origin of Outward-Propagating V-Shaped Ridges'. In: *J. Geol. Soc.* 152, pp. 1039–1045.

Winn Jr, R. D. and J. C. Steinmetz (1998). 'Upper Paleozoic Strata of the Chaco-Paraná Basin, Argentina, and the Great Gondwana Glaciation'. In: *Journal of South American Earth Sciences* 11.2, pp. 153–168. ISSN: 0895-9811. DOI: 10.1016/S0895-9811(98)00007-8.

Xue, M. and R. M. Allen (2005). 'Asthenospheric Channeling of the Icelandic Upwelling: Evidence from Seismic Anisotropy'. In: *Earth Planet. Sci. Lett.* 235, pp. 167–182.

Zapata Henao, S., E. Sobel and C. Del Papa (2018). 'Influence of Inherited Structures in Along-Strike Segmentation of the Foreland Basins in the Central Andes'. In: EGU General Assembly Conference Abstracts. Vol. 20, p. 7226. URL: http://adsabs.harvard.edu/abs/2018EGUGA..20.7226Z (visited on 18/04/2019).

Zhang, Y. and T. Lay (1999). 'Evolution of Oceanic Upper Mantle Structure'. In: *Phys Earth. Planet. In.* 114, pp. 71–80.

A. Crustal structure of the Andean foreland in northern Argentina

A.1. Calculation of average sediment density

Athy's law of compaction (Athy, 1930) expresses the density of a fluid-saturated rock as a function of depth z and porosity ϕ:

$$\rho(z) = \rho_S(1 - \phi(z)) + \phi(z)\rho_L \tag{A.1}$$

where ρ_S is the solid rock density and ρ_L is the density of the pore fluid. The porosity ϕ is given by

$$\phi(z) = \phi_0 \cdot e^{-kz} \tag{A.2}$$

with porosity ϕ_0 at time of deposition and a lithology-dependent compaction factor k. The average density $\bar{\rho}$ of a sediment package with thickness $t = z - 0$ is then calculated by integrating (A.1)

$$\bar{\rho}(z) = \frac{1}{z} \cdot \int_0^z \rho(z) \, dz \tag{A.3}$$

which yields

$$\bar{\rho}(z) = \rho_S + \frac{\phi_0}{zk}(\rho_L - \rho_S)\left(1 - e^{-kz}\right) \tag{A.4}$$

A.2. Shear-wave velocity to density conversion

Goes et al. (2000) calculated the shear wave velocity of a rock with composition X at pressure P and temperature T, including anharmonicity and anelasticity, by

$$v_s(P, T, X, \omega) = \sqrt{\frac{\mu(P, T, X)}{\rho(P, T, X)}}(1 - \xi(\omega, T, a)) \tag{A.5}$$

where ξ describes the attenuation term

$$\xi(\omega, T, a) = \frac{2}{Q(\omega, T) \cdot \tan(\pi a/2)} \tag{A.6}$$

where μ is the shear modulus, ρ the density, Q the attenuation due to anelasticity depending on the wave frequency ω and the frequency exponent a. For pressures up to about $6\,\mathrm{GPa}$, shear modulus and density can be expressed for each mineral phase in X with

$$M(P, T) = M_0 + (T - T_0)\frac{\partial M}{\partial T} + (P - P_0)\frac{\partial M}{\partial P} \tag{A.7}$$

$$\rho\left(P,T\right) = \rho_0 \left(1 - \alpha_0\left(T - T_0\right) + \frac{P - P_0}{K}\right) \tag{A.8}$$

where M is the bulk modulus K or shear modulus μ and α the isobaric expansion coefficient. The mineral properties ρ_0, M_0, $\partial M/\partial T$, $\partial M/\partial P$ and α for the mantle-rock forming minerals olivine, diopside and enstatite were adopted from Cammarano et al. (2003), for spinel from Goes et al. (2000) and the attenuation parameters for Q were obtained from Sobolev et al. (1996).

For all depths in the tomography dataset, v_s was calculated for temperatures between 300 and 3000 K in steps of 1 K, and stored in a table along with the density corresponding to each temperature. Depth was converted to pressure using AK135 (Kennett et al., 1995). For a given v_s at z of the tomography model, the appropriate density was then obtained by linearly interpolating the densities corresponding to the two closest calculated velocities v_s in the table. The benefit of the lookup method compared to a numerical solver as used by Goes et al. (2000) is that, for a limited amount of depth values in the dataset, it is significantly faster in an interpreter-based programming language like Python.

A.3. Bouguer terrain correction

As stated in section 2.1.2.2.1, we used gravity data that had been reduced to Bouguer using the simple Bouguer slab (Barthelmes and Köhler, 2012; Förste et al., 2014). This correction is efficient in terms of computation as it neither takes into account sphericity of the Earth nor the hills and valleys of the topography. To assess the effects of these simplifications on the results of our study, we have computed a full Bouguer correction including topographic correction using ETOPO1 expanded to degree and order 2190 downloaded from ICGEM (Barthelmes and Köhler, 2012). This topographic model was set up with a lateral resolution of 0.0822°, equivalent to the maximum degree and order of EIGEN-6C4 (Förste et al., 2014), and the corresponding Bouguer anomalies were calculated using *Tesseroids* by Uieda et al. (2016a). Figure A.1 compares gravity anomaly fields derived from simple and full Bouguer corrections and illustrates that especially in the Andes and Sierras Pampeanas short-wavelength differences exist. These differences, however, are negligibly small compared to the wavelengths of density variations of the crystalline crust, i.e. the unknown in the density modeling procedure.
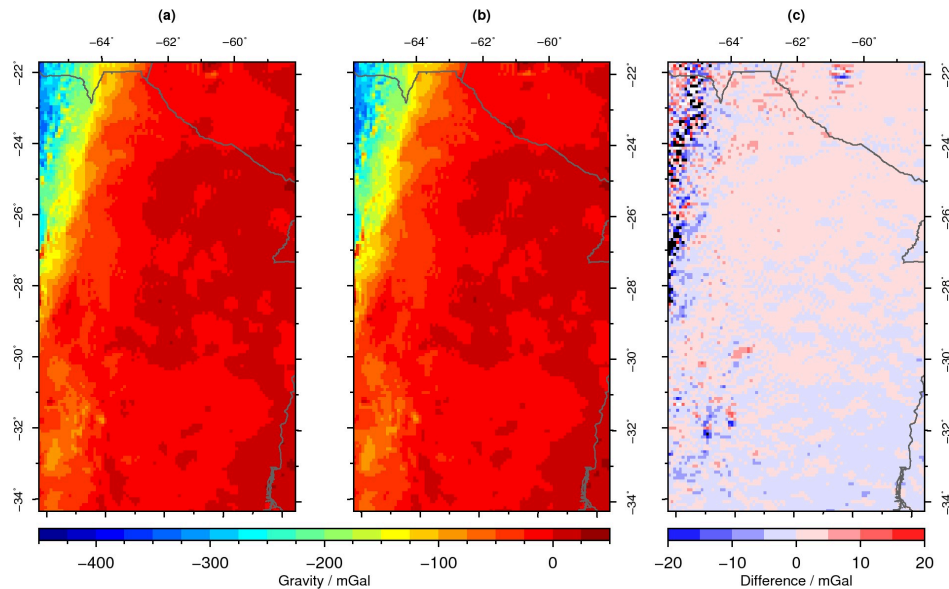
Figure A.1.: Impact of full Bouguer correction: **(a)** Gravity anomaly with simple Bouguer correction using the Bouguer slab (Barthelmes and Köhler, 2012; Förste et al., 2014); **(b)** gravity anomaly for a full spherical Bouguer correction using *tesseroids* (Uieda et al., 2016a) while considering the Earth's sphericity and topography; **(c)** difference between the anomaly fields in (a) and (b).

A.4. Supporting figures
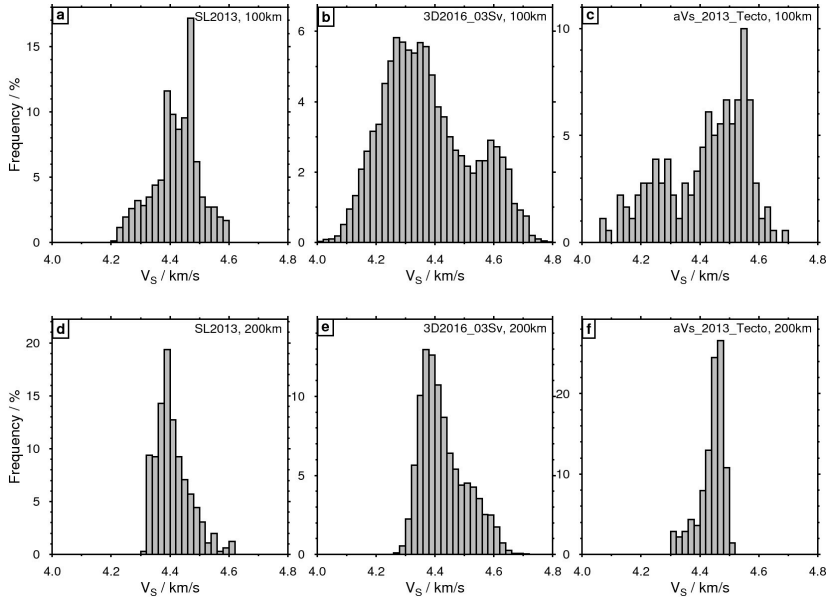
Figure A.2.: Histograms of shear wave velocities at 100 (area 67-55°W, 35-20°S) and 200 km (area 65-55°W, 35-20°S) depth. SL2013 is Schaeffer and Lebedev (2013), 3D2016_03Sv is Debayle et al. (2016), A2013 is Assumpção et al. (2013): **(a)** SL2013 at 100 km; **(b)** 3D2016_03Sv at 100 km; **(c)** A2013 at 100 km; **(d)** SL2013 at 200 km; **(e)** 3D2016_03Sv at 200 km; **(f)** A2013 at 200 km.
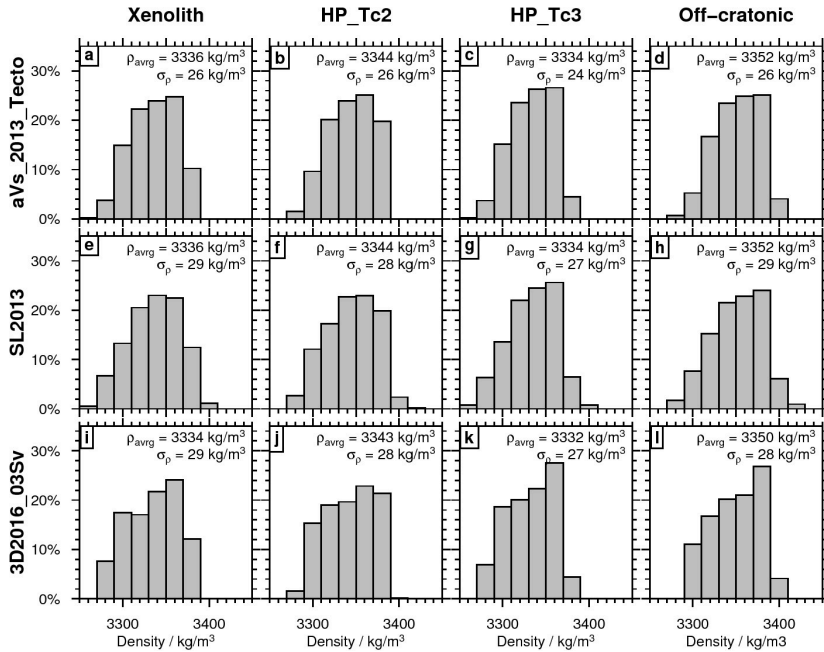
Figure A.3.: Density histograms of the lithospheric mantle between 50 to 200 km depth for different assemblages obtained from shear wave velocity models. Columns represent assumed mineralogy from Table 2.1, rows the used shear wave velocity model (aVs_2013_Tecto - Assumpção et al. (2013); SL2013 - Schaeffer and Lebedev (2013); 3D2016_03Sv - Debayle et al. (2016)). Given also is the average density ρ_{avrg} and the standard deviation σ_ρ. Average density maps are provided in the supplements, Fig. 11.
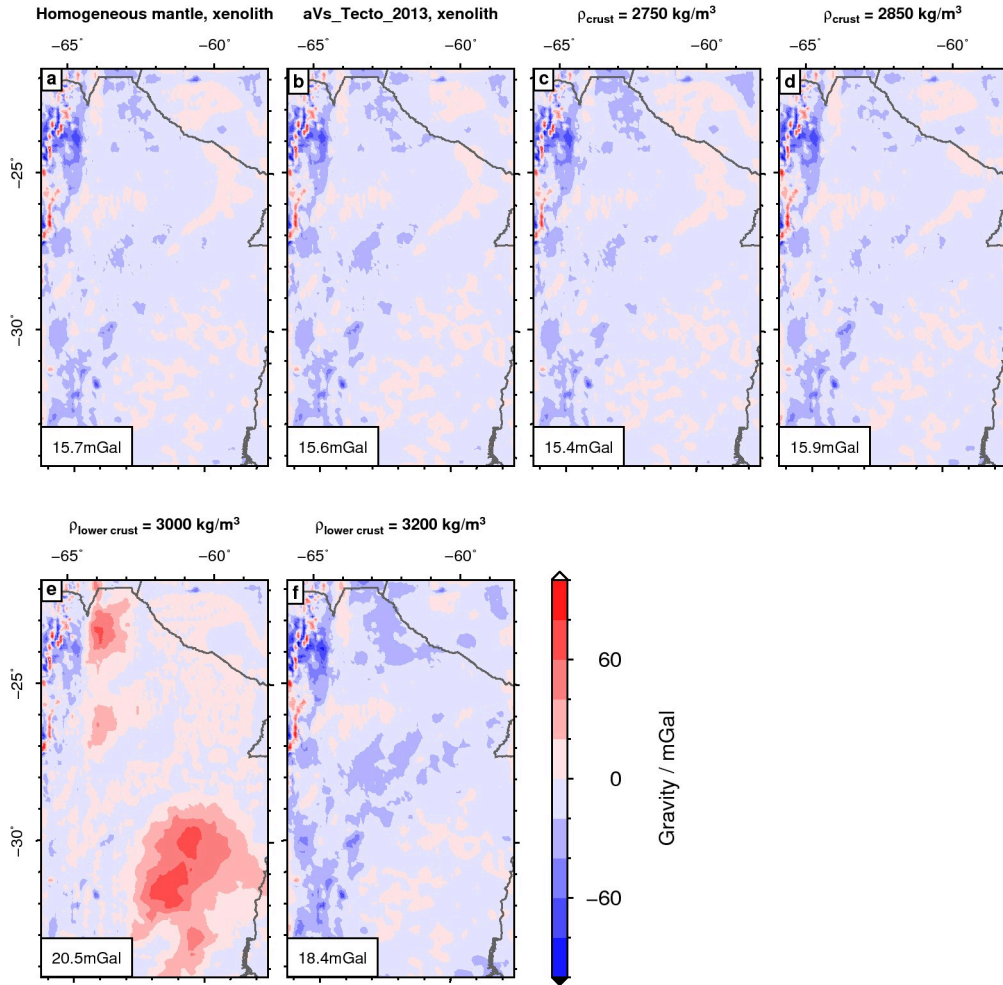
Figure A.4.: Gravity residuals after inversion. Boxes in the bottom left corners indicate the RMS of the field. **(a)** Homogeneous mantle with *Xenolith* assemblage; **(b)** mantle voxel from Assumpção et al. (2013) and *Xenolith* assemblage; **(c)** sensitivity model upper crust with $\rho_{UCrust} = 2750\,\mathrm{kg\,m^{-3}}$; **(d)** sensitivity model upper crust with $\rho_{UCrust} = 2850\,\mathrm{kg\,m^{-3}}$; **(e)** sensitivity model lower crust with $\rho_{LCrust} = 3200\,\mathrm{kg\,m^{-3}}$; **(f)** sensitivity model lower crust with $\rho_{LCrust} = 3000\,\mathrm{kg\,m^{-3}}$.
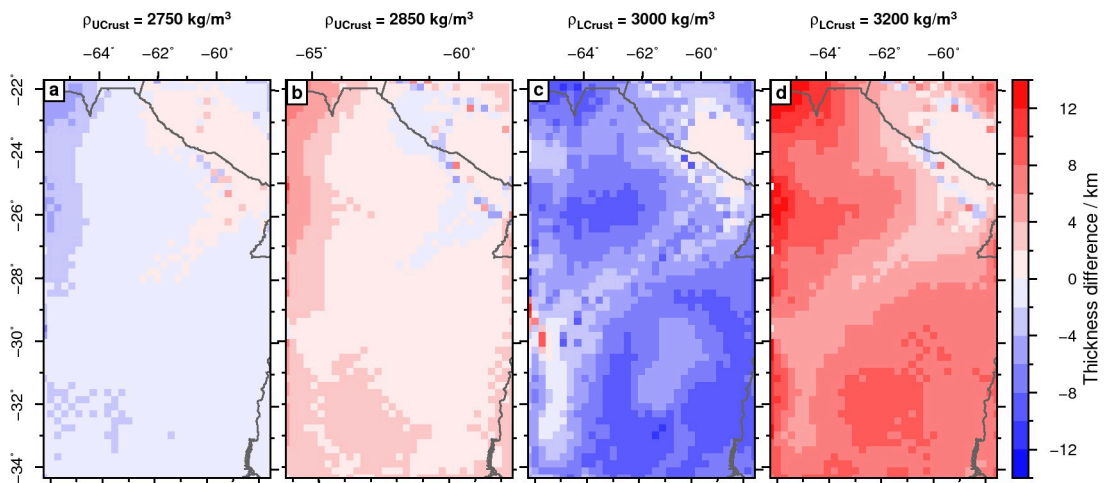
Figure A.5.: Sensitivity of the top of lower crust to density variations in the crystalline crust. For **(a)** density upper crust of $2750\,\mathrm{kg\,m^{-3}}$; **(b)** density upper crust of $2850\,\mathrm{kg\,m^{-3}}$; **(c)** density lower crust of $3000\,\mathrm{kg\,m^{-3}}$; **(d)** density lower crust of $3200\,\mathrm{kg\,m^{-3}}$.
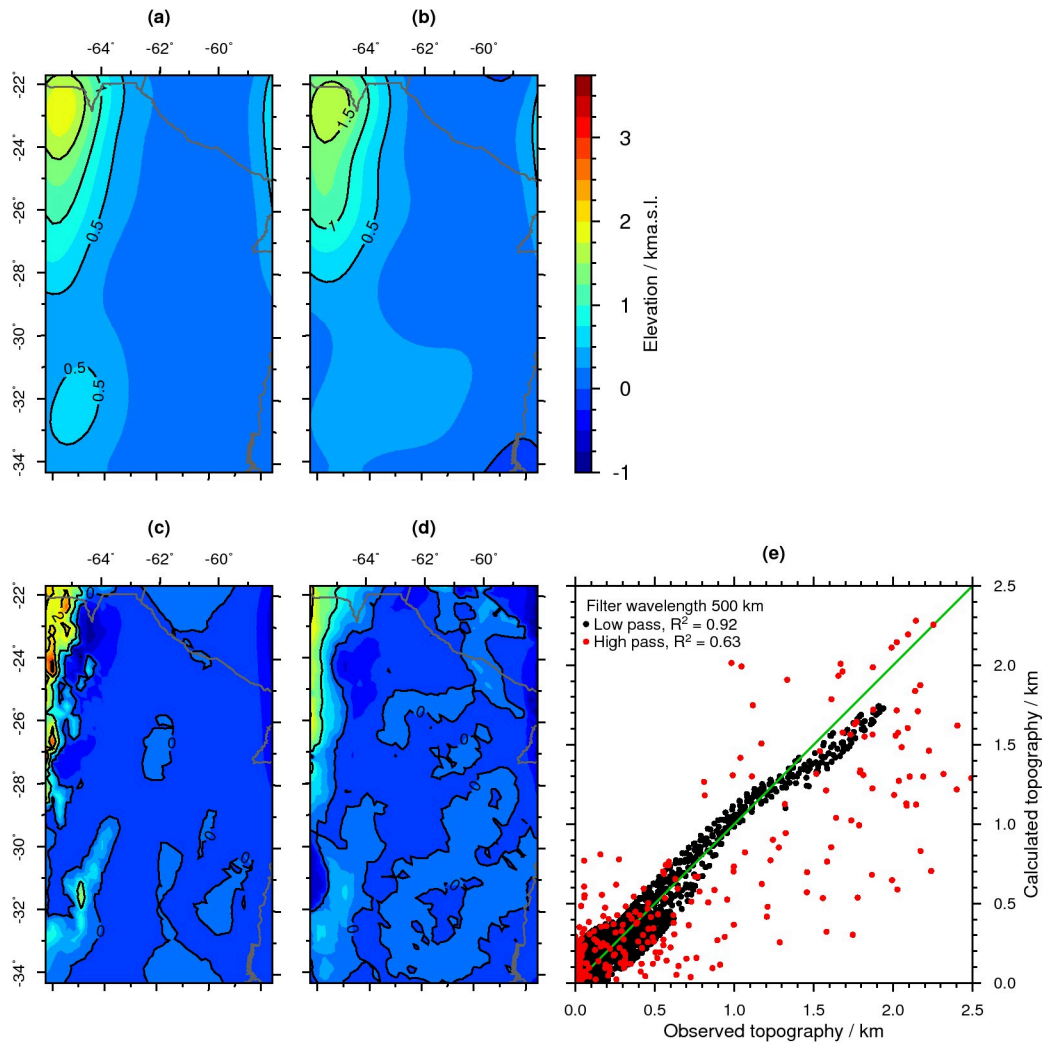
Figure A.6.: FFT-filtered topographic maps. Filtered using a Gaussian band-pass with $\lambda = 500$ km. **(a)** Low-pass ETOPO1; **(b)** low-pass isostatic topography; **(c)** high-pass ETOPO1; **(d)** high-pass isostatic topography; **(e)** cross-plot.

B. Density model of the Jan Mayen-East Greenland region

B.1. Density configuration of the mantle at depths below 50 km

The seismic wave velocity configuration of the mantle provides constraints on its thermal and hence density structure, although the proposed methods of wave velocity conversion differ significantly (Cammarano and Guerri, 2017). For the greater Jan Mayen-East Greenland Region, the velocity of horizontally polarized shear waves (V_{SH}) in the mantle can be derived from a tomographic model of the North Atlantic region (Rickers et al., 2013). It is based on non-linear full-waveform inversion techniques and measurements of the instantaneous phase misfit. Compared to the global S-wave model S20RTS (Ritsema et al., 1999) and European full-waveform model (EU-TF) (Fichtner and Trampert, 2011), the V_{SH} model (NA-IP) (Rickers et al., 2013) is characterized by a significantly improved resolution for both the upper and lower mantle; therefore, it images small-scale anomalies, such as spreading ridges and plume distribution under the NE Atlantic Region. The V_{SH} model comes with a horizontal grid spacing of 100 km and a depth-dependent vertical spacing of 10 km in the uppermost 350 km, 20 km between 350 and 700 km, and 50 km between 700 and 1300 km depth. Given the vertical grid size of the V_{SH} tomography (10 km) at shallow depths and the maximum Moho depth (> 28 km) (Fig. 2.13c), we suggest that the values of V_{SH} shallower than 50 km are likely to be artificially affected by the crustal velocities. In addition, compared to the V_{SH} constraints at greater depth (e.g. 100 km), the mantle between the Moho and 50 km is more likely represented by lithospheric mantle compared to asthenospheric mantle. Therefore, we restrict the usage of V_{SH} constraints to depths >50 km for 3D gravity modelling. First we convert the regional V_{SH} tomography model into mantle temperature. Then, the mantle density can be estimated as a function of pressure and temperature.

B.1.1. Conversion of shear-wave velocity to temperature

Based on an averaged shear wave velocity model and a generic thermal model for the Pacific oceanic lithosphere, Priestley and McKenzie (2006) proposed a set of empirical equations and constants to convert mantle shear wave velocity to temperature (T). The conversion method is based on the assumption that the shear-velocity structure of the oceanic upper mantle can be largely explained by its temperature, pressure, and some activation processes that are related to an elastic behaviour close to melting temperatures. Retained melt present at low concentration is expected to have a minor impact. Hence, this non-linear V_s-T-relationship is assumed to be valid for any mantle composition, while being most accurate for temperatures that exceed 1100 °C.

For the V_s-T-conversion, the original S wave model has been extracted for the depth range of $50 - 250$ km. The V_s model has been rescaled by applying the Triangulation Method of the software OpendTect (Huck, 2012) to create a regular grid with 10x10 km horizontal and 10 km vertical dimension. This node spacing is consistent with the upper crustal and sedimentary model. One variable to be predefined for the empirical equations to be solved is pressure (Priestley and McKenzie, 2006). In this study, we use sedimentary and crustal dens-
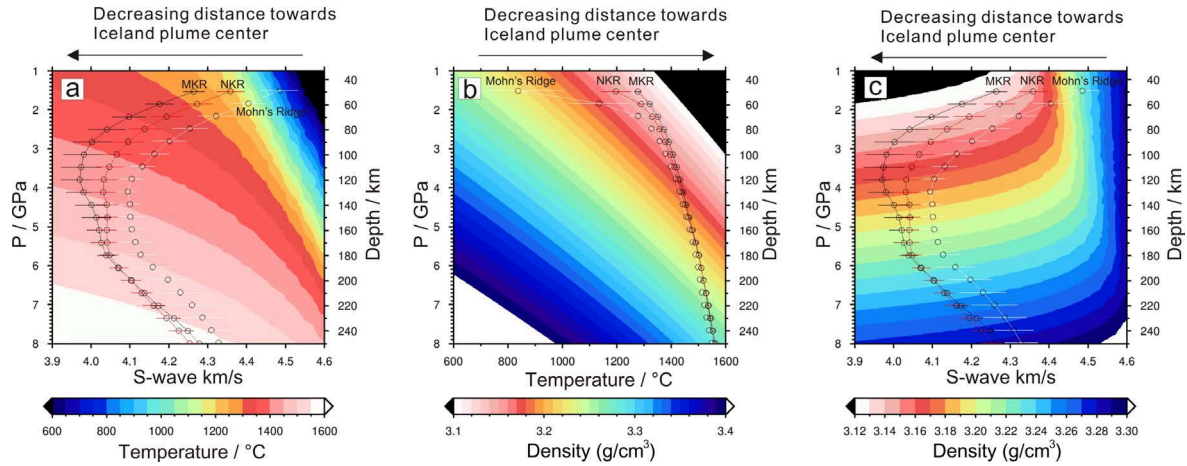
Figure B.1.: **(a)** Temperature field calculated by using the conversion of Priestley and McKenzie (2006). **(b)** Results of density calculation (Eqn. B.1 – B.5) applied to pressure and temperature ranges of 1 to 8 GPa and 600 to 1600 °C. **(c)** Calculated density as a function of the pressure and S wave velocity variations. Superimposed circles and bars represent the parameter variation obtained from sub-domains of the study area; the horizontal bars indicate the standard deviation of V_s (Fig. B.1a,c) and temperature (Fig. B.1b), while the mean is indicated by the circles. The black, red, and white lines show the data derived from MKR, NKR, and Mohn's Ridge domains (Fig. 2.13d) respectively.

ity structures (Tab. 2.5) and an assumed constant mantle density (3300 kg m^{-3}) to estimate the corresponding pressure variations. Figure B.1a shows the temperature configuration derived from the entire tomographic model in the parameter space of V_{SH}, depth and pressure. In general, the converted temperature is increasing as the depth increases and velocity decreases, but lateral temperature differences are much larger at shallow depths.

The V_s-to-T conversion is a strongly nonlinear function of temperature and the uncertainties of the temperature estimates decrease with increasing temperature (Priestley and McKenzie, 2006, 2013). As proposed by Priestley and McKenzie (2013), V_s derived temperatures below 900°C are associated with large uncertainties, where a change in V_s of 0.04 km/s would result in a 250 °C difference. The same V_s change at 1200°C would correspond to 100°C and at 1350°C, it would only be 30°C (Fig. B.1a).

B.1.2. Conversion of temperature to density

The density of the mantle is controlled by its composition and the *in situ* pressure and temperature conditions. Throughout this modelling study, we assume that the mantle of the greater Jan Mayen-East Greenland Region is compositionally homogeneous. Bai et al. (2014) have proposed a set of equations to calculate the density of mantle rock at given pressure and temperature. Thereby, both the thermal expansion coefficient (α_T) and the bulk modulus (K_T) are considered as temperature dependent, while the authors derive their formulation from laboratory measurements on olivine samples as described by Kroll et al. (2012), which is based on a large number of thermal expansivity measurements and an up-to-date summary of bulk modulus data. The mantle density affected by thermal expansion at temperature T is:

$$\rho_T = \rho_0[1 - \alpha_T(T - T_0)] \tag{B.1}$$

where T_0 is equal to 273 K, while ρ_0 is the mantle reference density (3300 kg m^{-3}) at temperature T_0. The relationship between α and T is estimated by Bai et al. (2014) with a nonlinear

function of temperature:

$$\alpha_T = (6 \cdot 10^{-10}T^3 - 2 \cdot 10^{-6}T^2 + 0.0039T + 1.727) \cdot 10^{-5} \tag{B.2}$$

The bulk modulus K represents the pressure change required for a given volume change. The bulk modulus can be calculated as a function of temperature (Kroll et al., 2012):

$$K_T = 127.97 - 0.0232(T - 300) \tag{B.3}$$

where the units for K_T and T is GPa and K, respectively.

The density changes related to the *in situ* pressure ($\Delta\rho_p$) at a specific pressure (P) and bulk modulus (K) can be calculated using the following function (Bai et al., 2014):

$$\Delta\rho_p = \rho_0 \left(P - P_0\right) K_T^{-1} \tag{B.4}$$

where P_0 is the standard atmospheric pressure and the unit for P is GPa.

Finally, the mantle density for a specific temperature and pressure is calculated:

$$\rho = \rho_T + \Delta\rho_p \tag{B.5}$$

Figure B.1b shows the density variation for pressure and temperature ranges of 1 to 8 GPa and 600 to 1600 °C, respectively. At a given depth, high mantle temperature corresponds to lower mantle density, while at a given temperature, the larger the pressure (greater depth) the higher the corresponding mantle density. Under a specific temperature and pressure, the modelled mantle density reveals similar results compared to mantle densities based on Grose and Afonso (2013) and Schutt and Lesher (2006) using the same reference mantle density (3300 kg m^{-3}).

B.1.3. Results

Figure B.1c shows the calculated mantle density variation as a function of the pressure and V_s variations. For most of the parameter field, density increases with depth. At depths shallower than 90 km, the mantle densities reveal large lateral variations due to large variations in mantle temperature (Fig. B.1a). The calculated mantle density range at 50 km depth is 151 kg m^{-3} (3127 – 3278 kg m^{-3}), decreasing to 10 kg m^{-3} (3145 – 3155 kg m^{-3}) at 90 km depth. The mantle densities at depths greater than 90 km have a range of less than 10 kg m^{-3} (Fig. B.1b).

The MKR, NKR, and Mohn's Ridge show significantly different V_s, mantle temperature and density configurations (Fig. B.1), in particular at depths shallower than 90 km. At a given depth, MKR has the lowest V_s, correspondingly highest mantle temperature and lowest mantle density. In contrast, the Mohn's Ridge shows the highest V_s, lowest mantle temperature and largest mantle density.

Figure B.1b shows that under the MKR domain, the thermal gradient is decreasing with increasing depth. At shallower depth (<90 km), the average thermal gradient is 2.5 K/km. At depths >90 km, thermal gradients decrease to an almost constant value around 0.8 K/km. The mantle densities at MKR are characterized by small changes (3130 to 3140 kg m^{-3}) at depth shallower than 90 km, which indicates that the temperature and pressure effects nearly compensate each other. At depths >90 km, the mantle density is mainly influenced by the pressure as it is gradually increasing with a constant density gradient of around 1 kg m^{-3}/km.

The mantle temperature below Mohn's Ridge is characterized by a significantly higher thermal gradient (>20 K/km) at depths between 50 and 70 km. However, where depths exceed 70 km, the thermal gradient is similar to the MKR. Under the Mohn's Ridge, the average mantle density is decreasing from 3230 kg m^{-3} (50 km depth) to 3150 kg m^{-3} (70 km
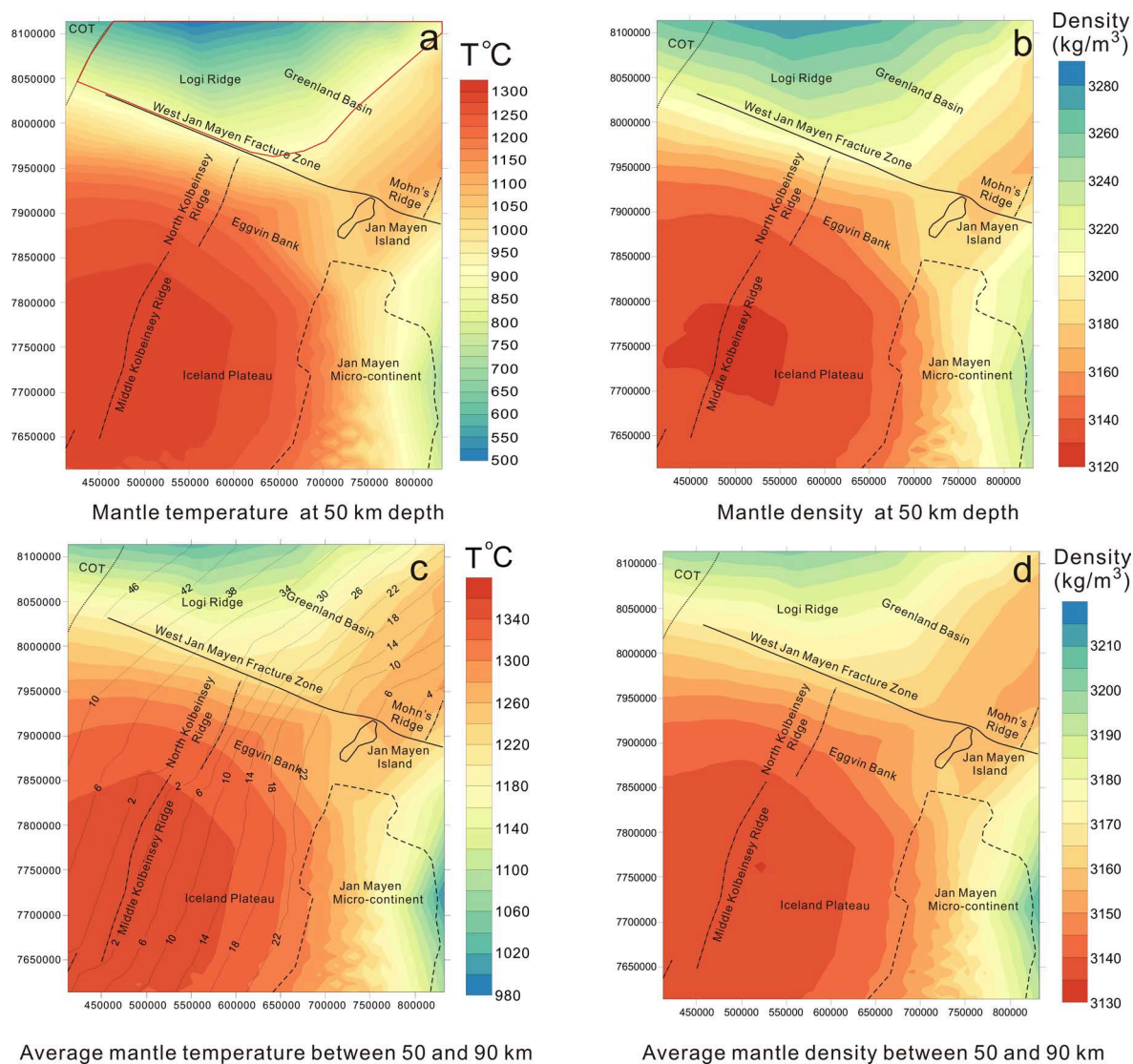
Figure B.2.: **(a)** Converted temperature variations at a depth of 50 km. The red solid line delineates an area within the Greenland basin with temperatures of less than 900 °C. **(b)** Corresponding density variations at a depth of 50 km. **(c)** Average mantle temperature between 50 and 90 km (T_{50-90}). The solid grey lines with numbers show the oceanic seafloor ages (Müller et al., 2008). **(d)** Average mantle density between 50 and 90 km (ρ_{50-90}).

depth) (Fig. B.2b). At depths larger than 70 km, the mantle density is gradually increasing (1 kg m^{-3}/km) as the pressure plays a more significant role to determine the mantle density. At a given depth, the average mantle temperature and density of the NKR domain are between those of the MKR and Mohn's Ridge.

As the largest lateral temperature and density variations are observed for depths between 50 and 90 km, we plot the average mantle temperature (T_{50-90}) and density (ρ_{50-90}) for this depth interval (Fig. B.2c-d). In general, this interval shows trends of decreasing T_{50-90} (increasing ρ_{50-90}) from MKR to NKR and to Mohn's Ridge, and each ridge also shows similar trends of decreasing temperature (increasing density) with increasing age of the oceanic crust. For example, under the MKR domain, T_{50-90} is 1350 °C under the ridge axis and gradually decreases to 1310 °C at locations where the oceanic crust is as old as 22 Ma. Under the Mohn's Ridge, the mantle temperature at the spreading centre is 1270 °C, while it decreases to 1050 °C at around 45 Ma. In contrast to the MKR and Mohn's Ridge, the mantle temperature and density under the NKR domains have large variations, where the mantle temperature decreases (density increases) northward.

B.2. Gravity checkerboard test
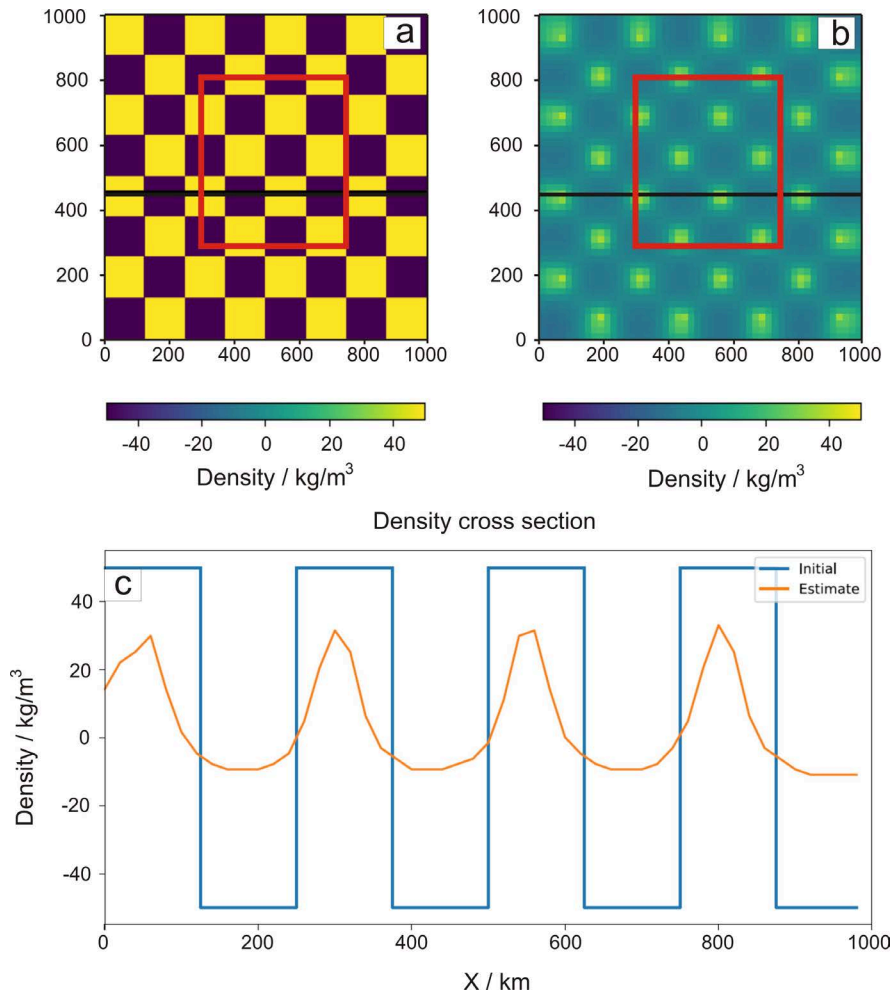
Figure B.3.: Checkerboard resolution test result performed using the gravity inversion algorithm *fatiando a terra* (Uieda et al., 2013). **(a)** Input density perturbations of ± 50 kg/m^3 with cell of 125 km · 125 km. **(b)** Recovered density perturbations from the checkerboard tests. **(c)** Input density and recovered density perturbations along a section (black line) in Fig. B.3a, b. Red boxes represent the size of our study area in relation to the extended model.

To determine the resolution of the 3D gravity inverse model, we imposed a checkerboard pattern with a dimension of 125 km × 125 km, and a density perturbation of ± 50 kg m^{-3} in the uppermost mantle (Fig. B.3). This configuration is comparable to the regional anomalies we are investigating. The results show that the inversion has an even response over the model area, without lateral offsetting the anomalies. However, the ability to recover the true amplitude of density anomalies seems significantly reduced at this scale, but the lateral dimensions of the anomalies are clearly resolvable. In reality, we do not expect strong density contrasts anywhere near what was used in the checkerboard tests, and the modelled density anomalies are expected to be nearer to the true values than seen in these tests.

C. Steady-state subduction

C.1. Definition of the transient boundary conditions

C.1.1. Oceanic slab: left boundary

For the transient thermal model we set the left boundary condition at the oceanic slab to the temperature profile of a slab with the appropriate age utilising the *plate* model by Hasterok (2013). This model is based on the solution of the heat equation by McKenzie (1967). We compute the temperatures T_P of the plate cooling model by

$$T_P\left(t,z\right) \;=\; T_m\left(\frac{z}{a} + \sum_{n=1}^{\infty}\frac{2}{n\pi}e^{-\beta_n x a^{-1}}\sin\frac{n\pi z}{a}\right) \tag{C.1}$$

$$\beta_n \;=\; \sqrt{Pe^2 + n^2\pi^2} - Pe \tag{C.2}$$

$$Pe \;=\; \frac{va}{2\kappa} \tag{C.3}$$

where T_m is the temperature at the base of the oceanic lithosphere, z the depth below sea floor, a the thickness of the oceanic plate, x the distance from the spreading ridge, Pe the Peclet Number, v the half spreading rate, and κ the thermal diffusivity. To obtain the correct temperature profile, we define that the half spreading rate is equal to the plate convergence rate, and substitute $x = vt$, where t is the age of the slab. The sum in Eqn. C.1 was computed for $n \in [1, 100]$, and 100 equally spaced points z from 0 to 90 km depth. Finally, the temperature profile was transferred to the left boundary of the model (Fig. 3.2b) using a piecewise linear interpolation.

C.1.2. Oceanic slab: lower boundary

The lower boundary of the oceanic slab was assigned a linear temperature increase

$$T\left(z\right) = T_m - \left(z - z_{lab}\right)\nabla T \tag{C.4}$$

where $T_m = 1364\,°\mathrm{C}$ is the temperature at the base of the *plate* model (Hasterok, 2013), z a depth, and $\nabla T = 0.3\,\mathrm{K\,km^{-1}}$ the mantle adiabat (Turcotte and Schubert, 2014).

D. Additional methods and data

D.1. Computation of lithospheric strength

Goetze and Evans (1979) first introduced the concept of the yield strength envelope to describe the strength of the lithosphere. The yield strength of the lithosphere is the amount of stress a rock can withstand without irrecoverably deforming by plastic flow or brittle failure. If the actual differential stress at a certain depth is below the yield strength, the rocks deform elastically. It is defined as the maximum differential stress $\Delta\sigma_{\max}$ that is the difference between the largest (σ_1) and smallest (σ_3) stress. Depending on the temperature (T) and pressure (P) conditions, different deformation mechanisms will act on the rocks.

At shallow depths, rocks will deform by brittle deformation. This mechanism has been empirically described by Byerlee (1978) and can be expressed as

$$\Delta\sigma_b = f_f\ gz\rho_{\text{bulk}}\ (1 - f_p) \tag{D.1}$$

where f_f is Byerlee's friction coefficient, ρ_{bulk} the bulk rock density, g the gravitational acceleration, z the depth of the rock below topography and f_p the pore fluid factor (Burov, 2011). The pore fluid factor is $f_p = \rho_f\rho_b^{-1}$ where ρ_f is the density of the fluid. Byerlee's friction coefficient depends on the applied external stress and is

$$f_f = \begin{cases} 1 - R^{-1} & \text{for normal faulting} \\ R - 1 & \text{for thrusting} \end{cases} \tag{D.2}$$

where R depends on the internal friction angle Φ:

$$R = \left(\sqrt{1 + \Phi^2} - \Phi\right)^{-2} \tag{D.3}$$

Byerlee (1978) found that, largely independent of the lithology, the friction coefficient $\mu_f = \tan\Phi$ is around 0.85 at normal stresses below $200\,\text{MPa}$, and about 0.6 for higher normal stresses. Along faults, friction coefficients have been reported as low as 0.1 to 0.2 at shallow depths (Carpenter et al., 2011, 2012), and around 0.3 to 0.4 near the brittle-ductile transition (Behnsen and Faulkner, 2012; Behr and Platt, 2014).

At sufficiently high temperature and pressure, rocks will start to deform by solid state creep. In this project, I regarded dislocation creep $\Delta\sigma_{dis}$ and Dorn's law creep $\Delta\sigma_{dorn}$:

$$\Delta\sigma_{\text{dis}} = \left(\frac{\dot{\epsilon}}{A_p}\right)^{\frac{1}{n}} \exp\frac{Q_p}{nRT} \tag{D.4}$$

$$\Delta\sigma_{\text{dorn}} = \sigma_D \left(1 - \sqrt{-\frac{RT}{Q_D}\ln\frac{\dot{\epsilon}}{A_D}}\right) \tag{D.5}$$

where $\dot{\epsilon}$ is the strain rate, A_p the pre-exponential scaling factor for dislocation creep, n the power law exponent, Q_p the activation energy, σ_D the Dorn's law stress, Q_D the Dorn's law activation energy, A_D the Dorn's law strain rate, R the universal gas constant and T the
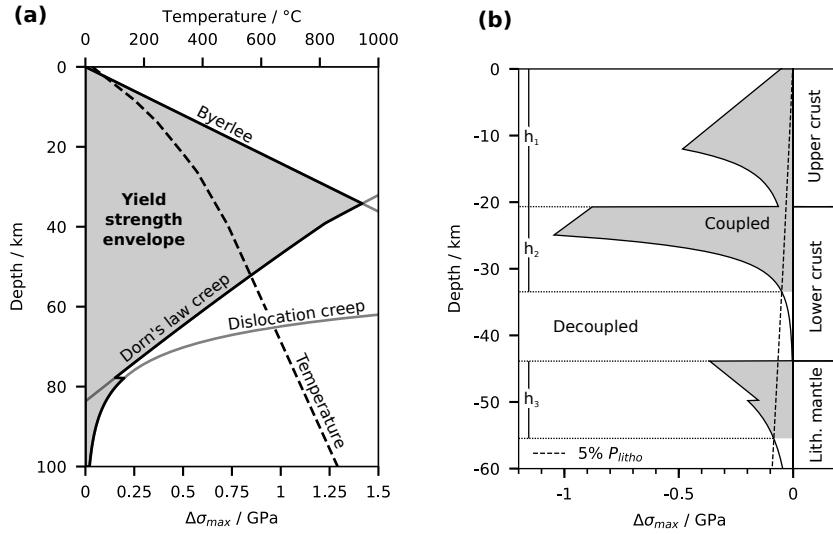
Figure D.1.: (a) Competing deformation mechanisms and the resulting yield strength envelope for dry peridotite by Hirth and Kohlstedt (2004) with Dorn's law parameters by Kameyama et al. (1999). The geotherm is by McKenzie et al. (2005). **(b)** Yield strength envelope of a 3-layered lithosphere. The lower bounds of the mechanical thicknesses h_1 to h_3 are defined where $\Delta\sigma_{max} < 5\% P_{\text{litho}}$ or $\Delta\sigma_{max} < 20\,\text{MPa}$. Note that in this example the upper and lower crust are coupled although the upper crust behaves ductile.

absolute temperature. In the crust and upper mantle, dislocation creep is the dominant creep mechanism (Kameyama et al., 1999; Karato and Wu, 1993). However, Goetze and Poirier (1978) found that Dorn's law better describes the ductile behaviour of the lithospheric mantle if differential stresses of dislocation creep exceed 200 MPa. Accordingly, the ductile yield stress is determined by

$$\Delta\sigma_d = \begin{cases} \sigma_{\text{dis}} & \text{if in the crust} \quad \vee \ \sigma_{\text{diff}} < 200\,\text{MPa} \\ \sigma_{\text{dorn}} & \text{if in the mantle} \ \wedge \ \sigma_{\text{diff}} \geq 200\,\text{MPa} \end{cases} \tag{D.6}$$

Finally, the yield strength $\Delta\sigma_{\text{max}}$ is obtained as

$$\Delta\sigma_{\text{max}} = \text{sign}\,(\dot{\epsilon}) \min\,(\Delta\sigma_b,\ \Delta\sigma_d) \tag{D.7}$$

where $\text{sign}(\dot{\epsilon})$ is negative for compression, and positive for extension. The strain rate $\dot{\epsilon}$ is defined as the temporal change of the strain ϵ

$$\dot{\epsilon} = \frac{d}{dt}\frac{L_1 - L_0}{L_0} \tag{D.8}$$

where L_0 is the width of a structure before it was shortened to width L_1 during the time t (e.g. Turcotte and Schubert, 2014). Over the past 25 Myr, the average shortening rate in the Central Andes is estimated between 8 to 13 mm yr^{-1} (Liu et al., 2000; Schmitz and Kley, 1997; Sheffels, 1990). Assuming that this shortening rate persists at present-day, and is equally distributed between trench and foreland, i.e. along a width of about 700 km (Fig. 3.10d), strain-rates of about $5\cdot10^{-16}\,\text{s}^{-1}$ should be acting at present-day. In the Santa-Barbara system, Kley and Monaldi (2002) reported shortening of 20 to 30 km along cross-sections with an initial width of about 160 km. Zapata Henao et al. (2018) found that uplift of the nearby Aconquija ranges was initiated at 10 Ma, which together with the shortening estimates by Kley and Monaldi (2002) yields a strain rate of $5\cdot10^{-16}\,\text{s}^{-1}$ as well. Given the consistency of

these estimates, I used this strain rate during strength-analyses in this project.

The friction coefficient for Byerlee's law was set to a constant $f_f = 2.0$. This regards the overall convergent regime in the study area and is equivalent to an internal friction angle of 33°. Note that the value of f_f may be as low as 0.8 within faults near the brittle-ductile transition, assuming $\mu_f = 0.3$. The pore fluid factor f_p was set to 0.35, and ρ_{bulk} taken from the respective rock types (Tab. 3.4).

D.2. Effective elastic thickness

According to Burov and Diament (1995), the effective elastic thickness T_e in a rheologically stratified lithosphere with n *decoupled* layers is computed using

$$T_e = \left(\sum_{i=1}^{n} \Delta h_i^3 \right)^{\frac{1}{3}} \tag{D.9}$$

and for n *coupled* layers as

$$T_e = \sum_{i=1}^{n} \Delta h_i \tag{D.10}$$

where Δh_i is the mechanical thickness of a layer. If a stratified lithosphere consists of multiple coupled and decoupled layers (Fig. D.1b), Δh_i of the coupled layers is summed according to D.10. Then, T_e is computed using the sum with Eqn. D.9. The mechanical thickness is measured from the top of the layer to the depth where either the differential stress is less than 0.01 to $0.05 P_{\text{litho}}$ (lithostatic pressure), or where it is below 10 to $20\,\text{MPa}\,\text{km}$. For the computation I used $0.05 P_{\text{litho}}$ and an absolute lower limit of $20\,\text{MPa}$. The resulting T_e mark the lower limit of what could be computed with the individual models.

D.3. Modelling the tectonic domains of northern Argentina

As outlined in Chapters 2.1.1.1 and 5.3, the modelling area comprises the Río de la Plata craton and the Pampia terrane. Additionally, Famatina, Arequipa-Antofalla, Cuyania and the Chilenia terranes are located within the extended modelling area (Fig. 2.1). To assess the differences between a model with and without terrane discrimation in the upper crust, I inverted the crustal structure for a model that discriminates between the aforementioned terranes. Apart from the upper crustal configuration, the approach followed is the same as described in Chapter 2.1.2.2.

The prevailing lithologies of the individual terranes and the densities that I assigned are outlined in Table D.3. The lithologies for the Pampia terrane are derived from average v_p of 5.8 to 6.0 $\text{km}\,\text{s}^{-1}$(Alvarado et al., 2009) using the compilation by Christensen and Mooney (1995). Density of the Chilenia terrane was obtained from the 3D model by Prezzi et al. (2009), using values from the upper crust of the Coastal- and the Pre-cordillera. The resulting depth to the top of the lower crust is shown in Fig. D.2b, and the average density distribution in Fig. D.3b. For a discussion of the results see Chapter 5.3.
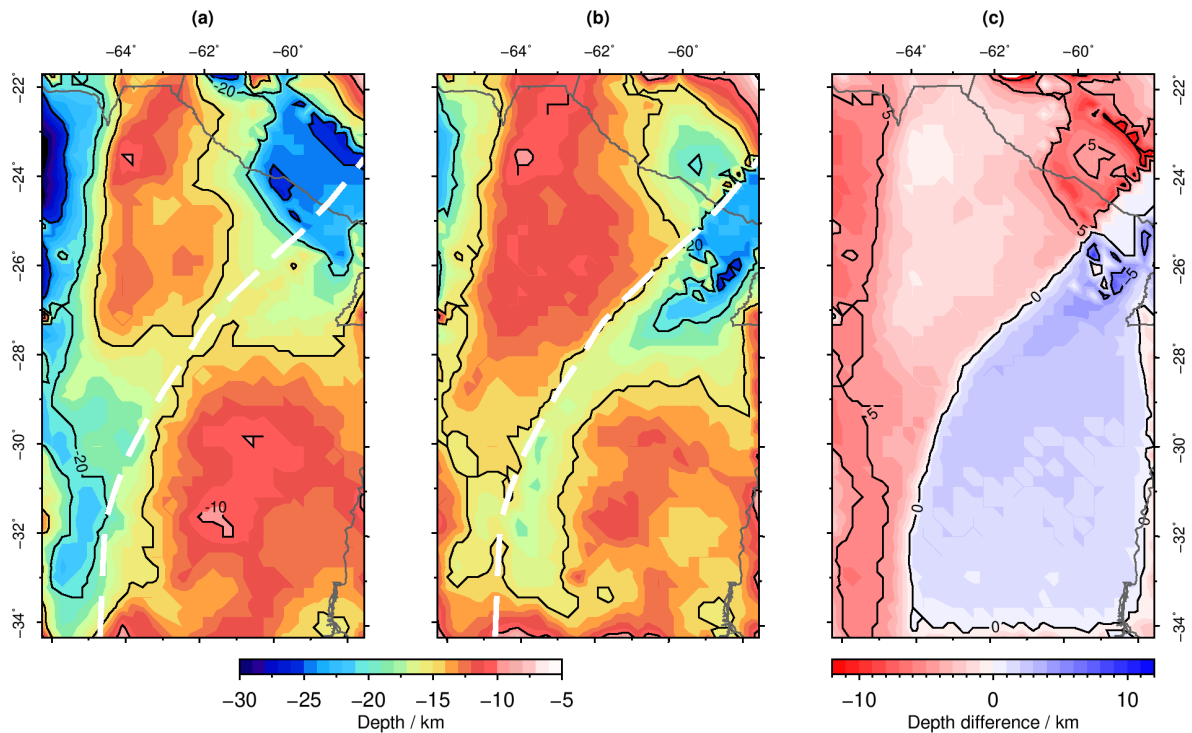
Figure D.2.: Comparison of the top of the lower crust with and without terrane subdivision. The dashed white line is the Transbrasilian Lineament and separates the Pampia Terrane (west) from the Río de la Plata craton (east). **(a)** model without terranes from Chapter 2.1, Fig. 2.6; **(b)** model with terranes; **(c)** difference (a)-(b).
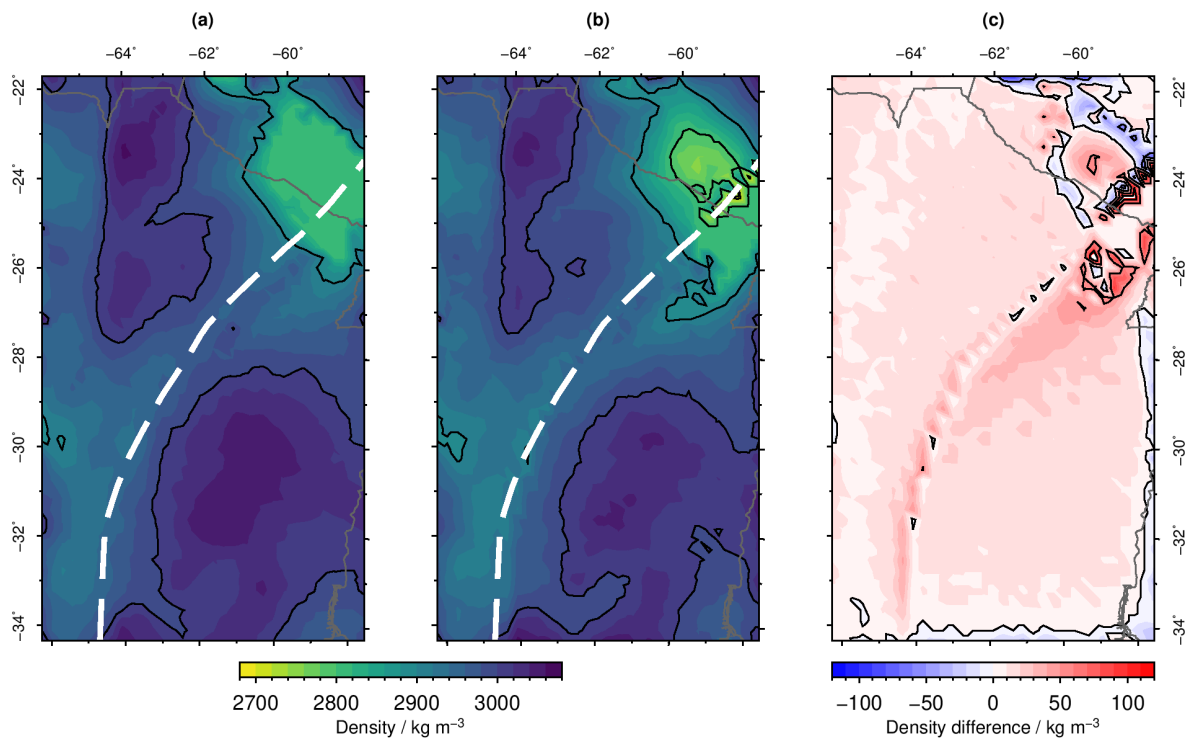
Figure D.3.: Comparison of the average density between **(a)** the model without differentiation of the tectonic domains, see Chapter 2.1, and **(b)** the model including the terranes according to Ramos et al. (2010); **(c)** shows the density difference.
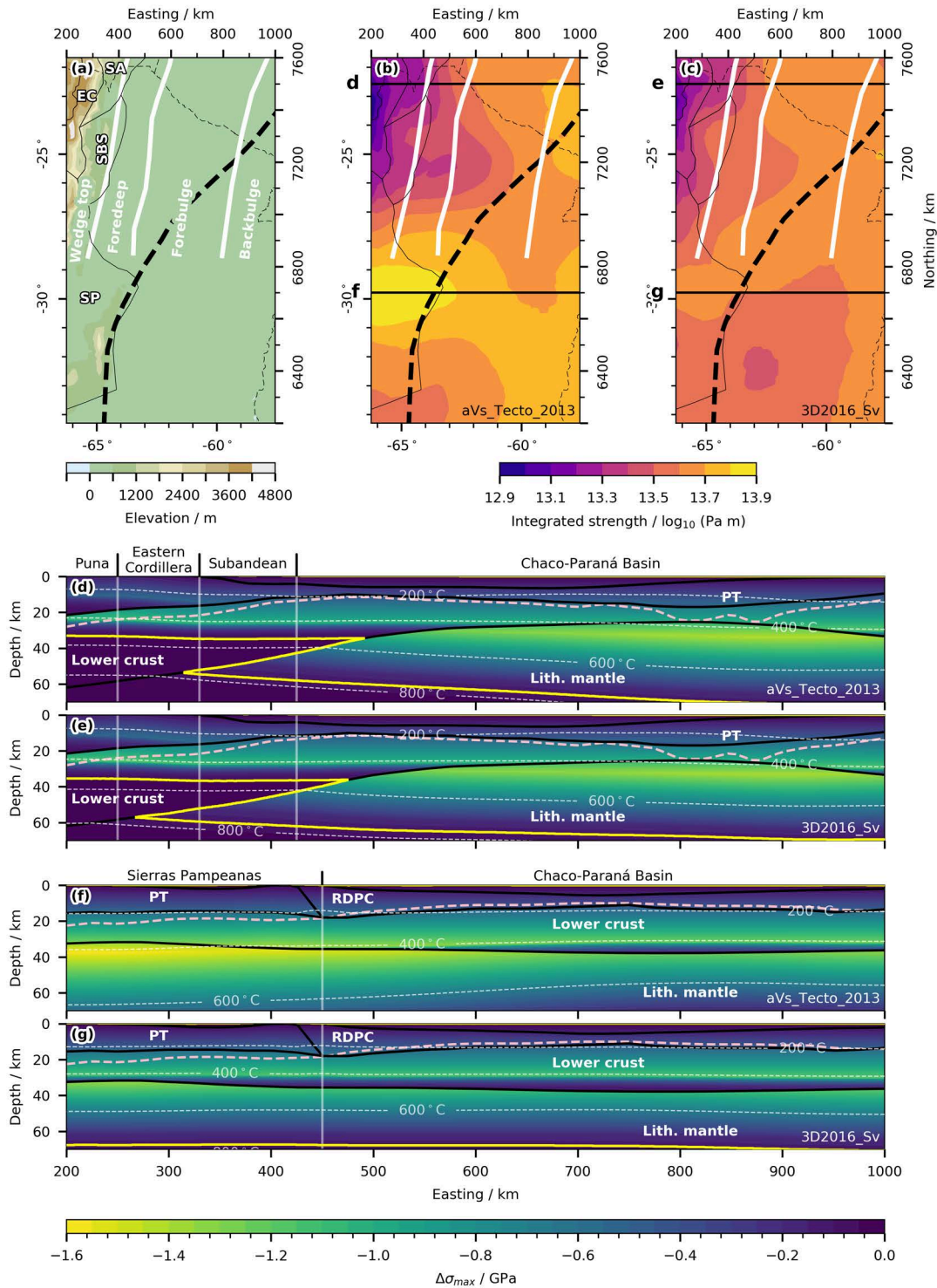
Figure D.4.: Lithospheric strength of the model with differentiated tectonic domains. **(a)** surface topography; **(b, c)** integrated lithospheric strength for model *aVs_Tecto_2013* and *3D2016_03Sv*; **(d, e)** strength profile in the northern CPB, see (a), for model *aVs_Tecto_2013* and *3D2016_03Sv*, the pink dashed line represents the top of the lower crust as derived in Chapter 2.1; **(f, g)** strength profile through the Sierras Pampeanas, see (a).

Table D.1.: Prevailing lithologies in the tectonic domains of the extended study area and the density assigned in the advanced model. See Fig. 2.1 for study area and domains.

Tectonic domain	Prevailing lithology	Density / kg m^{-3}
Río de la Plata craton	Gabbro, granodiorite, norites, Olivine-gabbro [a]	2800[b]
Pampia terrane	Andesite, quartzite, metasediments [c,d]	2670[d]
Famatina terrane	Granodiorites, tonalites [e]	2850[e]
Cuyania terrane	Granite, granodiorite, slate, phyllite, granitic gneiss, biotite-gneiss, paragranulite [d]	2680[d]
Chilenia terrane	Siliciclastics, granitoids [f]	2700[g]
Arequipa-Antofalla terrane	Argillites, metagreywacke, granitoids [h]	2710[g]

[a] Rapela et al. (2007) and Winn Jr and Steinmetz (1998); [b] Kirchner (1997), Lucassen et al. (2001) and Vilà et al. (2010); [c] Alvarado et al. (2007); [d] Christensen and Mooney (1995); [e] Otamendi et al. (2009); [f] Ramos et al. (1986); [g] Prezzi et al. (2009); [h] Segerstrom and Turner (1972)

D.4. Supplemental figures
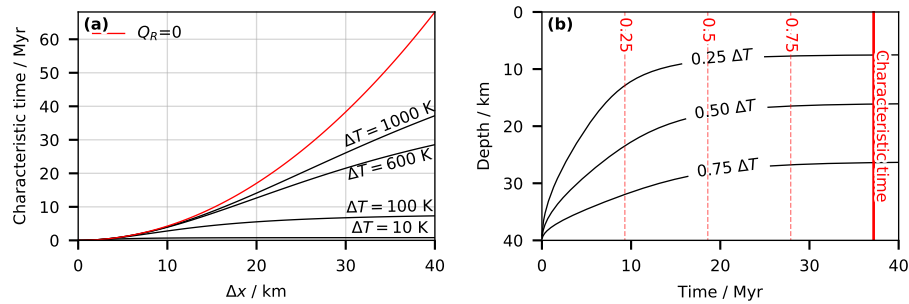
Figure D.5.: Characteristic time for diffusive processes (Eqn. 3.5). **(a)** Characteristic time depending on thickness Δx for the upper crust (Tab. 3.4) with different ΔT, and for the same material without radiogenic heat production ($Q_R = 0$); **(b)** solution for 1D heat diffusion for an applied temperature difference ΔT using parameters of (a) for $\Delta x = 20\,\mathrm{km}$.
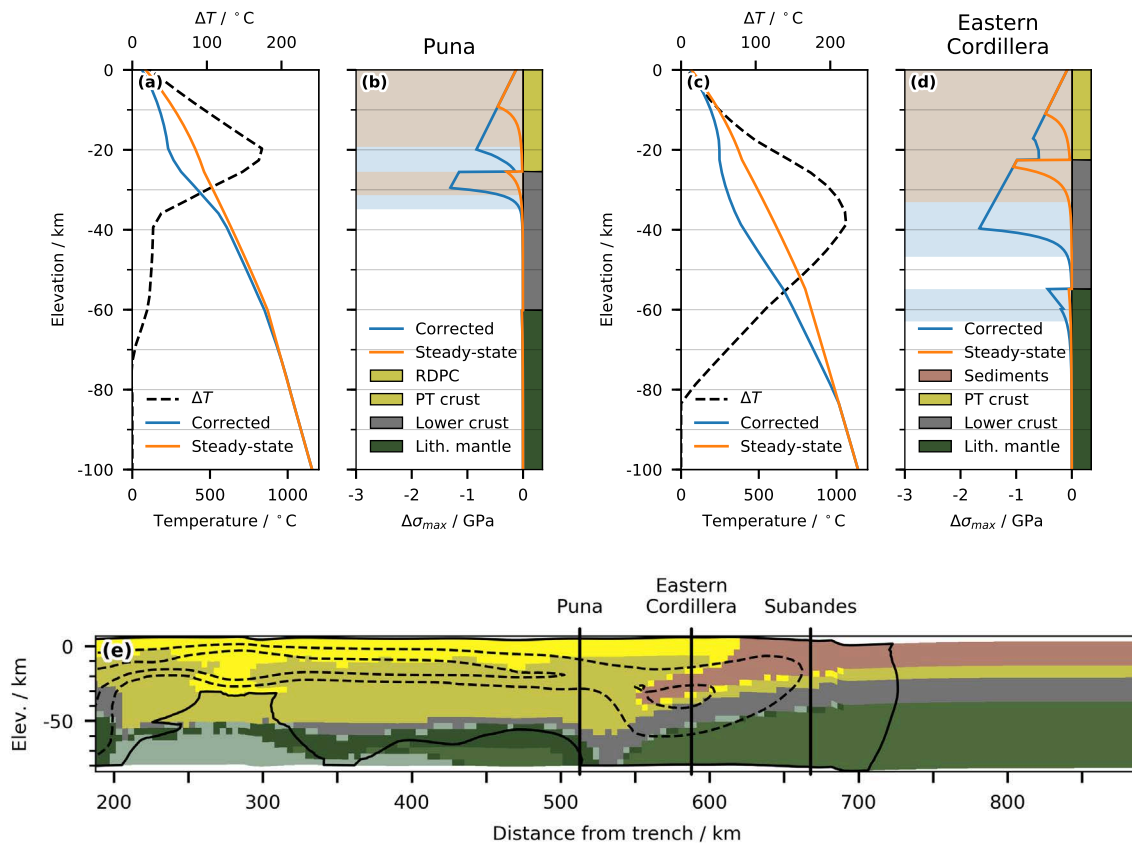
Figure D.6.: Estimates of the present-day rheology of the foreland lithosphere using the results of Chapter 3.2. Steady-state and corrected geotherms and yield strength envelopes in: **(a,b)** the Puna plateau, corresponding to 225 km Easting in Figure 4.4d (p. 96); **(c,d)** the Eastern Cordillera, at 300 km Easting in Fig. 4.4d; **(e)** final time step of the coupled geodynamic model by Sobolev et al. (2006) showing the locations of the extracted temperature differences in (a), (c) and Fig. 5.1a together with the temperature differences (Fig. 3.10d, p. 81) between steady-state and transient-state. Solid contour is 0 °C difference, dashed contours are in 100 °C intervals.
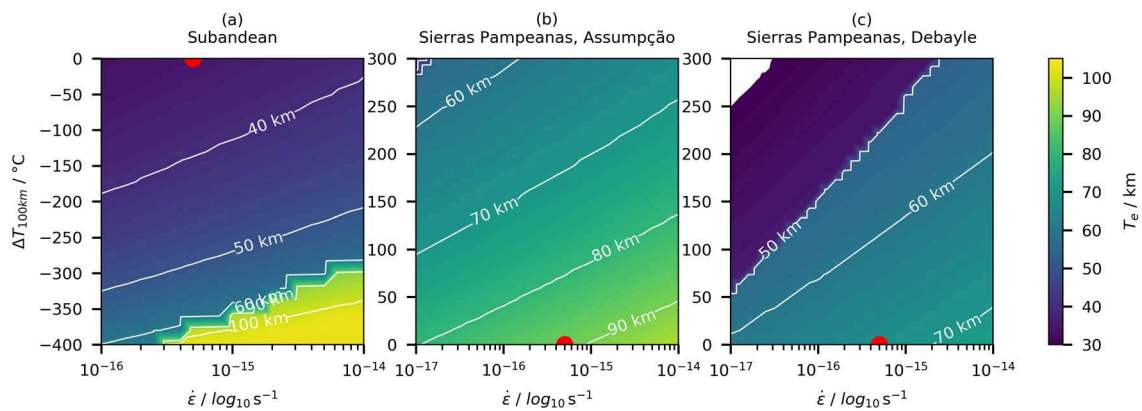
Figure D.7.: Changes in geothermal gradient and strain rate $\dot{\epsilon}$ required in the thermo-rheological models to agree with the hypothesis that thin-skinned deformation correlates to high effective elastic thickness (T_e), and thick-skinned deformation to low T_e. Ordinate plots $\Delta T_{100\,km}$, the temperature difference at $100\,\mathrm{km}$ depth with respect to the modelled geotherm. Negative values indicate that the geotherm was cooled, positive that it was heated. The temperature difference was linearly increased from surface to $100\,\mathrm{km}$ depth, and the red dots mark the values predicted by the models. **(a)** Subandean fold-and-thrust belt, situation similar in models *Assumpção* and *Debayle*; **(b)** Sierras Pampeanas in model *Assumpção*; **(c)** in model *Debayle*. The plots illustrate that if the structure and composition of the lithosphere stay constant, the temperatures at the lower boundary of the models would have to change by several hundred degrees in order to invert the predicted relationship between T_e and surface deformation style.

E. Data and code

The data repository to this document is available in C. Meeßen (2019a). *Data repository to "The thermal and rheological state of the Northern Argentinian foreland basins"*. Version v1.0. DOI: 10.5281/zenodo.3562215. URL: https://doi.org/10.5281/zenodo.3562215.

The code for the inversion of seismic velocities, used in Chapters 2.1 and 4 is available in C. Meeßen (2017). *VelocityConversion*. Version v1.0.1. DOI: 10.5880/GFZ.6.1.2017.001. URL: http://pmd.gfz-potsdam.de/panmetaworks/showshort.php?id=escidoc:2301889.

The code that was used to analyse the thermo-rheological models in Chapter 4 is available in C. Meeßen (2019b). *pyGMS: lithosphere-scale rheological analyses of GMS models in Python*. Version v1.0.0. DOI: 10.5281/zenodo.3338066. URL: https://doi.org/10.5281/zenodo.3338066.

Acknowledgements